UNIVERSIDAD DE CÓRDOBA

FACULTAD DE CIENCIAS

Instituto Universitario de Nanoquímica

Departamento de Química Inorgánica e Ingeniería Química

NUEVOS MATERIALES INORGÁNICOS FUNCIONALES PARA LA PREVENCIÓN DE LA CONTAMINACIÓN EN EL PATRIMONIO Y HÁBITAT URBANO

NEW FUNCTIONAL INORGANIC MATERIALS FOR THE PREVENTION OF POLLUTION IN HERITAGE AND URBAN HABITAT

Directores:

Prof. Ivana Pavlovic Milicevic

Prof. Luis Sánchez Granados

Memoria de Tesis Doctoral presentada por:

ADRIÁN PASTOR ESPEJO

Para aspirar al grado de *Doctor por la Universidad de Córdoba*

Córdoba, 29 de noviembre de 2021

TITULO: *NUEVOS MATERIALES INORGÁNICOS FUNCIONALES PARA LA PREVENCIÓN DE LA CONTAMINACIÓN EN EL PATRIMONIO Y HÁBITAT URBANO*

AUTOR: *Adrián Pastor Espejo*

© Edita: UCOPress. 2022
Campus de Rabanales
Ctra. Nacional IV, Km. 396 A
14071 Córdoba

https://www.uco.es/ucopress/index.php/es/
ucopress@uco.es

TÍTULO DE LA TESIS:

NUEVOS MATERIALES INORGÁNICOS FUNCIONALES PARA LA PREVENCIÓN DE LA CONTAMINACIÓN EN EL PATRIMONIO Y HÁBITAT URBANO

DOCTORANDO/A: Adrián Pastor Espejo

INFORME RAZONADO DEL/DE LOS DIRECTOR/ES DE LA TESIS

El trabajo científico que se recoge en la memoria que presenta el Licenciado en Química D. Adrián Pastor Espejo ha sido realizado bajo nuestra dirección en los laboratorios del departamento de Química Inorgánica e Ingeniería Química.

Este trabajo se desarrolla dentro de la línea de investigación de los grupos FQM-175 y FQM-214, dedicada al estudio de nuevos materiales fotocatalizadores para la eliminación de gases NO_X del entorno urbano. La puesta a punto de nuevas técnicas de análisis, así como la intensa labor investigadora realizada por el Ldo. Pastor ha permitido obtener una gran cantidad de resultados novedosos, como se constata en el hecho de que de este trabajo se han escrito 10 artículos (4 como primer autor), 6 aportaciones en libros científicos, y 18 comunicaciones a congresos nacionales e internacionales, recibiendo el Ldo. Pastor 4 premios de investigación y divulgación científica. Además, como complemento a su formación investigadora, el Ldo. Pastor realizó dos estancias de investigación (3 y 6 meses de duración) en un laboratorio de una institución

europea de máximo prestigio; Chemistry Research Laboratory, University of Oxford (Reino Unido).

En nuestra opinión, la memoria que se presenta reúne los requisitos necesarios para optar al grado de Doctor (doctorado con Mención Internacional) por la Universidad de Córdoba.

Por todo ello, se autoriza la presentación de la tesis doctoral.

Córdoba, 29 de noviembre de 2021

Firma del/de los director/es

PAVLOVIC MILICEVIC IVANA - 45943883A

Firmado digitalmente por PAVLOVIC MILICEVIC IVANA - 45943883A
Fecha: 2021.11.29 09:46:56 +01'00'

Fdo: Ivana Pavlovic Milicevic

SANCHEZ GRANADOS LUIS RAFAEL - 30524375V

Firmado digitalmente por SANCHEZ GRANADOS LUIS RAFAEL - 30524375V
DN: C=ES, SERIALNUMBER=IDCES-30524375V, G=LUIS RAFAEL, SN=SANCHEZ GRANADOS, CN=SANCHEZ GRANADOS LUIS RAFAEL - 30524375V
Razón: Soy el autor de este documento
Ubicación: la ubicación de su firma aquí
Fecha: 2021.11.29 08:02:04+01'00'
Foxit PDF Reader Versión: 11.0.1

Fdo: Luis Sánchez Granados

El éxito sin honor es el mayor de los fracasos.

Vicente del Bosque

No es mejor líder el que más grita, sino el que más empuja.

El problema de nuestra época consiste en que sus hombres no quieren ser útiles sino importantes.

Winston Churchill

Cuando quieras emprender algo, habrá un montón de gente que te dirá que no lo hagas. Cuando vean que no te pueden detener, te dirán cómo lo tienes que hacer. Cuando finalmente lo logres, dirán que siempre han creído en ti.

Dante Gebel

Puedes ser todo lo virtuoso que quieras, pero no eres nadie sin tu equipo.

Zinedine Zidane

Índice

Preámbulo

La Sociedad tiene una intensa relación con el patrimonio urbano. Es el medio que crea para su hábitat y confort, en el que trabaja, por el que se mueve y que aprecia preservando la herencia de generaciones anteriores. En este contexto, la Sociedad ha ido trasladando poco a poco su vida a las ciudades, las cuales han experimentado una profunda evolución a lo largo de la historia: desde el Neolítico, donde el desarrollo de la agricultura y el pastoreo favoreció la creación de los primeros asentamientos sedentarios, hasta la formación de las primeras civilizaciones agrícolas, como Mesopotamia (3500 a.C.). Posteriormente durante el siglo XVIII, época de la Revolución Industrial, se promovió un éxodo rural motivado por la presencia de fábricas, almacenes, estaciones de ferrocarril, etc. en las ciudades, llegando al primer gran aumento de los núcleos de población.

En la actualidad, más de 4200 millones de personas, en torno al 55 % de la población mundial, residen en las ciudades, donde existe un mayor crecimiento económico, como consecuencia de la industrialización y de la existencia de una red organizada de infraestructuras. Además, la Organización de Naciones Unidas (ONU) prevé un drástico aumento de la población, llegando a los 9700 millones de habitantes para el año 2050. De estos, se estima que en torno al 70 % vivirá en medios urbanos. En España, dicho porcentaje subirá hasta alcanzar un 88 % de cara al 2050, como se observa en la **Figura 1** (datos procedentes de División de Población de las Naciones Unidas (ONU)).

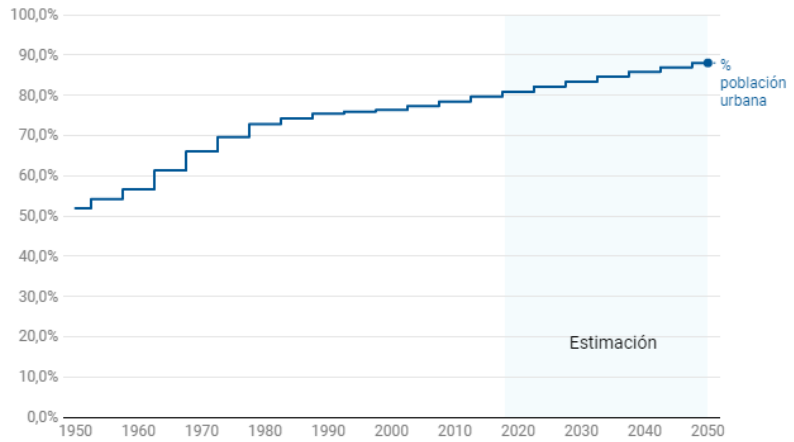

Figura 1. Evolución del porcentaje de población residiendo en áreas urbanas en España [División de Población de la ONU].

Este acelerado crecimiento de población urbana a nivel global viene inherentemente asociado con una mayor necesidad de recursos energéticos, un aumento de la utilización de los medios de transporte y una extensión de la industrialización en general. En consecuencia, todos estos factores hacen que el desarrollo sostenible del hábitat urbano tenga un papel crucial. En este aspecto, dos preocupaciones principales surgen en la Sociedad respecto a la conservación del patrimonio y hábitat urbano: i) prevenir el deterioro del mismo para que siga ejerciendo la funcionalidad para el que fue creado y ii) asegurar su correcta y sana habitabilidad.

Gran parte del patrimonio histórico urbano como fachadas, edificios, monumentos y esculturas está elaborado con piedras de diferente naturaleza (calizas, dolomitas, mármoles, etc.), morteros de cemento, o morteros de yeso y cal. La gran variedad de materiales y técnicas de ejecución que se emplean implica que las alteraciones que sufren son muy heterogéneas y complejas. Los procesos de alteración y deterioro se producen por el natural envejecimiento de los materiales y/o

por la acción inducida de agentes como la temperatura, el agua, sales, ciclos de hielo-deshielo o contaminantes medioambientales. De hecho, en los últimos años se ha observado un deterioro acelerado en los materiales del patrimonio urbano a causa del incremento de la contaminación urbana. Uno de los principales procesos de degradación de los materiales pétreos es el biodeterioro provocado por la contaminación microbiana. Diferentes variedades de microrganismos, como algas y hongos, pueden crecer en la superficie, poros o fisuras del material, originando procesos de biometeorización, cambios del color, alteraciones superficiales, fenómenos de disgregación-pulverización, pérdida de adhesión y cohesión entre los constituyentes mineralógicos y una progresiva pérdida de material y de su resistencia mecánica. Para evitar este tipo de contaminación, es común la utilización de sistemas químicos de conservación preventiva. Estos sistemas se basan en la aplicación de morteros de restauración que incorporan en su composición agentes biocidas (también denominados agentes antimicrobianos), es decir, compuestos químicos que poseen la propiedad de impedir el crecimiento microbiano en el material pétreo. No obstante, la efectividad y duración a largo plazo de la actividad antimicrobiana del material es muy limitada debido a la lixiviación y descomposición de los compuestos químicos que ejercen la actividad biocida. Por consiguiente, sería de interés el empleo de sistemas de liberación controlada de estos agentes químicos. De esta manera, dichos compuestos se encontrarían anclados a un soporte inorgánico, quedando más protegidos frente a agentes externos (luz, pH, etc.) y retrasándose la lixiviación al medio. Además, una mayor dispersión del principio activo en el soporte haría que se consiguiese el mismo rendimiento antimicrobiano con una menor

cantidad de agente químico, lo que mejoraría los costes de producción y la sostenibilidad del sistema.

Por otra parte, la salud del ciudadano requiere respirar aire de buena calidad. Su degradación o contaminación ocurre por la emisión a la atmósfera de contaminantes procedentes de la industria y, principalmente, del tráfico rodado. Disponer de un aire limpio en el hábitat urbano se ha convertido en un objetivo prioritario de la política ambiental y de las estrategias de desarrollo sostenible. Entre los contaminantes primarios del aire más habituales se encuentran los óxidos de nitrógeno (NO y NO_2, denominados conjuntamente como gases NO_X), los compuestos orgánicos volátiles (COVs), y las partículas en suspensión. Los gases NO_X son muy tóxicos (incluso más que el monóxido de carbono), por lo que originan efectos nocivos para la salud y además son responsables de serios problemas medioambientales: smog fotoquímico, lluvia ácida, ozono troposférico, disminución capa de ozono, etc., factores que también acentúan el desgate de los materiales urbanos. Aunque la recomendación de la Organización Mundial de la Salud (OMS) y la legislación europea establecen que no se puede superar la media anual de 40 $\mu g/m^3$ para el NO_2 (o 200 $\mu g/m^3$ por hora), desafortunadamente, muchas ciudades en el mundo, incluido ciudades españolas, superan estos valores (**Figura 2**). En consecuencia, se ha documentado que alrededor de 71.000 personas fallecen de forma prematura anualmente en la Unión Europea a causa de la inhalación de gases NO_x (datos del Informe de la Agencia Europea del Medioambiente, 2020).

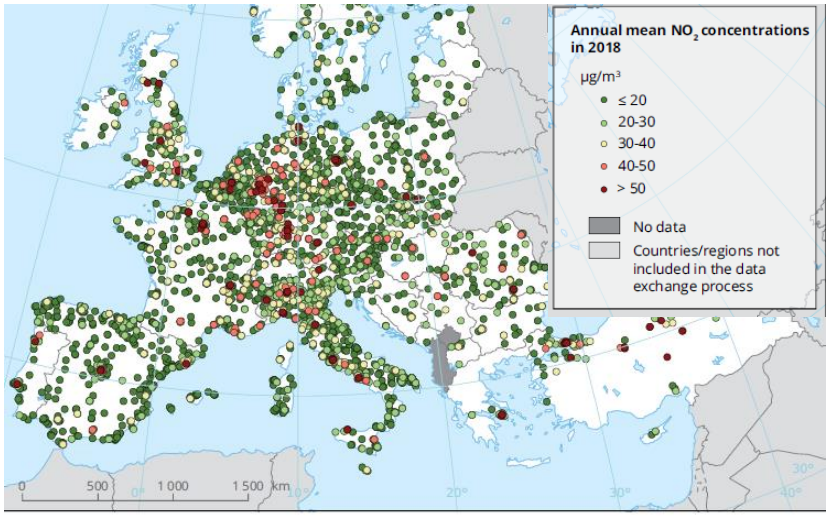

Figura 2. Concentraciones de NO_2 en Europa en 2018 [Informe de la Agencia Europea del Medioambiente, 2020].

La concentración atmosférica de NO_X de una ciudad podría reducirse in-situ (proceso llamado De-NO_x) mediante la creación de grandes superficies descontaminantes. En este sentido, se ha descrito la capacidad de los materiales urbanos (morteros, pinturas, pavimentos, etc.) para actuar como materiales auto-descontaminantes, gracias a la incorporación de aditivos basados en compuestos fotocatalizadores de TiO_2. A este respecto, la fotocatálisis es una tecnología muy prometedora, dado que la acción De-NO_x tiene lugar a temperatura ambiente y con el uso exclusivo de agua, moléculas de oxígeno y luz solar, componentes abundantes en la atmósfera urbana. Como resultado, los gases NO_x se retiran de la atmósfera cuando se oxidan a las especies nitratos y nitritos. No obstante, la remediación fotocatalítica es una tecnología que no tiene un uso extendido en la arquitectura urbana ya que, entre otras limitaciones, el coste de los compuestos basados en TiO_2 es muy elevado en comparación con las materias primas que constituyen los materiales urbanos. Por lo

tanto, la búsqueda de aditivos fotocatalizadores alternativos de bajo coste permanece como un reto pendiente de alcanzar.

En este contexto, este trabajo tiene dos objetivos globales. El primer objetivo de esta Tesis Doctoral se centra en el estudio de nuevos compuestos inorgánicos que puedan ser utilizados como aditivos para prevenir la contaminación microbiana de los morteros de rehabilitación usados en entornos urbanos. La investigación aborda la utilización de Carbendazima (CBZ), un fungicida de bajo coste inexplorado en este tipo de materiales. Asimismo, se ha estudiado la incorporación de CBZ a diferentes soportes inorgánicos basados en compuestos tipo arcilla. Estos compuestos poseen una gran capacidad adsorbente, un bajo coste de producción y aseguran una buena compatibilidad con la matriz del mortero.

El segundo objetivo global de este trabajo, también en consonancia con la preservación del hábitat urbano, es el desarrollo de nuevos aditivos inorgánicos con propiedades fotocatalíticas para el proceso De-NO_x, de manera que sean eficaces, económicos y viables para una utilización extensiva. En esta línea, se ha estudiado el uso del ZnO nanoparticulado, un fotocatalizador con baja toxicidad y gran capacidad de absorción de radiación UV. En su síntesis se ha utilizado la cáscara del arroz, un importante residuo agroindustrial, con el objetivo de mejorar la dispersión de las nanopartículas de ZnO y de reducir costes, sin crear un mayor impacto ambiental. Adicionalmente, la familia de compuestos Hidróxidos Dobles Laminares (HDLs) han sido aplicados de forma novedosa como fotocatalizadores De-NO_x. Estos compuestos se caracterizan por una síntesis sencilla y por una enorme versatilidad química y sostenibilidad ambiental, lo que los hace ideales para aplicarlos en esta tecnología fotocatalítica específica.

Preamble

The Society has a close relationship with urban heritage. It is the environment that he creates for his habitat and comfort, where he works, through which he moves and appreciates all whilst preserving the inheritance of previous generations. In this context, the Society has gradually transferred its life to cities, which have undergone a profound evolution throughout history: from the Neolithic Age, where the development of agriculture and pastoralism favoured the creation of the first sedentary settlements, to the formation of the first agricultural civilizations, such as Mesopotamia (3500 BC). Later during the 18th century, - the time of the Industrial Revolution - a rural exodus was promoted. This was motivated by the presence of factories, warehouses, railway stations, etc. in cities, and resulted in the first great increase in city centre populations.

Currently, more than 4.2 billion people - around 55% of the world's population - live in cities, where there is greater economic growth, as a consequence of industrialization and the existence of an organized network of infrastructures. Furthermore, the United Nations (UN) has foreseen a drastic increase in the total population, which it expected to reach 9700 million inhabitants by the year 2050. Of these extra inhabitants, it is estimated that around 70% will live in urban areas. In Spain, this percentage will rise to 88% by 2050, as shown in **Figure 1** (data from the Population Division of United Nations (UN)).

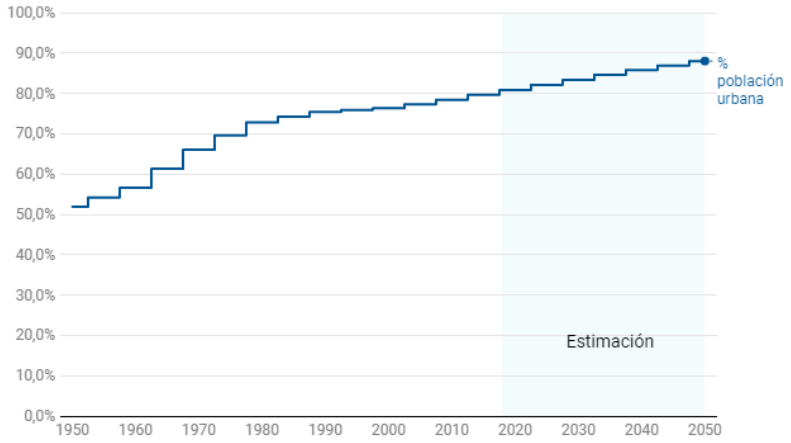

Figure 1. Evolution of the percentage of the population residing in urban areas in Spain [Population Division of UN].

This accelerated growth of urban population at a global level is inherently associated with, a greater need for energy resources, an increase in the use of transportation, and, mostly, an extension of industrialization. Consequently, all these factors make the sustainable development of urban habitat play a key role. In this regard, two main concerns arise in the Society regarding the conservation of heritage and urban habitat: i) prevent its deterioration, so that it continues to exercise the functionality for which it was created and ii) ensure its correct and healthy habitability.

Much of the urban historical heritage such as facades, buildings, monuments and sculptures are made with stones of different nature (limestones, dolomites, marbles etc.), cement mortars, or plaster and lime mortars. The great variety of materials and execution techniques used implies that the alterations they undergo are very heterogeneous and complex. The alteration and deterioration processes are produced by the

natural ageing of the materials and/or by the induced action of external agents such as temperature, water, salts, freeze-thaw cycles or environmental pollutants. In fact, in recent years there has been an accelerated deterioration of these materials due to the increase in urban pollution. One of the main degradation processes of stone materials, caused by microbial contamination, is biodegradation. Different varieties of microorganisms, such as algae and fungi, can grow on the surface, pores or fissures of the material, causing bio-weathering processes, colour changes, surface alterations, disintegration-pulverization phenomena, loss of adhesion and cohesion between the mineralogical constituents and a progressive loss of material and its mechanical resistance. To avoid this type of contamination, the use of chemical preventive conservation systems is common. These systems are based on the application of restoration mortars that incorporate biocidal agents (also called antimicrobial agents) in their composition, that is, chemical compounds that have the property of preventing microbial growth in stone material. The effectiveness and long-term duration of the material's antimicrobial activity is very limited however, due to the leaching and decomposition of the chemical compounds that exert the biocidal activity. Consequently, the use of controlled release systems for these chemical agents would be of interest. In this way, these compounds would be anchored to an inorganic support thus increasing protection from external agents (light, pH etc.) and delaying leaching to the environment. In addition, a greater dispersion of the active principle in the support would achieve the same antimicrobial performance yet a lower amount of chemical agent. This would improve the production cost and sustainability of the system.

Furthermore, the health of the citizens requires breathing good quality air. The degradation or contamination of the air occurs due to the

emission into the atmosphere of pollutants from industry and, mainly, from road traffic. Having clean air in the urban habitat has become a high priority objective of environmental policy and sustainable development strategies. Among the most common primary air pollutants are nitrogen oxides (NO and NO_2, collectively known as NO_X gases), Volatile Organic Compounds (VOCs), and suspended particles. NO_x gases are very toxic (even more so than carbon monoxide), so they cause harmful effects on health. They are also responsible for serious environmental problems: photochemical smog, acid rain, tropospheric ozone, ozone layer depletion, etc., factors that also accentuate the weathering of urban materials. Although the recommendation of the World Health Organization (WHO) and European legislation state that the annual average of 40 µg/m^3 for NO_2 (or 200 µg/m^3 per hour) must not be exceeded, unfortunately, many cities in the world, including Spanish cities, exceed these values (**Figure 2**). Consequently, it has been reported that, annually, around 71,000 people in the European Union die prematurely due to the inhalation of NO_x gases (data from the European Environment Agency, 2020 Report).

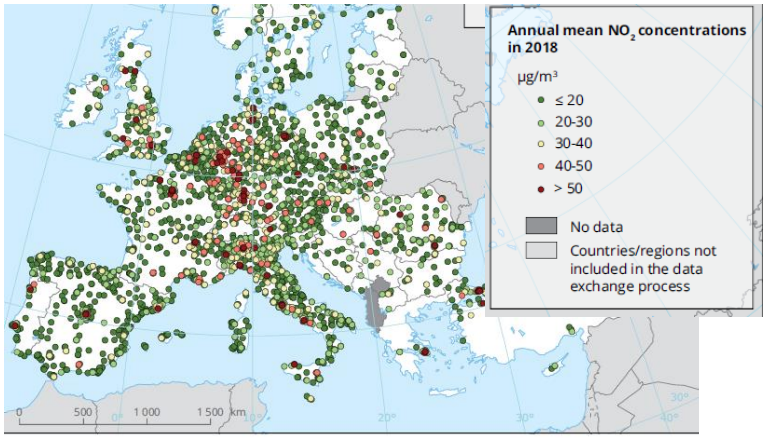

Figure 2. NO_2 concentrations in Europe in 2018 [European Environment Agency, 2020 Report].

The atmospheric concentration of NO_x in a city could be reduced in-situ (a process called De-NO_x) by creating large decontaminating surfaces. In this sense, the capacity of urban materials (mortars, paints, pavements, etc.) to act as self-decontaminating materials has been described, thanks to the incorporation of additives based on TiO_2 photocatalyst compounds. In this sense, photocatalysis is a very promising technology, since the De-NO_x action takes place at room temperature and with the exclusive use of water, oxygen and sunlight, components that are abundant in the urban atmosphere. As a result, NO_x gases are removed from the atmosphere when oxidized to nitrate and nitrite species. However, photocatalytic remediation is a technology that is not widely used in urban architecture since, among other limitations, the cost of TiO_2-based composites is very high compared to the raw materials that make up urban infrastructures. Therefore, the search for alternative low-cost photocatalyst additives remains a pending challenge.

In this context, this work has two global objectives. The first objective of this Doctoral Thesis is focused on the study of new inorganic compounds that can be used as additives to prevent microbial contamination of rehabilitation mortars used in urban environments. The research addresses the use of Carbendazim (CBZ), a low-cost fungicide unexplored in this type of materials. Likewise, the incorporation of CBZ to different inorganic supports based on clay-type compounds has been studied. These compounds have a high adsorptive capacity, a low production cost and ensure good compatibility with the mortar matrix.

The second global objective of this work, also in line with the preservation of urban habitat, is the development of new inorganic additives with photocatalytic properties for the De-NO_x process, so that they are effective, economical and viable for extensive use. Along these

lines, the use of ZnO nanoparticles, a photocatalyst with low toxicity and high UV radiation absorption capacity, has been studied. For its synthesis, rice husk, an important agro-industrial waste product, has been used with the aim of improving the dispersion of ZnO nanoparticles and reducing costs, without creating a greater environmental impact. Additionally, the family of Layered Double Hydroxides compounds (LDHs) have been applied in a novel way as De-NO_x photocatalysts. These compounds are known by its simple synthesis, enormous chemical versatility and environmental sustainability, which makes them ideal for application in this specific photocatalytic technology.

Capítulo 1.

Hipótesis y objetivos.

Hipótesis 1.

El crecimiento de los microrganismos en los poros, fisuras y grietas de los materiales pétreos presentes en el Patrimonio urbano (contaminación microbiana) provoca efectos negativos en estos, tales como cambios de tonalidad, pérdida de adhesión y cohesión entre los constituyentes mineralógicos y una progresiva pérdida de material y de su resistencia mecánica [1].

Actualmente, los morteros de restauración que se emplean en las tareas de rehabilitación contienen aditivos con propiedades antimicrobianas (compuestos biocidas) que protegen al material de la contaminación microbiana. Sin embargo, esta protección es muy limitada en el tiempo debido a la descomposición y lixiviación al medio exterior de los agentes antimicrobianos.

Para aumentar la duración del efecto antimicrobiano, los agentes biocidas podrían ser adsorbidos en un soporte inorgánico, de manera que se consiguiera una liberación controlada del princio activo (los compuestos biocida), a la vez que quedarían más protegidos frente a agentes externos (luz, pH, etc.) [2]. Conjuntamente, una mayor dispersión del principio activo en el soporte haría que se consiguiese el mismo rendimiento antimicrobiano, pero empleando una menor cantidad de agente biocida, lo que mejoraría los costes de producción y la sostenibilidad del sistema.

Las arcillas son filosilicatos cuya estructura se forma al apilar, mediante varias combinaciones, capas de estructura tetraédrica de silicatos $[SiO_4]^{4-}$ y octaédricas de iones hidroxilo con cationes Al^{3+} en los huecos octaédricos Entre las capas, se encuentran moléculas de agua y cationes que son fácilmente intercambiables. Además, la modificación de las arcillas para mejorar la adsorción de compuestos hidrofóbicos (organo-arcillas) es sencilla de llevar a cabo, existiendo organo-arcillas comerciales. La

abundancia, bajo coste y sostenibilidad de las arcillas hacen que sean utilizadas en un importante número de aplicaciones. A destacar, las arcillas se han utilizado como adsorbentes/sistemas de liberación controlada de pesticidas y herbicidas en la agricultura [3]. Sin embargo, apenas existe información acerca del empleo de las arcillas como sistemas de liberación controlada en el ámbito de los materiales pétreos del Patrimonio urbano.

La Carbendazima (metil-benzimidazol-2-il-carbamato; número CAS: 10605-21-7) es un fungicida de bajo coste y baja solubilidad en agua (8 mg L^{-1}) utilizado en la agricultura y en pinturas para fachadas [4, 5]. No obstante, su aplicación en los materiales de construcción permanece inexplorada.

Objetivo 1.

El primer objetivo de esta Tesis Doctoral se centra en el estudio de nuevos compuestos inorgánicos que puedan ser utilizados como aditivos para prevenir la contaminación microbiana de los morteros de rehabilitación usados en entornos urbanos. La investigación aborda la utilización de Carbendazima (CBZ) como fungicida, mientras que los soportes inorgánicos se basaron en compuestos tipo arcilla disponibles comercialmente. Se emplearon una arcilla de referencia, sin modificación química, y dos organo-arcillas para estudiar la influencia de la adsorción de la CBZ y conseguir un aditivo con un contenido elevado de agente fungicida.

Adicionalmente, como las organo-arcillas empleadas se encuentran modificadas con surfactantes catiónicos (amonio cuaternario), cuyas

propiedades alguicidas son conocidas [6], se espera que los aditivos preparados tengan una acción biocida doble (fungicida y alguicida).

Finalmente, los compuestos serán utilizados como aditivos en la preparación de un mortero de restauración en base cal, con el objeto de lograr unas propiedades biocidas y de lixiviación mejoradas.

Esta investigación se aborda en el artículo científico titulado: ***Carbendazim-clay complexes for its potential use as antimicrobial additives in mortars***

Clic aquí para ver la versión web del artículo

Hipótesis 2.

La contaminación atmosférica del hábitat urbano, y en particular la contaminación derivada de los gases óxidos de nitrógeno (NO_x = NO + NO_2) provoca una importante serie de efectos negativos a varios niveles: salud humana, medio ambiente y materiales del Patrimonio urbano.

La concentración atmosférica de NO_x de una ciudad podría reducirse *in-situ* (proceso llamado De-NO_x) mediante la creación de grandes superficies descontaminantes. En este sentido, se ha descrito la capacidad de los materiales de construcción usados en la arquitectura urbana (hormigón, morteros, pinturas, pavimentos, etc.) para actuar como materiales auto-descontaminantes, gracias a la incorporación de aditivos basados en compuestos fotocatalizadores, principalmente el dióxido de

titanio (TiO_2). Mediante el proceso fotocatalítico, en el que intervienen la luz solar y el agua y oxígeno atmosféricos, los gases NO_x son oxidados a las especies nitratos y nitritos y de este modo se retiran de la atmósfera [7].

No obstante, la remediación fotocatalítica es una tecnología que no tiene un uso extendido en la arquitectura urbana debido a ciertas limitaciones del TiO_2. Principalmente, el coste del aditivo fotocatalítico TiO_2 es muy elevado en comparación con las materias primas que constituyen los materiales de construcción [8]. Otra limitación se relaciona con la baja selectividad De-NO_x descrita para el TiO_2, lo que indica que gran parte del NO no es oxidado finalmente a especies nitritos/nitratos sino a NO_2 una especie intermedia mucho más tóxica que el NO [9]. Además, la Unión Europea ha indicado recientemente potenciales riesgos de padecer cáncer cuando se inhalan nanopartículas de TiO_2 [10], por lo que habría que tener en consideración los riesgos futuros de la utilización de dicho compuesto.

Se han estudiado fotocatalizadores alternativos al TiO_2 al objeto de conseguir un mejor rendimiento fotocatalítico en procesos De-NO_x así como ofrecer productos más económicos y sostenibles. Una de las acciones de mejora del rendimiento fotocatalítico pasa por conseguir compuestos con una elevada superficie específica expuesta a las moléculas reactantes, lo que se puede conseguir con soportes adecuados para la dispersión del fotocatalizador [11, 12]. A destacar, las cenizas de la combustión de la cáscara de arroz contienen un elevado porcentaje (> 90%) de SiO_2 amorfo con elevada superficie específica (> 200 $m^2\ g^{-1}$), por lo que se ha utilizado en diversas aplicaciones, por ejemplo, como soporte inorgánico de catalizadores [13].

Por otro lado, el ZnO es un compuesto con propiedades fotocatalíticas similares al TiO_2. Sin embargo, la preparación de ZnO nanoparticulado implica generalmente métodos hidrotermales, líquidos

iónicos o sol-gel [14], por lo que es preferible conseguir un procedimiento más económico y sencillo.

Objetivo 2.

El segundo objetivo está enfocado en la preparación, mediante una metodología simple y económica, de nuevos fotocatalizadores con actividad De-NO_x mejorada. En este contexto de potencial industrialización y sostenibilidad, se ha investigado la valorización de la cáscara de arroz, residuo agroindustrial muy abundante en el mundo. Este residuo supone un enorme problema medioambiental debido a la gran producción mundial de arroz, más de 700 millones de toneladas anuales, de las cuales un 20 % en peso es cáscara.

Durante la síntesis del fotocatalizador, basado en ZnO, se pretende que la cáscara de arroz actúe además como agente de plantilla para conseguir nanopartículas de ZnO que se encuentren dispersas sobre el soporte inorgánico de SiO_2. Se espera que el menor tamaño de partícula y la mejor dispersión del ZnO en la matriz porosa del SiO_2 amorfo produzca un aumento en la eficacia fotocatalítica De-NO_x.

Esta investigación se aborda en el artículo científico titulado:

ZnO on rice husk: A sustainable photocatalyst for urban air purification

Clic aquí para ver la versión web del artículo

Hipótesis 3.

Como se deriva de la hipótesis 2, actualmente existe gran interés en la preparación de fotocatalizadores De-NO_x alternativos al TiO_2, para su aplicación en superficies urbanas auto-descontaminantes.

Los Hidróxidos Dobles Laminares (LDH, del inglés) son una amplia familia de compuestos con una estructura laminar tipo brucita, donde existe una sustitución parcial isomórfica de cationes divalentes por trivalentes, generándose así la carga positiva en las láminas, que se compensa por intercalación de aniones entre ellas. Gracias a una gran capacidad de modificación de su composición, la facilidad y bajo coste de su síntesis y su gran versatilidad química, los LDH se han estudiado para un amplio abanico de aplicaciones [15].

Nuestro Grupo de Investigación fue pionero en la aplicación de los LDHs (basados en los cationes Zn^{2+} y Al^{3+}) como fotocatalizadores De-NO_x, demostrando muy buenos valores de eliminación de estos gases, así como una excelente selectividad del proceso De-NO_x [16]. Sin embargo, dichos compuestos, al igual que el TiO_2, no son activos frente a la luz del espectro Visible, por lo que se desaprovecha gran parte de la radiación solar, en torno a un 40%.

Objetivo 3.

En este objetivo se busca conseguir la preparación fácil y económica de LDHs, mediante un sencillo método de coprecipitación, con propiedades fotocatalíticas De-NO_x mejoradas, así como la profundización del mecanismo implicado.

Tomando como base el compuesto ZnAl-LDH, se pretende investigar el efecto que tiene el reemplazo gradual de Al^{3+} por Fe^{3+} en la

mejora del rendimiento De-NO_x. Se espera que la introducción de este nuevo elemento genere nuevos estados energéticos que permitan un mejor aprovechamiento de la luz visible, abra nuevas vías de desactivación de las fotocargas generadas (electrón/hueco) que retrasen su recombinación y, por ende, aumente la actividad fotocatalítica. Además, mediante el uso de técnicas como la Resonancia Paramagnética de Electrones (EPR) y la fotoluminiscencia (PL), se pretende explicar la potencial mejora del mecanismo fotocatalítico De-NO_x.

Esta investigación se aborda en el artículo científico titulado:

Effects of Fe^{3+} substitution on Zn-Al layered double hydroxides for enhanced NO photochemical abatement

Clic aquí para ver la versión web del artículo

Hipótesis 4.

Como se ha comentado en la hipótesis anterior, los compuestos LDHs se presentan como una familia de fotocatalizadores De-NO_x muy prometedora.

No obstante, los LDH sintetizadas con métodos tradicionales sufren un apilamiento de las láminas, lo que da como resultados agregados de partículas con poca área superficial específica y pequeño volumen de poro [17]. Esto da lugar a una baja dispersión de los sitios activos esenciales para

reacciones fotocatalíticas heterogéneas y con ello una menor interacción con las moléculas reactantes y un rendimiento fotoquímico más bajo

Para abordar este problema, es de interés la preparación de LDHs con partículas constituidas por una sola lámina o unas pocas laminas (2D-LDH). Sin embargo, los métodos más eficientes a temperatura ambiente a menudo requieren disolventes agresivos y peligrosos (por ejemplo, formamida), consumen mucho tiempo (por ejemplo, la intercalación previa de un anión adecuado) y ofrecen rendimientos muy bajos que impiden la recuperación de cantidades significativas de LDH [18].

Con el fin de producir grandes cantidades de 2D-LDHs de una manera mucho más sencilla, el Grupo del Prof. O'Hare ideó un método novedoso, denominado *Aqueous Miscible Organic Solvent Treatment* (AMOST) [17], donde el compuesto LDH recién formado es lavado y re-dispersado en un disolvente orgánico miscible con el agua, dando lugar a los compuestos denominados AMO-LDH que se caracterizan por presentar una alta dispersión de partículas bidimensionales y gran volumen de poro, lo que conlleva a obtener altos valores de superficie específica.

Objetivo 4.

Parte del trabajo del objetivo 4 ha sido realizado por el doctorando en el grupo del Prof. Dermot O'Hare, University of Oxford. En este objetivo se busca conseguir, mediante el método AMOST, la preparación de 2D-LDHs con propiedades fotocatalíticas De-NO_x mejoradas. Se pretende que la mayor dispersión de las nanoláminas de LDH aporte más sitios activos

para reaccionar con los gases NO_x durante el proceso fotocatalítico. Esta sería la primera vez que un AMO-LDH es aplicado como fotocatalizador.

El LDH estudiado se basa en los cationes Ni^{2+} y Ti^{4+}, ya que han sido documentadas sus buenas propiedades fotocatalíticas [19], si bien nunca ha sido aplicado como fotocatalizador De-NO_x.

Se estudiarán varios factores que podrían afectar al procedimiento AMOST: el tiempo de redispersión en el disolvente, la temperatura durante el proceso redispersión y la relación entre los cationes metálicos que forman las láminas (Ni^{2+} y Ti^{4+}).

Finalmente, mediante el uso de técnicas como la Resonancia Paramagnética de Electrones (EPR), espectroscopia de infrarroja de reflectancia difusa in situ por transformada de Fourier (DRIFT) y la fotoluminiscencia (PL), se pretende explicar la potencial mejora del mecanismo fotocatalítico De-NO_x.

Esta investigación se aborda en el artículo científico titulado:

Aqueous miscible organic solvent treated NiTi layered double hydroxide De-NO_x photocatalysts

Clic aquí para ver la versión web del artículo

Referencias:

[1] T. Warscheid, J. Braams, Biodeterioration of stone: a review, Int. Biodeterior. Biodegradation. 46 (2000) 343–368. doi:10.1016/S0964-8305(00)00109-8.

[2] C. Dresler, M.L. Saladino, C. Demirbag, E. Caponetti, D.F. Chillura Martino, R. Alduina, Development of controlled release systems of biocides for the conservation of cultural heritage, Int. Biodeterior. Biodegradation. 125 (2017) 150–156. doi:10.1016/J.IBIOD.2017.09.007.

[3] B. Gámiz, M.C. Hermosín, J. Cornejo, R. Celis, Hexadimethrine-montmorillonite nanocomposite: Characterization and application as a pesticide adsorbent, Appl. Surf. Sci. 332 (2015) 606–613. doi:10.1016/j.apsusc.2015.01.179.

[4] C. Dresler, M.L. Saladino, C. Demirbag, E. Caponetti, D.F. Chillura Martino, R. Alduina, Development of controlled release systems of biocides for the conservation of cultural heritage, Int. Biodeterior. Biodegradation. 125 (2017) 150–156. doi:10.1016/J.IBIOD.2017.09.007.

[5] A. Marco, S. Santos, J. Caetano, M. Pintado, E. Vieira, P.R. Moreira, Basil essential oil as an alternative to commercial biocides against fungi associated with black stains in mural painting, Build. Environ. 167 (2020) 106459. doi:10.1016/j.buildenv.2019.106459.

[6] M.M. Urbanczyk, K. Bester, N. Borho, U. Schoknecht, U.E. Bollmann, Influence of pigments on phototransformation of biocides in paints, J. Hazard. Mater. 364 (2019) 125–133. doi:10.1016/J.JHAZMAT.2018.10.018.

[7] J. Balbuena, M. Cruz-Yusta, L. Sánchez, Nanomaterials to Combat NO_x Pollution, J. Nanosci. Nanotechnol. 15 (2015) 6373–6385. doi:10.1166/jnn.2015.10871.

[8] P.J.M. Bartos, Editorial: Photocatalytic concrete, Http://Dx.Doi.Org/10.1680/Macr.13.00298. 66 (2015) 217–218. doi:10.1680/MACR.13.00298.

[9] J.Z. Bloh, A. Folli, D.E. Macphee, Photocatalytic NOx abatement: why the selectivity matters, RSC Adv. 4 (2014) 45726–45734. doi:10.1039/C4RA07916G.

[10] European Union law - Document 32020R0217, 2019. https://eur-lex.europa.eu/legal-content/EN/TXT/?uri=uriserv:OJ.L_.2020.044.01.0001.01.ENG&toc=OJ:L:2020:044:TOC (accessed July 5, 2021).

[11] N. Todorova, T. Giannakopoulou, S. Karapati, D. Petridis, T. Vaimakis, C. Trapalis, Composite TiO_2/clays materials for photocatalytic NOx oxidation, Appl. Surf. Sci. 319 (2014) 113–120. doi:10.1016/J.APSUSC.2014.07.020.

[12] X.F. Chen, S. run Lin, S.C. Kou, Effect of composite photo-catalysts prepared with recycled clay brick sands and nano-TiO_2 on methyl orange and NOx removal, Constr. Build. Mater. 171 (2018) 152–160. doi:10.1016/J.CONBUILDMAT.2018.03.099.

[13] R.M. Lattuada, C. Radtke, M.C.R. Peralba, J.H.Z. Dos Santos, Rice husk: Raw material in the catalyst preparation for advanced oxidative processes applied in the industrial effluent treatment and from acid drainage of a mine, Water. Air. Soil Pollut. 224 (2013). doi:10.1007/s11270-012-1396-x.

[14] E. Luévano-Hipólito, A. Martínez-de la Cruz, E. López Cuéllar, Performance of ZnO synthesized by sol-gel as photocatalyst in the photooxidation reaction of NO, Environ. Sci. Pollut. Res. 2016 247. 24 (2016) 6361–6371. doi:10.1007/S11356-016-7310-0.

[15] F. Cavani, F. Trifirò, A. Vaccari, Hydrotalcite-type anionic clays: Preparation, properties and applications., Catal. Today. 11 (1991) 173–301. doi:10.1016/0920-5861(91)80068-K.

[16] F. Rodriguez-Rivas, A. Pastor, C. Barriga, M. Cruz-Yusta, L. Sánchez, I. Pavlovic, Zn-Al layered double hydroxides as efficient photocatalysts for NOx abatement, Chem. Eng. J. 346 (2018) 151–158. doi:10.1016/j.cej.2018.04.022.

[17] Q. Wang, D. O'Hare, Large-scale synthesis of highly dispersed layered double hydroxide powders containing delaminated single layer nanosheets, Chem. Commun. 49 (2013) 6301. doi:10.1039/c3cc42918k.

[18] Q. Wang, D. O'Hare, Recent Advances in the Synthesis and Application of Layered Double Hydroxide (LDH) Nanosheets, Chem. Rev. 112 (2012) 4124–4155. doi:10.1021/cr200434v.

[19] Y. Zhao, P. Chen, B. Zhang, D.S. Su, S. Zhang, L. Tian, J. Lu, Z. Li, X. Cao, B. Wang, M. Wei, D.G. Evans, X. Duan, Highly dispersed TiO_6 units in a layered double hydroxide for water splitting, Chem. - A Eur. J. 18 (2012) 11949–11958. doi:10.1002/chem.201201065.

Chapter 1.

Hypotheses and objectives

Hypothesis 1.

The growth of microorganisms in the pores, fissures and cracks of the stone materials used in buildings of significant cultural heritage (microbial contamination) has a number of detrimental effects. These effects include changes in tonality, loss of adhesion and cohesion between the mineralogical constituents and a progressive loss of material and reduced mechanical resistance [1].

Currently, restoration mortars contain additives with antimicrobial properties (biocidal compounds) that protect the material from microbial contamination. However, this protection is ineffective over longer periods of time due to the decomposition and leaching of the antimicrobial agents.

In order to increase the duration of the antimicrobial effect, the biocidal agents could be adsorbed on an inorganic support to achieve a controlled release of the biocidal compound, thus becoming more protected from external agents (light, pH, etc.) as well [2]. Furthermore, a greater dispersion of the active agent (the biocidal compound) in the support would achieve the same antimicrobial performance, but using a smaller amount of biocidal agent, which would improve production costs and the sustainability of the system.

Clay minerals, mainly the 2:1-type phyllosilicates, whose structure is formed of octahedral alumina and two linked tetrahedral silicate layers, are good adsorbents for cationic compounds, as a consequence of their negatively charged surfaces. Furthermore, the affinity of these materials towards hydrophobic compounds can be improved by a simple modification of their surfaces, and there are organo-clays commercially available. Clay minerals have been used as adsorbents/controlled release systems for pesticides and herbicides in agriculture [3], but there is very

little information about their use as controlled release systems in the field of architectural conservation.

Carbendazim (methyl-benzimidazol-2-yl-carbamate; CAS number: 10605-21-7) is a low-cost fungicide with low water solubility (8 mg L^{-1}) used in agriculture and in facade paints [4, 5]. Nevertheless, its application in building materials remains unexplored.

Objective 1.

The first objective of this Doctoral Thesis is focused on the study of new inorganic compounds that can be used as additives to prevent microbial contamination of rehabilitation mortars used in urban environments. The research addresses the use of Carbendazim (CBZ) as a fungicide, while the inorganic supports were based on commercially available clay-like compounds. A reference clay, without chemical modification, and two organo-clays were used to study the influence of the adsorption of CBZ to obtain an additive with a high content of fungicidal agent.

Additionally, as the used organo-clays are modified with cationic surfactants (quaternary ammonium salts), whose algicidal properties are well known [6], it is expected that the prepared additives would have a broader spectrum of biocidal activity (fungicide and algaecide).

Finally, the compounds will be used as additives in the preparation of a lime-based restoration mortar to achieve improved biocidal and leaching properties.

This research is addressed in the scientific article entitled:

Carbendazim-clay complexes for its potential use as antimicrobial additives in mortars

Click here to see the web version of the article

Hypothesis 2.

Atmospheric pollution of urban environments, and in particular the pollution derived from nitrogen oxide gases (NO_x = NO + NO_2) causes a number of significant negative effects in various areas. These effects include human health, environment and materials of the urban heritage.

The atmospheric concentration of NO_x could be reduced in-situ (a process called De-NO_x) by creating large decontaminating surfaces. The ability of building materials used in urban architecture (concrete, mortars, paints, pavements, etc.) to act as self-decontaminating materials has been described. This action is due to the incorporation of additives based on photocatalytic compounds, mainly titanium dioxide (TiO_2). Through the photocatalytic process, with sunlight and atmospheric water and oxygen

presence, the harmful NO_x gases are oxidised to nitrates and nitrites species and, therefore, removed from the atmosphere [7].

However, photocatalytic remediation is a technology that is not widely used in urban architecture due to certain limitations of TiO_2.Namely, the TiO_2 photocatalytic additive is very expensive compared to the raw materials that make up construction materials [8]. Another limitation is related to the low De-NO_x selectivity reported for TiO_2, which means that much of the NO gas is not finally oxidized to nitrites/nitrates species but to NO_2, a highly toxic intermediate [9]. Moreover, the European Union has recently indicated potential risks of suffering cancer when TiO_2 nanoparticles are inhaled, so future risks of the use of this compound should be taken into account [10].

Alternative photocatalysts to TiO_2 have been studied in order to obtain enhanced photocatalytic performance in De-NO_x processes as well as to offer more economical and sustainable products. One of the actions to improve the photocatalytic performance is the preparation of compounds with a high specific surface area exposed to reactant molecules, which can be achieved with suitable supports for the dispersion of the photocatalyst [11, 12]. Notably, the ash from rice husk combustion contains a high percentage of amorphous SiO_2 (> 90%) with a high specific surface area (> 200 $m^2\ g^{-1}$), being used in various applications, for example , as an inorganic catalyst support [13].

On the other hand, ZnO is a compound with photocatalytic properties similar to TiO_2. However, the preparation of ZnO nanoparticles generally involves hydrothermal, ionic liquid methods or sol-gel [14], so it is preferable to achieve a cheaper and simpler process.

Objective 2.

The second objective is focused on the preparation of new photocatalysts with enhanced De-NOx activity, through simple and inexpensive methods. In the context of potential industrialization and sustainability, the use of rice husk, a very abundant world agro-industrial waste, has been investigated. This waste is a huge environmental problem due to the large world production of rice, more than 700 million tons per year, of which 20% by weight is husk.

During the synthesis of the photocatalyst, based on ZnO, it is expected that the rice husk also acts as a template agent to obtain ZnO nanoparticles that are dispersed on the SiO_2 inorganic support. The smaller particle size and better dispersion of ZnO in the porous matrix of amorphous SiO_2 is expected to produce an increase in De-NO_x photocatalytic efficiency.

This research is addressed in the scientific article entitled:

ZnO on rice husk: A sustainable photocatalyst for urban air purification

Click here to see the web version of the article

Hypothesis 3.

Following from hypothesis 2, there is currently great interest in the preparation of alternative De-NO_x photocatalysts to TiO_2, for their application to self-decontaminating urban surfaces.

Layered Double Hydroxides (LDHs) are a wide family of compounds with a brucite-type layered structure where divalent cation is isomorphically substituted by a trivalent one, thus creating positively charged layers which are balanced by which is balanced by intercalation of hydrated anions between layers. LDHs have been studied for a wide range of applications thanks to the highly modular composition, the ease and low cost of their synthesis and its great chemical versatility [15].

Our Research Group pioneered the application of LDHs (based on Zn^{2+} and Al^{3+} cations) as De-NO_x photocatalysts, demonstrating very promising elimination values for these gases, as well as excellent selectivity in the De-NO_x process [16]. However, similarly to TiO_2, these compounds are not active under Visible light and, therefore, a large fraction (40 %) of the sunlight is not harvested.

Objective 3.

This objective pursues the easy and economical preparation of LDHs, by means of a simple co-precipitation method, with improved De-NO_x photocatalytic properties, as well as an in-depth investigation of the involved mechanism.

Based on ZnAl-LDH , it is proposed to investigate the effect that the gradual replacement of Al^{3+} by Fe^{3+} has in the improvement of the De-NO_x performance. The introduction of this new element is expected to create new energetic states which would allow a better harvesting of visible light.

Moreover, new ways of deactivating generated photocharges (electron/hole pairs) might be created, thus delaying their recombination and increasing the photocatalytic activity. In this sense, using techniques such as Electron Paramagnetic Resonance (EPR) and photoluminescence (PL), it is intended to explain the potential improvement of the De-NO_x photocatalytic mechanism.

This research is addressed in the scientific article entitled:

Effects of Fe^{3+} substitution on Zn-Al layered double hydroxides for enhanced NO photochemical abatement

Click here to see the web version of the article

Hypothesis 4.

As commented in the previous hypothesis, LDHs compounds are a very promising family of De-NO_x photocatalysts.

However, LDHs synthesized by traditional methods undergo layer stacking, resulting in particle aggregates with low specific surface area and small pore volume [17]. This results in a low dispersion of active sites necessary for heterogeneous photocatalytic reactions and, therefore, a minor interaction with the reactant molecules and poor photochemical performance.

To tackle this problem, the preparation of LDHs with particles consisting of a single sheet or a few sheets (2D-LDH) is of interest.

Nevertheless, the most efficient reported methods to achieve these structures at room temperature often require aggressive and hazardous solvents (e.g. formamide), are time consuming (e.g. pre-intercalation of a suitable anion) and offer very low yields that prevent recovery of significant amounts of LDH [18].

In order to produce large amounts of 2D-LDHs in a much simpler way, the O'Hare Group devised a novel method, the *Aqueous Miscible Organic Solvent Treatment* (AMOST) [17], where newly formed LDH compound is washed with and redispersed in a water-miscible organic solvent, giving rise to the so-called AMO-LDH compounds. These are characterized by a high dispersion of 2D particles and large pore volume, allowing the obtention of high specific surface areas.

Objective 4.

Part of the work on objective 4 has been carried out by the doctoral student in the group of Prof. Dermot O'Hare, at the University of Oxford. The aim of this objective is to achieve the preparation of 2D-LDHs using the AMOST method with improved De-NO_x photocatalytic properties. It is expected that a greater dispersion of LDH nanosheets would provide more active sites to react with NO_x gases during the photocatalytic process. This would be the first time that AMO-LDHs are applied as photocatalysts.

The studied LDH is based on Ni^{2+} and Ti^{4+} cations, since its good photocatalytic properties have been documented [19], but it has never been applied as a De-NO_x photocatalyst.

Several factors affecting the AMOST procedure will be studied: the redispersion time in the solvent, the temperature during the redispersion

process and the ratio between the metal cations that form the sheets (Ni^{2+} and Ti^{4+}).

Finally, by using techniques such as Electron Paramagnetic Resonance (EPR), in situ diffuse reflectance infrared Fourier transform spectroscopy (DRIFT) and photoluminescence (PL), it is intended to explain the potential improvement of the De-NO_x photocatalytic mechanism.

This research is addressed in the scientific article entitled:

Aqueous miscible organic solvent treated NiTi layered double hydroxide De-NO_x photocatalysts

Click here to see the web version of the article

References:

[1] T. Warscheid, J. Braams, Biodeterioration of stone: a review, Int. Biodeterior. Biodegradation. 46 (2000) 343–368. doi:10.1016/S0964-8305(00)00109-8.

[2] C. Dresler, M.L. Saladino, C. Demirbag, E. Caponetti, D.F. Chillura Martino, R. Alduina, Development of controlled release systems of biocides for the conservation of cultural heritage, Int. Biodeterior. Biodegradation. 125 (2017) 150–156. doi:10.1016/J.IBIOD.2017.09.007.

[3] B. Gámiz, M.C. Hermosín, J. Cornejo, R. Celis, Hexadimethrine-montmorillonite nanocomposite: Characterization and application as a pesticide adsorbent, Appl. Surf. Sci. 332 (2015) 606–613. doi:10.1016/j.apsusc.2015.01.179.

[4] C. Dresler, M.L. Saladino, C. Demirbag, E. Caponetti, D.F. Chillura Martino, R. Alduina, Development of controlled release systems of biocides for the conservation of cultural heritage, Int. Biodeterior. Biodegradation. 125 (2017) 150–156. doi:10.1016/J.IBIOD.2017.09.007.

[5] A. Marco, S. Santos, J. Caetano, M. Pintado, E. Vieira, P.R. Moreira, Basil essential oil as an alternative to commercial biocides against fungi associated with black stains in mural painting, Build. Environ. 167 (2020) 106459. doi:10.1016/j.buildenv.2019.106459.

[6] M.M. Urbanczyk, K. Bester, N. Borho, U. Schoknecht, U.E. Bollmann, Influence of pigments on phototransformation of biocides in paints, J. Hazard. Mater. 364 (2019) 125–133. doi:10.1016/J.JHAZMAT.2018.10.018.

[7] J. Balbuena, M. Cruz-Yusta, L. Sánchez, Nanomaterials to Combat NO_x Pollution, J. Nanosci. Nanotechnol. 15 (2015) 6373–6385. doi:10.1166/jnn.2015.10871.

[8] P.J.M. Bartos, Editorial: Photocatalytic concrete, Http://Dx.Doi.Org/10.1680/Macr.13.00298. 66 (2015) 217–218. doi:10.1680/MACR.13.00298.

[9] J.Z. Bloh, A. Folli, D.E. Macphee, Photocatalytic NOx abatement: why the selectivity matters, RSC Adv. 4 (2014) 45726–45734. doi:10.1039/C4RA07916G.

[10] European Union law - Document 32020R0217, 2019. https://eur-lex.europa.eu/legal-content/EN/TXT/?uri=uriserv:OJ.L_.2020.044.01.0001.01.ENG&toc=OJ:L:2020:044:TOC (accessed July 5, 2021).

[11] N. Todorova, T. Giannakopoulou, S. Karapati, D. Petridis, T. Vaimakis, C. Trapalis, Composite TiO_2/clays materials for photocatalytic NOx oxidation, Appl. Surf. Sci. 319 (2014) 113–120. doi:10.1016/J.APSUSC.2014.07.020.

[12] X.F. Chen, S. run Lin, S.C. Kou, Effect of composite photo-catalysts prepared with recycled clay brick sands and nano-TiO_2 on methyl orange and NOx removal, Constr. Build. Mater. 171 (2018) 152–160. doi:10.1016/J.CONBUILDMAT.2018.03.099.

[13] R.M. Lattuada, C. Radtke, M.C.R. Peralba, J.H.Z. Dos Santos, Rice husk: Raw material in the catalyst preparation for advanced oxidative processes applied in the industrial effluent treatment and from acid drainage of a mine, Water. Air. Soil Pollut. 224 (2013). doi:10.1007/s11270-012-1396-x.

[14] E. Luévano-Hipólito, A. Martínez-de la Cruz, E. López Cuéllar, Performance of ZnO synthesized by sol-gel as photocatalyst in the photooxidation reaction of NO, Environ. Sci. Pollut. Res. 2016 247. 24 (2016) 6361–6371. doi:10.1007/S11356-016-7310-0.

[15] F. Cavani, F. Trifirò, A. Vaccari, Hydrotalcite-type anionic clays: Preparation, properties and applications., Catal. Today. 11 (1991) 173–301. doi:10.1016/0920-5861(91)80068-K.

[16] F. Rodriguez-Rivas, A. Pastor, C. Barriga, M. Cruz-Yusta, L. Sánchez, I. Pavlovic, Zn-Al layered double hydroxides as efficient photocatalysts for NOx abatement, Chem. Eng. J. 346 (2018) 151–158. doi:10.1016/j.cej.2018.04.022.

[17] Q. Wang, D. O'Hare, Large-scale synthesis of highly dispersed layered double hydroxide powders containing delaminated single layer nanosheets, Chem. Commun. 49 (2013) 6301. doi:10.1039/c3cc42918k.

[18] Q. Wang, D. O'Hare, Recent Advances in the Synthesis and Application of Layered Double Hydroxide (LDH) Nanosheets, Chem. Rev. 112 (2012) 4124–4155. doi:10.1021/cr200434v.

[19] Y. Zhao, P. Chen, B. Zhang, D.S. Su, S. Zhang, L. Tian, J. Lu, Z. Li, X. Cao, B. Wang, M. Wei, D.G. Evans, X. Duan, Highly dispersed TiO_6 units in a layered double hydroxide for water splitting, Chem. - A Eur. J. 18 (2012) 11949–11958. doi:10.1002/chem.201201065.

Capítulo 2.

Introducción

2.1. El patrimonio urbano

El patrimonio urbano es todo aquel conjunto de bienes arquitectónicos acumulados a lo largo de los siglos, que, por su significado artístico, arqueológico, etc., son objeto de protección especial por la legislación correspondiente. Ya en 1943, en la Carta de Atenas (manifiesto urbanístico que tuvo lugar en el IV Congreso Internacional de Arquitectura Moderna), se tomó consciencia de la importancia de preservar los cascos históricos y los entornos urbanos [1]. No obstante, en la actualidad resulta también de gran importancia la preservación de otro conjunto de instalaciones presentes en los espacios urbanos, como puede ser el mobiliario urbano, edificios de viviendas u otras infraestructuras básicas para el correcto y sano funcionamiento de una ciudad.

La labor de preservación de todas estas construcciones urbanas está justificada no solo por el gran valor cultural, sino también por la riqueza derivada de las diferentes actividades económicas que van unidas (gestión, puesta en valor, turismo, etc.) a la importancia del patrimonio urbano.

Con el objeto de preservar el patrimonio urbano, en las jurisprudencias de los diferentes países suelen estar recogidas las leyes de urbanismo y las leyes del patrimonio (por ejemplo, en España, Ley de Patrimonio Histórico Español) donde se marcan las normas y protocolos para llevar a cabo el mantenimiento preventivo y las posibles restauraciones de todo este tipo de arquitectura. Desafortunadamente, la gestión de patrimonio urbano actual no suele ser la adecuada [2], lo que hace que no se realicen todas las labores de preservación necesarias para mantener la estética e integridad de las construcciones. Además, el elevado

coste de las tareas mantenimiento suele influir en el retraso de la ejecución de los proyectos.

2.1.1. El deterioro de los materiales pétreos del patrimonio urbano

Existe una gran variabilidad de materiales pétreos presentes en el patrimonio urbano. Así, muchas de las construcciones pueden estar hechas de morteros [3] , estucos [4], granito [5], mármol [6], dolomita [7], piedra caliza [8], arenisca [9], etc. Toda esta diversidad hace que el estudio de su deterioro sea complejo y heterogéneo. En este sentido, uno de los factores que influirá sobre la evolución del deterioro del material será el tipo de estructura que presente. Así, la composición química, el tipo de agente cementante, la porosidad y permeabilidad al agua serán propiedades que influirán necesariamente. Otros factores externos con una gran relevancia en el deterioro urbano son:

1) Factores físicos: la acción del viento, cambios de humedad y temperatura, procesos de cristalización e hidratación de las sales que contienen los materiales, ciclos de hielo-deshielo, etc [10].
2) Factores químicos: reacciones químicas que se producen entre los componentes del material y los aerosoles [11] o los gases contaminantes presentes en medios urbanos, como los NO_x, el SO_2, el CO_2, etc. [12]. Además, el agua puede producir la disolución de diferentes compuestos que constituyen el material.
3) Factores biológicos/bioquímicos: la colonización de diferentes microorganismos y su metabolismo asociado producen diferentes especies como el CO_2, H^+ y ácidos orgánicos e inorgánicos, entre otras. Todos estos compuestos provocan la biometeorización del material, que unida a la penetración de ciertos microorganismos

con raíces e hifas, producen alteraciones superficiales y del color, microtensiones y una disminución del tamaño de los cristales del material. El metabolismo microbiano también genera diferentes tipos de exopolímeros y ácidos orgánicos que pueden provocar biocorrosión, mediante la formación de complejos con los metales [13].

Hay que tener en cuenta, por tanto, que todos estos factores incidirán en mayor o menor medida en los materiales urbanos, sobre todo si se considera que las construcciones que encontramos en la arquitectura urbana están planteadas para tener una larga vida útil.

2.2. Contaminación microbiana

La contaminación microbiana derivada de la colonización de los microorganismos es considerada como uno de los principales procesos del deterioro de los materiales pétreos urbanos (biodeterioro) [13]. Este término hace referencia a cualquier cambio no deseable en las propiedades del material causado por la actividad de los organismos [14]. La colonización de los microorganismos sobre las nuevas superficies de los materiales dependerá, por un lado, de factores ambientales (pH, humedad, irradiancia solar, temperatura, etc. [15]) y por otro, de la biorreceptividad del propio material [16,17]. Este término, empleado por primera vez por Guillitte [18], se define como la aptitud potencial de un material para ser colonizado por organismos vivos. Es evidente que la biorreceptividad de los materiales pétreos que se encuentran en los entornos urbanos será mayor

en comparación con otro tipo de materiales, al localizarse aquellos en el exterior, quedando más expuestos a los agentes de degradación.

Aunque se tiene constancia de las importantes consecuencias negativas (económicas, de gestión, etc.) derivadas del biodeterioro de los materiales pétreos de los entornos urbanos, resulta muy complejo calcular su impacto de una manera fiable. Esto es debido a que este proceso viene generalmente acompañado de otros factores (ver apartado 2.1.1) que lo aceleran, y a su vez el biodeterioro puede impulsar otros mecanismos de degradación. Un ejemplo de la estimación del impacto del biodeterioro, calculado mediante una serie de pautas [19], indica que cada año se pierden unos 40 mil millones de dólares en materiales (pinturas, fibras naturales, materiales pétreos, etc.) debido al ataque biológico causado por hongos [20]. En otro ejemplo de estimación aproximada, se ha informado de que el coste anual de mantenimiento de los edificios de la ciudad de Hamburgo por motivos de deterioro (biológico, químico y físico) se sitúa en torno al 1% del valor de las edificaciones de esa ciudad [21].

Los microorganismos colonizadores se pueden clasificar en diferentes tipos, según el lugar en el que son capaces de desarrollarse (**Figura 1**) [22–24]:

- Epilíticos: colonizan las superficies de las rocas y la piedra de construcción.
- Endolitos: crecen debajo de la superficie del material pétreo.
    - Criptoendolitos: colonizan el interior de cavidades y huecos en las rocas con mayor porosidad.
    - Casmoendolitos: se desarrollan en grietas y fisuras.

- Hipolitos e hipoendolitos: aquellos microorganismos (generalmente extremófilos) que existen en las capas más profundas.

Muchos de estos microorganismos son litótrofos, por lo que no solo utilizan el material como medio de fijación, sino que se nutren de minerales para mantener su metabolismo. Otra clasificación hace referencia a la función del microorganismo, según perfore activamente el sustrato rocoso (euendolitos) o contribuya a la formación de roca (autoendolitos) [25].

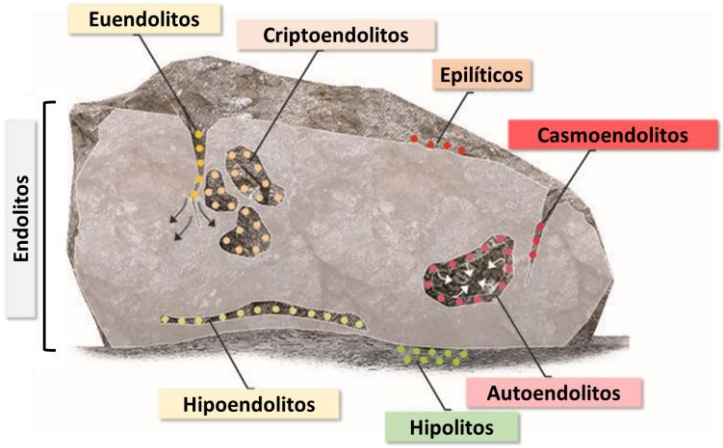

Figura 1. Diversidad de microrganismos que pueden encontrarse en los materiales pétreos (adaptado de [22]).

Existe una gran variabilidad de microorganismos que pueden desarrollarse en los materiales: algas, hongos, líquenes, bacterias, y arqueobacterias [26,27]. En los primeros momentos, la acción de los agentes físicos sobre en el material pétreo generará poros, grietas y fisuras. Es entonces cuando estos defectos estructurales actúan como un ecosistema para que diferentes microorganismos existentes en el aire se

vayan depositando y queden fijados al material (**Figura 2 (1)**). Una vez que se dan las condiciones ambientales favorables, los primeros microorganismos en iniciar su metabolismo suelen ser las algas, y las cianobacterias (**Figura 2, (2)**) [28,29]. Estos microorganismos, cuyo metabolismo es fotótrofo (utilizan la energía solar), pueden mejorar la retención del agua, polvo y tierra, promoviendo la formación de suelo y por tanto favoreciendo el crecimiento de otros tipos de microorganismos. Los líquenes (simbiosis alga-hongo) también pueden crecer en estas etapas iniciales. Todo este conjunto de microorganismos capta y transforma el CO_2 atmosférico en materia y ácidos orgánicos. En etapas posteriores (**Figura 2, (3)**), los litótrofos producen ácidos inorgánicos a partir de compuestos nitrogenados y de azufre. De esta manera, se pueden producir ácidos fuertes, como el nítrico y el sulfúrico, que producen la lixiviación de iones del material pétreo. Esto a su vez promueve el crecimiento de otros microorganismos fotótrofos. Tras la acción metabólica conjunta y la sucesiva creación de nuevos microambientes se formará un ecosistema más complejo, apareciendo bacterias y hongos, predominando los organismos con nutrición heterótrofa (aquellos que obtienen sus nutrientes y energía a partir de materia orgánica), como se ilustra en la **Figura 2, (4)**. Finalmente, los microorganismos colonizantes pueden formar una membrana biológica conocida como biofilm [30,31], matriz que permite la adherencia de los microrganismos a la superficie del material, favoreciendo tanto la retención de humedad como la fijación de otras sustancias presentes en el microambiente. El biofilm puede extenderse luego a otras áreas más grandes, acelerándose el biodeterioro del material (**Figura 2, (5) y (6**) [32,33].

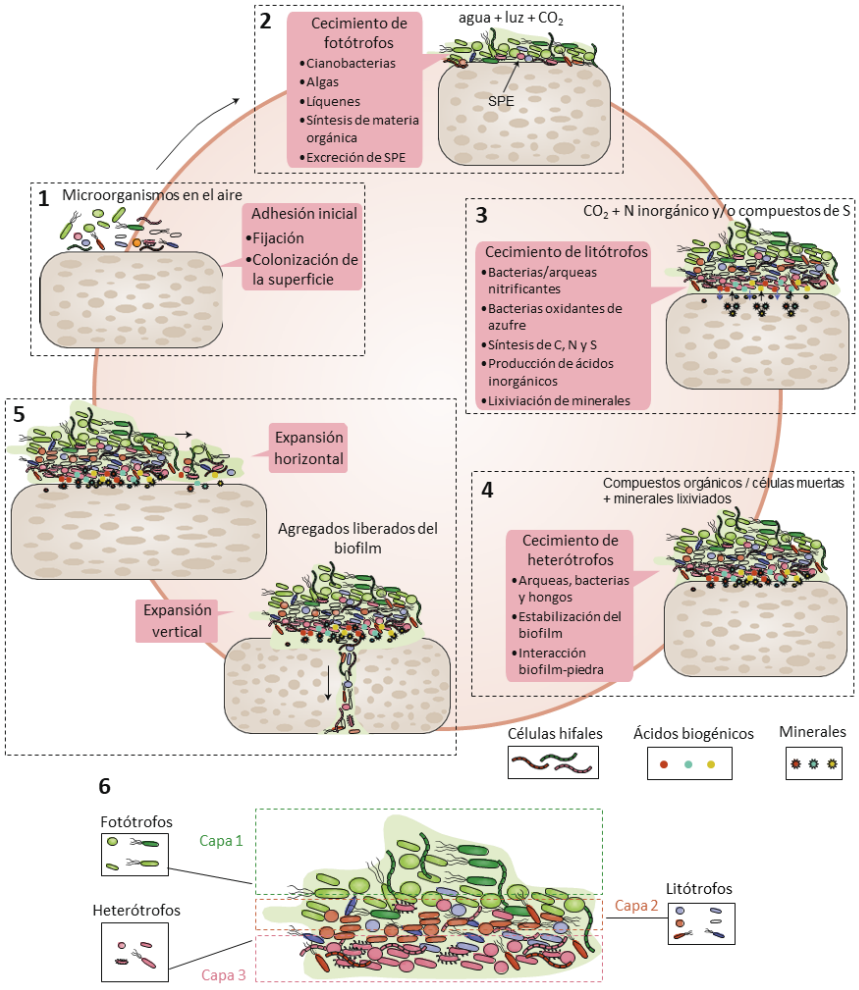

Figura 2. Formación del biofilm sobre la superficie de un material pétreo (adaptado de [32]).

2.2.1. Mecanismos de biodeterioro en los materiales pétreos

La contaminación microbiana en los materiales pétreos, además de afectar negativamente a la estética, provoca cambios no deseables en las propiedades físicas y/o químicas del material. Por un lado, el grado de deterioro biogeoquímico del material estará regido por la composición química de los minerales y de los compuestos cementantes existentes en

cada tipo de material. Por otro lado, los mecanismos de deterioro biogeofísicos dependerán en mayor medida de la porosidad o forma de los huecos y oquedades del material en cuestión [34].

2.2.1.1. Mecanismos de deterioro biogeoquímicos

Dentro de los mecanismos que provocan deterioros biogeoquímicos de los materiales pétreos se incluyen la acidólisis, la formación de complejos, reacciones de oxidación-reducción y procesos de acumulación de nutrientes orgánicos y suministro de oxígeno [34,35].

- **Acidólisis:** consiste en la reacción de ácidos (con poca o nula capacidad de formar un complejo) con los minerales del material. Estos ácidos (inorgánicos y orgánicos) proceden del metabolismo microbiano (ácidos biogénicos). La reacción química puede expresarse como:

$$M^+(\text{mineral})^- + H^+R^- \rightarrow H^+(\text{mineral})^- + M^+R^- \qquad (1)$$

donde R^- puede ser SO_4^{2-}, NO_3^-, HCO_3^-, $RCOO^-$. Este último representa al grupo de ácidos orgánicos de cadena corta, como son el láctico, fórmico, glucónico, acético, etc. Un ejemplo de acidólisis es el provocado por las bacterias nitrificantes que oxidan nitritos (procedentes de la polución atmosférica) a ácido nítrico. Posteriormente, la reacción de estos ácidos con los minerales conduce a la formación de sales mucho más solubles en agua que los compuestos del mineral original. La acidólisis es uno de los mecanismos biogeoquímicos que más se ha estudiado.

- **Formación de complejos**: los ácidos orgánicos excretados por los microorganismos pueden formar complejos con cationes metálicos

como el magnesio, calcio, silicio, aluminio, manganeso o hierro. Algunos de los ácidos son el cítrico, oxálico, fumárico, oxalacético, glucónico, 2-oxoglucónico o glioxálico. Además, el ácido carbónico generado en la respiración microbiana también puede actuar como agente complejante. Los hongos y líquenes son los microorganismos con más capacidad de degradar los minerales.

- **Reacciones de oxidación-reducción:** Ciertas cepas de hongos y bacterias pueden oxidar los cationes de hierro y manganeso de la matriz del mineral. De esta manera, se produce la movilización de estos cationes al medio exterior. El sucesivo transporte de estos cationes permite que se produzca un gradiente de concentración que hace que el proceso de lixiviación continúe. Este mecanismo conduce a una disminución de la resistencia del material.

- **Procesos de acumulación de nutrientes orgánicos y suministro de oxígeno:** los óxidos metálicos (producidos por las reacciones de oxidación-reducción) pueden quedar fijados a la superficie celular de los microorganismos, normalmente en asociación con algas y cianobacterias. Estos microrganismos autótrofos, a través de la fotosíntesis, producen oxígeno que favorecerá otras reacciones redox.

En la **Tabla 1** se pueden ver algunos ejemplos concretos del deterioro biogeoquímico.

Tabla 1. Ejemplos de procesos de deterioro biogeoquímicos en los materiales pétreos (adaptado de [36]).

Proceso biogeoquímico	Material susceptible	Ejemplo de microorganismo
Oxidación. $NH_4^+ \rightarrow NO_2^-$	Piedra, ladrillo, mortero, hormigón	Bacteria: *Nitrosomonas*, *Nitrosococcus*, *Nitrosospira*, *Nitrosolobus*
Oxidación. $NO_2^- \rightarrow NO_3^-$	Piedra, ladrillo, mortero, hormigón	Bacteria: *Nitrobacter*, *Nitrococcus*
Reducción. $NO_3^- \rightarrow NO_2^-$	Piedra, ladrillo, mortero, hormigón	Bacteria: *Escherichia*, *Pseudomonas*
Reducción. $NO_3^- \rightarrow NH_4^+$	Hormigón	Bacteria: *Clostridium*
Reducción. $SO_4^{2-} \rightarrow H_2S$	Piedra, ladrillo, mortero, hormigón	Bacteria: *Clostridium*; Bacterias reductoras de sulfato: *Desulfovibrio*, *Desulfomonas*, Desulfotomaculum
Oxidación. $H_2 \rightarrow H_2O$	Ladrillo, mortero, hormigón	Bacteria: *Alcaligenes*, *Micrococcus*, *Desulfovibrio*
Oxidación. S, compuestos reducidos de azufre $\rightarrow H_2SO_4$	Piedra, ladrillo, mortero, hormigón	Bacterias oxidantes de azufre: *Acidithiobacillus*, *Thiobacillus*, *Sulfobacillus*, *Sulfolobus* (*archaeon*)
Oxidación. $Fe^{2+} \rightarrow Fe^{3+}$	Piedra, ladrillo, mortero, hormigón	Bacteria: *Crenothrix*, *Gallionella*, *Leptothrix*, *Sphaerotilus*, *Sulfobacillus*, *Acidithiobacillus ferrooxidans*,
Oxidación. $Mn^{2+} \rightarrow Mn^{4+}$	Piedra, ladrillo, mortero, hormigón	Bacteria: *Bacillus*, *Gallionella*, *Pseudomonas*, *Sphaerotilus*
Procesos fermentativos. $C_{org} \rightarrow$ ácidos orgánicos; CO_2	Piedra, ladrillo, mortero, hormigón	Bacteria: *Achromobacter*, *Bacillus*, *Clostridium*, *Eschericha*, *Lactobacillus*, *Proteus*, *Pseudomonas* Alga: *Aphanocapsa*, *Chlorella*, *Chlorosarcinopsis*, *Desmococcus*, *Gomontia*, *Klebsormidium*, *Pleurococcus* Hongo: *Aspergillus*, *Ceratostomella*, *Cladosporium*, *Fusarium*, *Hormoconis*, *Penicillium*, *Spicardia*, *Trichosporon*

2.2.1.2. Mecanismos de deterioro biogeofísicos

Estos mecanismos son [34,35]:

- **Modificación de la porosidad total del material:** los compuestos coloidales generados por el biofilm penetran en el interior de los poros del material y ocasionan tensiones estructurales.

- **Cambios en la difusión de vapor de agua en la matriz mineral:** El biofilm contiene compuestos tensioactivos (glicolípidos, ácidos grasos, etc.) que disminuyen la tensión superficial del agua en los poros. Esto evita la pérdida de agua y protege a los microrganismos.

- **Tinción y decoloración de la superficie del material:** el metabolismo microbiano genera, entre otros, pigmentos como la melanina (color marrón), la clorofila (color verde) o carotenoides (color naranja) y compuestos de hierro o manganeso (Figura 3). Estos compuestos provocan cambios en las propiedades térmicas e hídricas de la superficie del mineral ya que se produce una alteración de la capacidad de absorción de la radiación solar.

- **Formación de costras negras en la superficie del material:** El biofilm favorece la absorción de partículas en suspensión y de gases contaminantes como los NO_x o el SO_2. Las costras formadas quedan fijadas al material y modifican ciertas propiedades físicas como la absorción/difusión de la humedad.

- **Procesos físicos:** la presión ejercida por las sustancias poliméricas extracelulares, hifas etc. en la matriz del material acentúa los efectos

negativos de procesos como los ciclos de hielo deshielo o la cristalización de sales.

- **Cambios en el grado de oxigenación de la superficie del material:** la posibilidad de colonización tanto de microorganismos aerobios como anaerobios altera la concentración de oxígeno en el biofilm, favoreciendo procesos de oxidación-reducción.

Figura 3. Cambio de coloración en una parte de los leones de la Fuente de los Leones del Palacio de la Alhambra en Granada, España (adaptado de [37]).

2.3. Sistemas de conservación preventiva

Con el objeto de remediar o evitar los problemas derivados de la contaminación microbiana en los materiales del patrimonio urbano, la aplicación de las técnicas de conservación preventiva se torna como una herramienta indispensable y a la vez compleja. La conservación preventiva se puede definir como una estrategia eficaz para proteger el patrimonio cultural y que proporciona un método de trabajo sistemático para identificar, evaluar, detectar y controlar los diversos riesgos de deterioro de los bienes culturales. Su objetivo principal es eliminar o minimizar, en la medida de lo posible, dichos riesgos, actuando sobre el foco del problema

(normalmente debido a factores externos al bien cultural). Por consiguiente, la conservación preventiva evita el deterioro y reduce la necesidad futura de acometer drásticos y costosos tratamientos aplicados sobre los propios materiales [38]. La conservación preventiva del material se lleva a cabo bajo la documentación del Plan de Conservación Preventiva, en el que se gestiona la programación, implantación y coordinación de las tareas de conservación. El Plan consta de varias fases, siendo el análisis de riesgos una de los más complejas, por lo que existen normas internacionales como la ISO 31000 (en España, UNE-ISO 31000) donde se detalla la metodología a seguir [39].

En el caso concreto de los materiales pétreos del patrimonio urbano, los tratamientos de conservación que se utilizan de forma más habitual sobre las zonas superficiales del material son: la limpieza, la aplicación de consolidantes, de hidrofugantes (o protectores) y el control biológico mediante agentes biocidas. Pasaremos a comentar con más detalle este último tipo de tratamiento.

2.3.1. Compuestos con propiedades biocidas

Se define como biocida a cualquier agente con capacidad para eliminar organismos. Dentro de este término, microbicida hace referencia a aquel que mata microorganismos. Los agentes alguicidas/fungicidas/etc. son aquellos que presentan alta eficacia contra las algas/hongos/etc. Por otro lado, si el agente no mata, sino que inhibe el crecimiento del organismo, se dice que el agente tiene un efecto microbioestático [40]. El mecanismo de acción de los biocidas generalmente se basa en la interacción específica con diferentes partes de la célula: pared celular, membrana citoplasmática y el citoplasma [41]. En cambio, otros compuestos biocidas, como por ejemplo el TiO_2, basan su efecto en la

capacidad oxidante de las diferentes especies reactivas de oxígeno ($\cdot O_2^-$, $\cdot OH$, etc.) que pueden generar [42].

Debido al fundamento de acción de los biocidas, estos pueden resultar potencialmente tóxicos para el medio ambiente o las personas. Por ello, los biocidas están sometidos a un control legislativo pormenorizado, siendo uno de los de productos químicos que acatan una regulación más estricta [43]. En Europa, la Agencia Europea de Sustancias y Mezclas Químicas (ECHA) es el organismo que se encarga de gestionar y aprobar/rechazar los principios activos que pueden ser comercializados [44]. Los biocidas se clasifican en 22 tipos de productos según su aplicación (conservantes en el área de alimentación, higiene, pesticidas, etc.), que a su vez se engloban en cuatro grandes grupos [45]:

- Grupo 1: Desinfectantes.
- Grupo 2: Conservantes.
- Grupo 3: Plaguicidas.
- Grupo 4: Otros biocidas.

Los biocidas dedicados a la conservación de los materiales urbanos aparecen dentro del Grupo 2. En este contexto, a finales del siglo XX se comenzaron a usar familias de compuestos como las sales de mercurio y otros derivados de metales pesados, que pronto se descartaron por su elevada toxicidad [34]. Igualmente, otros compuestos utilizados hace unas décadas, como el pentaclorofenol o el bromuro de metilo no están permitidos actualmente [46]. Con el paso del tiempo, los grandes avances en la Química han conducido a compuestos biocidas más selectivos y efectivos, con una toxicidad reducida. Para que un compuesto biocida

pueda ser aplicado en el ámbito de la restauración y conservación, este debe cumplir una serie de requisitos [47–49]:

- gran eficacia biocida
- estabilidad química
- baja solubilidad en agua para evitar su lixiviación al medio exterior
- nula interferencia con los materiales que constituyen la obra (no generar cambios de color, precipitación de sales, etc.)
- baja toxicidad para la salud humana
- respetuoso con el medio ambiente
- económico
- en caso de que el biocida se aplique en estado líquido, debe de tener baja viscosidad para permitir una buena penetración en el sustrato

Por ejemplo, ciertos compuestos que han demostrado una gran eficacia biocida en otros campos de estudio, como los derivados de la plata o las nanopartículas de cobre, resultan de menor aplicabilidad debido al elevado coste o al cambio de color que producen en el material, respectivamente [50,51]. Otros compuestos orgánicos muy conocidos son la metil-isotiazolinona y la clorometil-isotiazolinona (MIT y CMIT), también deben de descartarse para las tareas de restauración de materiales urbanos debido a su elevada solubilidad en agua [52].

En consecuencia, aunque existe un gran número de familias de compuestos biocidas (alcoholes, fenoles, ácidos, ésteres de ácido, aldehídos, amidas, carbamatos, sales de amonio cuaternario, etc. [53–55]),

actualmente existen muy pocos productos especialmente diseñados para la conservación del patrimonio cultural. Esto se debe a que no se han realizado suficientes estudios que abarquen la compatibilidad de los componentes de los materiales (aglutinantes, pigmentos, etc.) con los agentes biocidas en cuestión. Asimismo, existen pocos estudios que investiguen los diversos efectos a largo plazo que los biocidas pueden potencialmente provocar sobre el material [56].

Además de los compuestos orgánicos, ciertos compuestos inorgánicos como el ZnO y el TiO_2 se han empleado como agentes antimicrobianos. En este sentido, la nanotecnología ha permitido un gran avance en la preparación de este tipo de compuestos, mejorando las propiedades consolidantes o biocidas [51,57,58]. También se ha descrito que los tratamientos superficiales del material basados en la combinación de agentes biocidas e hidrofugantes pueden mejorar la actividad antimicrobiana [48,59].

En la **Tabla 2** se muestran algunos ejemplos de los biocidas (inorgánicos u orgánicos) utilizados en diferentes tipos de materiales urbanos. Profundizando en este marco, se puede encontrar bibliografía muy completa en la que se detallan las características y propiedades de los diferentes tipos de biocidas [40,54,55]. El modo de aplicación de los agentes biocidas sobre el material varía dependiendo de cada caso particular, ya que se debe tener en cuenta varios aspectos como el tipo de material sobre el que se aplican, el estado de conservación del material, el tipo producto biocida a seleccionar, etc. Los productos biocidas disponibles en el mercado se encuentran en forma de líquidos, polvos dispersables o emulsiones (ambas en base de agua o de disolventes orgánicos), por lo que se pueden aplicar de diferentes maneras: cepillado, inyección, inmersión, mediante compresas o en forma de aerosol [40]. Además, una amplia gama

de productos empleados en construcción y en tareas de restauración y conservación, como pinturas o morteros, contienen aditivos biocidas al objeto de prevenir la contaminación microbiana del material donde se aplican [60–63]. De hecho, el empleo de este tipo de productos representa más del 95% del mercado correspondiente al aislamiento de fachadas de los edificios [64]. En este contexto, el capítulo 2.4 de la presente memoria refiere los aditivos antimicrobianos empleados en uno de los materiales más utilizados en las labores de conservación: los morteros de restauración.

Tabla 2. Ejemplos de compuestos biocidas empleados en los materiales urbanos.

Nombre comercial del biocida	Principio activo	Material en el que se aplica	Referencia
Acticide CF	2-N-octil-4-isotiazolin-3-ona y un derivado de 2,4-diamino 6-metiltio-1,3,5-triazina	Cerámica, dolomita	[65,66]
Acticide IPW 50	3-yodo-2-propinil N-butil carbamato	Pintura, enlucido	[67,68]
Acticide OTW 16	2-N-octil-4-isotiazolin-3-ona	Pintura, enlucido	[67,68]
Algon P Paste	Diuron	Pintura, enlucido	[67,69]
Algon PS Paste	Terbutrina	Pintura, enlucido	[67,69]
Konservan ZSW	Carbendazima	Pintura, enlucido	[67,69]
ROCIMA 103	2-octil-2H-isotiazol-3-ona y cloruro de didecil dimetilamonio	Mármol, arenisca, ladrillo revestido de yeso	[70]
Mirecide	3-yodo-2-propinil N-butil carbamato y 2-N-octil-4-isotiazolin-3-ona	Mármol, arenisca, ladrillo revestido de yeso	[70]
Kimistone	cloruro de didecil dimetilamonio y cloruro de benzalconio	Mármol, arenisca, ladrillo revestido de yeso	[70]
Fungipol CP 237	Diuron, Carbendazima y 2-octil-2H-isotiazol-3-ona	Pintura, otros materiales de rehabilitación	[71]
P25	TiO_2	Mortero	[72]
Biotin T	cloruro de alquil-benzil-dimetil-amonio e isopropil alcohol	Mortero, granito, arenisca	[72–74]
Biotin R	2-octil-2H-isotiazol-3-ona y 3-yodo-2-propinil N-butil carbamato	Granito, arenisca	[73,74]
Preventol RI80	cloruro de benzalconio	Granito, arenisca	[73,74]
Anios D.D.S.H	propionato de n-didecil-n-metil-poli (oxietil) amonio y acetato de alquil-propilen-diamineguanidio	Mortero	[72]
Algophase	2,3,5,6-tetracloro-4-metilsulfonil-piridina	Mármol	[75]
-	H_2O_2	Mármol	[75]
Hyvar X	5-bromo-3-sec-butil-6-metil uracilo	Granito	[76]
-	cloruro de benzalconio	Granito, arenisca	[74,76]
-	Quitosano	Caliza	[77]
-	$AgNO_3$	Caliza	[77]
Glifene SL	N-(phosphonomethyl)glycine	Arenisca	[74]
DesNovo	cloruro de benzalconio	Arenisca	[74]
Lichenicida	4,5-dicloro-2-octil-4-isotiazolin-3-ona, 3-yodo-2-propinil N-butil carbamato, 2-N-octil-4-isotiazolin-3-ona, y alcohol benciílico	Arenisca	[74]
Usnic Acid	2,6-diacetil-7,9-dihidroxi-8,9b-dimetildibenzofuran-1,3 (2H, 9bH) -diona	Arenisca	[74]
Microban B	2,4,4-tricloro-2-hidroxidifenil éter	Hormigón	[78]
-	ZnO	Dolomita, caliza	[13]

2.3.2. Biocidas aplicados a los materiales urbanos

Como se comentó anteriormente, un modo muy frecuente de utilización de los biocidas consiste en su aplicación directa sobre el material urbano (mortero, madera, mármol, pintura, etc.) para intentar proteger la superficie de una futura contaminación microbiana. Sin embargo, esta metodología suele requerir elevadas dosis de producto biocida si se desea conseguir un efecto duradero, ya que los agentes biocidas quedan expuestos a factores ambientales (lluvia, viento, temperaturas extremas, radiación UV, etc.) que provocan su degradación a compuestos inactivos y su lixiviación al medio ambiente [79,80]. En este sentido, los compuestos biocidas más empleados suelen ser moléculas orgánicas de un tamaño relativamente pequeño, con un elevado coeficiente de difusión, y por ende con mayor tendencia a la lixiviación [81–83]. Para paliar la pérdida de eficacia biocida se suele realizar una aplicación con una mayor cantidad de producto, lo que conlleva una mayor utilización de los disolventes/dispersantes orgánicos de la formulación a aplicar [84]. Como resultado, estos factores aumentan de forma significativa el riesgo de contaminación de los usuarios y del medio ambiente, así como el desperdicio del producto biocida.

Otro método común de prevenir la contaminación microbiana en los materiales pétreos urbanos está basado en la aplicación de pinturas y/o morteros de restauración. Estas formulaciones contienen aditivos antimicrobianos que dotan al material donde se aplica con propiedades biocidas [60–63]. Si bien estos recubrimientos protegen al material por periodos más largos, de entre 6 meses y 2 años, existe una necesidad urgente de prolongar el efecto biocida de forma considerable, teniendo en cuenta que la vida útil de las construcciones urbanas es de al menos 10 años [85]. A destacar, la vida de los materiales pertenecientes al Patrimonio

Cultural se estima en mucho más tiempo al objeto de conseguir transmitirlos a las generaciones venideras. Aunque aumentar la concentración del principio activo en la formulación haría que el efecto antimicrobiano fuera más duradero [79], hay que considerar que esta operación no es en absoluto viable desde un punto de vista medioambiental y/o legal. Asimismo, el elevado coste de los principios activos y la alteración de las propiedades mecánicas de la formulación hacen descartar definitivamente dicha opción [81,86].

Una estrategia factible para aumentar la eficacia biocida a largo plazo es la utilización de sistemas de liberación controlada (SLC) de los principios activos que se encuentran en la formulación. Esta tecnología ha sido aplicada con éxito en áreas de muy alto nivel tecnológico para encapsular/adsorber diferentes tipos de productos químicos (antibióticos, herbicidas, conservantes, etc.). Por ejemplo, se pueden destacar el área de la medicina [87], el sector farmacéutico [88,89], el de los cosméticos [88,90], la agricultura [91,92] y la alimentación [93,94].

En esta tecnología, el agente activo (un compuesto con propiedades antimicrobianas, por ejemplo) se incorpora a la superficie o al interior de la estructura de un compuesto adecuado que actúa como soporte o portador (de naturaleza inorgánica u orgánica), de manera que se consigue una liberación del agente activo más sostenida a lo largo del tiempo, desde el soporte al medio externo [95–97]. Como resultado, no solo se amplía el tiempo en que la formulación presenta actividad biocida, sino que el soporte también puede dotar al principio activo de una protección ante la exposición a diferentes factores externos (elevados pHs, radiación UV, etc.) que podrían dar lugar a su descomposición. Asimismo, como el principio activo se encuentra adherido al soporte, se reduce la posibilidad de lixiviación del compuesto biocida al medio ambiente, con el

consecuente beneficio en términos de sostenibilidad y toxicidad (**Figura 4**) [98]. Todas estas acciones conducen a una menor necesidad de futuros tratamientos reiterados sobre las estructuras en las cuales se aplicarían estas formulaciones, disminuyendo por tanto el coste económico y de gestión de esas tareas de mantenimiento.

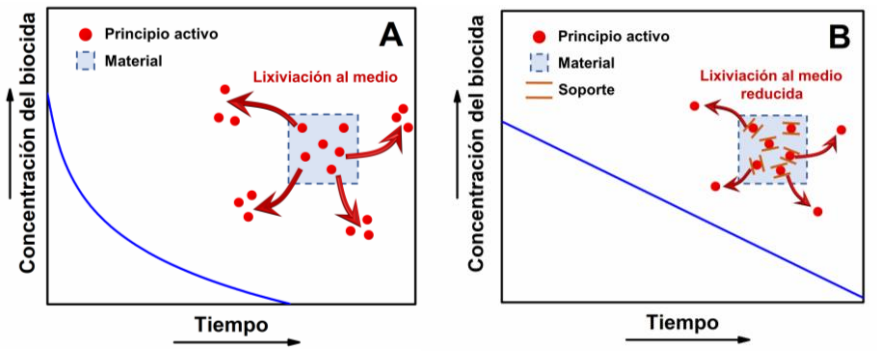

Figura 4. Perfil de liberación de un compuesto biocida a lo largo de la vida útil de un material: (A) biocida sin soportar; (B) biocida soportado

Una vía para lograr la liberación controlada del biocida es la microencapsulación [99–101]. En este proceso, la formación de cápsulas de tamaño micrométrico o nanométrico (micro- o nanocápsulas) permiten atrapar en su interior el agente activo. También es posible obtener otro tipo de estructura soporte, las microesferas, donde el agente activo se encuentra disperso por toda la matriz que conforma la microesfera [101].

Otra estrategia para soportar los agentes biocidas se basa en la adsorción (fisicoquímica o física) del compuesto activo sobre un material inorgánico que actúa como soporte [102] . En el procedimiento de la adsorción fisicoquímica, el primer paso reside en la funcionalización química de la superficie del soporte inorgánico, lo que permitirá en una fase posterior formar enlaces químicos con el agente antimicrobiano en

cuestión [103–105]. Esta fuerte unión entre el soporte y el compuesto biocida se traduce en una liberación del biocida más controlada. Sin embargo, este modo de adsorción es complejo, costoso y requiere un tiempo de síntesis elevado y es específico para cada tipo de agente biocida [95]. Por otro lado, en la adsorción física, una metodología muy común es la de preparar una dispersión del soporte inorgánico en una disolución del agente antimicrobiano que se quiere adsorber [97,106]. En este caso, la metodología es más sencilla y se puede conseguir la adsorción de diferentes clases de agentes antimicrobianos en función del disolvente empleado [95]. En este sentido, los soportes más demandados en estos procedimientos de adsorción suelen ser los nanomateriales que presentan elevados valores de superficie específica y un gran volumen de poro, ya que presentan potencialmente una gran capacidad para cargar compuestos en su estructura porosa. En este sentido, se han utilizado como soportes de biocidas las zeolitas [107] y nanopartículas de sílice mesoporosa [108–111], destacando las estructuras con poros ordenados del tipo SBA [52] y MCM [112–114].

También se han investigado otros soportes inorgánicos cuya obtención sea más sencilla y rápida, como óxidos, hidróxidos dobles laminares y arcillas. En la **Tabla 3** se recogen diversos estudios sobre este área, indicando el biocida adsorbido y el material donde se aplicaría la formulación.

Tabla 3. Ejemplos de óxidos, hidróxidos y arcillas empleados como soportes de liberación controlada de agentes biocidas.

Soporte/s	Biocida/s	Potencial aplicación	Referencia
Al_2O_3	Carbendazima	Madera	[115]
Al_2O_3, MgO, SiO_2, CuO, ZnO y TiO_2	Clorotalonil, Diclofluanida, Diurón, Irgarol, Seanina y Tolilfluanida	Recubrimientos de embarcaciones	[116]
Hidróxido Doble Laminar $[Mg_{0.66}Al_{0.33}(OH)_2](NO_3)_{0.33}$ n H_2O	Paeonol	Resina	[117]
Hidróxido Doble Laminar $[Zn_{0.66}Al_{0.33}(OH)_2](NO_3)_{0.33}$ n H_2O	Paeonol	Pintura	[118]
Humo de sílice, sepiolita, montmorillonita	Cloruro de benzalconio	Compresas para rehabilitación de Patrimonio Urbano	[119,120]
Montmorillonita modificada con lecitina	Monoterpenos: citronelol, citral y linalool	Pintura	[121]
Haloisita	Carbonato de yodobutilpropilo	Pintura	[122]
Haloisita	4,5-diclorooctilisotiazolona (DCOIT)	Resina	[123]

Existen un buen número de trabajos enfocados al estudio de recubrimientos del tipo de resinas y pinturas. Sin embargo, son pocos los estudios dedicados a la incorporación de biocidas soportados sobre compuestos inorgánicos para su aplicación en materiales pétreos del patrimonio urbano. A destacar, se ha estudiado la aplicación sobre el hormigón de un recubrimiento que incorporaba la composición patentada AgION™, basada en una zeolita como soporte de cationes de plata que actúan como biocidas [124]. Este sistema resultó ser mucho más eficaz que el recubrimiento sin AgION™, evitando la contaminación microbiana (Acidithiobacillus thiooxidans) [125,126]. Por otra parte, De Muynck et al. [78] investigaron la eficacia antimicrobiana de morteros (en base de cemento) aditivados con varios sistemas comerciales: Microban® B (fibras con el biocida triclosán [127]) o Zeomic (zeolitas de plata y cobre [128]).

Hay que destacar también algunos trabajos en los que las arcillas con biocidas adsorbidos han sido añadidas a la composición de ciertos

materiales pétreos. En este campo, Scarfato et al. emplearon la arcilla del tipo haloisita para adsorber una formulación biocida comercial (Biotin T), posteriormente incorporando el composite a un mortero en base de cemento. Para algunos de los morteros estudiados se observó una acción biocida a partir del segundo año, lo que se atribuyó a la liberación controlada del agente activo desde la haloisita. Asimismo, el composite hizo disminuir la adsorción capilar del mortero debido a cambios en la microestructura de este, lo que conduciría a una mejora de la durabilidad del sistema [129]. En otra investigación pionera, el grupo de investigación de Puertas Maroto utilizó la sepiolita como adsorbente del biocida pentaclorofenol para su aplicación en morteros de restauración (en base cal [130]), estudiando en detalle varios efectos de la adición de la arcilla y del composite sobre el mortero y se determinó la adecuada compatibilidad de esta arcilla con el mortero, además de un cierto grado de protección del mortero frente a algunos agentes externos [131–134]. Hay que mencionar es que la sepiolita no posee gran afinidad por moléculas hidrofóbicas como pueden ser los propios compuestos biocidas, por lo que necesita ser modificada para conseguir una organo-sepiolita [135,136]. En esta dirección, Eversdijk at al. desarrollaron una arcilla del tipo montmorillonita modificada con surfactantes catiónicos (basados en sales de amonio cuaternario) para mejorar la adsorción de varios biocidas en el yeso (propiconazol, imazalil y betoxacina), encontrando que la liberación de estos durante los ensayos de lixiviación fue menor cuando se utilizaron surfactantes con un carácter hidrofóbico [137].

2.4. Morteros de restauración

La intervención en un edificio o monumento a rehabilitar debe de comenzar por un análisis exhaustivo de su historia y los materiales utilizados en su construcción. Conjuntamente, resulta crucial diagnosticar las patologías del material, de manera que se pueda lograr una adecuada selección de los productos y las técnicas a emplear [138]. Para ello, es necesario el desarrollo de una investigación multidisciplinar donde intervienen áreas como la química, petrología, geología, historia, arquitectura, etc.

En este contexto, los morteros de restauración son uno de los materiales que se emplean con más frecuencia en las labores de intervención dedicadas a los materiales pertenecientes a las construcciones históricas y arqueológicas [139–141]. En el ámbito de la restauración y de la construcción, un mortero se define como una mezcla homogénea de áridos, conglomerantes inorgánicos y agua, a la que en ciertas ocasiones se le añaden diversos tipos de aditivos. Cuando aún no se ha añadido agua a la mezcla, el mortero es llamado "seco" (**Figura 5**), mientras que una vez que se ha añadido el agua y se ha realizado el amasado, el mortero es llamado "fresco" y está listo para su aplicación.

La realización de las técnicas de rehabilitación de los materiales del patrimonio está regulada al objeto de conseguir un acabado adecuado. Por ejemplo, la norma española UNE 41807 IN:2012 describe las técnicas de intervención para la reparación de revocos de mortero en fachadas de edificios [142]. Esta norma incluye el procedimiento a aplicar para los edificios o bienes catalogados de interés cultural y define los tipos de morteros apropiados para realizar las intervenciones. Así, se indica que los

morteros a utilizar deben ser morteros de cal compatibles con los soportes tradicionales.

Figura 5. Saco de 25 Kg de un mortero de rehabilitación comercial [143].

2.4.1. Morteros de cal

El mortero de cal es uno de los más empleados en obras de rehabilitación y restauración de patrimonio histórico, aunque también pueden aplicarse a obras nuevas (por ejemplo: revoques tradicionales, saneamiento de paredes, pavimentos, etc.). El conglomerante de estos morteros está compuesto principalmente por el hidróxido de calcio, $Ca(OH)_2$, también llamado como cal apagada. Cuando se procede con la amasada de estos morteros tiene lugar el inicio del fraguado, que consiste en la reacción química entre el $Ca(OH)_2$ y el CO_2 presente en el aire [144].

$$Ca(OH)_2 + CO_2 \rightarrow CaCO_3 + H_2O \quad (2)$$

Esta reacción es muy lenta, y puede tardar muchos años e incluso siglos en completarse. Varios factores ambientales, como la temperatura,

humedad y concentración de dióxido de carbono influyen en el proceso de la carbonatación [145].

Existen dos grupos de morteros de cal bien diferenciados, haciendo referencia al tipo de cal que incorporan en su composición:

- **Cal aérea:** principalmente compuesta por $Ca(OH)_2$. Puede contener también hidróxido de magnesio, $Mg(OH)_2$. El proceso de fraguado se produce por el CO_2 atmosférico, según la reacción anterior.

- **Cal hidráulica:** además del $Ca(OH)_2$, esta contiene silicatos y aluminatos de calcio que le confieren propiedades hidráulicas. Así, esta cal puede fraguar y endurecer cuando se mezcla con agua (hidratación de los silicatos de calcio) y también por reacción del hidróxido de calcio con el CO_2 atmosférico [146].

El mecanismo de fraguado de los morteros de cal hidráulica da lugar a unas propiedades específicas que se adaptan a las condiciones requeridas en las obras de rehabilitación y que permiten un endurecimiento del mortero en ambientes húmedos. Entre estas propiedades se pueden destacar [139,147]:

- **Compatibilidad:** los morteros de cal son adecuados para rehabilitación y restauración debido a su excelente compatibilidad con los soportes antiguos. Por un lado, estos morteros presentan buenas propiedades mecánicas (baja resistencia a la compresión), por lo que se consigue una mejor adaptación a los soportes donde se aplican, que suelen tener bajas resistencias. Por otro lado, la compatibilidad química viene derivada de la ausencia de sales solubles en la composición del mortero,

evitando la precipitación de compuestos que pueden afectar negativamente a la integridad de este.

- **Permeabilidad:** la formación de poros y capilares en el seno del mortero permite una alta permeabilidad. Esto se traduce en una reducción del riesgo de humedades al permitir el intercambio de vapor y se garantiza una mayor durabilidad de la obra.

- **Trabajabilidad y flexibilidad:** los morteros de cal poseen excelente trabajabilidad (elevado tiempo de utilización en estado fresco), derivado de la lentitud del proceso de carbonatación. Además, tienen una gran plasticidad y un módulo de elasticidad bajo, por lo que pueden adaptarse a los pequeños movimientos y vibraciones producidos por los materiales donde se aplican.

No obstante, no siempre se han utilizado este tipo de morteros en la rehabilitación, debido a la gran revolución que supuso la llegada del cemento portland (conglomerante) en el mundo de los materiales de construcción, a principios de siglo. Los buenos resultados que se estaban obteniendo con la utilización de los morteros de cemento en el área de la construcción, llevaron también a su empleo en los procesos de reparación. Sin embargo, no se tuvieron en cuenta las diferentes propiedades de los morteros de cemento (elevada resistencia mecánica, inflexible e impermeable) y el mortero de cal (baja resistencia mecánica, elevada permeabilidad al vapor, deformabilidad) al que reemplazaba o acompañaba.

Todo ello trajo efectos negativos en la conservación de los materiales donde se aplicaron [148]. Ante esta situación, surgió la

necesidad de utilizar los morteros basados en cal para estas aplicaciones. Estos morteros satisfacen el principio de la mínima intervención sobre las obras patrimoniales, al ser materiales análogos a los empleados en las edificaciones originales.

2.5. Contaminación atmosférica en el hábitat urbano

La definición de contaminación atmosférica realizada por el Ministerio para la Transición Ecológica y el Reto Demográfico (Gobierno de España) hace referencia a la presencia en la atmósfera de materias, sustancias o formas de energía que implican molestia grave, riesgo o daño para la seguridad o la salud de las personas, el medio ambiente y demás bienes de cualquier naturaleza [149]. Dicha contaminación se presenta como un grave problema global, originado especialmente por la continua extensión de la industrialización, medios de transporte y producción tanto en países desarrollados como en aquellos que se encuentran en vías de desarrollo. De hecho, las restricciones de movilidad y de producción en ciertos sectores del trabajo derivadas de la pandemia global de COVID-19 han puesto de manifiesto la significativa disminución de la concentración de los contaminantes atmosféricos [150–152].

En este contexto, resulta primordial alcanzar un *desarrollo que cubra las necesidades del presente sin comprometer la capacidad de generaciones futuras*, concepto conocido como “desarrollo sostenible”. Esta concienciación de la Sociedad y de los organismos gubernamentales se comenzó a establecer hace varias décadas con en el Informe Brundtland [153], lográndose, en general, mejoras en la gestión de los recursos y el

control en las emisiones gaseosas. Sin embargo, actualmente la contaminación atmosférica sigue presente en el día a día de las personas, pues el 91 % de la población mundial vive en lugares donde la calidad del aire excede los límites establecidos por la OMS [154]. En particular, los efectos adversos que implica la contaminación del aire son más acentuados en los medios urbanos, que son puntos críticos de emisiones gaseosas [155]. En este sentido, la contaminación del aire implica varios riesgos a diferentes niveles:

- Salud humana: aunque los efectos concretos sobre el cuerpo humano dependen de varios factores (tipo de contaminante, tiempo de exposición, etc.), las principales enfermedades están relacionadas con el sistema respiratorio y cardiovascular (**Figura 6**). Otras evidencias recientes asocian la contaminación del aire con el trastorno neurocognitivo (demencia) [156], el bajo peso al nacer [157] y a la diabetes del tipo 2 [158]. Todos estos riesgos llevan a que alrededor de 4,2 millones de personas fallezcan cada año de forma prematura en todo el mundo (datos de 2016) [154]. Como comparativa, el número de fallecidos en accidentes de tráfico a nivel global se estima en 1,3 millones anuales [159].

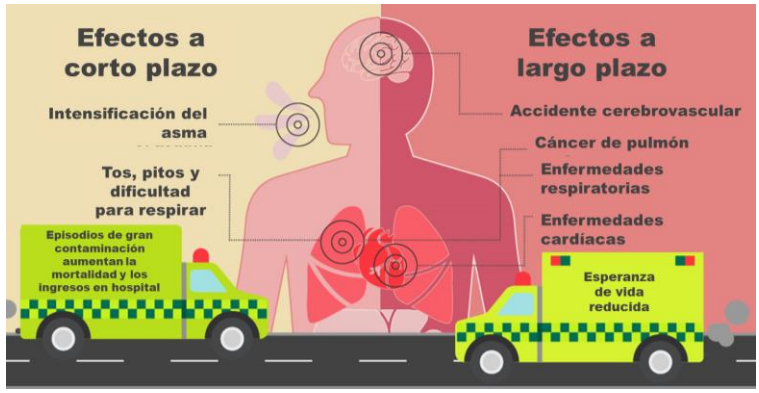

Figura 6. Principales efectos de la contaminación atmosférica en la salud humana. Adaptado de [160].

- Medio ambiente: entre otros muchos, se pueden citar la disminución de la capa de ozono, la eutrofización y acidificación de las aguas (que afectan a la diversidad de los ecosistemas), crecimiento reducido de las especies vegetales y alteración de sus procesos fisiológicos y bioquímicos, reducción de los rendimientos de la agricultura, etc. [161]

- Materiales urbanos: como sea comentado en esta memoria, los gases y vapores contaminantes pueden tener una naturaleza corrosiva inherente, o bien pueden reaccionar químicamente en la atmósfera para dar compuestos muy reactivos [12,161,162]. En definitiva, se contribuye al deterioro tanto del Patrimonio como de las infraestructuras urbanas (carreteras, redes eléctricas, puentes, etc.). Estos efectos se traducen en pérdidas económicas y culturares [163,164].

Hay que señalar que las fuentes de emisión de los gases contaminantes pueden ser antropogénicas o naturales, si bien la evolución de estas últimas no se considera preocupante al formar parte del equilibrio

natural (erupciones volcánicas, incendios forestales naturales, flatulencias de la digestión de los animales, etc.) [165]. Entre las fuentes antropogénicas más importantes se pueden citar la quema de combustibles fósiles para la obtención de energía (calor/electricidad), ciertos procesos industriales (metalurgia, construcción, etc.) y los medios de transporte [165,166]. Entre otros, los contaminantes atmosféricos más importantes son:

- Partículas (PM): las partículas en suspensión están constituidas por una mezcla compleja de sustancias sólidas y líquidas que varían en composición, forma y tamaño. La composición de las PM varía enormemente y depende de muchos factores, como la ubicación geográfica, las fuentes de emisión y el clima. Las PM se clasifican atendiendo a su tamaño, siendo las más perjudiciales las menores o igual a 10 µm (PM_{10}) y las menores o igual a 2,5 µm ($PM_{2.5}$). Estas últimas conllevan una peligrosidad mayor, pues además de alojarse en los pulmones, pueden atravesar la barrera pulmonar y entrar en el sistema circulatorio [154,161,167]. Como componentes principales se pueden encontrar el hollín (carbono elemental u orgánico), iones inorgánicos (sulfatos, nitratos), cloruro de sodio, amoníaco, polvos minerales y el agua.

- Ozono (O_3): este compuesto aparece en núcleos urbanos cuando varios contaminantes atmosféricos (Compuestos Orgánicos Volátiles, óxidos de nitrógeno, etc.) reaccionan de manera fotoquímica [168], y su inhalación provoca diversas afecciones en el sistema respiratorio [169].

- Óxidos de azufre (SO_x): la contribución antropogénica de estos contaminantes (monóxido y dióxido de azufre) se debe a ciertos

procesos industriales (fundición de menas) y a la combustión de los combustibles fósiles, en cuya composición suele aparecer el azufre. El SO_2 afecta al sistema respiratorio, provoca irritación ocular y participa en la formación de la lluvia ácida [154].

- Compuestos Orgánicos Volátiles (COVs): abarcan un conjunto de compuestos químicos de diversa procedencia. Se pueden clasificar como COVs o como COVNM (COV No Metano) si no se incluye a dicho gas. Las mayores fuentes antropogénicas derivan del uso de los combustibles fósiles en el transporte y las industrias químicas. Como ejemplos se pueden citar el metano (contribución al calentamiento global), acetileno, benceno, xileno, 1,3-butadieno, (compuestos cancerígenos), etc. [165,170].

- Óxidos de carbono (CO y CO_2): el CO se genera como producto intermedio en la combustión incompleta de combustibles fósiles. Es muy tóxico y peligroso por su afinidad a unirse al hierro de la hemoglobina impidiendo la unión y transporte del O_2 y además carece de olor y es incoloro. Este gas se puede concentrar en tramos rodados con poca ventilación y gran tráfico, derivadas de las emisiones de los vehículos [165]. En cuanto al CO_2, su emisión antropogénica se debe a ciertos procesos industriales como la producción del cemento y, principalmente, a la combustión de combustibles fósiles. Aunque no está considerado como un gas tóxico [171], su capacidad como gas de efecto invernadero hacen que sus emisiones estén reguladas.

- Otros contaminantes: amoniaco, compuestos clorofluorocarbonados, radón, plomo y demás metales pesados.

- Óxidos de nitrógeno (NO_x): los NO_x (NO + NO_2) se generan de forma natural (relámpagos, microorganismos, volcanes, etc.), si bien la principal fuente de estos gases es la combustión de combustibles fósiles derivada de los vehículos de motor y de las centrales eléctricas. Debido a su gran impacto ambiental y en la salud humana, están considerados como uno de los contaminantes más importantes [172].

De los contaminantes citados, hay que destacar que la Unión Europea identifica 7 como principales: PM, O_3, SO_2, COVNM, CO, amoniaco y NO_x [173]. De estos, los más abundantes en el hábitat urbano son el dióxido de nitrógeno, las partículas y el ozono [174] . Los contaminantes atmosféricos se encuentran regulados en la Unión Europea (Directivas 2008/50/CE, 2004/107/CE y 2015/1480) además de las directrices fijadas por la OMS en 2005, que próximamente esperan ser actualizadas (**Tabla 4**) [175,176]. En este sentido, se ha descrito que los valores límite existentes para todos los contaminantes deberían de ser reducidos para lograr una mayor seguridad en la salud del ciudadano [177].

Tabla 4. Comparativa entre los valores límite de los contaminantes del aire legislados por la UE y los recomendados por la OMS.

Contaminante	Valor legislado UE	Valor guía OMS
SO_2 (horario)	350 µg/m^3 (>24 veces/año)	-
SO_2 (diario)	125 µg/m^3 (>3 veces/año)	20 µg/m^3
NO_2 (horario)	200 µg/m^3 (>18 veces/año)	200 µg/m3
NO_2 (anual)	40 µg/m^3	40 µg/m^3
PM_{10} (diario)	50 µg/ m^3 (> 35 veces/año)	50 µg/ m^3 (> 3 veces/año)
PM_{10} (anual)	40 µg/m^3	20 µg/m^3
$PM_{2,5}$ (diario)	-	25 µg/m^3 (> 3 veces/año)
$PM_{2,5}$ (anual)	25 µg/m^3	10 µg/m^3
O_3 (máximo diario 8h)	120 µg/m^3	100 µg/m^3
CO	10 mg/m^3 (máximo diario octohorario anual)	10 mg/m^3 (8h)
Pb (anual)	0,5 µg/m^3	0,5 µg/m^3
As (anual)	6 ng/m^3	-
Cd (anual)	5 ng/m^3	5 ng/m^3
Ni (anual)	20 ng/m^3	-
Benceno (anual)	5 µg/m^3	-
Benzopireno	1 ng/m^3	-

2.5.1. Contaminación por óxidos de nitrógeno y métodos de mitigación

Los NO_x, suma de los gases NO y NO_2, son considerados como unos de los contaminantes del aire más importantes [172]. El NO es un gas insoluble en agua, sin color ni olor, mientras que el NO_2 sí es soluble en

agua, es de color marrón-rojizo y posee un olor desagradable y ácido. En cuanto a la peligrosidad, el NO_2 es mucho más tóxico que el NO.

El NO tiene una vida media relativamente corta, (de minutos a horas), pues puede reaccionar fotoquímicamente para dar NO_2:

$$2\ NO + O_2 \rightarrow 2\ NO_2 \qquad (3)$$

Este gas también puede originarse por la reacción del monóxido de nitrógeno con el ozono:

$$2\ NO + O_3 \rightarrow NO_2 + O_2 \quad (4)$$

El NO_2 puede sufrir fotólisis bajo la irradiación ultravioleta solar, lo que desencadena la generación de ozono:

$$NO_2 + hv \rightarrow NO + O^* \quad (5)$$

$$O^* + O_2 + M \rightarrow O_3 + M \quad (6)$$

donde M es una molécula (principalmente N_2 u O_2). El ozono a su vez puede reaccionar con el monóxido de nitrógeno [161]:

$$O_3 + NO + \rightarrow O_2 + NO_2 \quad (7)$$

Como se aprecia en las anteriores ecuaciones, existe una relación entre los NO_x y el ozono (**Figura 7**), en el que además participan radicales derivados de la oxidación de los COVs (**Figura 7**) [178]. Este hecho es particularmente importante en los entornos urbanos, donde la presencia

de ambos contaminantes puede resultar perjudicial. Además, los NO_x juegan un papel importante en la emisión de las PM, ya que dichos gases pueden reaccionar con el amoníaco y otros compuestos en presencia de vapor de agua para producir aerosoles. Otro conjunto de contaminantes derivados de los NO_x son los ácidos nítrico y nitroso (HNO_3 y HNO_2, respectivamente), el nitrato de peroxiacetilo (PAN), el óxido nitroso (N_2O) y el anhídrido nítrico (N_2O_5) [161]. Hay que destacar que la reactividad asociada a los NO_x no es la misma durante el día (mientras hay luz solar) y la noche, por lo que la concentración de aquellos en el hábitat urbano no es constante [179,180].

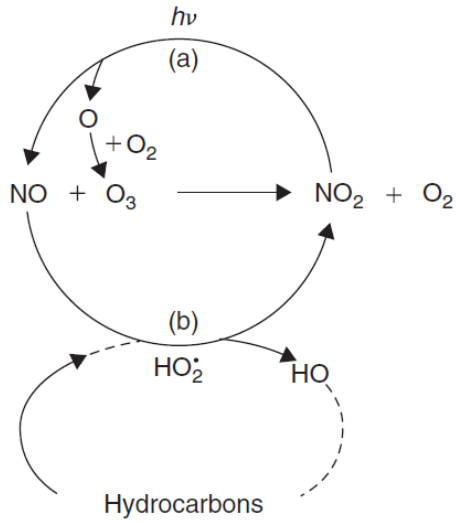

Figura 7. Principales reacciones entre NO, NO_2, O_3, y radicales libres [161].

En lo que respecta a la emisión antropogénica de los NO_x, en Europa, el sector del transporte contribuyó al 39 % de las emisiones en 2018 (**Figura 8**). Sin embargo, esta contribución es considerablemente mayor en las zonas urbanas, pues las emisiones del transporte por carretera se

localizan cerca del suelo y se distribuyen en áreas densamente pobladas [181].

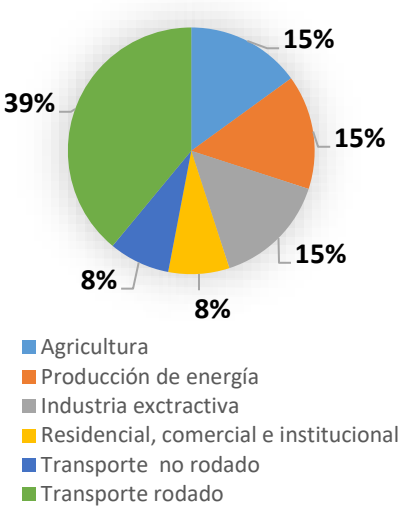

Figura 8. Contribución de las emisiones de NO_x en Europa durante el año 2018.

Los efectos de la contaminación de los NO_x, tanto a largo como a corto plazo son sensiblemente negativas:

- Salud: la inhalación de los NO_x produce una serie de afecciones: asma, infecciones respiratorias, bronquitis, disminución de la capacidad y del crecimiento pulmonar, etc. [182,183]. De hecho, se estima que solo en la Unión Europea fallecen de forma prematura unas 70.000 personas al año a causa de los efectos de los NO_x [177].

- Medio ambiente: además de su implicación en la producción de ozono a nivel de suelo, los NO_x participan en la formación del smog (**Figura 9**)

y contribuyen al efecto invernadero mediante la formación del gas N_2O. Otro efecto directo causado por los NO_x es la deposición ácida, es decir, la introducción de sustancias de carácter ácido en los ecosistemas terrestres y acuáticos. En concreto, uno de los efectos más conocidos es la lluvia ácida, referida también como como deposición "húmeda" (precipitaciones con valores de pH que suelen ser menores a 5,7).

Figura 9. Smog en la ciudad de Madrid (España) en 2016 [184].

- Materiales pétreos del patrimonio urbano: los daños directos provocados por los NO_x derivan de su capacidad para formar ácidos cuando se disuelven en agua. Además, es particularmente importante su sinergia con el SO_2, actuando como oxidante de este [185]:

$$SO_2 + NO_2 + H_2O \rightarrow H_2SO_4 + NO \qquad (8)$$

En el caso de los materiales calcáreos, muy comunes en el Patrimonio Histórico, los ácidos generados reaccionarán disolviendo el carbonato cálcico, formando nitrato de calcio que es fácilmente lixiviable,

por lo que los materiales sufren una pérdida de su consistencia original. De igual manera, la deposición ácida en morteros y hormigones generará sales del tipo bicarbonato, sulfato, nitrato que procederán a lixiviarse progresivamente.

A pesar de las limitaciones de concentración de NO_x legisladas (**Tabla 4**), muchas ciudades suelen sobrepasar los valores establecidos [186]. Por ejemplo, 19 países del continente europeo excedieron los límites en el año 2018. Además, el 95% de las estaciones de medida donde se registraron valores medios superiores al permitido se correspondieron con estaciones de tráfico [181]. Esto conlleva a un aumento potencial de los efectos adversos de estos contaminantes.

Con el objeto de controlar las emisiones de los NO_x, se han desarrollado varios métodos basados en diferentes principios. En los métodos denominados "primarios" se evita, en la medida de lo posible, la generación de NO_x mediante el control de los parámetros que afectan al proceso de combustión (temperatura, tiempo de residencia de los gases, concentración de oxígeno en la cámara de combustión, etc.). Algunos de estos métodos son: empleo de quemadores de bajo NO_x, recirculación de humos de combustión, la inyección escalonada del aire, etc. Los métodos "secundarios" consisten en la disminución de la concentración de los NO_x que se han generado durante un proceso determinado. Estos pueden ser implementados en conjunto con las medidas primarias. A destacar, una de las medidas secundarias más extendidas es la reducción selectiva del NO_x, medida basada en la reducción química de los NO_x para formar nitrógeno molecular (N_2) [172,187]. Existen dos tipos de estas medidas basadas en reducción:

- Reducción selectiva no catalítica (SNCR): durante el tratamiento de los gases de combustión se inyecta un agente químico reductor, normalmente urea o un compuesto amoniacal (NH_2, NH_3).

- Reducción catalítica selectiva (SCR): aunque el principio es similar a la SNCR, en este caso se emplea un catalizador basado en zeolitas, carbono activado, óxidos de titanio, etc.

Otros métodos secundarios son la oxidación de los NO_x mediante inyección de ozono [188], la adsorción (mediante carbón, óxido de aluminio, etc. [189]) o el almacenamiento y reducción de los NO_x (NSR) [190]. No obstante, ninguna de estas medidas está diseñada para disminuir la concentración de los NO_x de manera directa en los hábitats urbanos, lugares donde se concentran la mayor parte de estos contaminantes [181].

En este contexto, durante las últimas décadas ha surgido la alternativa de utilizar el proceso de la fotocatálisis como una tecnología sostenible para la eliminación de estos gases, así como de otros contaminantes, cuya discusión se desarrolla en los apartados siguientes.

2.6. Principios de fotocatálisis

La fotocatálisis es un proceso mediante el cual una reacción química es acelerada gracias a la acción de una radiación lumínica de una determinada longitud de onda sobre un compuesto químico denominado fotocatalizador, que no es consumido en la reacción. Dicho proceso tiene lugar, principalmente, a temperatura y presión ambientales. El trabajo publicado en 1972 por los investigadores Akira Fujishima y Kenichi Honda supuso un significativo avance en la tecnología fotocatalítica. Estos autores

describieron la capacidad de un semiconductor (TiO_2) para producir, sobre su superficie, la hidrólisis del agua cuando es irradiado con luz ultravioleta [191]. A raíz de este artículo (más de 21000 citas), surgió en la comunidad científica un gran interés sobre la fotocatálisis, pues se conseguía la producción de hidrógeno de una manera más sostenible. No obstante, las primeras menciones a la fotocatálisis fueron anteriores a este trabajo (1911-1913) [192–194].

Existen dos tipos de fotocatálisis en cuanto a las fases involucradas:

- Fotocatálisis homogénea: el fotocatalizador y los reactivos se encuentran en la misma fase. Por ejemplo, los sistemas basados en ozono (fotocatalizador) disuelto en agua. En este tipo de fotocatálisis la separación de los productos de reacción del fotocatalizador puede suponer una limitación.
- Fotocatálisis heterogénea: fotocatalizador y reactivos están en una fase diferente (por ejemplo, el fotocatalizador en estado sólido y los reactivos en estado líquido o gaseoso).

2.6.1. Generalidades de los semiconductores

La mayoría de los fotocatalizadores heterogéneos, son compuestos sólidos semiconductores, poseen una estructura electrónica característica claramente diferenciable de la de los metales y materiales aislantes. Todos estos materiales se diferencian según el comportamiento de su conductividad eléctrica al variar la temperatura. Mientras que en los materiales conductores la conductividad de estos aumenta a medida que se disminuye la temperatura, en los semiconductores ocurre lo contrario.

Por otro lado, los materiales aislantes presentan una conductividad eléctrica nula o muy baja [195].

La estructura electrónica de todos estos materiales puede ser explicada considerando la Teoría de Orbitales Moleculares (TOM), donde el sólido en su conjunto es tratado como una molécula con un número muy elevado de átomos. De esta manera, los valores de energía de los OM enlazantes se aproximan tanto que logran formar un nivel único de energía casi continuo. A este nivel se le denominada Banda de Valencia (BV). De igual manera, los OM antienlazantes formarán la llamada Banda de Conducción (BC). Según la naturaleza de la interacción entre los OM, ambos tipos de bandas pueden ser solapadas o existir un salto entre ambas ("Band Gap"), en el cual no existe ningún estado energético posible (**Figura 10**) [196].

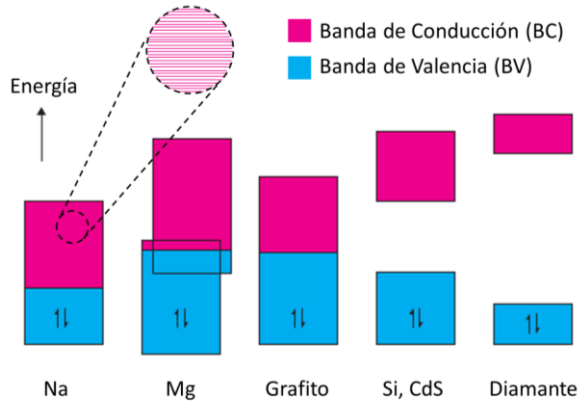

Figura 10. Ejemplos de la posición de bandas electrónicas en diferentes compuestos. Adaptado de [197].

El solapamiento de bandas es típico en el enlace metálico, donde los átomos interaccionan de una manera más débil y sin dirección preferente. En cambio, el salto de energía entre bandas suele darse en

compuestos con enlaces covalentes direccionales (aislantes o semiconductores). Si la diferencia energética entre las bandas es considerable, estaremos hablando de un aislante, mientras que si la diferencia no es tan significativa, el material será un semiconductor. De manera general, se suele considerar que un material es aislante si el salto de energía es superior a 4 eV [198].

En este contexto, hay que mencionar el Nivel de Fermi, que es un valor de energía tomado para un sólido: se define como el valor de energía más elevado que se encuentra ocupado por electrones, tomado a una temperatura de 0 K. En los semiconductores, dicho nivel queda localizado a un valor de energía perteneciente al salto prohibido de energía entre bandas, y por ende, no se corresponde a ningún estado energético real [196]. Sin embargo, en los conductores, el nivel de Fermi se localiza dentro de alguna banda. De esta manera, si la Banda de Valencia no se encuentra completamente llena, se puede producir el paso de los electrones cercanos al nivel de Fermi hacia niveles cercanos en energía que estén vacíos. Es decir, los electrones exhibirían cierta movilidad a través del sólido, produciendo una determinada conductividad eléctrica [195]. Por otro lado, los diferentes comportamientos de la conductividad eléctrica de semiconductores y conductores frente a la temperatura pueden ser explicados mediante la distribución de Fermi [199].

2.6.2. Mecanismo de la fotocatálisis

En un semiconductor, la fotocatálisis comienza con la irradiación de aquel con fotones que posean una energía igual o mayor al valor del band gap del semiconductor. Hay que tener en cuenta que parte de los fotones que alcanzan al semiconductor pueden no ser absorbidos por este, pues

pueden tener lugar otros mecanismos ópticos como la reflexión o la dispersión de la radiación [196]. La absorción de los fotones (energía) por parte del semiconductor lleva a que los electrones de la BV promocionen hacia la BC (e^-_{BC}), creándose por tanto huecos positivos en la BV (h^+_{BV}). Hay que señalar que este proceso ocurre de manera extremadamente rápida (femtosegundos) [200,201]. Posteriormente, estos portadores de carga se pueden trasladar por el sólido, pudiendo alcanzar la superficie del material semiconductor, donde participará en reacciones químicas con las moléculas del medio de reacción que se puedan encontrar adsorbidas en su superficie. Sin embargo, el par electrón-hueco generado suele sufrir el proceso de recombinación, es decir, la anulación entre ambos portadores de carga. De hecho, se ha reportado que alrededor del 85% de la excitación de electrones cae en el proceso de recombinación tras 10 nanosegundos de irradiación [202]. Es decir, la recombinación es un fenómeno no deseable a la hora de invertir la energía absorbida en el desarrollo de las reacciones químicas con las especies adsorbidas en el semiconductor.

Existen dos tipos principales de recombinación: la radiativa (fotoluminiscencia) y la no radiativa. Mientras que la primera depende de las propiedades fisicoquímicas de cada semiconductor, la recombinación no radiativa puede reducirse si se disminuye la densidad de los defectos en la estructura del semiconductor, en los que los electrones/huecos generados son atrapados [203].

2.6.2.1. Eliminación de contaminantes mediante reacciones de oxidación fotocatalítica

Una de las aplicaciones derivada de la tecnología fotocatalítica es la degradación de contaminantes mediante el Proceso de Oxidación Avanzada (POA), donde intervienen especies muy oxidantes encargadas de

eliminar los contaminantes. Estas especies son nombradas especies reactivas de oxígeno (ROS) y consisten en radicales que contiene el átomo de oxígeno, como el ·OH (radical hidroxilo) y $\cdot O_2^-$ (radical superóxido), entre otros. Las ventajas de este proceso de oxidación residen en que ocurre en condiciones suaves, esto es, a temperatura y presión ambientales [204]. Adicionalmente, mediante la fotocatálisis heterogénea, el fotocatalizador (en estado sólido) podría ser utilizado para descontaminar fases acuosas o fases gaseosas.

Para que el semiconductor (fotocatalizador) puedan generar las ROS y que estas participen en reacciones químicas, los electrones y huecos fotogenerados deben alcanzar la superficie (evitando la recombinación) y transferirse a las moléculas adsorbidas en la superficie del semiconductor. Así, los huecos positivos (h^+_{BV}) podrán intervenir en procesos de oxidación mediante la captación de electrones desde las moléculas adsorbidas. Por su parte, los electrones generados en el semiconductor (e^-_{BC}) podrán ser cedidos a una molécula adsorbida, produciéndose una reducción química. Para que estos eventos tengan lugar, el potencial de oxidación de los h^+_{BV} debe ser mayor que el de la molécula donadora de los electrones, mientras que potencial de reducción de los e^-_{BC} debe ser menor que el de la molécula aceptora de estos electrones. En consecuencia, la energía absoluta de la BV y la BC del semiconductor es un parámetro que considerar [198]. Como ejemplo, en la **Figura 11** se puede observar la posición energética de las bandas de algunos semiconductores comparada con los potenciales estándar en agua de varias especies de interés en diferentes aplicaciones fotocatalíticas.

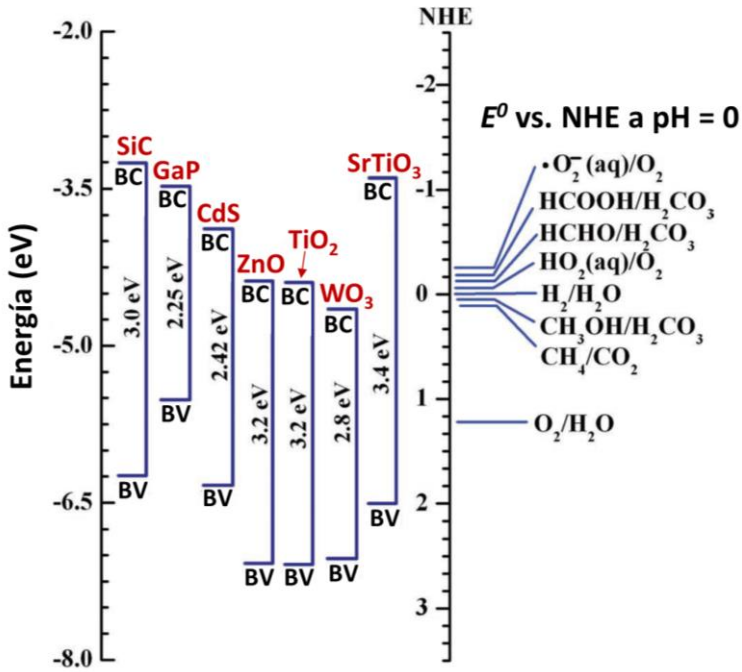

Figura 11. Posiciones energéticas de algunos semiconductores y potenciales redox de especies de interés. Adaptado de [205].

La generación de las especies ROS puede darse por diversos mecanismos. Por ejemplo, el oxígeno adsorbido en el semiconductor se reducirá por acción de los electrones fotogenerados, produciendo radicales superóxido ($\cdot O_2^-$) que posteriormente pueden reaccionar para formar radicales hidroperoxilo ($\cdot HO_2$), peróxido de hidrógeno (H_2O_2) y finalmente radicales hidroxilo (·OH) o agua. De igual manera, los huecos pueden oxidar el agua o los OH^- adsorbidos para dar radicales hidroxilo (·OH). Estas especies poseen un potencial de oxidación muy elevado, por lo que cuando se produce el contacto con compuestos contaminantes adsorbidos en el fotocatalizador se produce la descomposición de estos. De esta manera, los contaminantes serán oxidados progresivamente hasta alcanzar su grado de oxidación máximo. En el caso de los contaminantes orgánicos ocurre su

mineralización, resultando así moléculas de agua y compuestos/ácidos inorgánicos [198]. El mecanismo, por tanto, puede resumirse de la siguiente forma:

$$\text{Fotocatalizador} + h\nu \rightarrow e^-_{BC} + h^+_{BV} \quad (9)$$

$$h^+ + OH^-_{ads} \rightarrow \cdot OH_{ads} \quad (10)$$

$$e^- + O_2 \rightarrow \cdot O_2^-{}_{ads} \quad (11)$$

$$H^+ + \cdot O_2^-{}_{ads} \rightarrow \cdot HO_2 \quad (12)$$

$$\text{Cotaminante}_{ads} + \text{ROS} \rightarrow \text{Productos Inorgánicos } (CO_2, H_2O, H^+, \text{etc.}) \quad (13)$$

La capacidad descontaminante del proceso fotocatalítico dependerá de una serie de factores: las propiedades fisicoquímicas del fotocatalizador (composición, área superficial, etc.), el tipo y concentración de contaminantes y sus propiedades de adsorción, la configuración del fotorreactor, la fuente de radiación (longitud de onda e irradiancia) y las condiciones de reacción (temperatura, oxígeno disuelto, pH o humedad relativa) [206].

2.6.2.2. Procesos fotocatalíticos De-NO_x

El proceso de eliminación de los gases NO_x se denomina proceso o acción De-NO_x [207–209]. La reacción fotoquímica que ocurre con los gases NO_X y un semiconductor (fotocatalizador) sigue un mecanismo similar al explicado en la sección anterior: una vez que el fotocatalizador es irradiado con una longitud de onda igual o superior a su band gap y se produce la generación de los pares electrón/hueco, los portadores de carga que podrán alcanzar la superficie del fotocatalizador, donde intervendrán en procesos redox para producir las ROS. En este punto, los radicales superóxido ($\cdot O_2^-$) oxidarán las moléculas de óxido de nitrógeno (NO)

adsorbidas a nitratos (NO_3^-), principalmente. Al mismo tiempo, los radicales hidroxilo (·OH) procederán con la misma reacción, mediante varios pasos intermedios ($NO \rightarrow HNO_2 \rightarrow NO_2 \rightarrow NO_3^-$) [209]. Por consiguiente, se logra la eliminación de unas sustancias gaseosas peligrosas mediante su transformación a sólidos de naturaleza benigna (nitritos y nitratos). Dicho mecanismo puede ilustrarse de manera resumida en la **Figura 12**. Hay que resaltar que, si la actividad del fotocatalizador no es óptima, el NO puede ser oxidado a NO_2 además de a nitratos. Este fenómeno no es nada deseable desde el punto de vista medioambiental, pues se estaría emitiendo un gas que es mucho más tóxico que el NO [210].

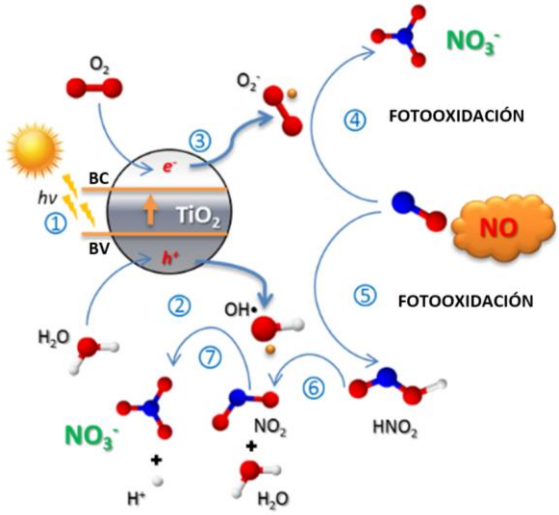

Figura 12. Mecanismo resumido de oxidación fotocatalítica de NOx sobre el fotocatalizador TiO_2. Los números indican el orden de las etapas. Adaptado de [209].

No obstante, el mecanismo real resulta complejo, según se recoge en [211], distinguiéndose diferentes reacciones e intermedios que ocurren en ausencia o presencia de luz. En condiciones de oscuridad, las especies de oxígeno pueden generar otras especies como por ejemplo el oxígeno

atómico (O) o el O^- [212]. Al mismo tiempo, las moléculas de NO adsorbidas pueden dar lugar a una variedad de intermedios. En este sentido, una de las etapas clave del mecanismo De-NO_x es la adsorción de las moléculas de NO. Mediante esta adsorción, se pueden formar especies adsorbidas como NO_3^-, NO^- o $N_2O_2^{2-}$ [213]. Por otro lado, el NO_2 fisisorbido podrá formar HNO_2 o HNO_3 (según la concentración de NO_2) mediante los intermedios N_2O_4 y NO^+, respectivamente [214–217]. Adicionalmente, es conocido que la cantidad de agua involucrada en el sistema tiene gran influencia en la reacción. Por un lado, las moléculas de agua facilitan la absorción de las moléculas de NO y, como se ha visto, generan radicales hidroxilo [218–221]. Por otro lado, si se aumenta el valor de la humedad, los sitios activos del fotocatalizador pueden ser ocupados por las moléculas de agua en lugar de los demás reactivos [222]. Todos estos procesos se ilustran en la **Figura 13**.

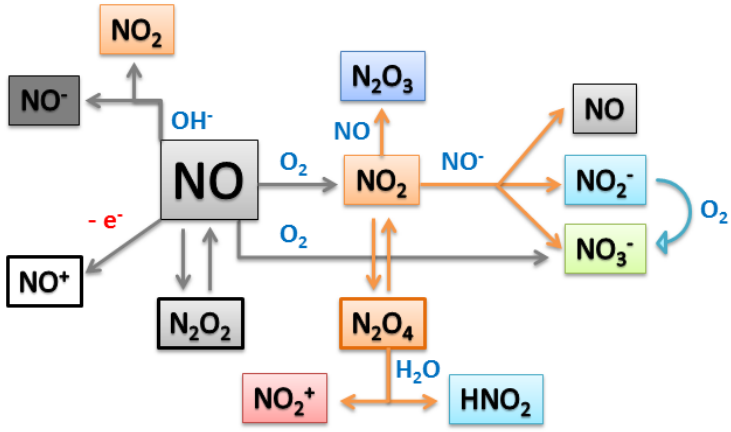

Figura 13. Conversión del monóxido de nitrógeno adsorbido en la superficie del fotocatalizador en ausencia de irradiación [211].

Cuando el fotocatalizador es iluminado, los nitratos son el principal producto de la reacción fotocatalítica De-NO_x. Sin embargo, durante este

proceso pueden formarse otras especies como NO^+, N_2O_3, N_2O, NO_2 o NO_2^+ mediante varios mecanismos. Por otro lado, los nitritos (NO_2^-) pueden formarse cuando el NO_2 toma un electrón. De manera semejante, se ha reportado la formación de NO^- y $N_2O_2^{2-}$ mediante la captación de electrones del fotocatalizador por parte del NO y NO_2, respectivamente [223]. Además, la desproporción de las moléculas adsorbidas de NO pueden dar el intermedio NO^- [224,225]. Finalmente, el NO también puede ceder electrones al fotocatalizador, generando NO^+ [226–229]. La **Figura 14** representa de forma esquemática los procesos explicados.

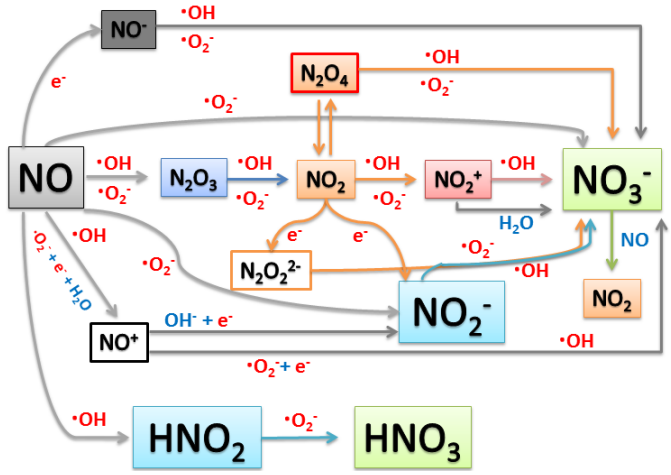

Figura 14. Conversión del monóxido de nitrógeno adsorbido en la superficie del fotocatalizador bajo irradiación [211].

Como se puede deducir, en el proceso De-NO_x no solo hay que considerar las propiedades electrónicas del fotocatalizador y su interacción con la luz, sino también la reactividad superficial de este. Esta última también establecerá el comportamiento reactivo de los portadores de

carga generados con las moléculas adsorbidas en la superficie del fotocatalizador.

2.7. Materiales de construcción fotocatalíticos

Una manera de reducir la contaminación atmosférica del hábitat urbano, donde residen los ciudadanos, consistiría en la implantación de amplias superficies arquitectónicas (edificios, pavimentos, ventanas, etc.) con propiedades descontaminantes. Dichas propiedades derivan de la inclusión de compuestos fotocatalíticos en los materiales que forman parte de una infraestructura determinada (morteros, pinturas, hormigón, etc.). Durante el día, la radiación solar incidente en dichos materiales activará el proceso fotocatalítico, y por ende, tendrá lugar la foto-oxidación de los contaminantes atmosféricos. Al mismo tiempo, las especies ROS generadas, gracias a su poder oxidante, también conseguirán destruir a los microorganismos adheridos al material, por lo que estos materiales poseen propiedades autolimpiantes cuando reciben la irradiación [230,231] .

La mayoría de los materiales de construcción fotocatalíticos que se comercializan en la actualidad están basados en el uso de TiO_2. En la bibliografía reciente se encuentran publicadas revisiones que engloban los avances de la aplicación del TiO_2 en los materiales urbanos [232,233]. La elección de este fotocatalizador estriba en sus convenientes propiedades: elevado band gap (3,2 eV), estabilidad química, alta actividad fotocatalítica y compatibilidad con materiales de construcción tradicionales [234]. Algunos ejemplos de materiales comerciales son TX Active® [235] y TioCem® [236] (cementos), Morcemsec® Active (mortero) [237], Betonella®

CM 6 (hormigón) [238], Activ™ (vidrios) [239], EcoClean™ y Reynobond® (paneles de aluminio) [240], KEIM Soldalit-ME [241] y PhotoDeco [242] (pinturas), etc.

La eficacia de descontaminante de los materiales de construcción fotocatalíticos ha sido comprobada tanto en ensayos de laboratorio [243–245] como en condiciones reales [246–249]. En este contexto, se pueden citar varios ejemplos de infraestructuras urbanas constituidas con esta clase de materiales (**Figura 15**): el cemento de la iglesia del Jubileo (Roma, Italia) [250], el hormigón del Hospital General Dr. Manuel Gea González (Ciudad de México, México) [251], los paneles de hormigón GRC (*Glass Reinforced Concrete*", es decir, hormigón armado con fibra de vidrio) de la fachada Pabellón Real Madrid Arena (Madrid, España) [252] o la pintura de la fachada del edificio Santa Lucía (Sevilla, España) [253].

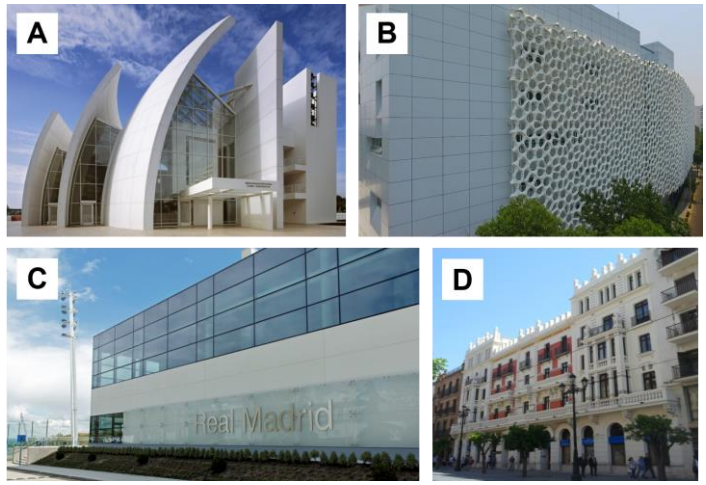

Figura 15. Ejemplos de infraestructuras constituidas con materiales fotocatalíticos: (A) iglesia del Jubileo; (B) Hospital General Dr. Manuel Gea González; (C) Pabellón Real Madrid Arena; (D) edificio Santa Lucía.

En estos materiales, a medida que se produzca el proceso fotocatalítico De-NO_x, los nitratos se generarán y quedarán adsorbidos en la superficie del material [209]. Como resultado, la capacidad de eliminación de los NO_x irá decreciendo paulatinamente debido a que los sitios activos del material quedarán bloqueados. Sin embargo, cuando estos materiales se aplican en ambientes externos, los nitratos y nitritos generados (especies muy solubles) son arrastrados por el agua de lluvia o de rocío, donde se incorporan a las aguas fluviales que son tratadas de manera convencional en las Estaciones Depuradoras de Aguas Residuales (EDAR). Esto hace que la superficie del material quede de nuevo limpia y disponible para continuar con la acción De-NO_x [209,254–256].

No obstante, la extensa implantación de los materiales fotocatalíticos en el hábitat urbano permanece aún lejos de ser alcanzada [257]. Una de las limitaciones que surgen es el coste del TiO_2, que es muy elevado en comparación con las materias primas empleadas en los materiales urbanos. En especial, el precio se ve incrementado en el TiO_2 P25 AEROXIDE® (polvo nanoparticulado, mezcla de las fases cristalinas rutilo y anatasa) que es un producto comercial empleado como estándar por su elevada actividad fotocatalítica [258,259]. En este contexto, el precio de un cemento fotocatalítico basado en TiO_2 es unas 8 veces superior al de un cemento convencional [257].

Otra limitación de este semiconductor es que absorbe únicamente en la región ultravioleta del espectro electromagnético (**Figura 16**). , siendo esta solo el 4-5% de la energía solar que alcanza la superficie de la Tierra, desaprovechándose así la mayor parte de la irradiación solar [260,261]. Como resultado, la eficacia fotocatalítica de estos materiales se ve limitada, especialmente si se considera una aplicación en zonas urbanas localizadas en elevadas latitudes, con niveles bajos de radiación ultravioleta [262]. De

igual manera, la capacidad de absorción de luz de las infraestructuras localizadas en las zonas más sombrías de las ciudades tampoco sería óptima para lograr una acción fotocatalítica completa.

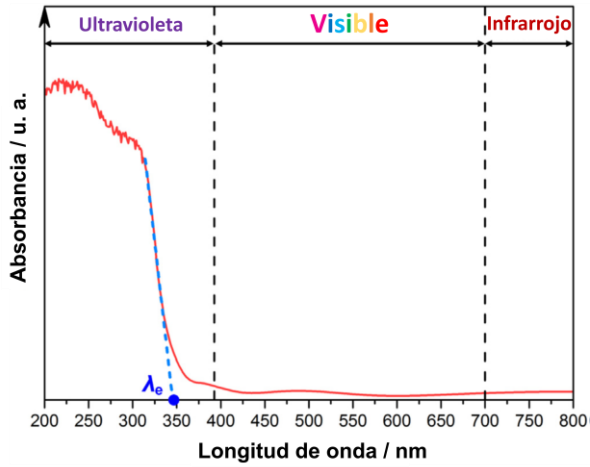

Figura 16. Ejemplo de espectro de absorbancia UV-vis de una película delgada de TiO_2 sobre vidrio. Adaptado de [261].

Por otra parte, se conoce que el TiO_2 P25 exhibe una baja selectividad en el proceso De-NO_x, lo que significa que una parte importante del monóxido de nitrógeno es foto-oxidado a dióxido de nitrógeno en lugar de a nitratos/nitritos [208,263]. Como se indicó en la sección 2.6.2.2, esto no es deseable para una aplicación medioambiental. Este fenómeno también se ha observado en una serie de estudios de campo, empleando materiales basados en TiO_2: Copenague (Dinamarca) [264], Hong Kong [265] y La Haya (Países Bajos) [266]. Por tanto, este conjunto de factores hace que la eficacia De-NO_x no sea suficiente desde un punto de vista práctico [267].

Finalmente, la Unión Europea ha indicado recientemente potenciales riesgos de padecer cáncer cuando se inhalan nano-partículas

de TiO_2, por lo que habría que tener en consideración los riesgos futuros de la utilización de dicho compuesto [268].

2.8. Fotocatalizadores alternativos con efecto De-NO_x

Para lograr una amplia utilización de los materiales fotocatalíticos De-NO_x en el hábitat urbano, resulta primordial desarrollar fotocatalizadores de bajo coste, con una mayor capacidad para absorber la radiación solar y que además muestren una actividad De-NO_x elevada y selectiva (baja emisión de NO_2). De forma general, las direcciones a seguir para conseguir estos objetivos se basan en modificar la estructura y/o composición del semiconductor, disminuir la recombinación e^-/h^+, aumentar la superficie específica, mejorar la capacidad de absorción de luz e incrementar la eficiencia y selectividad del proceso De-NO_x. En este abanico de posibilidades, se han investigado diferentes tipos de compuestos. A continuación, sin llegar a ser exhaustivo, se resumen los principales estudios en varios subapartados.

2.8.1. Fotocatalizadores TiO_2 modificados

Una estrategia común para mejorar los procesos fotocatalíticos consiste en el *dopado del semiconductor* con diferentes elementos como por ejemplo cationes metálicos, metales nobles, no metales, etc. Esto permite la creación de niveles de energía intermedios entre BV y la BC, que reducen la recombinación e^-/h^+ e incluso la mejorar la absorción de absorción de luz. Por ejemplo, He et al. prepararon nanocristales de TiO_2 (fase anatasa) dopados con carbono (**Figura 17**). La mejorada superficie

especifica y la disminución de la recombinación e^-/h^+ respecto al compuesto sin dopar explican el gran aumento de eficacia De-NO (~ 70 vs 20%) [269].

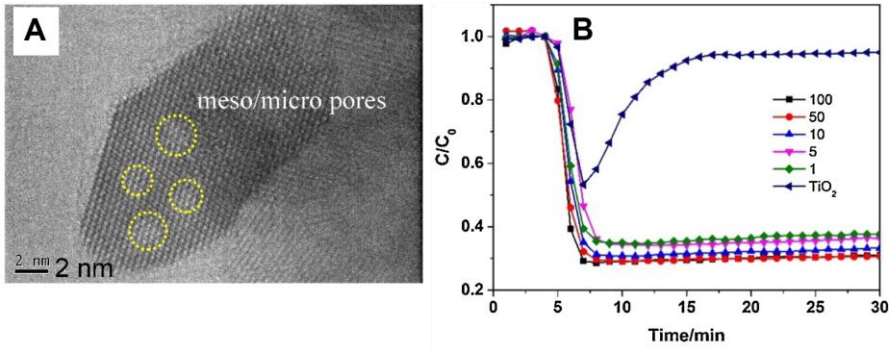

Figura 17. A: imagen HRTEM de la nanoestructura de TiO_2 dopado con carbono; B: evolución de la concentración de NO en función del tiempo del ensayo fotocatalítico (la irradiación comienza en el minuto 5 y finaliza en el minuto 30) para las diferentes muestras, donde *TiO_2* hace referencia a la muestra sin dopar [269].

También se estudió el dopaje de TiO_2 con estaño mediante un método de reducción, El Sn-TiO_2 azul obtenido logró una eficacia De-NO_x de un 72% y una menor liberación de NO_2 (~ 29%). Los buenos resultados se atribuyeron a la existencia de un nuevo nivel de energía entre la BV y la BC (Ti^{4+}, Ti^{3+} Sn^{2+} y Sn^{4+}), que promueve la retención de las fotocargas [270].

En un ejemplo de dopaje con varios elementos, el TiO_2 codopado con wolfragmio y nitrógeno mostró una selectividad De-NO_x mayor al 90%. La presencia de sitios trampa como W^{5+} y Ti^{3+} hace que los electrones fotogenerados tomen nuevas rutas de transferencia (reducción del oxígeno

en lugar de los nitratos) consiguiendo que se libere una menor cantidad del intermedio NO_2 [271].

Respecto al dopaje con metales nobles, se encuentran diversos ejemplos en la literatura [272–274]. Por ejemplo, Hernández Rodríguez et al. empleó Pt o Au (Pt-TiO_2, Au-TiO_2) como elementos dopantes del TiO_2 P25. El dopaje con oro aumentó el rendimiento De-NO_x tanto con irradiación visible como con UV. En cambio, la respuesta UV del Pt-TiO_2 no se vio afectada. Se observó que la morfología de las nanopartículas del fotocatalizador fue un factor clave, obteniéndose los mejores resultados De-NO_x en las muestras con partículas esféricas menores de 5 nm [275].

La introducción de *defectos en la red estructural* del TiO_2, provoca la aparición de niveles de energía entre la BV y la BC. En consecuencia, las propiedades electrónicas del compuesto se ven afectadas, pudiéndose modificar la capacidad de absorción de la luz solar. Por ejemplo, se pueden introducir vacantes de oxígeno (O_v) mediante un dopado (como se comentó en la sección anterior) o mediante ciertos procedimientos de síntesis. En este sentido, Hu et al. prepararon microesferas huecas de O_v-TiO_2 mediante un proceso de calcinación de titanato de hidrógeno con urea. El mayor contenido de O_v en las muestras se vio reflejado en el mayor rendimiento bajo irradiación del espectro visible, la disminución de la recombinación e^-/h^+ y en la mejor adsorción y activación de las moléculas de NO y O_2 en la superficie del fotocatalizador [276].

En otro ejemplo Tan et al. prepararon mesocristales de TiO_2 con Ti^{3+} como defecto estructural. Las muestras fueron obtenidas por un proceso de hidrolisis hidrotermal, seguido de una calcinación en vacío. Los mesocristales exhibieron una actividad mejorada bajo luz visible y nula

emisión de NO_2, factores atribuibles fundamentalmente a las especies de Ti^{3+} y a la estructura mesoporosa, respectivamente [277].

Otro factor que tiene incidencia en las propiedades fotocatalíticas del TiO_2 es la orientación de los cristales, pues la cara (*001*) es más reactiva que la cara (*101*), que termodinámicamente es la más estable [278]. En este sentido, el TiO_2 (fase anatasa) con las caras (*001*) predominantes muestra una mayor superficie específica y una mejorada actividad De-NO_x [279].

Otro aspecto interesante es la preparación de *heterouniones electrónicas*. Una heterounión se crea cuando dos semiconductores diferentes, que presentan una estructura de bandas electrónicas desigual, entran en contacto íntimo de manera que las bandas quedan acopladas entre sí (**Figura 18**) [280]. La nueva disposición energética de las respectivas bandas de conducción y de valencia hace que se mejore la movilidad de los portadores de carga, además de ampliar la capacidad de absorción de luz por parte de la heterounión. En el caso del TiO_2, esta estrategia se ha utilizado con éxito para aumentar su rendimiento fotoquímico y su actividad bajo irradiación del espectro visible.

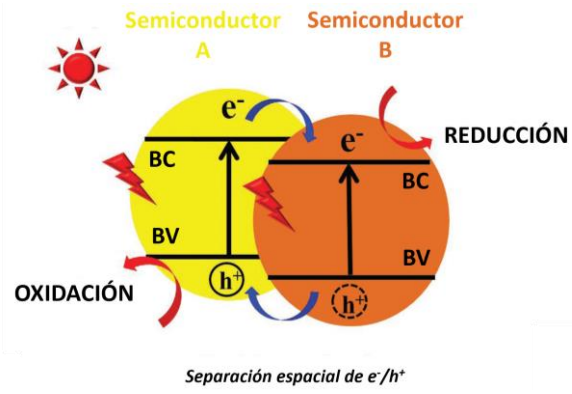

Figura 18. Ilustración de una posible heterounión entre dos semiconductores, A y B. Adaptado de [280].

Uno de los semiconductores elegidos para lograr heterouniones es el nitruro de carbono (C_3N_4) debido a que posee un band gap de 2,7 eV, que le permite absorber radiación del espectro visible. En este sentido, las heterouniones preparadas con TiO_2 resultan ser más activas bajo irradiación de luz visible debido a una combinación de las propiedades ópticas y electrónicas de la heterounión [223].

En otro trabajo, se preparó de manera análoga la heterounión g-C_3N_4/TiO_2 acoplada con $CaCO_3$. Además de la respuesta mejorada de las muestras bajo irradiación del espectro visible, el carácter básico del $CaCO_3$ disminuyó la emisión del intermedio NO_2 [281].

Por otro lado, las excelentes propiedades conductoras del grafeno, entre otras, hacen que haya sido un candidato atractivo para formar heterouniones. En este contexto, Trapalis et al. desarrollaron heterouniones de grafeno u óxido de grafeno con TiO_2, empleando un proceso solvotermal con isopropóxido de titanio como precursor. Las heterouniones consiguieron un rendimiento superior al TiO_2 puro, lo que fue atribuido al papel del grafeno como trampa de electrones y al efecto fotosensibilizador en el caso del óxido de grafeno (GO) [282–285].

Otros ejemplos con GO/TiO_2 [283–285], o incluso con grafeno insertado en nanofibras de TiO_2/ZnO/Bi_2O_3 pueden encontrarse en la bibliografía [286].

Por otro lado, también se pueden mencionar heterouniones de Ti_3C_2, quantun dots (QDs) u óxidos de metales de transición. Por ejemplo, C_3N_4/TiO_2-Ti_3C_2 [287], QD-CdTe/TiO_2 [288], QD-carbono/N-TiO_2 [289], WO_3/TiO_2 [290,291], MoO_3/TiO_2 [292], PtO_2/ TiO_2 [293], $ZnFe_2O_4$/TiO_2 [294].

Otra estrategia empleada por diversos autores consiste en inmovilizar las partículas de TiO_2 en un *soporte adecuado* con el fin de reducir la aglomeración de las partículas. Se han estudiados composites de

TiO_2 con: arcillas (talco; arcilla tipo montmorillonita) [295], zeolitas (HZSM-5) [296], arenas recicladas (procedente de ladrillos para la construcción) [297], hidroxiapatita [298], Al_2O_3 [299,300], CaO [301], SiO_2 [302,303], proteína adhesiva de mejillón [304], etc.; exhibiendo todos los composites mejor eficacia De-NO_x que el TiO_2 puro.

2.8.2. Óxidos basados en titanio

Los semiconductores de tipo perovskita que contienen titanio en su composición muestran gran estabilidad química y una excelente movilidad de los portadores de carga [305]. Por ello, también se han aplicado como fotocatalizadores De-NO_x. Por ejemplo, Zhang et al. prepararon nanocomposites de Ag-$SrTiO_3$, variando la cantidad de plata depositada. Este metal, gracias al efecto plasmónico, permitió mejorar el rendimiento fotocatalítico De-NO_x bajo irradiación del espectro visible [306].

Otros autores han optado por el dopaje de la estructura de $SrTiO_3$, por ejemplo, con Cr^{3+} [307] o con Fe^{3+} [308], para ampliar la efectividad fotocatalítica en el rango espectral del visible.

Las heterouniones son también una vía explorada en estos tipos de estructuras. Por ejemplo, composiciones de $LaTiO_3$-$SrTiO_3$ resultaron tener una excelente actividad De-NO_x bajo excitación de luz visible en comparación con el semiconductor base (~ 40 vs 10%, respectivamente). Esto fue atribuido, en especial, a la gran supresión de la recombinación de las fotocargas en la heterounión [309].

Otros tipos de perovskitas basadas en titanio con elevados valores De-NO_x son: $SrTiO_3$ decorado con $SrCO_3$ [310], $Na_{0.5}Bi_{0.5}TiO_3$ [311], $Pb_2Bi_4Ti_5O_{18}$ [312] y N-$La_2Ti_2O_7$ [313].

2.8.3. Fotocatalizadores g-C_3N_4

El nitruro de carbono grafítico, g-C_3N_4, es un semiconductor polimérico no metálico que ha atraído la atención en la última década en aplicaciones fotocatalíticas. Su estabilidad química, band gap (2,7 eV) y adecuada posición de la BC y la BV (BC = −1,1 eV; BV = 1,6 eV, valores respecto al electrodo estándar de hidrógeno) dan cuenta de este interés. Sin embargo, este compuesto presenta limitaciones, como la elevada tasa recombinación de los pares electrón/hueco, la baja área de superficie específica (en torno a 10 m^2g^{-1}) o el bajo poder oxidante [314]. Como consecuencia, los investigadores han trazado diferente estrategias para mejorar el comportamiento De-NO_x.

Sano et al. realizaron un tratamiento alcalino hidrotermal que logró aumentar la superficie específica más de 8 veces [315]. En otro trabajo similar, se informó que la concentración de la disolución alcalina influyó en el valor de la superficie específica [316].

El grupo de Fan Dong investigó el efecto de la temperatura y tiempo de la pirólisis de ciertos precursores (urea o tiourea) sobre la microestructura y actividad fotocatalítica del g-C_3N_4, llegando a los mejores valores de eliminación de NO cuando el tiempo/temperatura fueron mayores. Los resultados se adscribieron a la mejor cristalinidad y área de superficie específica, así como a la modificación del band-gap [317,318].

También se han realizado modificaciones de la estructura del g-C_3N_4: nanoláminas porosas [318,319], estructura tipo panal [320], láminas distorsionadas [321] y láminas enrolladas [322].

El dopado de g-C_3N_4 también ha sido investigado. Por ejemplo, en se ha estudiado el codopado con los cationes sodio y calcio mediante un tratamiento térmico. Se consiguió un efecto sinérgico: el dopaje con sodio disminuyó la tasa de recombinación de las fotocargas y el calcio mejoró la

adsorción del intermedio NO_2 a causa de la formación de carbonato cálcico [323]. En otra publicación reciente, En este estudio, se utilizó un residuo de las plantas de coque para preparar g-C_3N_4 dopado con azufre y con vacantes de carbono. El band gap se vio aumentado (2,94 eV), se mejoró la adsorción de O_2, y se redujo la generación de NO_2 [324].

Recientemente, se ha conseguido preparar nitruro de carbono amorfo con 3 vacantes de nitrógeno coordinadas, fotocatalizador que alcanza un índice De-NO_x del 57% bajo irradiación del espectro visible (**Figura 19**). Los resultados se debieron a un incremento de la absorción de luz visible y a la enorme disminución de la energía de activación de los enlaces N-O [325].

Finalmente, existen un gran número de publicaciones referentes a la formación de heterouniones y composites de g-C_3N_4. Las heterouniones con compuestos basados en TiO_2 han sido descritas previamente, en la subsección 2.8.1. Otras heterouniones se basan en las nanopartículas de plata [326] o bismuto [327–329] para aprovechar el efecto de resonancia de plasmón superficial (SRP), así como otras basadas en el propio g-C_3N_4 [330] y otros compuestos: CeO_2 [331], $BiVO_4$ [332], BiOBr [333], $Bi_2O_2CO_3$ [334].

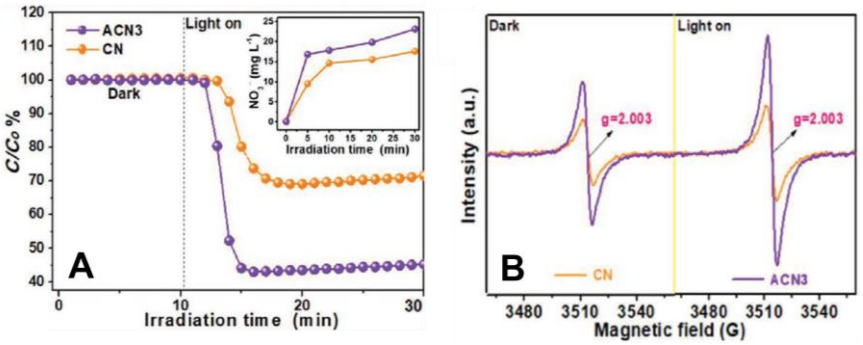

Figura 19. A: evolución de la concentración de NO en función del tiempo del ensayo fotocatalítico (la irradiación comienza en el minuto 10 y finaliza en el minuto 30) para las diferentes muestras, donde *ACN3* es el g-C_3N_4 con vacantes de nitrógeno; B: espectro de resonancia paramagnética electrónica de las muestras, demostrando la mayor existencia de vacantes para la muestra *ACN3* [325].

2.8.4. Compuestos basados en bismuto

Existe una extensa bibliografía relacionada con los compuestos basados en bismuto como fotocatalizadores De-NO_x. Esta dilatada área de investigación viene derivada de la capacidad fotocatalítica de estos materiales para absorber radiación del espectro visible. Entre este tipo de compuestos se pueden encontrar los óxidos binarios, los subcarbonatos, los óxidos multicomponente y los oxihaluros.

Dentro de los óxidos binarios, Ai et al. investigaron el compuesto α-Bi_2O_3. La muestra sintetizada, con un band gap de 2,72 eV, mostró un índice De-NO_x mayor que el TiO_2 P25, bajo irradiación del espectro visible [335]. El rendimiento de Bi_2O_3 ha sido también mejorado mediante su acoplamiento con bismuto metálico por el efecto SRP [336,337].

En relación con los subcarbonatos, Dong et al. prepararon microesferas huecas de $(BiO)_2CO_3$ con forma de rosas empleando un método hidrotermal. Dicha muestra logró un De-NO_x ~ 48% bajo

irradiación del espectro visible. La estructura hueca favoreció tanto la difusión de los intermedios de reacción como la eficiencia de la absorción de luz, explicando así la buena respuesta fotocatalítica [338]. El mismo grupo de investigación demostró que las caras (*001*) del $(BiO)_2CO_3$ son más eficientes que las caras (*110*) para la acción De-NO_x debido a una mayor facilidad para activar las moléculas de agua y oxígeno, y NO [339]. Otras estrategias, aplicadas a veces en conjunto, están dedicadas a mejorar la actividad de $(BiO)_2CO_3$. Por ejemplo: la modulación de O_v [340], el dopaje con nitrógeno [225] o lantano [341], la formación de composites con grafeno [342], la creación de heterouniones [334,343,344] o la decoración con nanopartículas metálicas de Bi [224], Fe [345], Ag [346] o Pt [347,348].

Respecto a los óxidos multicomponente con bismuto, se pueden citar el Bi_2WO_6 y el Bi_2MoO_6. Con relación al primero, el grupo de investigación de Fan Dong llevó a cabo una modulación de las vacantes de oxígeno de la estructura. La muestra con mayor concentración de O_v presentó un band gap reducido de 2,48 eV, un rendimiento De-NO_x del 47% bajo irradiación visible, y solo redujo su actividad en un 17% tras ensayos de irradiación extendidos (2 horas y media) [349,350]. Haciendo referencia al Bi_2MoO_6, el bromo [351], bismuto [352], MoO_3 [353], o el carbonato [354] son especies empleadas para mejorar la baja eficiencia del compuesto puro. Respecto a las heterouniones con Bi_2WO_6, se pueden encontrar en bibliografía Bi_2WO_6/Bi/Bi_2O_3 [355] y fósforo negro/Bi_2WO_6 [356].

Otro compuesto con bismuto es el $BiPO_4$, que debido a su band gap (4,1 eV) necesita el acoplamiento con otras especies para disminuir la elevada recombinación de las fotocargas, como por ejemplo realiza Li et al, explotando el efecto de resonancia de plasmón superficial (SRP) del bismuto metálico [357]. En la misma línea de trabajo, en bibliografía se pueden encontrar otros óxidos multicomponente de bismuto que emplean

el efecto SRP del bismuto metálico: $Bi/Bi_2O_2SiO_3$ [358], Bi/Bi_2GeO_5 [359] y Bi_4MoO_9 [360].

Por otro lado, la familia de los oxihaluros de bismuto son otra alternativa bastante trabajada por los investigadores. Por ejemplo, el grupo de Fan Dong investigó la serie BiOX (X = Cl, Br o I) sintetizada mediante precipitación a temperatura ambiente. Se encontró que el band gap y la estabilidad térmica del fotocatalizador disminuían al aumentar el tamaño del halógeno enlazado. BiOBr mostró la mayor actividad fotocatalítica De-NO_x (~ 25%), debido a la menor dimensión de las nanoplacas, mayor, área superficial y la adecuada estructura de las bandas electrónicas [361].

Diversos estudios propusieron mejorar el rendimiento fotocatalítico del BiOCl mediante, la preparación de vacantes de oxígeno [362], la deposición de nanopartículas de Ag/AgCl [363], bismuto metálico [364] (efectos SRP) o estableciendo heterouniones con otros derivados de bismuto: Bi_2WO_6 [365], Cu_2BiO_4 [366] o BiOI [367].

En el caso del BiOBr, se ha descrito que se puede mejorar su rendimiento De-NO_x mediante el dopaje con iodo [368], preparando disoluciones en estado sólido ($BiOCl_xBr_{1-x}$) [369,370], enriqueciendo las caras (*110*) del BiOBr [371], o preparando heterouniones con C_3N_4 [333], y con $Bi_{12}O_{17}Br_2$ [372].

En lo que respecta al sistema BiOI, y de forma similar a lo anterior mente comentado, la mejora DeNO_x se alcanza mediante disoluciones sólidas tipo $(BiO)_2CO_3/BiOI$ [373] o heterouniones con BiOBr [374], $BiOIO_3$ [375], g-C_3N_4 [376] y $SrCO_3$ [377].

2.8.5. Óxidos basados en zinc y estaño

Los fotocatalizadores basados en óxidos de zinc y estaño han sido estudiados debido a su elevada actividad bajo irradiación ultravioleta o visible, respectivamente.

Con relación a los compuestos de estaño, se pueden encontrar, por ejemplo, trabajos basados en SnO_2 nanoparticulado y Ag@SnO_2. En el primer fotocatalizador, el índice De-NO_x alcanzó un 64% [378], mientras que en el segundo el rendimiento fue 70%, asistido por la transferencia de carga existente desde las partículas de plata hacia el SnO_2 [379]. En vistas de los buenos resultados, se han desarrollado heterouniones de SnO_2/TiO_2, aunque obteniendo unos reducidos valores De-NO_x (~ 59%) [380].

En otro artículo, la espinela de Zn_2SnO_4 (band gap = 3,25 eV) logró superar el rendimiento De-NO_x del ZnO o del SnO_2 puros (70, 42, 33%, respectivamente) [381]. Los buenos resultados observados fueron relacionados con la estructura porosa de la espinela y por la estructura de bandas electrónicas mejorada. Por otro lado, se han descrito heterouniones de SnO_2/Zn_2SnO_4/grafeno con mejoras muy significativas en el comportamiento De-NO_x frente a la muestra sin grafeno (59% vs 7,5%, respectivamente) [382].

En cuanto a los fotocatalizadores basados en ZnO, hay que señalar el trabajo del grupo de Long et al., donde investigaron el efecto de la morfología de las partículas del fotocatalizador en el proceso De-NO_x, siendo la superficie específica un factor clave [383]. También se ha mejorado la eficiencia fotocatalítica de ZnO mediante la preparación de microesferas porosas [384] o con el incremento de los planos cristalinos (002) [385].

Por otro lado, con el objeto de mejorar la eficacia de estos fotocatalizadores, se han descrito varias decoraciones con nanopartículas,

como por ejemplo ZnO/Ag (mejora De-NO_x del 35 %) [386] o ZnO/WO_3 (mejora De-NO_x del 15 %) [387], así como dopajes con Cr [388], ZnO soportado en SiO_2 [389] y heterouniones con TiO_2 [390,391] o CdO [392].

2.8.6. Óxidos de metales de transición

Además del TiO_2, ya comentado en secciones anteriores, se pueden destacar: las diferentes variantes de óxido de hierro, ferritas de zinc, óxidos basados en wolframio y los óxidos basados en vanadio.

Haciendo referencia al óxido de hierro, hay que destacar que este compuesto fue por primera vez estudiado como fotocatalizador De-NO_x en nuestro Grupo de Investigación (FQM-175). En concreto, mediante un tratamiento térmico de residuos industriales con cierto contenido de hierro se consiguieron composites ricos en α-Fe_2O_3 (fase hematita). Estos compuestos se usaron como aditivos para obtener materiales de construcción fotocatalíticos [393,394]. En otro trabajo posterior, se fabricaron láminas delgadas con nanoestructuras de α- y β-Fe_2O_3 mediante la técnica de deposición química de vapor (CVD). La mayor eficiencia De-NO_x de la fase α-Fe_2O_3 se atribuyó a la mayor porosidad y área específica de dicha nanoestructura [395].

En la misma línea de investigación, se prepararon muestras en polvo de nanopartículas de α-Fe_2O_3 mediante calcinación de la fase de maghemita comercial (γ- Fe_2O_3). Para mejorar el pobre rendimiento De-NO_x de la muestra, (causado por la inadecuada posición de la BC y la elevada recombinación de las fotocargas) se prepararon composites de C/α-Fe_2O_3. El fotocatalizador consiguió aumentar la eficacia De-NO_x en un 17% y disminuir la liberación de NO_2 (**Figura 20**), hechos derivados de la capacidad del carbono para adsorber el intermedio NO_2 y disminuir la recombinación

de las fotocargas [396]. Otros estudios describen composites de Quantun Dots de carbono (CQD) y FeOOH con una actividad De-NO_x superior al FeOOH puro [397].

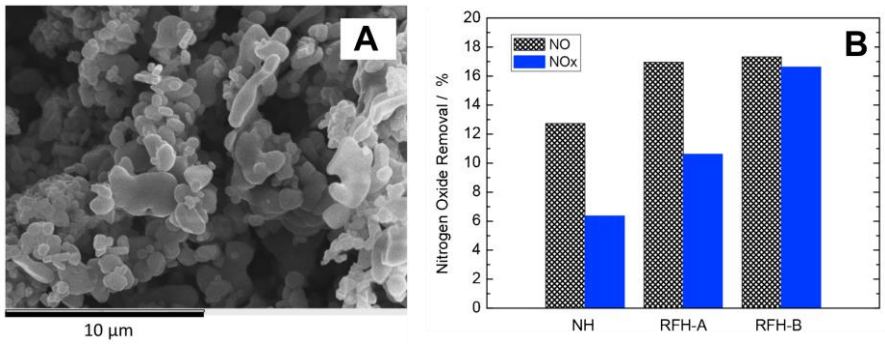

Figura 20. A: microestructura de la muestra *RFH-B* (composite de C/α-Fe_2O_3; ratio precursor:Fe = 4:1); B: eliminación de gas NO durante los ensayos fotocatalíticos. *NH* (α-Fe_2O_3); *RFH-A* (composite de C/α-Fe_2O_3; ratio precursor:Fe = 1:4) [396].

Se han desarrollado diferentes estrategias para continuar mejorando la eficacia fotocatalítica De-NO_x de la fase hematita. Por ejemplo, se pueden citar las nanoestructuras de α-Fe_2O_3: nanofibras [398] y nanotubos/nanoescamas [399] preparadas por electrospinning. En el caso de los nanotubos/nanoescamas porosas α-Fe_2O_3, se consiguió un rendimiento De-NOx cercano al TiO_2 P25 gracias a la capacidad de adsorción de NO_2 sobre la la red de microporos de la nanoestructura [399]. Además de las nanoestructuras, se han reportado heterouniones con TiO_2 [400] y con TiO_2/$CaAl_2O_4$:(Eu, Nd) [401]. En este último caso, la fluorescencia persistente procedente del $CaAl_2O_4$:(Eu, Nd) asiste el proceso De-NO_x en condiciones de oscuridad. Finalmente, merece la pena destacar

otra publicación donde se aplica Fe_3O_4/SiO_2 para aprovechar el efecto fototérmico en el proceso fotocatalítico De-NO_x [402].

Otra familia de compuestos aplicados como fotocatalizadores De-NO_x son las ferritas de zinc. Por ejemplo, la ferrita $ZnFe_2O_4$ (band gap = 1,96 eV) ha sido investigada para mejorar su elevada recombinación de fotocargas y su incapacidad para producir radicales superóxido. En este sentido, se han desarrollado heterouniones como CDQs/$ZnFe_2O_4$ [403], a $Bi_2O_2CO_3/ZnFe_2O_4$ [404] o $TiO_2/ZnFe_2O_4$ [294].

Con relación a los óxidos basados en wolframio, la wolframita ($ZnWO_4$) [405] consiguió una eliminación de gas NO del 35% bajo irradiación solar simulada. Dicha eficacia fue posteriormente mejorada en otro trabajo, mediante el sistema Bi/Bi^{3+}-$ZnWO_4$ [406].

Para finalizar, los óxidos basados en vanadio son otro campo de investigación. En particular, las microesferas de $BiVO_4$ mostraron una actividad fotocatalítica De-NO_x ~ 50% bajo irradiación del espectro visible [407]. También se han trabajado heterouniones con este compuesto, como $BiVO_4/CaIn_2S_4$ [408] con valores De-NOx del 80%, bajo cortos tiempos de iradiación. En otro estudio, se prepararon heterouniones en forma de aerogeles de C_3N_4QDs/GO-$InVO_4$ (C_3N_4 QDs = quantum dots de C_3N_4; GO = óxido de grafeno). El valor De-NO_x reportado fue de un 65% para la composición óptima [409].

2.8.7. Compuestos tipo MOFs

Los MOFs (Metal-Organic Frameworks) son un grupo de compuestos que han sido recientemente aplicados como fotocatalizadores De-NO_x debido a la elevada superficie específica, porosidad y capacidad de modulación los metales y linkers orgánicos. Por ejemplo, Nguyen et al. estudiaron MOF basados en Fe (MIL-101, MIL-88B y MIL-53, MIL:

Materiales del Instituto Lavoisier). De ellos, MIL-101 logró un elevado valor De-NO_x de 76% bajo irradiación solar simulada, debido a la gran área superficial y volumen de poro, así como a la característica coordinación del Fe. No obstante, el fotocatalizador mostró signos de descomposición tras 8 ciclos de reacción [410].

En otro trabajo pionero, se sintetizó un nuevo polímero de organotitanio tipo MOF decorado con partículas de Ag, mediante un proceso asistido por microondas. La estructura formada consiguió un valor de eliminación de gas NO del 50% bajo irradiación visible, gracias a la coordinación de enlace y al efecto de las partículas de plata metálica [411].

Otro MOF que ha captado la atención es el MIL-125(Ti) que presenta un band gap de 3,6 eV y está constituido por ligandos de ácido tereftálico (H2BDC) y clusters de TiO_4. Para remediar la elevada recombinación de las fotocargas se ha acoplado con N-CQD [412]. En esta investigación, se concluyó que los ligandos orgánicos fueron responsables de la absorción de la irradiación UV emitida por los N-CQD, transfieren los electrones a los sitios activos del cluster. Simultáneamente, los centros Ti^{III}-Ti^{IV} de MIL-125(Ti) actúan como centros activos para captar la luz visible. En consecuencia, la actividad de-NO_x fue del 50% para el sistema óptimo, mientras que el MOF puro no mostró fotoactividad alguna.

En otra publicación relevante, se insertaron especies de Cu(I) y Cu(II) en el MOF NH_2-UiO-66(Zr). Esto hizo que se acelerara de manera muy significativa la transferencia de cargas desde los linkers a las especies de

cobre. Como resultado, se obtuvo una actividad De-NO_x = 88% bajo irradiación del espectro visible [413].

2.8.8. Hidróxidos Dobles Laminares

Los Hidróxidos Dobles Laminares (LDHs) presentan una estructura laminar tipo brucita ($Mg(OH_2)$), donde las sustituciones isomórficas de los cationes divalentes M(II) por cationes tri/tetra valentes M(III/IV) generan cargas positivas, que son compensadas con aniones (A) situados entre láminas [414,415]. La fórmula se puede expresar como $[M^{2+}_{1-x}M_x^{3+/4+}(OH)_2]^{x+}A_{m/x}\cdot nH_2O$ donde:

- M^{2+} (metal divalente) = Mg^{2+}, Zn^{2+}, Ni^{2+}, Co^{2+}, Cu^{2+}, etc.
- $M^{3+/4+}$ (metal tri/tetra-valente) = Al^{3+}, Fe^{3+}, Cr^{3+}, Ti^{4+}, Zr^{4+}, etc.
- A^{m-} (anión interlaminar) = Cl^-, CO_3^{2-}, ácidos grasos, dodecilsulfato, etc.
- *x* varía entre 0,2 y 0,4.

Debido a la extensa capacidad de modulación de su composición, la facilidad y bajo coste de su síntesis, y su gran versatilidad química, estos materiales se han estudiado para un amplio espectro de aplicaciones [416–420]. También, se han estudiado y mostrado sus buenas propiedades fotocatalíticas [421,422]. En este sentido, nuestro Grupo de Investigación fue pionero en la aplicación de los LDHs como fotocatalizadores De-NO_x, demostrando valores de eliminación de estos gases del 50% bajo

irradiación solar simulada, junto con valores excelentes de selectividad (90%) [423].

En otro trabajo posterior, el grupo de Fan Dong investigó la influencia de varios aniones interlaminares (OH^-, CO_3^{2-} y MoO_4^{2-}) sobre el LDH basado en los cationes metálicos de zinc y aluminio con una relación atómica de 2:1 (denominado como Zn_2Al), encontrando la mejor respuesta De-NO_x (47%) para el LDH con el carbonato como anión interlaminar (Zn_2Al-CO_3) [424]. En otro trabajo más reciente, el mismo grupo investigó el mecanismo sobre la serie $Mg_{2-x}Ni_xAl$-CO_3. La relación metálica óptima fue $Mg_{1.5}Ni_{0.5}Al$, con un De-NO_x = 45 % bajo irradiación UV, aunque ninguna muestra fue activa bajo irradiación del espectro visible. A destacar, se demostró que los OH^- de la estructura del LDH podían atrapar los huecos fotogenerados para producir radicales hidroxilo [425].

En otro trabajo de nuestro Grupo de Investigación, los LDHs basados en $Zn_3Al_{1-x}Cr_x$-CO_3 con diferentes niveles de sustitución del catión Al^{3+} por Cr^{3+} fueron estudiados, al objeto de mejorar el rendimiento fotocatalítico De-NO_x bajo irradiación del espectro Visible. La muestra con la mayor cantidad de Cr^{3+} exhibió el mejor comportamiento fotocatalítico, logrando una gran eficiencia de eliminación de NO (55%), una selectividad sobresaliente (90%) y una buena reutilización tras 4 ciclos de 6 horas de irradiación [426].

En un reciente artículo, también elaborado por nuestro Grupo, el LDH basado en Mg_3Al fue empleado como un compuesto descontaminante de doble función. Por un lado, el LDH de Mg_3Al-CO_3 fue calcinado y utilizado como adsorbente del contaminante cromato (CrO_4^{2-}) desde el agua. Por otro lado, tras el proceso de adsorción, el sólido formado (Mg_3Al-CrO_4) fue aplicado como fotocatalizador De-NO_x. El cromato presente en la estructura del LDH hizo mejorar la absorción de luz del espectro visible y la

generación de radicales superóxido (**Figura 21**), resultando en un aumento de un 20% en la eliminación de NO en comparación con la LDH con carbonato como anión interlaminar [427].

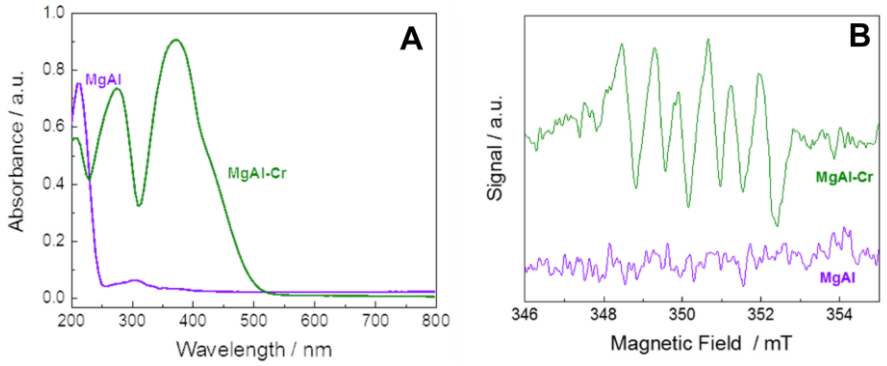

Figura 21. Espectros de absorción UV-Vis (A) y espectros de resonancia paramagnética electrónica de atrapamiento de radicales (B) para los LDHs: *MgAl* (Mg_3Al-CO_3) y *MgAl-Cr* (Mg_3Al-CrO_4) [427].

2.9. Referencias

[1] The Getty Conservation Institute, Charter of Athens (1933), (n.d.). https://www.getty.edu/conservation/publications_resources/research_resources/charters/charter04.html (accessed October 5, 2021).

[2] G. de E. Ministerio de Cultura y Deporte, Plan Nacional de investigación en Patrimonio. ANEXO I. La importancia económica del patrimonio cultural, (n.d.). http://www.mcu.es/estadisticas/docs/CSCE/avance_resultados_csce-2010.pdf (accessed October 5, 2021).

[3] X. Mas, M. Sánchez, L. Osete, S. Kröner, Study and Characterization of Stone Mortars Used as a Volumetric Reconstruction Material in Conservation-Restoration of Monumental Heritage, in: C. Llinares-Millán, I. Fernández-Plazaola, F. Hidalgo-Delgado, M.M. Martínez-Valenzuela, F.J. Medina-Ramón, I. Oliver-Faubel, I. Rodríguez-Abad, A. Salandin, R. Sánchez-Grandia, I. Tort-Ausina (Eds.), Constr. Build. Res., Springer Netherlands, Dordrecht, 2014: pp. 345–354.

[4] S.E. Favero-Longo, F. Brigadeci, A. Segimiro, S. Voyron, M. Cardinali, M. Girlanda, R. Piervittori, Biocide efficacy and consolidant effect on the mycoflora of historical stuccos in indoor environment, J. Cult. Herit. 34 (2018) 33–42. doi:10.1016/J.CULHER.2018.03.017.

[5] J.T. Hannibal, S. Kramar, B.J. Cooper, Worldwide examples of global heritage stones: an introduction, Geol. Soc. London, Spec. Publ. 486 (2020) 1–6. doi:10.1144/SP486-2020-84.

[6] M.H.B. de O. Frascá, R. Neves, N.F. Castro, The white marbles of Brasília, a World Heritage site and capital of Brazil, Geol. Soc. London, Spec. Publ. 486 (2020) 217–227. doi:10.1144/SP486-2018-31.

[7] L. Catarino, R. Figueiredo, F.P. Figueiredo, P. Andrade, J. Duarte, The Use of Dolostone in Historical Buildings of Coimbra (Central Portugal), Sustain. 2019, Vol. 11, Page 4158. 11 (2019) 4158. doi:10.3390/SU11154158.

[8] T. Dreyfuss, Artificially induced calcium oxalate on limestone in urban environments – New findings, J. Cult. Herit. 42 (2020) 56–63. doi:10.1016/J.CULHER.2019.06.011.

[9] H. Morillas, J. García-Galan, M. Maguregui, I. Marcaida, C. García-Florentino, J.A. Carrero, J.M. Madariaga, Assessment of marine and urban-industrial environments influence on built heritage sandstone using X-ray fluorescence spectroscopy and complementary techniques, Spectrochim. Acta Part B At. Spectrosc. 123 (2016) 76–88. doi:10.1016/J.SAB.2016.07.015.

[10] D. Camuffo, Microclimate for Cultural Heritage: Measurement, Risk Assessment, Conservation, Restoration, and Maintenance of Indoor and Outdoor Monuments, Elsevier, 2019.

[11] A. Bonazza, P. De Nuntiis, P. Mandrioli, C. Sabbioni, Aerosol Impact on Cultural Heritage: Deterioration Processes and Strategies for Preventive Conservation, Atmos. Aerosols. (2016) 645–670. doi:10.1002/9783527336449.CH11.

[12] C. Varotsos, C. Tzanis, A. Cracknell, The enhanced deterioration of the cultural heritage monuments due to air pollution, Environ. Sci. Pollut. Res. 2009 165. 16 (2009) 590–592. doi:10.1007/S11356-009-0114-8.

[13] A. Sierra-Fernandez, S.C.D. la Rosa-García, L.S. Gomez-Villalba, S. Gómez-Cornelio, M.E. Rabanal, R. Fort, P. Quintana, Synthesis, Photocatalytic, and Antifungal Properties of MgO, ZnO and Zn/Mg Oxide Nanoparticles for the Protection of Calcareous Stone Heritage, ACS Appl. Mater. Interfaces. 9 (2017) 24873–24886. doi:10.1021/ACSAMI.7B06130.

[14] E. Di Carlo, G. Barresi, F. Palla, Biodeterioration, Biotechnol. Conserv. Cult. Herit. (2017) 1–30. doi:10.1007/978-3-319-46168-7_1.

[15] E. Stanaszek-Tomal, Environmental Factors Causing the Development of Microorganisms on the Surfaces of National Cultural Monuments Made of Mineral Building Materials—Review, Coatings 2020, Vol. 10, Page 1203. 10 (2020) 1203. doi:10.3390/COATINGS10121203.

[16] A.Z. Miller, P. Sanmartín, L. Pereira-Pardo, A. Dionísio, C. Saiz-Jimenez, M.F. Macedo, B. Prieto, Bioreceptivity of building stones: A review, Sci. Total Environ. 426 (2012) 1–12. doi:10.1016/J.SCITOTENV.2012.03.026.

[17] P. Sanmartín, A.Z. Miller, B. Prieto, H.A. Viles, Revisiting and reanalysing the concept of bioreceptivity 25 years on, Sci. Total

Environ. 770 (2021) 145314. doi:10.1016/J.SCITOTENV.2021.145314.

[18] O. Guillitte, Bioreceptivity: a new concept for building ecology studies, Sci. Total Environ. 167 (1995) 215–220. doi:10.1016/0048-9697(95)04582-L.

[19] D. Allsopp, K.J. Seal, C.C. Gaylarde, Introduction to biodeterioration, (2004) 237.

[20] D. Allsopp, Worldwide wastage: the economics of biodeterioration, Microbiol. Today. (2011) 150–152. https://microbiologysociety.org/publication/past-issues/microeconomics.html.

[21] W. Sand, E. Bock, Biodeterioration of ceramic materials by biogenic acids, Int. Biodeterior. 27 (1991) 175–183. doi:10.1016/0265-3036(91)90009-G.

[22] V. Amarelle, V. Carrasco, E. Fabiano, The Hidden Life of Antarctic Rocks, (2019) 221–237. doi:10.1007/978-3-030-02786-5_10.

[23] S. Golubic, E.I. Friedmann, J. Schneider, The lithobiontic ecological niche, with special reference to microorganisms, J. Sediment. Res. 51 (1981) 475–478. doi:10.1306/212F7CB6-2B24-11D7-8648000102C1865D.

[24] C.C. Gaylarde, P.M. Gaylarde, B.A. Neilan, Endolithic Phototrophs in Built and Natural Stone, Curr. Microbiol. 2012 652. 65 (2012) 183–188. doi:10.1007/S00284-012-0123-6.

[25] J. Marlow, J. Peckmann, V. Orphan, Autoendoliths: a distinct type of rock-hosted microbial life, Geobiology. 13 (2015) 303–307. doi:10.1111/GBI.12131.

[26] C.J. McNamara, R. Mitchell, Microbial deterioration of historic stone, Front. Ecol. Environ. 3 (2005) 445–451. doi:10.1890/1540-9295(2005)003[0445:MDOHS]2.0.CO;2.

[27] S. Scheerer, O. Ortega-Morales, C. Gaylarde, Chapter 5 Microbial Deterioration of Stone Monuments—An Updated Overview, Adv. Appl. Microbiol. 66 (2009) 97–139. doi:10.1016/S0065-2164(08)00805-8.

[28] G.B. Goffredo, S. Accoroni, C. Totti, Nanotreatments to inhibit microalgal fouling on building stone surfaces, Nanotechnol. Eco-

Efficient Constr. Mater. Process. Appl. (2019) 619–647. doi:10.1016/B978-0-08-102641-0.00025-6.

[29] C.A. Crispim, C.C. Gaylarde, Cyanobacteria and biodeterioration of cultural heritage: a review, Microb. Ecol. 49 (2005) 1–9.

[30] B. Cwalina, Understanding Biocorrosion: Fundamentals and Applications, Biodeterior. Concr. Brick Other Miner. Build. Mater. Woodhead Publ. (2014) 281–312.

[31] P.D. Martino, What about biofilms on the surface of stone monuments?, in: Open Conf. Proc. J., 2016.

[32] X. Liu, R.J. Koestler, T. Warscheid, Y. Katayama, J.-D. Gu, Microbial deterioration and sustainable conservation of stone monuments and buildings, Nat. Sustain. 2020 312. 3 (2020) 991–1004. doi:10.1038/s41893-020-00602-5.

[33] A. Negi, I.P. Sarethy, Microbial Biodeterioration of Cultural Heritage: Events, Colonization, and Analyses, Microb. Ecol. 2019 784. 78 (2019) 1014–1029. doi:10.1007/S00248-019-01366-Y.

[34] T. Warscheid, J. Braams, Biodeterioration of stone: a review, Int. Biodeterior. Biodegradation. 46 (2000) 343–368. doi:10.1016/S0964-8305(00)00109-8.

[35] C. Gaylarde, M. Ribas Silva, T. Warscheid, Microbial impact on building materials: an overview, Mater. Struct. 2003 365. 36 (2003) 342–352. doi:10.1007/BF02480875.

[36] B. Cwalina, Biodeterioration of Concrete, Archit. Civ. Eng. Environ. 4 (2008) 133–140. doi:10.1201/9781315119557.

[37] M.I. Sarró, A.M. García, V.M. Rivalta, D.A. Moreno, I. Arroyo, Biodeterioration of the Lions Fountain at the Alhambra Palace, Granada (Spain), Build. Environ. 41 (2006) 1811–1820. doi:10.1016/J.BUILDENV.2005.07.029.

[38] Fundamentos de conservación preventiva. Plan Nacional de Conservación Preventiva, 2015. https://oibc.oei.es/uploads/attachments/184/CONSERVACIÓN_PREVENTIVA.pdf.

[39] Asociación Española de Normalización y Certificación (AENOR), UNE-ISO 31000:2018 Gestión del riesgo. Directrices., (2018). https://tienda.aenor.com/norma-une-iso-31000-2018-n0059900

(accessed October 6, 2021).

[40] D. Pinna, Coping with Biological Growth on Stone Heritage Objects : Methods, Products, Applications, and Perspectives, Coping with Biol. Growth Stone Herit. Objects. (2017). doi:10.1201/9781315365510.

[41] S.P. Denyer, G.S.A.B. Stewart, Mechanisms of action of disinfectants, Int. Biodeterior. Biodegradation. 41 (1998) 261–268. doi:10.1016/S0964-8305(98)00023-7.

[42] S. Veltri, A.M. Palermo, G. De Filpo, F. Xu, Subsurface treatment of TiO_2 nanoparticles for limestone: Prolonged surface photocatalytic biocidal activities, Build. Environ. 149 (2019) 655–661. doi:10.1016/J.BUILDENV.2018.10.038.

[43] D.J. Knight, M. Cooke, The Biocides Business, Biocides Bus. (2002). doi:10.1002/352760197X.

[44] European Chemicals Agency (ECHA), Information on biocides, (n.d.). https://echa.europa.eu/es/information-on-chemicals/biocidal-products (accessed October 6, 2021).

[45] Ministerio para la Transición Ecológica y el Reto Demográfico. Gobierno de España, Biocidas, (n.d.). https://www.miteco.gob.es/es/calidad-y-evaluacion-ambiental/temas/productos-quimicos/biocidas/ (accessed October 6, 2021).

[46] M.P. Nugari, O. Salvadori, Biodeterioration control of cultural heritage: Methods and products, in: Mol. Biol. Cult. Herit., Primera edición, Routledge, 2003: pp. 233–242. doi:10.1201/9780203746578-31.

[47] G. Caneva, M.P. Nugari, O. Salvadori, La biología en la restauración: arte y restauración, Editor. Nerea, Madrid/Sevilla, España. (2000).

[48] R. Snethlage, K. Sterflinger, Stone Conservation, Stone Archit. Prop. Durab. (2011) 411–544. doi:10.1007/978-3-642-14475-2_7.

[49] E. Doehne, C.A. Price, Stone Conservation. An Overview of Current Research, Second Edi, Getty Conservation Institute, 2010. www.gettypublications.org (accessed October 6, 2021).

[50] K. Mijnendonckx, N. Leys, J. Mahillon, S. Silver, R. Van Houdt, Antimicrobial silver: uses, toxicity and potential for resistance,

BioMetals 2013 264. 26 (2013) 609–621. doi:10.1007/S10534-013-9645-Z.

[51] A. Sierra-Fernandez, L.S. Gomez-Villalba, M.E. Rabanal, R. Fort, New nanomaterials for applications in conservation and restoration of stony materials: A review, Mater. Constr. 67 (2017). doi:10.3989/MC.2017.07616.

[52] L.E. Mardones, M.S. Legnoverde, S. Simonetti, E.I. Basaldella, Theoretical and experimental study of isothiazolinone adsorption onto ordered mesoporous silica, Appl. Surf. Sci. 389 (2016) 790–796. doi:10.1016/J.APSUSC.2016.07.113.

[53] W. Paulus, Directory of microbicides for the protection of materials: a handbook, Springer Science & Business Media, 2005.

[54] M. Falkiewicz-Dulik, K. Janda, G. Wypych, Handbook of material biodegradation, biodeterioration, and biostablization, Elsevier, 2015.

[55] G. Caneva, M.P. Nugari, M.P. Nugari, O. Salvadori, Plant biology for cultural heritage: biodeterioration and conservation, Getty Publications, 2008.

[56] K. Sterflinger, G. Piñar, Microbial deterioration of cultural heritage and works of art — tilting at windmills?, Appl. Microbiol. Biotechnol. 97 (2013) 9637–9646. doi:10.1007/S00253-013-5283-1.

[57] A. Sierra-Fernandez, L.S. Gomez-Villalba, S.C. De la Rosa-García, S. Gomez-Cornelio, P. Quintana, M.E. Rabanal, R. Fort, Inorganic nanomaterials for the consolidation and antifungal protection of stone heritage, in: Adv. Mater. Conserv. Stone, Springer, 2018: pp. 125–149.

[58] J. Becerra, A.P. Zaderenko, M.A. Gómez-Morón, P. Ortiz, Nanoparticles Applied to Stone Buildings, Int. J. Archit. Herit. 15 (2019) 1320–1335. doi:10.1080/15583058.2019.1672828.

[59] S. Eyssautier-Chuine, I. Calandra, N. Vaillant-Gaveau, G. Fronteau, C. Thomachot-Schneider, J. Hubert, J. Pleck, M. Gommeaux, A new preventive coating for building stones mixing a water repellent and an eco-friendly biocide, Prog. Org. Coatings. 120 (2018) 132–142. doi:10.1016/J.PORGCOAT.2018.03.022.

[60] J. von Werder, H. Venzmer, The potential of pulse amplitude modulation fluorometry for evaluating the resistance of building

materials to algal growth, Int. Biodeterior. Biodegradation. 84 (2013) 227–235. doi:10.1016/J.IBIOD.2012.03.009.

[61] Deflecta Antimicrobial - Concrete Antimicrobial Biocide and Sanitiser, (n.d.). https://www.deflecta.com.au/products/bacteria-control/antimicrobial (accessed October 6, 2021).

[62] S. Martínez, F. Puertas, M.T. Blanco-Varela, Mortero con propiedades biocidas, ES2102315 A1, 1997. https://consultas2.oepm.es/InvenesWeb/detalle?referencia=P9401732.

[63] F.S.R. Antonio Aguado De Cea; Ignacio Segura Pérez; José María Vaquero Martínez, Aditivo inhibidor del crecimiento biológico en estructuras de hormigón y uso, WO2016005641A1, 2016. https://patents.google.com/patent/WO2016005641A1/es (accessed October 6, 2021).

[64] M. Burkhardt, S. Zuleeg, R. Vonbank, P. Schmid, S. Hean, X. Lamani, K. Bester, M. Boller, Leaching of additives from construction materials to urban storm water runoff, Water Sci. Technol. 63 (2011) 1974–1982. doi:10.2166/WST.2011.128.

[65] J. Pena-Poza, C. Ascaso, M. Sanz, S. Pérez-Ortega, M. Oujja, J. Wierzchos, V. Souza-Egipsy, M. V. Cañamares, M. Urizal, M. Castillejo, M. García-Heras, Effect of biological colonization on ceramic roofing tiles by lichens and a combined laser and biocide procedure for its removal, Int. Biodeterior. Biodegradation. 126 (2018) 86–94. doi:10.1016/J.IBIOD.2017.10.003.

[66] B. Cámara, A. De los Ríos, M. Urizal, M. Álvarez de Buergo, M. Jose Varas, R. Fort, C. Ascaso, Characterizing the Microbial Colonization of a Dolostone Quarry: Implications for Stone Biodeterioration and Response to Biocide Treatments, Environ. Microbiol. 62 (2011) 299–313. doi:10.1007/s00248-011-9815-x.

[67] U. Schoknecht, T. Sommerfeld, N. Borho, E. Bagda, Interlaboratory comparison for a laboratory leaching test procedure with façade coatings, Prog. Org. Coatings. 76 (2013) 351–359. doi:10.1016/J.PORGCOAT.2012.10.001.

[68] THOR Specialties, Inc – Industrial Biocides for USA and Canada, (n.d.). https://www.thor.com/usa/biocidesindustrialusacanada.html (accessed October 6, 2021).

[69] M.M. Urbanczyk, K. Bester, N. Borho, U. Schoknecht, U.E. Bollmann, Influence of pigments on phototransformation of biocides in paints, J. Hazard. Mater. 364 (2019) 125–133. doi:10.1016/J.JHAZMAT.2018.10.018.

[70] D. Pinna, B. Salvadori, M. Galeotti, Monitoring the performance of innovative and traditional biocides mixed with consolidants and water-repellents for the prevention of biological growth on stone, Sci. Total Environ. 423 (2012) 132–141. doi:10.1016/J.SCITOTENV.2012.02.012.

[71] Paints and coatings dry-film preservatives, (n.d.). https://www.chemipol.com/en/paints-and-coatings-dry-film-preservatives/ (accessed October 6, 2021).

[72] A.J. Fonseca, F. Pina, M.F. Macedo, N. Leal, A. Romanowska-Deskins, L. Laiz, A. Gómez-Bolea, C. Saiz-Jimenez, Anatase as an alternative application for preventing biodeterioration of mortars: Evaluation and comparison with other biocides, Int. Biodeterior. Biodegrad. 64 (2010) 388–396. doi:10.1016/j.ibiod.2010.04.006.

[73] P. Sanmartín, A. Rodríguez, U. Aguiar, Medium-term field evaluation of several widely used cleaning-restoration techniques applied to algal biofilm formed on a granite-built historical monument, Int. Biodeterior. Biodegradation. 147 (2020) 104870. doi:10.1016/J.IBIOD.2019.104870.

[74] S.E. Favero-Longo, R. Benesperi, S. Bertuzzi, E. Bianchi, G. Buffa, P. Giordani, S. Loppi, P. Malaspina, E. Matteucci, L. Paoli, S. Ravera, A. Roccardi, A. Segimiro, A. Vannini, Species- and site-specific efficacy of commercial biocides and application solvents against lichens, Int. Biodeterior. Biodegradation. 123 (2017) 127–137. doi:10.1016/J.IBIOD.2017.06.009.

[75] F. Villa, D. Gulotta, L. Toniolo, L. Borruso, C. Cattò, F. Cappitelli, Aesthetic Alteration of Marble Surfaces Caused by Biofilm Formation: Effects of Chemical Cleaning, Coatings 2020, Vol. 10, Page 122. 10 (2020) 122. doi:10.3390/COATINGS10020122.

[76] S. Pozo, C. Montojo, T. Rivas, A.J. López-Díaz, M.P. Fiorucci, M.E. López de Silanes, Comparison between methods of biological crust removal on granite, in: Key Eng. Mater., Trans Tech Publ, 2013: pp. 317–325.

[77] S. Eyssautier-Chuine, N. Vaillant-Gaveau, M. Gommeaux, C.

Thomachot-Schneider, J. Pleck, G. Fronteau, Efficacy of different chemical mixtures against green algal growth on limestone: A case study with Chlorella vulgaris, Int. Biodeterior. Biodegradation. 103 (2015) 59–68. doi:10.1016/J.IBIOD.2015.02.021.

[78] W. De Muynck, N. De Belie, W. Verstraete, Antimicrobial mortar surfaces for the improvement of hygienic conditions, J. Appl. Microbiol. 108 (2010) 62–72. doi:10.1111/j.1365-2672.2009.04395.x.

[79] M. Edge, N.S. Allen, D. Turner, J. Robinson, K. Seal, The enhanced performance of biocidal additives in paints and coatings, Prog. Org. Coatings. 43 (2001) 10–17. doi:10.1016/S0300-9440(01)00244-2.

[80] S. Coutu, C. Rota, L. Rossi, D.A. Barry, Modelling city-scale facade leaching of biocide by rainfall, Water Res. 46 (2012) 3525–3534. doi:10.1016/J.WATRES.2012.03.064.

[81] L. Nordstierna, A.A. Abdalla, M. Masuda, G. Skarnemark, M. Nydén, Molecular release from painted surfaces: Free and encapsulated biocides, Prog. Org. Coatings. 69 (2010) 45–48. doi:10.1016/J.PORGCOAT.2010.05.002.

[82] J. Bergek, M. Andersson Trojer, A. Mok, L. Nordstierna, Controlled release of microencapsulated 2-n-octyl-4-isothiazolin-3-one from coatings: Effect of microscopic and macroscopic pores, Colloids Surfaces A Physicochem. Eng. Asp. 458 (2014) 155–167. doi:10.1016/J.COLSURFA.2014.02.057.

[83] B. Song, E. Zhang, X. Han, H. Zhu, Y. Shi, Z. Cao, Engineering and Application Perspectives on Designing an Antimicrobial Surface, ACS Appl. Mater. Interfaces. 12 (2020) 21330–21341. doi:10.1021/ACSAMI.9B19992.

[84] S. Jämsä, R. Mahlberg, U. Holopainen, J. Ropponen, A. Savolainen, A.C. Ritschkoff, Slow release of a biocidal agent from polymeric microcapsules for preventing biodeterioration, Prog. Org. Coatings. 76 (2013) 269–276. doi:10.1016/J.PORGCOAT.2012.09.018.

[85] P. Somasundaran, Encyclopedia of surface and colloid science, 2004 update supplement, CRC Press, 2014.

[86] J.M. Vaquero, V. Cugat, I. Segura, M.A. Calvo, A. Aguado, Development and experimental validation of an overlay mortar with biocide activity, Cem. Concr. Compos. 74 (2016) 109–119.

doi:10.1016/j.cemconcomp.2016.09.004.

[87] R.S. Langer, D.L. Wise, Medical applications of controlled release, CRC press, 2019.

[88] J. Pardeike, A. Hommoss, R.H. Müller, Lipid nanoparticles (SLN, NLC) in cosmetic and pharmaceutical dermal products, Int. J. Pharm. 366 (2009) 170–184. doi:10.1016/J.IJPHARM.2008.10.003.

[89] F. Sousa, D. Ferreira, S. Reis, P. Costa, Current Insights on Antifungal Therapy: Novel Nanotechnology Approaches for Drug Delivery Systems and New Drugs from Natural Sources, Pharmaceuticals. 13 (2020) 1–30. doi:10.3390/PH13090248.

[90] R. Costa, L. Santos, Delivery systems for cosmetics - From manufacturing to the skin of natural antioxidants, Powder Technol. 322 (2017) 402–416. doi:10.1016/J.POWTEC.2017.07.086.

[91] B.D. Mattos, B.L. Tardy, W.L.E. Magalhães, O.J. Rojas, Controlled release for crop and wood protection: Recent progress toward sustainable and safe nanostructured biocidal systems, J. Control. Release. 262 (2017) 139–150. doi:10.1016/j.jconrel.2017.07.025.

[92] J.S. Duhan, R. Kumar, N. Kumar, P. Kaur, K. Nehra, S. Duhan, Nanotechnology: The new perspective in precision agriculture, Biotechnol. Reports. 15 (2017) 11–23. doi:10.1016/J.BTRE.2017.03.002.

[93] K.L. Yam, X. Zhu, Controlled release food and beverage packaging, Emerg. Food Packag. Technol. (2012) 13–26. doi:10.1533/9780857095664.1.13.

[94] C. Nerin, F. Silva, S. Manso, R. Becerril, The Downside of Antimicrobial Packaging: Migration of Packaging Elements into Food, Antimicrob. Food Packag. (2016) 81–93. doi:10.1016/B978-0-12-800723-5.00006-1.

[95] L. Ruggiero, E. Di Bartolomeo, T. Gasperi, I. Luisetto, A. Talone, F. Zurlo, D. Peddis, M.A. Ricci, A. Sodo, Silica nanosystems for active antifouling protection: nanocapsules and mesoporous nanoparticles in controlled release applications, J. Alloys Compd. 798 (2019) 144–148. doi:10.1016/J.JALLCOM.2019.05.215.

[96] Y. Gao, Z. Zhou, X. Chen, Y. Tian, Y. Li, H. Wang, X. Li, X. Yu, Y. Cao, Controlled release of herbicides by 2,4-D-, MCPA-, and bromoxynil-intercalated hydrotalcite nanosheets, Green Chem. 23 (2021) 4560–

4566. doi:10.1039/D1GC01349A.

[97] F. Bruna, I. Pavlovic, R. Celis, C. Barriga, J. Cornejo, M.A. Ulibarri, Organohydrotalcites as novel supports for the slow release of the herbicide terbuthylazine, Appl. Clay Sci. 42 (2008) 194–200. doi:10.1016/J.CLAY.2008.02.001.

[98] B.D. Mattos, L.R. da Silva, I.R. de Souza, W.L.E. Magalhães, D.M. Leme, Slow delivery of biocide from nanostructured, microscaled, particles reduces its phytoxicity: A model investigation, J. Hazard. Mater. 367 (2019) 513–519. doi:10.1016/J.JHAZMAT.2018.12.117.

[99] M.A. Trojer, L. Nordstierna, M. Nordin, M. Nydén, K. Holmberg, Encapsulation of actives for sustained release, Phys. Chem. Chem. Phys. 15 (2013) 17727–17741. doi:10.1039/C3CP52686K.

[100] S.K. Ghosh, Functional Coatings and Microencapsulation: A General Perspective, Funct. Coatings. (2006) 1–28. doi:https://doi.org/10.1002/3527608478.ch1.

[101] M. Alonso Alonso, Microencapsulación de biocidas, Universidad del País Vasco, 2011. https://addi.ehu.es/bitstream/handle/10810/6944/0- Indice %28Tesis-Alonso%29.pdf?sequence=6&isAllowed=y.

[102] A.C. Chan, M. Bravo Cadena, H.E. Townley, M.D. Fricker, I.P. Thompson, Effective delivery of volatile biocides employing mesoporous silicates for treating biofilms, J. R. Soc. Interface. 14 (2017) 20160650. doi:10.1098/rsif.2016.0650.

[103] K. Rózga-Wijas, U. Mizerska, W. Fortuniak, J. Chojnowski, R. Hałasa, W. Werel, Quaternary Ammonium Salts (QAS) Modified Polysiloxane Biocide Supported on Silica Materials, J. Inorg. Organomet. Polym. Mater. 17 (2007) 605–613. doi:10.1007/s10904-007-9153-0.

[104] B.D. Mattos, B.L. Tardy, M. Pezhman, T. Kämäräinen, M. Linder, W.H. Schreiner, W.L.E. Magalhães, O.J. Rojas, Controlled biocide release from hierarchically-structured biogenic silica: surface chemistry to tune release rate and responsiveness, Sci. Rep. 8 (2018) 1–11. doi:10.1038/s41598-018-23921-2.

[105] K. Kermannezhad, A. Najafi Chermahini, M.M. Momeni, B. Rezaei, Application of amine-functionalized MCM-41 as pH-sensitive nano container for controlled release of 2-mercaptobenzoxazole

corrosion inhibitor, Chem. Eng. J. 306 (2016) 849–857. doi:10.1016/J.CEJ.2016.08.004.

[106] L.E. Mardones, M.S. Legnoverde, E.I. Basaldella, Inorganic mesoporous silica foams for use in stabilization and controlled release of isothiazolinone-based biocides: influence of silica textural properties, Adsorption. 26 (2020) 217–223. doi:10.1007/s10450-019-00114-5.

[107] G.E. Machado, A.M. Pereyra, V.G. Rosato, M.S. Moreno, E.I. Basaldella, Improving the biocidal activity of outdoor coating formulations by using zeolite-supported silver nanoparticles, Mater. Sci. Eng. C. 98 (2019) 789–799. doi:10.1016/J.MSEC.2019.01.040.

[108] A. Presentato, F. Armetta, A. Spinella, D.F. Chillura Martino, R. Alduina, M.L. Saladino, Formulation of Mesoporous Silica Nanoparticles for Controlled Release of Antimicrobials for Stone Preventive Conservation, Front. Chem. 8 (2020) 699. doi:10.3389/fchem.2020.00699.

[109] M. V. Loureiro, M. Vale, A. De Schrijver, J.C. Bordado, E. Silva, A.C. Marques, Hybrid custom-tailored sol-gel derived microscaffold for biocides immobilization, Microporous Mesoporous Mater. 261 (2018) 252–258. doi:10.1016/J.MICROMESO.2017.10.056.

[110] L. Ruggiero, A. Sodo, M. Cestelli-Guidi, M. Romani, A. Sarra, P. Postorino, M.A. Ricci, Raman and ATR FT-IR investigations of innovative silica nanocontainers loaded with a biocide for stone conservation treatments, Microchem. J. 155 (2020) 104766. doi:10.1016/J.MICROC.2020.104766.

[111] M. Zuena, L. Ruggiero, G. Della Ventura, E. Bemporad, M.A. Ricci, A. Sodo, Effectiveness and Compatibility of Nanoparticle Based Multifunctional Coatings on Natural and Man-Made Stones, Coatings. 11 (2021). doi:10.3390/coatings11040480.

[112] C. Dresler, M.L. Saladino, C. Demirbag, E. Caponetti, D.F. Chillura Martino, R. Alduina, Development of controlled release systems of biocides for the conservation of cultural heritage, Int. Biodeterior. Biodegradation. 125 (2017) 150–156. doi:10.1016/J.IBIOD.2017.09.007.

[113] A. Popat, J. Liu, Q. Hu, M. Kennedy, B. Peters, G.Q. (Max) Lu, S.Z. Qiao, Adsorption and release of biocides with mesoporous silica nanoparticles, Nanoscale. 4 (2012) 970–975.

doi:10.1039/C2NR11691J.

[114] M. Michailidis, E. Gutner-Hoch, R. Wengier, R. Onderwater, R.A. D'Sa, Y. Benayahu, A. Semenov, V. Vinokurov, D.G. Shchukin, Highly Effective Functionalized Coatings with Antibacterial and Antifouling Properties, ACS Sustain. Chem. Eng. 8 (2020) 8928–8937. doi:10.1021/acssuschemeng.0c00998.

[115] B.D. Mattos, W.L.E. Magalhães, Design and preparation of carbendazim-loaded alumina nanoparticles as a controlled-release biocide for wood protection, Int. Biodeterior. Biodegrad. 123 (2017) 174–181. doi:10.1016/j.ibiod.2017.06.019.

[116] L. Shtykova, C. Fant, P. Handa, A. Larsson, K. Berntsson, H. Blanck, R. Simonsson, M. Nydén, H. Ingelsten Härelind, Adsorption of antifouling booster biocides on metal oxide nanoparticles: Effect of different metal oxides and solvents, Prog. Org. Coatings. 64 (2009) 20–26. doi:10.1016/J.PORGCOAT.2008.07.005.

[117] M. Yang, L. Gu, B. Yang, L. Wang, Z. Sun, J. Zheng, J. Zhang, J. Hou, C. Lin, Antifouling composites with self-adaptive controlled release based on an active compound intercalated into layered double hydroxides, Appl. Surf. Sci. 426 (2017) 185–193. doi:10.1016/J.APSUSC.2017.07.207.

[118] Z. Sun, L. Gu, J. Zheng, J. Zhang, L. Wang, F. Xu, C. Lin, A controlled release strategy of antifouling agent in coating based on intercalated layered double hydroxides, Mater. Lett. 172 (2016) 105–108. doi:10.1016/J.MATLET.2016.02.151.

[119] C. Gallo, P. Rizzo, G. Guerra, Antimicrobial release from cleaning poultices for the conservation and disinfection of stone surfaces, Appl. Clay Sci. 193 (2020) 105667. doi:10.1016/J.CLAY.2020.105667.

[120] C. Gallo, P. Rizzo, G. Guerra, Intercalation compounds of a smectite clay with an ammonium salt biocide and their possible use for conservation of cultural heritage, Heliyon. 5 (2019). doi:10.1016/J.HELIYON.2019.E02991.

[121] M.A. Fernández, L. Barberia Roque, E. Gámez Espinosa, C. Deyá, N. Bellotti, Organo-montmorillonite with biogenic compounds to be applied in antifungal coatings, Appl. Clay Sci. 184 (2020) 105369. doi:10.1016/J.CLAY.2019.105369.

[122] Y.M. Lvov, D.G. Shchukin, H. Möhwald, R.R. Price, Halloysite Clay

Nanotubes for Controlled Release of Protective Agents, ACS Nano. 2 (2008) 814–820. doi:10.1021/nn800259q.

[123] Y. Fu, W. Wang, L. Zhang, V. Vinokurov, A. Stavitskaya, Y. Lvov, Development of Marine Antifouling Epoxy Coating Enhanced with Clay Nanotubes, Materials (Basel). 12 (2019) 4195. doi:10.3390/MA12244195.

[124] AgION Technologies Inc. Agion™ Technology , (n.d.). http://www.agion-tech.com/ (accessed October 7, 2021).

[125] T. Haile, G. Nakhla, A Novel Zeolite Coating for Protection of Concrete Sewers from Biological Sulfuric Acid Attack, Geomicrobiol. J. 25 (2008) 322–331. doi:10.1080/01490450802258428.

[126] T. Haile, G. Nakhla, E. Allouche, Evaluation of the resistance of mortars coated with silver bearing zeolite to bacterial-induced corrosion, Corros. Sci. 50 (2008) 713–720. doi:10.1016/J.CORSCI.2007.08.012.

[127] Microban, (n.d.). https://www.microban.com/ (accessed October 7, 2021).

[128] Silver-base inorganic antimicrobial agent “Zeomic”. Sinanen Zeomic Co., Ltd., (n.d.). https://www.zeomic.co.jp/en/product/zeomic/index.html (accessed October 7, 2021).

[129] P. Scarfato, E. Avallone, L. Incarnato, L. Di Maio, Development and evaluation of halloysite nanotube-based carrier for biocide activity in construction materials protection, Appl. Clay Sci. 132–133 (2016) 336–342. doi:10.1016/j.clay.2016.06.027.

[130] M. del Del Sagrario Martínez, Desarrollo de nuevos morteros de reparación resistentes al ataque biológico. Empleo de la sepiolita como material soporte de los biocidas, Universidad Complutense de Madrid, 1995.

[131] S. Martínez-Ramírez, F. Puertas, M.T.B. Varela, Carbonation process and properties of a new lime mortar with added sepiolite, Cem. Concr. Res. 25 (1995) 39–50. doi:10.1016/0008-8846(94)00110-K.

[132] S. Martinez-Ramirez, F. Puertas Maroto, M.T. Blanco Varela, Morteros de reparación basados en cal. Ensayos de envejecimiento acelerado, Mater. Construcción. 45 (1995) 35–45. http://materconstrucc.revistas.csic.es.

[133] S. Martinez-Ramirez, F. Puertas, M.T. Blanco-Varela, G.E. Thompson, Effect of dry deposition of pollutants on the degadation of lime mortals with sepiolite., Cem. Concr. Res. 28 (1998) 125–133.

[134] S. Martínez-Ramírez, F. Puertas, M.T. Blanco-Varela, G.E. Thompson, P. Almendros, Behaviour of Repair Lime Mortars by Wet Deposition Process, Cem. Concr. Res. 28 (1998) 221–229. doi:10.1016/S0008-8846(97)00262-7.

[135] L.B. Fitaroni, T. Venâncio, F.H. Tanaka, J.C.F. Gimenez, J.A.S. Costa, S.A. Cruz, Organically modified sepiolite: Thermal treatment and chemical and morphological properties, Appl. Clay Sci. 179 (2019) 105149. doi:10.1016/J.CLAY.2019.105149.

[136] J. Wu, Y. Wang, Z. Wu, Y. Gao, X. Li, Adsorption properties and mechanism of sepiolite modified by anionic and cationic surfactants on oxytetracycline from aqueous solutions, Sci. Total Environ. 708 (2020) 134409. doi:10.1016/J.SCITOTENV.2019.134409.

[137] J. Eversdijk, S.J.F. Erich, S.P.M. Hermanns, O.C.G. Adan, M. De Bolle, K. De Meyer, D. Bylemans, M. Bekker, A.T. Ten Cate, Development and evaluation of a biocide release system for prolonged antifungal activity in finishing materials, Prog. Org. Coatings. 74 (2012) 640–644. doi:10.1016/j.porgcoat.2011.09.029.

[138] A.M. Forster, Building conservation philosophy for masonry repair: part 2 – “principles,” Struct. Surv. 28 (2010) 165–188. doi:10.1108/02630801011058906.

[139] La importancia de los morteros de cal para la mínima intervención en la rehabilitación - Infoconstrucción, (2020). https://www.infoconstruccion.es/noticias/20200424/anfapa-cal-rehabilitacion (accessed October 7, 2021).

[140] K.A. Gour, R. Ramadoss, T. Selvaraj, Revamping the traditional air lime mortar using the natural polymer – Areca nut for restoration application, Constr. Build. Mater. 164 (2018) 255–264. doi:10.1016/J.CONBUILDMAT.2017.12.056.

[141] B. Yildizlar, B. Sayin, C. Akcay, A Case Study on the Restoration of A Historical Masonry Building Based on Field Studies and Laboratory Analyses, Int. J. Archit. Herit. 14 (2020) 1341–1359. doi:10.1080/15583058.2019.1607625.

[142] Asociación Española de Normalización, UNE 41807:2012 IN .

Reparación de revocos de morteros., (2012). https://www.une.org/encuentra-tu-norma/busca-tu-norma/norma?c=N0050001 (accessed October 7, 2021).

[143] Morcem® Cal Porógeno R. Grupo Puma, (n.d.). https://www.grupopuma.com/es-ES/productos/ver/morcem-cal-porgeno-r-es-es (accessed October 7, 2021).

[144] T. Oates, Lime and Limestone, Kirk-Othmer Encycl. Chem. Technol. (2002). doi:https://doi.org/10.1002/0471238961.1209130507212019.a01.pub2.

[145] M.A. Oliveira, M. Azenha, P.B. Lourenço, A. Meneghini, E.T. Guimarães, F. Castro, D. Soares, Experimental analysis of the carbonation and humidity diffusion processes in aerial lime mortar, Constr. Build. Mater. 148 (2017) 38–48. doi:10.1016/J.CONBUILDMAT.2017.04.120.

[146] J. Grilo, P. Faria, R. Veiga, A. Santos Silva, V. Silva, A. Velosa, New natural hydraulic lime mortars – Physical and microstructural properties in different curing conditions, Constr. Build. Mater. 54 (2014) 378–384. doi:10.1016/J.CONBUILDMAT.2013.12.078.

[147] H.B.T.-B.M. in C.E. Zhang, ed., 3 - Air Hardening Binding Materials, in: Woodhead Publ. Ser. Civ. Struct. Eng., Woodhead Publishing, 2011: pp. 29–423. doi:https://doi.org/10.1533/9781845699567.29.

[148] R.P.J. van Hees, L. Binda, I. Papayianni, E. Toumbakari, Characterisation and damage analysis of old mortars, Mater. Struct. 37 (2004) 644–648. doi:10.1007/BF02483293.

[149] Ministerio para la Transición Ecológica y el Reto Demográfico (Gobierno de España), Contam. Glosario Términos. (n.d.). https://www.miteco.gob.es/es/calidad-y-evaluacion-ambiental/temas/atmosfera-y-calidad-del-aire/Cap7_Glosario_tcm30-183391.pdf (accessed October 7, 2021).

[150] X. Querol, J. Massagué, A. Alastuey, T. Moreno, G. Gangoiti, E. Mantilla, J.J. Duéguez, M. Escudero, E. Monfort, C. Pérez García-Pando, H. Petetin, O. Jorba, V. Vázquez, J. de la Rosa, A. Campos, M. Muñóz, S. Monge, M. Hervás, R. Javato, M.J. Cornide, Lessons from the COVID-19 air pollution decrease in Spain: Now what?, Sci. Total Environ. 779 (2021) 146380. doi:10.1016/J.SCITOTENV.2021.146380.

[151] F. Dutheil, J.S. Baker, V. Navel, COVID-19 as a factor influencing air pollution?, Environ. Pollut. 263 (2020) 114466. doi:10.1016/J.ENVPOL.2020.114466.

[152] Then and now: Pandemic clears the air - BBC News, (n.d.). https://www.bbc.co.uk/news/science-environment-57149747 (accessed October 7, 2021).

[153] Informe Brundtland. Naciones Unidas, (1987). https://undocs.org/es/A/42/427 (accessed October 7, 2021).

[154] Ambient (outdoor) air pollution. World Health Organization, (n.d.). https://www.who.int/news-room/fact-sheets/detail/ambient-(outdoor)-air-quality-and-health (accessed October 7, 2021).

[155] E. von Schneidemesser, K. Steinmar, E.C. Weatherhead, B. Bonn, H. Gerwig, J. Quedenau, Air pollution at human scales in an urban environment: Impact of local environment and vehicles on particle number concentrations, Sci. Total Environ. 688 (2019) 691–700. doi:10.1016/J.SCITOTENV.2019.06.309.

[156] R. Peters, N. Ee, J. Peters, A. Booth, I. Mudway, K.J. Anstey, Air Pollution and Dementia: A Systematic Review, J. Alzheimer's Dis. 70 (2019) S145–S163. doi:10.3233/JAD-180631.

[157] B. Bekkar, S. Pacheco, R. Basu, N. DeNicola, Association of Air Pollution and Heat Exposure With Preterm Birth, Low Birth Weight, and Stillbirth in the US: A Systematic Review, JAMA Netw. Open. 3 (2020) e208243–e208243. doi:10.1001/jamanetworkopen.2020.8243.

[158] M. Yang, H. Cheng, C. Shen, J. Liu, H. Zhang, J. Cao, R. Ding, Effects of long-term exposure to air pollution on the incidence of type 2 diabetes mellitus: a meta-analysis of cohort studies, Environ. Sci. Pollut. Res. 27 (2020) 798–811. doi:10.1007/s11356-019-06824-1.

[159] Road traffic injuries. World Health Organization, (n.d.). https://www.who.int/news-room/fact-sheets/detail/road-traffic-injuries (accessed October 7, 2021).

[160] Health matters: air pollution - UK Government, (n.d.). https://www.gov.uk/government/publications/health-matters-air-pollution/health-matters-air-pollution#call-to-action-reducing-air-pollution (accessed October 7, 2021).

[161] D. Vallero, Fundamentals of Air Pollution, Academic Press, Boston,

2014. doi:https://doi.org/10.1016/B978-0-12-401733-7.01001-X.

[162] F.H. Haynie, J.W. Spence, Air Pollution Damage to Exterior Household Paints, J. Air Pollut. Control Assoc. 34 (1984) 941–944. doi:10.1080/00022470.1984.10465840.

[163] T. Grøntoft, A. Verney-Carron, J. Tidblad, Cleaning Costs for European Sheltered White Painted Steel and Modern Glass Surfaces Due to Air Pollution Since the Year 2000, Atmosphere (Basel). 10 (2019). doi:10.3390/atmos10040167.

[164] P. Spezzano, Mapping the susceptibility of UNESCO World Cultural Heritage sites in Europe to ambient (outdoor) air pollution, Sci. Total Environ. 754 (2021) 142345. doi:10.1016/J.SCITOTENV.2020.142345.

[165] F. Popescu, I. Ionel, Anthropogenic air pollution sources, Air Qual. (2010) 1–22.

[166] Air pollution sources. European Environment Agency, (n.d.). https://www.eea.europa.eu/themes/air/air-pollution-sources-1 (accessed October 7, 2021).

[167] S.R. A., A. Zachariah, F.M. M., W.J. Jason, The Impact of Individual Anthropogenic Emissions Sectors on the Global Burden of Human Mortality due to Ambient Air Pollution, Environ. Health Perspect. 124 (2016) 1776–1784. doi:10.1289/EHP177.

[168] K.J. Maji, W.F. Ye, M. Arora, S.M.S. Nagendra, Ozone pollution in Chinese cities: Assessment of seasonal variation, health effects and economic burden, Environ. Pollut. 247 (2019) 792–801. doi:10.1016/J.ENVPOL.2019.01.049.

[169] D. Nuvolone, D. Petri, F. Voller, The effects of ozone on human health, Environ. Sci. Pollut. Res. 25 (2018) 8074–8088. doi:10.1007/s11356-017-9239-3.

[170] A. Kansal, Sources and reactivity of NMHCs and VOCs in the atmosphere: A review, J. Hazard. Mater. 166 (2009) 17–26. doi:10.1016/j.jhazmat.2008.11.048.

[171] J. Gale, J. Davison, Transmission of CO_2—safety and economic considerations, Energy. 29 (2004) 1319–1328. doi:10.1016/J.ENERGY.2004.03.090.

[172] K. Skalska, J.S. Miller, S. Ledakowicz, Trends in NO_x abatement: A

review, Sci. Total Environ. 408 (2010) 3976–3989. doi:10.1016/j.scitotenv.2010.06.001.

[173] C.D. Koolen, G. Rothenberg, Air Pollution in Europe, ChemSusChem. 12 (2019) 164–172. doi:https://doi.org/10.1002/cssc.201802292.

[174] G. D'Amato, L. Cecchi, M. D'amato, G. Liccardi, Urban air pollution and climate change as environmental risk factors of respiratory allergy: an update, J. Investig. Allergol. Clin. Immunol. 20 (2010) 95–102.

[175] Evaluación de la calidad de aire en España Año 2020, 2020.

[176] Guías de calidad del aire de la OMS relativas al material particulado, el ozono, el dióxido de nitrógeno y el dióxido de azufre. , 2005. https://apps.who.int/iris/bitstream/handle/10665/69478/WHO_SDE_PHE_OEH_06.02_spa.pdf;jsessionid=568942180BC3EDA6BC120210C1B3DB9E?sequence=1 (accessed October 7, 2021).

[177] S. Khomenko, M. Cirach, E. Pereira-Barboza, N. Mueller, J. Barrera-Gómez, D. Rojas-Rueda, K. de Hoogh, G. Hoek, M. Nieuwenhuijsen, Premature mortality due to air pollution in European cities: a health impact assessment, Lancet Planet. Heal. 5 (2021) e121–e134. doi:10.1016/S2542-5196(20)30272-2.

[178] M.A.K. Khalil, Steady states and transport processes in urban ozone balances, Npj Clim. Atmos. Sci. 1 (2018) 22. doi:10.1038/s41612-018-0035-7.

[179] H.S. Kenagy, T.L. Sparks, C.J. Ebben, P.J. Wooldrige, F.D. Lopez-Hilfiker, B.H. Lee, J.A. Thornton, E.E. McDuffie, D.L. Fibiger, S.S. Brown, D.D. Montzka, A.J. Weinheimer, J.C. Schroder, P. Campuzano-Jost, D.A. Day, J.L. Jimenez, J.E. Dibb, T. Campos, V. Shah, L. Jaeglé, R.C. Cohen, NO_x Lifetime and NO_y Partitioning During WINTER, J. Geophys. Res. Atmos. 123 (2018) 9813–9827. doi:https://doi.org/10.1029/2018JD028736.

[180] P. Pancholi, A. Kumar, D.S. Bikundia, S. Chourasiya, An observation of seasonal and diurnal behavior of O_3–NO_x relationships and local/regional oxidant ($O_X = O_3 + NO_2$) levels at a semi-arid urban site of western India, Sustain. Environ. Res. 28 (2018) 79–89. doi:10.1016/J.SERJ.2017.11.001.

[181] European Environment Agency (EEA), Air quality in Europe - 2020 report, 2020. https://www.eea.europa.eu//publications/air-

quality-in-europe-2020-report.

[182] M. Kampa, E. Castanas, Human health effects of air pollution, Environ. Pollut. 151 (2008) 362–367. doi:10.1016/j.envpol.2007.06.012.

[183] Nitrogen Dioxide (NO_2) Pollution. United States Environmental Protection Agency, (n.d.). https://www.epa.gov/no2-pollution/basic-information-about-no2#Effects (accessed October 7, 2021).

[184] La contaminación causó 38.600 muertes en España en 2015, una subida del 23% . EL PAÍS, (2018). https://elpais.com/sociedad/2018/10/29/actualidad/1540813829_874914.html (accessed October 7, 2021).

[185] Y. Bai, G.E. Thompson, S. Martinez-Ramirez, Effects of NO_2 on oxidation mechanisms of atmospheric pollutant SO_2 over Baumberger sandstone, Build. Environ. 41 (2006) 486–491. doi:10.1016/J.BUILDENV.2005.02.007.

[186] G.H. Kerr, D.L. Goldberg, S.C. Anenberg, COVID-19 pandemic reveals persistent disparities in nitrogen dioxide pollution, Proc. Natl. Acad. Sci. 118 (2021) e2022409118. doi:10.1073/pnas.2022409118.

[187] I.P. Fernández, Tecnologías de reducción de contaminantes en procesos termoenergéticos: eliminación de partículas, eliminación de óxidos de azufre, reducción de emisiones de óxidos de nitrógeno, precipitadores electrostáticos: curso, Universidad de Oviedo, 1994.

[188] F. Lin, Z. Wang, Z. Zhang, Y. He, Y. Zhu, J. Shao, D. Yuan, G. Chen, K. Cen, Flue gas treatment with ozone oxidation: An overview on NO_x, organic pollutants, and mercury, Chem. Eng. J. 382 (2020) 123030. doi:10.1016/J.CEJ.2019.123030.

[189] A.A. Abdulrasheed, A.A. Jalil, S. Triwahyono, M.A.A. Zaini, Y. Gambo, M. Ibrahim, Surface modification of activated carbon for adsorption of SO_2 and NO_x: A review of existing and emerging technologies, Renew. Sustain. Energy Rev. 94 (2018) 1067–1085. doi:10.1016/J.RSER.2018.07.011.

[190] J.R. González-Velasco, B. Pereda-Ayo, U. De-La-Torre, M. Urrutxua, R. López-Fonseca, NO_x Storage and Reduction Coupled with Selective Catalytic Reduction for NO_x Removal in Light-Duty Vehicles, ChemCatChem. 10 (2018) 2928–2940.

doi:10.1002/CCTC.201800392.

[191] A. FUJISHIMA, K. HONDA, Electrochemical Photolysis of Water at a Semiconductor Electrode, Nature. 238 (1972) 37–38. doi:10.1038/238037a0.

[192] A. Eibner, Action of light on pigments I, Chem-Ztg. 35 (1911) 753–755.

[193] L. Bruner, J. Kozak, Information on the photocatalysis I the light reaction in uranium salt plus oxalic acid mixtures, Z. Elktrochem. Angew. Phys. Chem. 17 (1911) 354–360.

[194] M. Landau, Le Phénomène de la Photocatalyse, Comptes Rendus Chim. (1913) 1894–1896.

[195] P. Atkins, T. Overton, Shriver and Atkins' inorganic chemistry, Oxford University Press, USA, 2010.

[196] J.M. Coronado, Photons, electrons and holes: fundamentals of photocatalysis with semiconductors, in: Des. Adv. Photocatalytic Mater. Energy Environ. Appl., Springer, 2013: pp. 5–33.

[197] A.R. West, Solid state chemistry and its applications, John Wiley & Sons, 2014.

[198] J.M. Coronado, F. Fresno, M.D. Hernández-Alonso, R. Portela, Design of advanced photocatalytic materials for energy and environmental applications, Springer, 2013.

[199] S.A. Holgate, Understanding solid state physics, CRC Press, 2021.

[200] M.R. Hoffmann, S.T. Martin, W. Choi, D.W. Bahnemann, Environmental applications of semiconductor photocatalysis, Chem. Rev. 95 (1995) 69–96.

[201] Y. Tamaki, A. Furube, M. Murai, K. Hara, R. Katoh, M. Tachiya, Dynamics of efficient electron–hole separation in TiO_2 nanoparticles revealed by femtosecond transient absorption spectroscopy under the weak-excitation condition, Phys. Chem. Chem. Phys. 9 (2007) 1453–1460. doi:10.1039/B617552J.

[202] M.A. Henderson, A surface science perspective on TiO_2 photocatalysis, Surf. Sci. Rep. 66 (2011) 185–297. doi:10.1016/J.SURFREP.2011.01.001.

[203] T.L. Thompson, J.T. Yates, Surface Science Studies of the

Photoactivation of TiO_2 - New Photochemical Processes, Chem. Rev. 106 (2006) 4428–4453. doi:10.1021/cr050172k.

[204] K.E. O'Shea, D.D. Dionysiou, Advanced oxidation processes for water treatment, (2012).

[205] H. Tong, S. Ouyang, Y. Bi, N. Umezawa, M. Oshikiri, J. Ye, Nano-photocatalytic Materials: Possibilities and Challenges, Adv. Mater. 24 (2012) 229–251. doi:https://doi.org/10.1002/adma.201102752.

[206] M.N. Chong, B. Jin, C.W.K. Chow, C. Saint, Recent developments in photocatalytic water treatment technology: A review, Water Res. 44 (2010) 2997–3027. doi:10.1016/J.WATRES.2010.02.039.

[207] V. Nguyen, J. Che-Chin Yu, C. Huang, J.C.-S. Wu, Recent advances in the development of photocatalytic NO_x abatement, in: Curr. Dev. Photocatal. Photocatalytic Mater., Elsevier, 2020: pp. 211–229. doi:10.1016/B978-0-12-819000-5.00014-X.

[208] J.Z. Bloh, A. Folli, D.E. Macphee, Photocatalytic NO_x abatement: Why the selectivity matters, RSC Adv. 4 (2014) 45726–45734. doi:10.1039/c4ra07916g.

[209] J. Balbuena, M. Cruz-Yusta, L. Sánchez, Nanomaterials to Combat NO_x Pollution, J. Nanosci. Nanotechnol. 15 (2015) 6373–6385. doi:10.1166/jnn.2015.10871.

[210] R.J.L. N.I. Sax, Sax's Dangerous Properties of Industrial Materials, 12th ed, Van Nostrand Reinhold, New York, 2012.

[211] M. Cruz-Yusta, M. Sánchez, L. Sánchez, Metal oxide nanomaterials for nitrogen oxides removal in urban environments - Chapter 7, in: D. Barreca, C. Maccato (Eds.), Tailored Funct. Oxide Nanomater. From Des. to Multi-Purpose Appl., Wiley-VCH, n.d.

[212] M. Kaneko, I. Okura, Photocatalysis: science and technology, Springer, 2002.

[213] K. Hadjiivanov, H. Knözinger, Species formed after NO adsorption and $NO+O_2$ co-adsorption on TiO_2: an FTIR spectroscopic study, Phys. Chem. Chem. Phys. 2 (2000) 2803–2806. doi:10.1039/B002065F.

[214] Y. Bedjanian, A. El Zein, Interaction of NO_2 with TiO_2 Surface Under UV Irradiation: Products Study, J. Phys. Chem. A. 116 (2012) 1758–1764. doi:10.1021/jp210078b.

[215] A.L. Goodman, G.M. Underwood, V.H. Grassian, Heterogeneous Reaction of NO_2 : Characterization of Gas-Phase and Adsorbed Products from the Reaction, $2NO_2$ (g) + H_2O(a) → HONO(g) + HNO_3 (a) on Hydrated Silica Particles, J. Phys. Chem. A. 103 (1999) 7217–7223. doi:10.1021/jp9910688.

[216] K.A. Ramazan, D. Syomin, B.J. Finlayson-Pitts, The photochemical production of HONO during the heterogeneous hydrolysis of NO_2, Phys. Chem. Chem. Phys. 6 (2004) 3836–3843. doi:10.1039/B402195A.

[217] B.J. Finlayson-Pitts, Reactions at surfaces in the atmosphere: integration of experiments and theory as necessary (but not necessarily sufficient) for predicting the physical chemistry of aerosols, Phys. Chem. Chem. Phys. 11 (2009) 7760–7779. doi:10.1039/B906540G.

[218] Q.L. Yu, H.J.H. Brouwers, Indoor air purification using heterogeneous photocatalytic oxidation. Part I: Experimental study, Appl. Catal. B Environ. 92 (2009) 454–461. doi:10.1016/j.apcatb.2009.09.004.

[219] O. Rosseler, M. Sleiman, V.N. Montesinos, A. Shavorskiy, V. Keller, N. Keller, M.I. Litter, H. Bluhm, M. Salmeron, H. Destaillats, Chemistry of NO_x on TiO_2 Surfaces Studied by Ambient Pressure XPS: Products, Effect of UV Irradiation, Water, and Coadsorbed K^+, J. Phys. Chem. Lett. 4 (2013) 536–541. doi:10.1021/jz302119g.

[220] S.-C. Li, P. Jacobson, S.-L. Zhao, X.-Q. Gong, U. Diebold, Trapping Nitric Oxide by Surface Hydroxyls on Rutile TiO_2(110), J. Phys. Chem. C. 116 (2012) 1887–1891. doi:10.1021/jp209290a.

[221] L. Yang, A. Hakki, F. Wang, D.E. Macphee, Different Roles of Water in Photocatalytic DeNO_x Mechanisms on TiO_2: Basis for Engineering Nitrate Selectivity?, ACS Appl. Mater. Interfaces. 9 (2017) 17034–17041. doi:10.1021/acsami.7b01989.

[222] R. Portela, M.D. Hernández-Alonso, Environmental applications of photocatalysis, in: Des. Adv. Photocatalytic Mater. Energy Environ. Appl., Springer, 2013: pp. 35–66.

[223] G. Jiang, J. Cao, M. Chen, X. Zhang, F. Dong, Photocatalytic NO oxidation on N-doped TiO_2/g-C_3N_4 heterojunction: Enhanced efficiency, mechanism and reaction pathway, Appl. Surf. Sci. 458 (2018) 77–85. doi:10.1016/J.APSUSC.2018.07.087.

[224] Y. Lu, Y. Huang, Y. Zhang, T. Huang, H. Li, J. ji Cao, W. Ho, Effects of H_2O_2 generation over visible light-responsive $Bi/Bi_2O_{2-x}CO_3$ nanosheets on their photocatalytic NO_x removal performance, Chem. Eng. J. 363 (2019) 374–382. doi:10.1016/j.cej.2019.01.172.

[225] Y. Zhou, Z. Zhao, F. Wang, K. Cao, D.E. Doronkin, F. Dong, J.D. Grunwaldt, Facile synthesis of surface N-doped $Bi_2O_2CO_3$: Origin of visible light photocatalytic activity and in situ DRIFTS studies, J. Hazard. Mater. 307 (2016) 163–172. doi:10.1016/J.JHAZMAT.2015.12.072.

[226] J. Liao, W. Cui, J. Li, J. Sheng, H. Wang, X. Dong, P. Chen, G. Jiang, Z. Wang, F. Dong, Nitrogen defect structure and NO+ intermediate promoted photocatalytic NO removal on H_2 treated g-C_3N_4, Chem. Eng. J. 379 (2020) 122282. doi:10.1016/j.cej.2019.122282.

[227] W. Cui, L. Chen, J. Li, Y. Zhou, Y. Sun, G. Jiang, S.C. Lee, F. Dong, Ba-vacancy induces semiconductor-like photocatalysis on insulator $BaSO_4$, Appl. Catal. B Environ. 253 (2019) 293–299. doi:10.1016/j.apcatb.2019.04.070.

[228] W. Cui, J. Li, F. Dong, Y. Sun, G. Jiang, W. Cen, S.C. Lee, Z. Wu, Highly Efficient Performance and Conversion Pathway of Photocatalytic NO Oxidation on SrO-Clusters@Amorphous Carbon Nitride, Environ. Sci. Technol. 51 (2017) 10682–10690. doi:10.1021/acs.est.7b00974.

[229] W. Cui, J. Li, W. Cen, Y. Sun, S.C. Lee, F. Dong, Steering the interlayer energy barrier and charge flow via bioriented transportation channels in g-C_3N_4: Enhanced photocatalysis and reaction mechanism, J. Catal. 352 (2017) 351–360. doi:10.1016/J.JCAT.2017.05.017.

[230] J. Chen, C. sun Poon, Photocatalytic construction and building materials: From fundamentals to applications, Build. Environ. 44 (2009) 1899–1906. doi:10.1016/J.BUILDENV.2009.01.002.

[231] L.P. Singh, R.K. Dhaka, D. Ali, I. Tyagi, U. Sharma, S.N. Banavath, Remediation of noxious pollutants using nano-titania-based photocatalytic construction materials: a review, Environ. Sci. Pollut. Res. 28 (2021) 34087–34107. doi:10.1007/s11356-021-14189-7.

[232] F. Hamidi, F. Aslani, TiO_2-based Photocatalytic Cementitious Composites: Materials, Properties, Influential Parameters, and Assessment Techniques, Nanomaterials. 9 (2019). doi:10.3390/nano9101444.

[233] A.-I. Gopalan, J.-C. Lee, G. Saianand, K.-P. Lee, P. Sonar, R. Dharmarajan, Y. Hou, K.-Y. Ann, V. Kannan, W.-J. Kim, Recent Progress in the Abatement of Hazardous Pollutants Using Photocatalytic TiO_2-Based Building Materials, Nanomaterials. 10 (2020). doi:10.3390/nano10091854.

[234] C. Pei, J.H. Zhu, F. Xing, Photocatalytic property of cement mortars coated with graphene/TiO_2 nanocomposites synthesized via sol–gel assisted electrospray method, J. Clean. Prod. 279 (2021) 123590. doi:10.1016/J.JCLEPRO.2020.123590.

[235] TX Active Cement - Lehigh Hanson, Inc., (n.d.). https://www.lehighhanson.com/products/cement/tx-active (accessed October 8, 2021).

[236] TioCem® - Hanson UK, (n.d.). https://www.hanson.co.uk/system/files_force/assets/document/hanson-tiocem.pdf?download=1 (accessed October 8, 2021).

[237] Morcemsec® Active Proyectable CR CSIV W2 - Cladding mortars. Grupo Puma, (n.d.). https://www.grupopuma.com/en-WW/products/show/morcemsec-active-proyectable-cr-csiv-w2-ww-en-1 (accessed October 8, 2021).

[238] Photocatalytic Paving blocks | Archiproducts, (n.d.). https://www.archiproducts.com/en/products/paving-blocks/photocatalytic (accessed October 8, 2021).

[239] Pilkington Activ™ Range, (n.d.). https://www.pilkington.com/en-gb/uk/products/product-categories/self-cleaning/pilkington-activ-range (accessed October 8, 2021).

[240] Reynobond ® with EcoClean ™ Powered by HYDROTECT ™, (n.d.). https://altechpanel.com/Prods/EcoClean_Brochure.pdf (accessed October 8, 2021).

[241] KEIM. Mineral Paints – The photocatalytic difference, (n.d.). https://www.keim.com/fileadmin/user_upload/download-center/uk/product-brochures/mini-brochures/Photocatalytic_Difference_-_Technical_Information.pdf (accessed October 8, 2021).

[242] Pinturas fotocataliticas - MYPHOR Materiales Especiales, S.L., (n.d.). https://www.myphor.com/pinturasfotocataliticas/ (accessed October 8, 2021).

[243] R. Sugrañez, J.I. Álvarez, M. Cruz-Yusta, I. Mármol, J. Morales, J. Vila, L. Sánchez, Enhanced photocatalytic degradation of NO_x gases by regulating the microstructure of mortar cement modified with titanium dioxide, Build. Environ. 69 (2013) 55–63. doi:10.1016/J.BUILDENV.2013.07.014.

[244] M.F. La Russa, N. Rovella, M. Alvarez De Buergo, C.M. Belfiore, A. Pezzino, G.M. Crisci, S.A. Ruffolo, Nano-TiO_2 coatings for cultural heritage protection: The role of the binder on hydrophobic and self-cleaning efficacy, Prog. Org. Coatings. 91 (2016) 1–8. doi:10.1016/J.PORGCOAT.2015.11.011.

[245] F. Salvadores, O.M. Alfano, M.M. Ballari, Kinetic study of air treatment by photocatalytic paints under indoor radiation source: Influence of ambient conditions and photocatalyst content, Appl. Catal. B Environ. 268 (2020) 118694. doi:10.1016/J.APCATB.2020.118694.

[246] M.M. Ballari, H.J.H. Brouwers, Full scale demonstration of air-purifying pavement, J. Hazard. Mater. 254–255 (2013) 406–414. doi:10.1016/J.JHAZMAT.2013.02.012.

[247] E. Boonen, A. Beeldens, Recent Photocatalytic Applications for Air Purification in Belgium, Coatings . 4 (2014). doi:10.3390/coatings4030553.

[248] E. Jiménez-Relinque, R. Hingorani, F. Rubiano, M. Grande, Á. Castillo, M. Castellote, In situ evaluation of the NO_x removal efficiency of photocatalytic pavements: statistical analysis of the relevance of exposure time and environmental variables, Environ. Sci. Pollut. Res. 26 (2019) 36088–36095. doi:10.1007/s11356-019-04322-y.

[249] P.D. Pedersen, N. Lock, H. Jensen, Removing NO_x Pollution by Photocatalytic Building Materials in Real-Life: Evaluation of Existing Field Studies, J. Photocatal. 2 (2021) 84–96.

[250] Un edificio de cemento que devora la contaminación - EL PAÍS, (n.d.). https://elpais.com/cultura/2012/04/24/actualidad/1335290393_194683.html (accessed October 8, 2021).

[251] I.B. Topçu, E. Akkan, T. Uygunoğlu, K. Çalişkan, Self-Cleaning Concretes: An Overview, J. Cem. Based Compos. 1 (2020) 6–12. doi:10.36937/cebacom.2020.002.002.

[252] Pabellón Real Madrid Arena | FYM, (n.d.). https://www.fym.es/es/pabellon-real-madrid-arena (accessed October 8, 2021).

[253] Edificio Santa Lucía - Keimfarben, (n.d.). https://www.keim.com/es-es/referencias/vista-en-detalle/edificio-santa-lucia/ (accessed October 8, 2021).

[254] Air Quality Expert Group. Paints and Surfaces for the Removal of Nitrogen Oxides, 2016. https://uk-air.defra.gov.uk/assets/documents/reports/cat11/1604130958_PB14425_Paints_and_Surfaces_for_the_Removal_of_Nitrogen_Oxides.pdf (accessed October 10, 2021).

[255] L. Yang, A. Hakki, F. Wang, D.E. Macphee, Photocatalyst efficiencies in concrete technology: The effect of photocatalyst placement, Appl. Catal. B Environ. 222 (2018) 200–208. doi:10.1016/J.APCATB.2017.10.013.

[256] H.S. Russell, L.B. Frederickson, O. Hertel, T. Ellermann, S.S. Jensen, A Review of Photocatalytic Materials for Urban NO_x Remediation, Catalysts. 11 (2021). doi:10.3390/catal11060675.

[257] P.J.M. Bartos, Editorial: Photocatalytic concrete, Http://Dx.Doi.Org/10.1680/Macr.13.00298. 66 (2015) 217–218. doi:10.1680/MACR.13.00298.

[258] Evonik Industries - Aeroxide® TiO_2 P25, (n.d.). https://corporate.evonik.com/en/products/search-products/pages/product-details.aspx?productId=43469 (accessed October 10, 2021).

[259] B. Ohtani, O.O. Prieto-Mahaney, D. Li, R. Abe, What is Degussa (Evonik) P25? Crystalline composition analysis, reconstruction from isolated pure particles and photocatalytic activity test, J. Photochem. Photobiol. A Chem. 216 (2010) 179–182. doi:10.1016/J.JPHOTOCHEM.2010.07.024.

[260] J. Ma, H. Wu, Y. Liu, H. He, Photocatalytic removal of NO_x over visible light responsive oxygen-deficient TiO_2, J. Phys. Chem. C. 118 (2014) 7434–7441. doi:10.1021/jp500116n.

[261] H. Ren, P. Koshy, W.F. Chen, S. Qi, C.C. Sorrell, Photocatalytic materials and technologies for air purification, J. Hazard. Mater. 325 (2017) 340–366. doi:10.1016/J.JHAZMAT.2016.08.072.

[262] A. Folli, J.Z. Bloh, M. Strøm, T.P. Madsen, T. Henriksen, D.E. Macphee, Efficiency of Solar-Light-Driven TiO_2 Photocatalysis at Different Latitudes and Seasons. Where and When Does TiO_2 Really Work?, J. Phys. Chem. Lett. 5 (2014) 830–832. doi:10.1021/JZ402704N.

[263] T. Martinez, A. Bertron, E. Ringot, G. Escadeillas, Degradation of NO using photocatalytic coatings applied to different substrates, Build. Environ. 46 (2011) 1808–1816. doi:10.1016/j.buildenv.2011.03.001.

[264] A. Folli, M. Strøm, T.P. Madsen, T. Henriksen, J. Lang, J. Emenius, T. Klevebrant, Å. Nilsson, Field study of air purifying paving elements containing TiO_2, Atmos. Environ. 107 (2015) 44–51. doi:10.1016/J.ATMOSENV.2015.02.025.

[265] W. Fan, K.Y. Chan, C. Zhang, K. Zhang, Z. Ning, M.K.H. Leung, Solar photocatalytic asphalt for removal of vehicular NO_x: A feasibility study, Appl. Energy. 225 (2018) 535–541. doi:10.1016/J.APENERGY.2018.04.134.

[266] J. Kerrod, R. Mcintyre, The Effectiveness of CristalACTiV™ for Depollution in Tunnels with Low Levels of Light, Lincolnshire (United Kingdom), 2014. https://www.cristalactiv.com/wp-content/uploads/2021/02/Tronox-case-study-Konningstunnel-Trial.pdf (accessed October 10, 2021).

[267] V.H. Nguyen, B.S. Nguyen, C.W. Huang, T.T. Le, C.C. Nguyen, T.T. Nhi Le, D. Heo, Q.V. Ly, Q.T. Trinh, M. Shokouhimehr, C. Xia, S.S. Lam, D.V.N. Vo, S.Y. Kim, Q. Van Le, Photocatalytic NO_x abatement: Recent advances and emerging trends in the development of photocatalysts, J. Clean. Prod. 270 (2020) 121912. doi:10.1016/J.JCLEPRO.2020.121912.

[268] European Union law - Document 32020R0217, 2019. https://eur-lex.europa.eu/legal-content/EN/TXT/?uri=uriserv:OJ.L_.2020.044.01.0001.01.ENG&toc=OJ:L:2020:044:TOC (accessed July 5, 2021).

[269] D. He, Y. Li, I. Wang, J. Wu, Y. Yang, Q. An, Carbon wrapped and doped TiO_2 mesoporous nanostructure with efficient visible-light photocatalysis for NO removal, Appl. Surf. Sci. 391 (2017) 318–325. doi:10.1016/j.apsusc.2016.06.186.

[270] A. Martinez-Oviedo, S.K. Ray, H.P. Nguyen, S.W. Lee, Efficient photo-oxidation of NO_x by Sn doped blue TiO_2 nanoparticles, J. Photochem.

Photobiol. A Chem. 370 (2019) 18–25. doi:10.1016/J.JPHOTOCHEM.2018.10.032.

[271] A. Folli, J.Z. Bloh, K. Armstrong, E. Richards, D.M. Murphy, L. Lu, C.J. Kiely, D.J. Morgan, R.I. Smith, A.C. Mclaughlin, D.E. Macphee, Improving the Selectivity of Photocatalytic NO_x Abatement through Improved O_2 Reduction Pathways Using $Ti_{0.909}W_{0.091}O_2N_x$ Semiconductor Nanoparticles: From Characterization to Photocatalytic, ACS Catal. 8 (2018) 6927–6938. doi:10.1021/ACSCATAL.8B00521.

[272] K. Batalović, N. Bundaleski, J. Radaković, N. Abazović, M. Mitrić, R.A. Silva, M. Savić, J. Belošević-Čavor, Z. Rakočević, C.M. Rangel, Modification of N-doped TiO_2 photocatalysts using noble metals (Pt, Pd) – a combined XPS and DFT study, Phys. Chem. Chem. Phys. 19 (2017) 7062–7071. doi:10.1039/C7CP00188F.

[273] S. Song, Z. Sheng, Y. Liu, H. Wang, Z. Wu, Influences of pH value in deposition-precipitation synthesis process on Pt-doped TiO_2 catalysts for photocatalytic oxidation of NO, J. Environ. Sci. 24 (2012) 1519–1524. doi:10.1016/S1001-0742(11)60980-7.

[274] Y. Hu, X. Song, S. Jiang, C. Wei, Enhanced photocatalytic activity of Pt-doped TiO_2 for NO_x oxidation both under UV and visible light irradiation: A synergistic effect of lattice Pt_{4+} and surface PtO, Chem. Eng. J. 274 (2015) 102–112. doi:10.1016/J.CEJ.2015.03.135.

[275] M.J. Hernández Rodríguez, E. Pulido Melián, D. García Santiago, O. González Díaz, J.A. Navío, J.M. Doña Rodríguez, NO photooxidation with TiO_2 photocatalysts modified with gold and platinum, Appl. Catal. B Environ. 205 (2017) 148–157. doi:10.1016/j.apcatb.2016.12.006.

[276] Z. Hu, K. Li, X. Wu, N. Wang, X. Li, Q. Li, L. Li, K. Lv, Dramatic promotion of visible-light photoreactivity of TiO_2 hollow microspheres towards NO oxidation by introduction of oxygen vacancy, Appl. Catal. B Environ. 256 (2019) 117860. doi:10.1016/J.APCATB.2019.117860.

[277] B. Tan, X. Zhang, Y. Li, H. Chen, X. Ye, Y. Wang, J. Ye, Anatase TiO_2 Mesocrystals: Green Synthesis, In Situ Conversion to Porous Single Crystals, and Self-Doping Ti^{3+} for Enhanced Visible Light Driven Photocatalytic Removal of NO, Chem. – A Eur. J. 23 (2017) 5478–5487. doi:10.1002/chem.201605294.

[278] D. Zhang, G. Li, H. Wang, K.M. Chan, J.C. Yu, Biocompatible Anatase Single-Crystal Photocatalysts with Tunable Percentage of Reactive Facets, Cryst. Growth Des. 10 (2010) 1130–1137. doi:10.1021/cg900961k.

[279] M.-V. Sofianou, C. Trapalis, V. Psycharis, N. Boukos, T. Vaimakis, J. Yu, W. Wang, Study of TiO_2 anatase nano and microstructures with dominant {001} facets for NO oxidation, Environ. Sci. Pollut. Res. 19 (2012) 3719–3726. doi:10.1007/S11356-012-0747-X.

[280] J. Low, J. Yu, M. Jaroniec, S. Wageh, A.A. Al-Ghamdi, Heterojunction Photocatalysts, Adv. Mater. 29 (2017) 1601694. doi:10.1002/ADMA.201601694.

[281] I. Papailias, N. Todorova, T. Giannakopoulou, J. Yu, D. Dimotikali, C. Trapalis, Photocatalytic activity of modified g-C_3N_4/TiO_2 nanocomposites for NO_x removal, Catal. Today. 280 (2017) 37–44. doi:10.1016/J.CATTOD.2016.06.032.

[282] A. Trapalis, N. Todorova, T. Giannakopoulou, N. Boukos, T. Speliotis, D. Dimotikali, J. Yu, TiO_2/graphene composite photocatalysts for NO_x removal: A comparison of surfactant-stabilized graphene and reduced graphene oxide, Appl. Catal. B Environ. 180 (2016) 637–647. doi:10.1016/J.APCATB.2015.07.009.

[283] W. Yang, C. Li, L. Wang, S. Sun, X. Yan, Solvothermal fabrication of activated semi-coke supported TiO_2-rGO nanocomposite photocatalysts and application for NO removal under visible light, Appl. Surf. Sci. 353 (2015) 307–316. doi:10.1016/J.APSUSC.2015.04.140.

[284] T. Zhiltsova., N. Martins, M.R.F. Silva, C.F. Da Silva, M.A.O. Lourenço, D.M. Tobaldi, D. Covita, M.P. Seabra, P. Ferreira, Experimental and Computational Analysis of NO_x Photocatalytic Abatement Using Carbon-Modified TiO_2 Materials, Catalysts. 10 (2020) 1366. doi:10.3390/CATAL10121366.

[285] N. Seifvand, E. Kowsari, Novel TiO_2/graphene oxide functionalized with a cobalt complex for significant degradation of NO_x and CO, RSC Adv. 5 (2015) 93706–93716. doi:10.1039/C5RA13620B.

[286] C.C. Pei, K. Kin Shing Lo, W.W.F. Leung, Titanium-zinc-bismuth oxides-graphene composite nanofibers as high-performance photocatalyst for gas purification, Sep. Purif. Technol. 184 (2017) 205–212. doi:10.1016/J.SEPPUR.2017.04.016.

[287] X. Hu, Y. Wang, Z. Ling, H. Song, Y. Cai, Z. Li, D. Zu, C. Li, Ternary g-C_3N_4/TiO_2/Ti_3C_2 MXene S-scheme heterojunction photocatalysts for NO_x removal under visible light, Appl. Surf. Sci. 556 (2021) 149817. doi:10.1016/J.APSUSC.2021.149817.

[288] M. Balci Leinen, D. Dede, M.U. Khan, M. Çağlayan, Y. Koçak, H.V. Demir, E. Ozensoy, CdTe Quantum Dot-Functionalized P25 Titania Composite with Enhanced Photocatalytic NO_2 Storage Selectivity under UV and Vis Irradiation, ACS Appl. Mater. Interfaces. 11 (2019) 865–879. doi:10.1021/acsami.8b18036.

[289] N.C.T. Martins, J. Ângelo, A.V. Girão, T. Trindade, L. Andrade, A. Mendes, N-doped carbon quantum dots/TiO_2 composite with improved photocatalytic activity, Appl. Catal. B Environ. 193 (2016) 67–74. doi:10.1016/J.APCATB.2016.04.016.

[290] E. Luévano-Hipólito, A. Martínez-De La Cruz, E. López-Cuellar, Q.L. Yu, H.J.H. Brouwers, Synthesis, characterization and photocatalytic activity of WO_3/TiO_2 for NO removal under UV and visible light irradiation, Mater. Chem. Phys. 148 (2014) 208–213. doi:10.1016/J.MATCHEMPHYS.2014.07.034.

[291] N.O. Balayeva, M. Fleisch, D.W. Bahnemann, Surface-grafted WO_3/TiO_2 photocatalysts: Enhanced visible-light activity towards indoor air purification, Catal. Today. 313 (2018) 63–71. doi:10.1016/J.CATTOD.2017.12.008.

[292] L. Wang, L. Zhang, Y. Jiang, P. Li, Morphology Control of Molybdenum Titanium Oxide and Its Enhanced NO Removal Performance, Catal. Lett. 2019 1506. 150 (2019) 1707–1713. doi:10.1007/S10562-019-03076-Z.

[293] Z. Wu, Z. Sheng, Y. Liu, H. Wang, J. Mo, Deactivation mechanism of PtO_x/TiO_2 photocatalyst towards the oxidation of NO in gas phase, J. Hazard. Mater. 185 (2011) 1053–1058. doi:10.1016/J.JHAZMAT.2010.10.013.

[294] S. Zhao, M. Fu, Y. Li, X. Hu, C. Yuan, R. Pan, Facile hydrothermal preparation of a $ZnFe_2O_4$/TiO_2 heterojunction for NO_x removal, Mol. Catal. 507 (2021) 111570. doi:10.1016/J.MCAT.2021.111570.

[295] N. Todorova, T. Giannakopoulou, S. Karapati, D. Petridis, T. Vaimakis, C. Trapalis, Composite TiO_2/clays materials for photocatalytic NO_x oxidation, Appl. Surf. Sci. 319 (2014) 113–120. doi:10.1016/J.APSUSC.2014.07.020.

[296] G. Guo, Y. Hu, S. Jiang, C. Wei, Photocatalytic oxidation of NO_x over TiO_2/HZSM-5 catalysts in the presence of water vapor: Effect of hydrophobicity of zeolites, J. Hazard. Mater. 223–224 (2012) 39–45. doi:10.1016/J.JHAZMAT.2012.04.043.

[297] X.F. Chen, S. run Lin, S.C. Kou, Effect of composite photo-catalysts prepared with recycled clay brick sands and nano-TiO_2 on methyl orange and NO_x removal, Constr. Build. Mater. 171 (2018) 152–160. doi:10.1016/J.CONBUILDMAT.2018.03.099.

[298] Jie Yao, Yufei Zhang, Yawen Wang, Meijuan Chen, Yu Huang, Junji Cao, Wingkei Ho, S. Cheng Lee, Enhanced photocatalytic removal of NO over titania/hydroxyapatite (TiO_2/HAp) composites with improved adsorption and charge mobility ability, RSC Adv. 7 (2017) 24683–24689. doi:10.1039/C7RA02157G.

[299] A.M. Soylu, M. Polat, D.A. Erdogan, Z. Say, C. Yildirim, Ö. Birer, E. Ozensoy, TiO_2-Al_2O_3 binary mixed oxide surfaces for photocatalytic NO_x abatement, Appl. Surf. Sci. (2014) 16–21. doi:10.1016/j.apsusc.2014.02.065.

[300] M. Polat, A.M. Soylu, D. a. Erdogan, H. Erguven, E.I. Vovk, E. Ozensoy, Influence of the sol–gel preparation method on the photocatalytic NO oxidation performance of TiO_2/Al_2O_3 binary oxides, Catal. Today. 241 (2015) 25–32. doi:10.1016/j.cattod.2014.04.001.

[301] M. Çağlayan, M. Irfan, K.E. Ercan, Y. Kocak, E. Ozensoy, Enhancement of photocatalytic NO_x abatement on titania via additional metal oxide NO_x-storage domains: Interplay between surface acidity, specific surface area, and humidity, Appl. Catal. B Environ. 263 (2020) 118227. doi:10.1016/j.apcatb.2019.118227.

[302] M. Luna, J.M. Gatica, H. Vidal, M.J. Mosquera, Use of Au/N-TiO_2/SiO_2 photocatalysts in building materials with NO depolluting activity, J. Clean. Prod. 243 (2020) 118633. doi:10.1016/J.JCLEPRO.2019.118633.

[303] M. Luna, J.M. Gatica, H. Vidal, M.J. Mosquera, Au-TiO_2/SiO_2 photocatalysts with NO_x depolluting activity: Influence of gold particle size and loading, Chem. Eng. J. 368 (2019) 417–427. doi:10.1016/J.CEJ.2019.02.167.

[304] J.H. Kim, J.H. Han, Y.C. Jung, Y.A. Kim, Mussel adhesive protein-coated titanium oxide nanoparticles for effective NO removal from

versatile substrates, Chem. Eng. J. 378 (2019) 122164. doi:10.1016/J.CEJ.2019.122164.

[305] Z. Ma, Y. Wang, Y. Lu, H. Ning, J. Zhang, Tackling Challenges in Perovskite-Type Metal Oxide Photocatalysts, Energy Technol. 9 (2021) 2001019. doi:10.1002/ENTE.202001019.

[306] Q. Zhang, Y. Huang, L. Xu, J. Cao, W. Ho, S.C. Lee, Visible-Light-Active Plasmonic Ag–$SrTiO_3$ Nanocomposites for the Degradation of NO in Air with High Selectivity, ACS Appl. Mater. Interfaces. 8 (2016) 4165–4174. doi:10.1021/ACSAMI.5B11887.

[307] H. Li, S. Yin, Y. Wang, T. Sekino, S.W. Lee, T. Sato, Roles of Cr^{3+} doping and oxygen vacancies in $SrTiO_3$ photocatalysts with high visible light activity for NO removal, J. Catal. 297 (2013) 65–69. doi:10.1016/J.JCAT.2012.09.019.

[308] Q. Zhang, Y. Huang, S. Peng, T. Huang, J. ji Cao, W. Ho, S. Lee, Synthesis of $SrFe_xTi_{1-x}O_{3-\delta}$ nanocubes with tunable oxygen vacancies for selective and efficient photocatalytic NO oxidation, Appl. Catal. B Environ. 239 (2018) 1–9. doi:10.1016/J.APCATB.2018.07.076.

[309] Q. Zhang, Y. Huang, S. Peng, Y. Zhang, Z. Shen, J. Cao, W. Ho, S.C. Lee, D.Y.H. Pui, Perovskite $LaFeO_3$ -$SrTiO_3$ composite for synergistically enhanced NO removal under visible light excitation, Appl. Catal. B Environ. 204 (2017) 346–357. doi:10.1016/j.apcatb.2016.11.052.

[310] S. Jin, G. Dong, J. Luo, F. Ma, C. Wang, Improved photocatalytic NO removal activity of $SrTiO_3$ by using $SrCO_3$ as a new co-catalyst, Appl. Catal. B Environ. 227 (2018) 24–34. doi:10.1016/J.APCATB.2018.01.020.

[311] Z. Ai, G. Lu, S. Lee, Efficient photocatalytic removal of nitric oxide with hydrothermal synthesized $Na_{0.5}Bi_{0.5}TiO_3$ nanotubes, J. Alloys Compd. 613 (2014) 260–266. doi:10.1016/J.JALLCOM.2014.06.039.

[312] R. Hailili, G. Dong, Y. Ma, S. Jin, C. Wang, T. Xu, Layered Perovskite $Pb_2Bi_4Ti_5O_{18}$ for Excellent Visible Light-Driven Photocatalytic NO Removal, Ind. Eng. Chem. Res. 56 (2017) 2908–2916. doi:10.1021/ACS.IECR.6B04706.

[313] J. Wang, Y. Asakura, T. Hasegawa, S. Yin, High-concentration N-doped $La_2Ti_2O_7$ nanocrystals: Effects of nano-structuration and doping sites on enhancing the photocatalytic activity, Chem. Eng. J.

423 (2021) 130220. doi:10.1016/J.CEJ.2021.130220.

[314] Q. Zhang, X. Liu, M. Chaker, D. Ma, Advancing Graphitic Carbon Nitride-Based Photocatalysts toward Broadband Solar Energy Harvesting, ACS Mater. Lett. 3 (2021) 663–697. doi:10.1021/ACSMATERIALSLETT.1C00160.

[315] T. Sano, S. Tsutsui, K. Koike, T. Hirakawa, Y. Teramoto, N. Negishi, K. Takeuchi, Activation of graphitic carbon nitride (g-C_3N_4) by alkaline hydrothermal treatment for photocatalytic NO oxidation in gas phase, J. Mater. Chem. A. 1 (2013) 6489–6496. doi:10.1039/C3TA10472A.

[316] H. Nie, M. Ou, Q. Zhong, S. Zhang, L. Yu, Efficient visible-light photocatalytic oxidation of gaseous NO with graphitic carbon nitride (g–C_3N_4) activated by the alkaline hydrothermal treatment and mechanism analysis, J. Hazard. Mater. 300 (2015) 598–606. doi:10.1016/J.JHAZMAT.2015.07.066.

[317] F. Dong, Z. Wang, Y. Sun, W.K. Ho, H. Zhang, Engineering the nanoarchitecture and texture of polymeric carbon nitride semiconductor for enhanced visible light photocatalytic activity, J. Colloid Interface Sci. 401 (2013) 70–79. doi:10.1016/J.JCIS.2013.03.034.

[318] F. Dong, M. Ou, Y. Jiang, S. Guo, Z. Wu, Efficient and Durable Visible Light Photocatalytic Performance of Porous Carbon Nitride Nanosheets for Air Purification, Ind. Eng. Chem. Res. 53 (2014) 2318–2330. doi:10.1021/IE4038104.

[319] F. Dong, Y. Li, Z. Wang, W.K. Ho, Enhanced visible light photocatalytic activity and oxidation ability of porous graphene-like g-C_3N_4 nanosheets via thermal exfoliation, Appl. Surf. Sci. 358 (2015) 393–403. doi:10.1016/J.APSUSC.2015.04.034.

[320] Z. Wang, W. Guan, Y. Sun, F. Dong, Y. Zhou, W.-K. Ho, Water-assisted production of honeycomb-like g-C_3N_4 with ultralong carrier lifetime and outstanding photocatalytic activity, Nanoscale. 7 (2015) 2471–2479. doi:10.1039/C4NR05732E.

[321] W. Ho, Z. Zhang, M. Xu, X. Zhang, X. Wang, Y. Huang, Enhanced visible-light-driven photocatalytic removal of NO: Effect on layer distortion on g-C_3N_4 by H_2 heating, Appl. Catal. B Environ. 179 (2015) 106–112. doi:10.1016/J.APCATB.2015.05.010.

[322] W. Ho, Z. Zhang, W. Lin, S. Huang, X. Zhang, X. Wang, Y. Huang, Copolymerization with 2,4,6-Triaminopyrimidine for the Rolling-up the Layer Structure, Tunable Electronic Properties, and Photocatalysis of g-C_3N_4, ACS Appl. Mater. Interfaces. 7 (2015) 5497–5505. doi:10.1021/AM509213X.

[323] Z.Z. Lu, S.Q. Li, J.Y. Xiao, Synergetic Effect of Na–Ca for Enhanced Photocatalytic Performance in NO_x Degradation by g-C_3N_4, Catal. Letters. 151 (2021) 370–381. doi:10.1007/S10562-020-03318-5.

[324] L. Duan, G. Li, S. Zhang, H. Wang, Y. Zhao, Y. Zhang, Preparation of S-doped g-C_3N_4 with C vacancies using the desulfurized waste liquid extracting salt and its application for NO_x removal, Chem. Eng. J. 411 (2021). doi:10.1016/J.CEJ.2021.128551.

[325] Y. Duan, Y. Wang, L. Gan, J. Meng, Y. Feng, K. Wang, K. Zhou, C. Wang, X. Han, X. Zhou, Amorphous Carbon Nitride with Three Coordinate Nitrogen (N_3C) Vacancies for Exceptional NO_x Abatement in Visible Light, Adv. Energy Mater. 11 (2021) 2004001. doi:10.1002/AENM.202004001.

[326] Y. Sun, T. Xiong, Z. Ni, J. Liu, F. Dong, W. Zhang, W.K. Ho, Improving g-C_3N_4 photocatalysis for NO_x removal by Ag nanoparticles decoration, Appl. Surf. Sci. 358 (2015) 356–362. doi:10.1016/J.APSUSC.2015.07.071.

[327] F. Dong, Z. Zhao, Y. Sun, Y. Zhang, S. Yan, Z. Wu, An Advanced Semimetal–Organic Bi Spheres–g-C_3N_4 Nanohybrid with SPR-Enhanced Visible-Light Photocatalytic Performance for NO Purification, Environ. Sci. Technol. 49 (2015) 12432–12440. doi:10.1021/ACS.EST.5B03758.

[328] G. Jiang, X. Li, M. Lan, T. Shen, X. Lv, F. Dong, S. Zhang, Monodisperse bismuth nanoparticles decorated graphitic carbon nitride: Enhanced visible-light-response photocatalytic NO removal and reaction pathway, Appl. Catal. B Environ. 205 (2017) 532–540. doi:10.1016/J.APCATB.2017.01.009.

[329] Y. Li, K. Lv, W. Ho, Z. Zhao, Y. Huang, Enhanced visible-light photo-oxidation of nitric oxide using bismuth-coupled graphitic carbon nitride composite heterostructures, Chinese J. Catal. 38 (2017) 321–329. doi:10.1016/S1872-2067(16)62573-1.

[330] F. Dong, Z. Zhao, T. Xiong, Z. Ni, W. Zhang, Y. Sun, W.-K. Ho, In Situ Construction of g-C_3N_4/g-C_3N_4 Metal-Free Heterojunction for

Enhanced Visible-Light Photocatalysis, ACS Appl. Mater. Interfaces. 5 (2013) 11392–11401. doi:10.1021/AM403653A.

[331] N. Tian, H. Huang, C. Liu, F. Dong, T. Zhang, X. Du, S. Yu, Y. Zhang, In situ co-pyrolysis fabrication of CeO_2/g-C_3N_4 n–n type heterojunction for synchronously promoting photo-induced oxidation and reduction properties, J. Mater. Chem. A. 3 (2015) 17120–17129. doi:10.1039/C5TA03669K.

[332] M. Ou, Q. Zhong, S. Zhang, L. Yu, Ultrasound assisted synthesis of heterogeneous g-C_3N_4/$BiVO_4$ composites and their visible-light-induced photocatalytic oxidation of NO in gas phase, J. Alloys Compd. 626 (2015) 401–409. doi:10.1016/J.JALLCOM.2014.11.148.

[333] Y. Sun, W. Zhang, T. Xiong, Z. Zhao, F. Dong, R. Wang, W.K. Ho, Growth of BiOBr nanosheets on C_3N_4 nanosheets to construct two-dimensional nanojunctions with enhanced photoreactivity for NO removal, J. Colloid Interface Sci. 418 (2014) 317–323. doi:10.1016/J.JCIS.2013.12.037.

[334] Z. Wang, Y. Huang, W. Ho, J. Cao, Z. Shen, S.C. Lee, Fabrication of $Bi_2O_2CO_3$/g-C_3N_4 heterojunctions for efficiently photocatalytic NO in air removal: In-situ self-sacrificial synthesis, characterizations and mechanistic study, Appl. Catal. B Environ. 199 (2016) 123–133. doi:10.1016/J.APCATB.2016.06.027.

[335] Z. Ai, Y. Huang, S. Lee, L. Zhang, Monoclinic α-Bi_2O_3 photocatalyst for efficient removal of gaseous NO and HCHO under visible light irradiation, J. Alloys Compd. 509 (2011) 2044–2049. doi:10.1016/J.JALLCOM.2010.10.132.

[336] M. Chen, Y. Li, Z. Wang, Y. Gao, Y. Huang, J. Cao, W. Ho, S. Lee, Controllable Synthesis of Core–Shell Bi@Amorphous Bi_2O_3 Nanospheres with Tunable Optical and Photocatalytic Activity for NO Removal, Ind. Eng. Chem. Res. 56 (2017) 10251–10258. doi:10.1021/ACS.IECR.7B02497.

[337] X. Li, Y. Sun, T. Xiong, G. Jiang, Y. Zhang, Z. Wu, F. Dong, Activation of amorphous bismuth oxide via plasmonic Bi metal for efficient visible-light photocatalysis, J. Catal. 352 (2017) 102–112. doi:10.1016/J.JCAT.2017.04.025.

[338] F. Dong, W.-K. Ho, S.C. Lee, Z. Wu, M. Fu, S. Zou, Y. Huang, Template-free fabrication and growth mechanism of uniform $(BiO)_2CO_3$ hierarchical hollow microspheres with outstanding photocatalytic

activities under both UV and visible light irradiation, J. Mater. Chem. 21 (2011) 12428–12436. doi:10.1039/C1JM11840D.

[339] P. Chen, Y. Sun, H. Liu, Y. Zhou, G. Jiang, S.C. Lee, Y. Zhang, F. Dong, Facet-dependent photocatalytic NO conversion pathways predetermined by adsorption activation patterns, Nanoscale. 11 (2019) 2366–2373. doi:10.1039/C8NR09147A.

[340] S. Yu, Y. Zhang, F. Dong, M. Li, T. Zhang, H. Huang, Readily achieving concentration-tunable oxygen vacancies in $Bi_2O_2CO_3$: Triple-functional role for efficient visible-light photocatalytic redox performance, Appl. Catal. B Environ. 226 (2018) 441–450. doi:10.1016/J.APCATB.2017.12.074.

[341] C. Yuan, R. Chen, J. Wang, H. Wu, J. Sheng, F. Dong, Y. Sun, La-doping induced localized excess electrons on $(BiO)_2CO_3$ for efficient photocatalytic NO removal and toxic intermediates suppression, J. Hazard. Mater. 400 (2020) 123174. doi:10.1016/j.jhazmat.2020.123174.

[342] M. Chen, Y. Huang, J. Yao, J. ji Cao, Y. Liu, Visible-light-driven N-$(BiO)_2CO_3$/Graphene oxide composites with improved photocatalytic activity and selectivity for NO_x removal, Appl. Surf. Sci. 430 (2018) 137–144. doi:10.1016/J.APSUSC.2017.06.056.

[343] T. Xiong, M. Wen, F. Dong, J. Yu, L. Han, B. Lei, Y. Zhang, X. Tang, Z. Zang, Three dimensional Z-scheme $(BiO)_2CO_3/MoS_2$ with enhanced visible light photocatalytic NO removal, Appl. Catal. B Environ. 199 (2016) 87–95. doi:10.1016/j.apcatb.2016.06.032.

[344] Y. Jia, S. Li, J. Gao, G. Zhu, F. Zhang, X. Shi, Y. Huang, C. Liu, Highly efficient $(BiO)_2CO_3$-BiO_{2-x}-graphene photocatalysts: Z-Scheme photocatalytic mechanism for their enhanced photocatalytic removal of NO, Appl. Catal. B Environ. 240 (2019) 241–252. doi:10.1016/J.APCATB.2018.09.005.

[345] X. Feng, W. Zhang, Y. Sun, H. Huang, F. Dong, Fe(III) cluster-grafted $(BiO)_2CO_3$ superstructures: in situ DRIFTS investigation on IFCT-enhanced visible light photocatalytic NO oxidation, Environ. Sci. Nano. 4 (2017) 604–612. doi:10.1039/C6EN00637J.

[346] X. Feng, W. Zhang, H. Deng, Z. Ni, F. Dong, Y. Zhang, Efficient visible light photocatalytic NO_x removal with cationic Ag clusters-grafted $(BiO)_2CO_3$ hierarchical superstructures, J. Hazard. Mater. 322 (2017) 223–232. doi:10.1016/J.JHAZMAT.2016.05.007.

[347] P. Chen, H. Liu, Y. Sun, J. Li, W. Cui, L. Wang, W. Zhang, X. Yuan, Z. Wang, Y. Zhang, F. Dong, Bi metal prevents the deactivation of oxygen vacancies in $Bi_2O_2CO_3$ for stable and efficient photocatalytic NO abatement, Appl. Catal. B Environ. 264 (2020) 118545. doi:10.1016/j.apcatb.2019.118545.

[348] X. Dong, W. Zhang, W. Cui, Y. Sun, H. Huang, Z. Wu, F. Dong, Pt quantum dots deposited on N-doped $(BiO)_2CO_3$: enhanced visible light photocatalytic NO removal and reaction pathway, Catal. Sci. Technol. 7 (2017) 1324–1332. doi:10.1039/C6CY02444K.

[349] W. Huo, W. Xu, T. Cao, X. Liu, Y. Zhang, F. Dong, Carbonate-intercalated defective bismuth tungstate for efficiently photocatalytic NO removal and promotion mechanism study, Appl. Catal. B Environ. 254 (2019) 206–213. doi:10.1016/j.apcatb.2019.04.099.

[350] W.C. Huo, X. Dong, J.Y. Li, M. Liu, X.Y. Liu, Y.X. Zhang, F. Dong, Synthesis of Bi_2WO_6 with gradient oxygen vacancies for highly photocatalytic NO oxidation and mechanism study, Chem. Eng. J. 361 (2019) 129–138. doi:10.1016/J.CEJ.2018.12.071.

[351] S. Wang, X. Ding, N. Yang, G. Zhan, X. Zhang, G. Dong, L. Zhang, H. Chen, Insight into the effect of bromine on facet-dependent surface oxygen vacancies construction and stabilization of Bi_2MoO_6 for efficient photocatalytic NO removal, Appl. Catal. B Environ. 265 (2020) 118585. doi:10.1016/j.apcatb.2019.118585.

[352] X. Ding, W. Ho, J. Shang, L. Zhang, Self doping promoted photocatalytic removal of no under visible light with bi2moo6: Indispensable role of superoxide ions, Appl. Catal. B Environ. 182 (2016) 316–325. doi:10.1016/j.apcatb.2015.09.046.

[353] H. Ma, Y. He, X. Li, J. Sheng, J. Li, F. Dong, Y. Sun, In situ loading of MoO_3 clusters on ultrathin Bi_2MoO_6 nanosheets for synergistically enhanced photocatalytic NO abatement, Appl. Catal. B Environ. 292 (2021) 120159. doi:10.1016/J.APCATB.2021.120159.

[354] W. Huo, W. Xu, T. Cao, Z. Guo, X. Liu, G. Ge, N. Li, T. Lan, H.C. Yao, Y. Zhang, F. Dong, Carbonate doped Bi_2MoO_6 hierarchical nanostructure with enhanced transformation of active radicals for efficient photocatalytic removal of NO, J. Colloid Interface Sci. 557 (2019) 816–824. doi:10.1016/J.JCIS.2019.09.089.

[355] W. He, Y. Sun, G. Jiang, H. Huang, X. Zhang, F. Dong, Activation of

amorphous Bi_2WO_6 with synchronous Bi metal and Bi_2O_3 coupling: Photocatalysis mechanism and reaction pathway, Appl. Catal. B Environ. 232 (2018) 340–347. doi:10.1016/J.APCATB.2018.03.047.

[356] J. Hu, D. Chen, Z. Mo, N. Li, Q. Xu, H. Li, J. He, H. Xu, J. Lu, Z-Scheme 2D/2D Heterojunction of Black Phosphorus/Monolayer Bi_2WO_6 Nanosheets with Enhanced Photocatalytic Activities, Angew. Chemie Int. Ed. 58 (2019) 2073–2077. doi:10.1002/ANIE.201813417.

[357] J. Li, W. Zhang, M. Ran, Y. Sun, H. Huang, F. Dong, Synergistic integration of Bi metal and phosphate defects on hexagonal and monoclinic $BiPO_4$: Enhanced photocatalysis and reaction mechanism, Appl. Catal. B Environ. 243 (2019) 313–321. doi:10.1016/J.APCATB.2018.10.055.

[358] X. Li, W. Zhang, J. Li, G. Jiang, Y. Zhou, S.C. Lee, F. Dong, Transformation pathway and toxic intermediates inhibition of photocatalytic NO removal on designed Bi metal@defective $Bi_2O_2SiO_3$, Appl. Catal. B Environ. 241 (2019) 187–195. doi:10.1016/j.apcatb.2018.09.032.

[359] X. Li, W. Zhang, W. Cui, J. Li, Y. Sun, G. Jiang, H. Huang, Y. Zhang, F. Dong, Reactant activation and photocatalysis mechanisms on Bi-metal@Bi_2GeO_5 with oxygen vacancies: A combined experimental and theoretical investigation, Chem. Eng. J. 370 (2019) 1366–1375. doi:10.1016/j.cej.2019.04.003.

[360] W. He, Y. Sun, G. Jiang, Y. Li, X. Zhang, Y. Zhang, Y. Zhou, F. Dong, Defective Bi_4MoO_9/Bi metal core/shell heterostructure: Enhanced visible light photocatalysis and reaction mechanism, Appl. Catal. B Environ. 239 (2018) 619–627. doi:10.1016/J.APCATB.2018.08.064.

[361] W. Zhang, Q. Zhang, F. Dong, Visible-Light Photocatalytic Removal of NO in Air over BiOX (X = Cl, Br, I) Single-Crystal Nanoplates Prepared at Room Temperature, Ind. Eng. Chem. Res. 52 (2013) 6740–6746. doi:10.1021/IE400615F.

[362] H. Li, H. Shang, X. Cao, Z. Yang, Z. Ai, L. Zhang, Oxygen Vacancies Mediated Complete Visible Light NO Oxidation via Side-On Bridging Superoxide Radicals, Environ. Sci. Technol. 52 (2018) 8659–8665. doi:10.1021/acs.est.8b01849.

[363] W. Zhang, X. Dong, Y. Liang, Y. Sun, F. Dong, Ag/AgCl nanoparticles assembled on BiOCl/$Bi_{12}O_{17}Cl_2$ nanosheets: Enhanced plasmonic

visible light photocatalysis and in situ DRIFTS investigation, Appl. Surf. Sci. 455 (2018) 236–243. doi:10.1016/j.apsusc.2018.05.171.

[364] H. Wang, W. Zhang, X. Li, J. Li, W. Cen, Q. Li, F. Dong, Highly enhanced visible light photocatalysis and in situ FT-IR studies on Bi metal@defective BiOCl hierarchical microspheres, Appl. Catal. B Environ. 225 (2018) 218–227. doi:10.1016/J.APCATB.2017.11.079.

[365] W. Wang, C. Wen, J. Guan, H. Man, J. Bian, Insight on photocatalytic oxidation of high concentration NO over BiOCl/Bi_2WO_6 under visible light, J. Ind. Eng. Chem. 103 (2021) 305–313. doi:10.1016/J.JIEC.2021.07.045.

[366] S. Wu, X. Yu, J. Zhang, Y. Zhang, Y. Zhu, M. Zhu, Construction of BiOCl/$CuBi_2O_4$ S-scheme heterojunction with oxygen vacancy for enhanced photocatalytic diclofenac degradation and nitric oxide removal, Chem. Eng. J. 411 (2021) 128555. doi:10.1016/J.CEJ.2021.128555.

[367] F. Dong, Y. Sun, M. Fu, Z. Wu, S.C. Lee, Room temperature synthesis and highly enhanced visible light photocatalytic activity of porous BiOI/BiOCl composites nanoplates microflowers, J. Hazard. Mater. 219–220 (2012) 26–34. doi:10.1016/J.JHAZMAT.2012.03.015.

[368] R. Li, J. Liu, X. Zhang, Y. Wang, Y. Wang, C. Zhang, X. Zhang, C. Fan, Iodide-modified $Bi_4O_5Br_2$ photocatalyst with tunable conduction band position for efficient visible-light decontamination of pollutants, Chem. Eng. J. 339 (2018) 42–50. doi:10.1016/J.CEJ.2018.01.109.

[369] Y. Bai, P. Yang, P. Wang, Z. Fan, H. Xie, P.K. Wong, L. Ye, Solid phase fabrication of Bismuth-rich $Bi_3O_4Cl_xBr_{1-x}$ solid solution for enhanced photocatalytic NO removal under visible light, J. Taiwan Inst. Chem. Eng. 82 (2018) 273–280. doi:10.1016/J.JTICE.2017.10.021.

[370] T. Wu, X. Li, D. Zhang, F. Dong, S. Chen, Efficient visible light photocatalytic oxidation of NO with hierarchical nanostructured 3D flower-like $BiOCl_xBr_{1-x}$ solid solutions, J. Alloys Compd. 671 (2016) 318–327. doi:10.1016/j.jallcom.2016.01.267.

[371] J.M. Montoya-Zamora, A. Martínez-de la Cruz, E. López-Cuéllar, F.A. Pérez González, BiOBr photocatalyst with high activity for NO_x elimination, Adv. Powder Technol. 31 (2020) 3618–3627. doi:10.1016/J.APT.2020.07.009.

[372] R. Li, F. Xie, J. Liu, C. Zhang, X. Zhang, C. Fan, Room-temperature hydrolysis fabrication of BiOBr/$Bi_{12}O_{17}Br_2$ Z-Scheme photocatalyst with enhanced resorcinol degradation and NO removal activity, Chemosphere. 235 (2019) 767–775. doi:10.1016/J.CHEMOSPHERE.2019.06.231.

[373] M. Ou, F. Dong, W. Zhang, Z. Wu, Efficient visible light photocatalytic oxidation of NO in air with band-gap tailored $(BiO)_2CO_3$–BiOI solid solutions, Chem. Eng. J. 255 (2014) 650–658. doi:10.1016/J.CEJ.2014.06.086.

[374] X. Shi, P. Wang, W. Li, Y. Bai, H. Xie, Y. Zhou, L. Ye, Change in photocatalytic NO removal mechanisms of ultrathin BiOBr/BiOI via NO_{3-} adsorption, Appl. Catal. B Environ. 243 (2019) 322–329. doi:10.1016/J.APCATB.2018.10.037.

[375] F. Dong, T. Xiong, Y. Sun, Y. Zhang, Y. Zhou, Controlling interfacial contact and exposed facets for enhancing photocatalysis via 2D–2D heterostructures, Chem. Commun. 51 (2015) 8249–8252. doi:10.1039/C5CC01993A.

[376] N. Tian, Y. Zhang, C. Liu, S. Yu, M. Li, H. Huang, g-C_3N_4/$Bi_4O_5I_2$ 2D–2D heterojunctional nanosheets with enhanced visible-light photocatalytic activity, RSC Adv. 6 (2016) 10895–10903. doi:10.1039/C5RA24672E.

[377] H. Wang, Y. Sun, G. Jiang, Y. Zhang, H. Huang, Z. Wu, S.C. Lee, F. Dong, Unraveling the Mechanisms of Visible Light Photocatalytic NO Purification on Earth-Abundant Insulator-Based Core-Shell Heterojunctions, Environ. Sci. Technol. 52 (2018) 1479–1487. doi:10.1021/acs.est.7b05457.

[378] T.H. Huy, B.D. Phat, C.M. Thi, P. Van Viet, High photocatalytic removal of NO gas over SnO_2 nanoparticles under solar light, Environ. Chem. Lett. 2018 171. 17 (2018) 527–531. doi:10.1007/S10311-018-0801-0.

[379] D.P. Bui, M.T. Nguyen, H.H. Tran, S.J. You, Y.F. Wang, P. Van Viet, Green synthesis of Ag@SnO_2 nanocomposites for enhancing photocatalysis of nitrogen monoxide removal under solar light irradiation, Catal. Commun. 136 (2020) 105902. doi:10.1016/J.CATCOM.2019.105902.

[380] T.H. Huy, D.P. Bui, F. Kang, Y.F. Wang, S.H. Liu, C.M. Thi, S.J. You, G.M. Chang, V.V. Pham, SnO_2/TiO_2 nanotube heterojunction: The

first investigation of NO degradation by visible light-driven photocatalysis, Chemosphere. 215 (2019) 323–332. doi:10.1016/J.CHEMOSPHERE.2018.10.033.

[381] Z. Ai, S. Lee, Y. Huang, W. Ho, L. Zhang, Photocatalytic removal of NO and HCHO over nanocrystalline Zn_2SnO_4 microcubes for indoor air purification, J. Hazard. Mater. 179 (2010) 141–150. doi:10.1016/J.JHAZMAT.2010.02.071.

[382] Y. Li, X. Wu, W. Ho, K. Lv, Q. Li, M. Li, S.C. Lee, Graphene-induced formation of visible-light-responsive SnO_2-Zn_2SnO_4 Z-scheme photocatalyst with surface vacancy for the enhanced photoreactivity towards NO and acetone oxidation, Chem. Eng. J. 336 (2018) 200–210. doi:10.1016/J.CEJ.2017.11.045.

[383] T. Long, X. Dong, X. Liu, J. Liu, S. Yin, T. Sato, Synthesis of ZnO crystals with unique morphologiesby a low-temperature solvothermal process and their photocatalytic deNO_x properties, Res. Chem. Intermed. 36 (2010) 61–67. doi:10.1007/s11164-010-0114-9.

[384] T.H. Le, Q.D. Truong, T. Kimura, H. Li, C. Guo, S. Yin, T. Sato, Y.C. Ling, Synthesis of hierarchical porous ZnO microspheres and its photocatalytic deNO_x activity, Ceram. Int. 38 (2012) 5053–5059. doi:10.1016/J.CERAMINT.2012.03.007.

[385] E. Luévano-Hipólito, A. Martínez-de la Cruz, E. López Cuéllar, Performance of ZnO synthesized by sol-gel as photocatalyst in the photooxidation reaction of NO, Environ. Sci. Pollut. Res. 2016 247. 24 (2016) 6361–6371. doi:10.1007/S11356-016-7310-0.

[386] F. Wu, C. Pu, M. Zhang, B. Liu, J. Yang, Silver embedded in defective twin brush-like ZnO for efficient and stable photocatalytic NO removal, Surfaces and Interfaces. 25 (2021) 101298. doi:10.1016/J.SURFIN.2021.101298.

[387] A. Gasparotto, G. Carraro, C. Maccato, C. Sada, J. Balbuena, M. Cruz-Yusta, L. Sánchez, N. Vodišek, U. Lavrencic Štangar, D. Barreca, WO_3-decorated ZnO nanostructures for light-activated applications, CrystEngComm. 20 (2018) 1282–1290. doi:10.1039/c7ce02148h.

[388] S.N. Nguyen, T.K. Truong, S.-J. You, Y.-F. Wang, T.M. Cao, V. Van Pham, Investigation on Photocatalytic Removal of NO under Visible Light over Cr-Doped ZnO Nanoparticles, ACS Omega. 4 (2019) 12853–12859. doi:10.1021/ACSOMEGA.9B01628.

[389] I. Kitsou, P. Panagopoulos, T. Maggos, A. Tsetsekou, ZnO-coated SiO_2 nanocatalyst preparation and its photocatalytic activity over nitric oxides as an alternative material to pure ZnO, Appl. Surf. Sci. 473 (2019) 40–48. doi:10.1016/J.APSUSC.2018.12.146.

[390] N. Todorova, T. Giannakopoulou, K. Pomoni, J. Yu, T. Vaimakis, C. Trapalis, Photocatalytic NO_x oxidation over modified ZnO/TiO_2 thin films, Catal. Today. 252 (2015) 41–46. doi:10.1016/j.cattod.2014.11.008.

[391] C.C. Pei, W.W.F. Leung, Enhanced photocatalytic activity of electrospun TiO_2/ZnO nanofibers with optimal anatase/rutile ratio, Catal. Commun. 37 (2013) 100–104. doi:10.1016/J.CATCOM.2013.03.029.

[392] E. Kowsari, S. Abdpour, Investigation performance of rod-like ZnO/CdO composites, synthesized in ionic liquid medium as photocatalytic for degradation of air pollutants (SO_2 and NO_x), Optik (Stuttg). 127 (2016) 11567–11576. doi:10.1016/J.IJLEO.2016.09.084.

[393] R. Sugrañez, M. Cruz-Yusta, I. Mármol, J. Morales, L. Sánchez, Preparation of sustainable photocatalytic materials through the valorization of industrial wastes, ChemSusChem. 6 (2013) 2340–2347. doi:10.1002/cssc.201300449.

[394] J. Balbuena, L. Sánchez, M. Cruz-Yusta, Use of Steel Industry Wastes for the Preparation of Self-Cleaning Mortars, Mater. 2019, Vol. 12, Page 621. 12 (2019) 621. doi:10.3390/MA12040621.

[395] G. Carraro, R. Sugrañez, C. Maccato, A. Gasparotto, D. Barreca, C. Sada, M. Cruz-Yusta, L. Sánchez, Nanostructured iron(III) oxides: From design to gas- and liquid-phase photo-catalytic applications, Thin Solid Films. 564 (2014) 121–127. doi:10.1016/J.TSF.2014.05.048.

[396] R. Sugrañez, J. Balbuena, M. Cruz-yusta, F. Martín, J. Morales, L. Sánchez, Efficient behaviour of hematite towards the photocatalytic degradation of NOx gases, Appl. Catal. B Environ. 165 (2015) 529–536. doi:10.1016/j.apcatb.2014.10.025.

[397] Y. Huang, Y. Gao, Q. Zhang, Y. Zhang, J. ji Cao, W. Ho, S.C. Lee, Biocompatible FeOOH-Carbon quantum dots nanocomposites for gaseous NO_x removal under visible light: Improved charge separation and High selectivity, J. Hazard. Mater. 354 (2018) 54–62.

doi:10.1016/j.jhazmat.2018.04.071.

[398] J. Balbuena, M. Cruz-Yusta, A.L. Cuevas, M.C. López-Escalante, F. Martín, A. Pastor, L. Sánchez, Enhanced activity of α-$Fe_2O_3$for photocatalytic NO removal, RSC Adv. 6 (2016). doi:10.1039/c6ra19167c.

[399] J. Balbuena, M. Cruz-Yusta, A.L. Cuevas, F. Martín, A. Pastor, R. Romero, L. Sánchez, Hematite porous architectures as enhanced air purification photocatalyst, J. Alloys Compd. 797 (2019) 166–173. doi:10.1016/j.jallcom.2019.05.113.

[400] J. Balbuena, G. Carraro, M. Cruz, A. Gasparotto, C. Maccato, A. Pastor, C. Sada, D. Barreca, L. Sánchez, Advances in photocatalytic NOx abatement through the use of Fe2 O3/TiO2 nanocomposites, RSC Adv. 6 (2016) 74878–74885. doi:10.1039/C6RA15958C.

[401] H. Li, S. Yin, Y. Wang, T. Sato, Efficient persistent photocatalytic decomposition of nitrogen monoxide over a fluorescence-assisted $CaAl_2O_4$:(Eu, Nd)/(Ta, N)-codoped TiO_2/Fe_2O_3, Appl. Catal. B Environ. 132–133 (2013) 487–492. doi:10.1016/J.APCATB.2012.12.026.

[402] J. Hu, H. Wang, F. Dong, Z. Wu, A new strategy for utilization of NIR from solar energy—Promotion effect generated from photothermal effect of Fe_3O_4@SiO_2 for photocatalytic oxidation of NO, Appl. Catal. B Environ. 204 (2017) 584–592. doi:10.1016/j.apcatb.2016.12.009.

[403] Y. Huang, Y. Liang, Y. Rao, D. Zhu, J.J. Cao, Z. Shen, W. Ho, S.C. Lee, Environment-Friendly Carbon Quantum Dots/$ZnFe_2O_4$ Photocatalysts: Characterization, Biocompatibility, and Mechanisms for NO Removal, Environ. Sci. Technol. 51 (2017) 2924–2933. doi:10.1021/acs.est.6b04460.

[404] Y. Huang, D. Zhu, Q. Zhang, Y. Zhang, J. ji Cao, Z. Shen, W. Ho, S.C. Lee, Synthesis of a $Bi_2O_2CO_3$/$ZnFe_2O_4$ heterojunction with enhanced photocatalytic activity for visible light irradiation-induced NO removal, Appl. Catal. B Environ. 234 (2018) 70–78. doi:10.1016/j.apcatb.2018.04.039.

[405] Y. Huang, Y. Gao, Q. Zhang, J.J. Cao, R.J. Huang, W. Ho, S.C. Lee, Hierarchical porous $ZnWO_4$ microspheres synthesized by ultrasonic spray pyrolysis: Characterization, mechanistic and photocatalytic NO_x removal studies, Appl. Catal. A Gen. 515 (2016) 170–178. doi:10.1016/J.APCATA.2016.02.007.

[406] S. Li, L. Chang, J. Peng, J. Gao, J. Lu, F. Zhang, G. Zhu, M. Hojamberdiev, Bi^0 nanoparticle loaded on Bi^{3+}-doped $ZnWO_4$ nanorods with oxygen vacancies for enhanced photocatalytic NO removal, J. Alloys Compd. 818 (2020) 152837. doi:10.1016/J.JALLCOM.2019.152837.

[407] Z. Ai, S. Lee, Morphology-dependent photocatalytic removal of NO by hierarchical $BiVO_4$ microboats and microspheres under visible light, Appl. Surf. Sci. 280 (2013) 354–359. doi:10.1016/J.APSUSC.2013.04.160.

[408] S. Wan, M. Ou, W. Cai, S. Zhang, Q. Zhong, Preparation, characterization, and mechanistic analysis of $BiVO_4$/$CaIn_2S_4$ hybrids that photocatalyze NO removal under visible light, J. Phys. Chem. Solids. 122 (2018) 239–245. doi:10.1016/J.JPCS.2018.06.035.

[409] J. Hu, D. Chen, N. Li, Q. Xu, H. Li, J. He, J. Lu, Fabrication of graphitic-C_3N_4 quantum dots/graphene-$InVO_4$ aerogel hybrids with enhanced photocatalytic NO removal under visible-light irradiation, Appl. Catal. B Environ. 236 (2018) 45–52. doi:10.1016/j.apcatb.2018.04.080.

[410] H.P. Nguyen, M. Matsuoka, T.H. Kim, S.W. Lee, Iron(III)-based metal-organic frameworks as potential visible light-driven catalysts for the removal of NO_x: A solution for urban air purification, J. Photochem. Photobiol. A Chem. 367 (2018) 429–437. doi:10.1016/J.JPHOTOCHEM.2018.09.008.

[411] W. Zhu, P. Liu, S. Xiao, W. Wang, D. Zhang, H. Li, Microwave-assisted synthesis of Ag-doped MOFs-like organotitanium polymer with high activity in visible-light driven photocatalytic NO oxidization, Appl. Catal. B Environ. 172–173 (2015) 46–51. doi:10.1016/J.APCATB.2015.02.003.

[412] M. Chen, X. Wei, L. Zhao, Y. Huang, S. Lee, W. Ho, K. Chen, Novel N/Carbon Quantum Dot Modified MIL-125(Ti) Composite for Enhanced Visible-Light Photocatalytic Removal of NO, Ind. Eng. Chem. Res. 59 (2020) 6470–6478. doi:10.1021/ACS.IECR.9B06816.

[413] X. Chen, Y. Cai, R. Liang, Y. Tao, W. Wang, J. Zhao, X. Chen, H. Li, D. Zhang, NH_2-UiO-66(Zr) with fast electron transfer routes for breaking down nitric oxide via photocatalysis, Appl. Catal. B Environ. 267 (2020) 118687. doi:10.1016/J.APCATB.2020.118687.

[414] F. Cavani, F. Trifirò, A. Vaccari, Hydrotalcite-type anionic clays:

Preparation, properties and applications., Catal. Today. 11 (1991) 173–301. doi:10.1016/0920-5861(91)80068-K.

[415] V. Rives, Layered Double Hydroxides: Present and Future, Nova Science Publishers Inc, New York, 2001.

[416] V.K. Ameena Shirin, R. Sankar, A.P. Johnson, H. V. Gangadharappa, K. Pramod, Advanced drug delivery applications of layered double hydroxide, J. Control. Release. 330 (2021) 398–426. doi:10.1016/J.JCONREL.2020.12.041.

[417] Z.H. Xie, H.Y. Zhou, C.S. He, Z.C. Pan, G. Yao, B. Lai, Synthesis, application and catalytic performance of layered double hydroxide based catalysts in advanced oxidation processes for wastewater decontamination: A review, Chem. Eng. J. 414 (2021) 128713. doi:10.1016/J.CEJ.2021.128713.

[418] D. Zhou, P. Li, X. Lin, A. McKinley, Y. Kuang, W. Liu, W.-F. Lin, X. Sun, X. Duan, Layered double hydroxide-based electrocatalysts for the oxygen evolution reaction: identification and tailoring of active sites, and superaerophobic nanoarray electrode assembly, Chem. Soc. Rev. 50 (2021) 8790–8817. doi:10.1039/D1CS00186H.

[419] H. Yang, C. Xiong, X. Liu, A. Liu, T. Li, R. Ding, S.P. Shah, W. Li, Application of layered double hydroxides (LDHs) in corrosion resistance of reinforced concrete-state of the art, Constr. Build. Mater. 307 (2021) 124991. doi:10.1016/J.CONBUILDMAT.2021.124991.

[420] S. Tang, Y. Yao, T. Chen, D. Kong, W. Shen, H.K. Lee, Recent advances in the application of layered double hydroxides in analytical chemistry: A review, Anal. Chim. Acta. 1103 (2020) 32–48. doi:10.1016/J.ACA.2019.12.065.

[421] L. Mohapatra, K. Parida, A review on the recent progress, challenges and perspective of layered double hydroxides as promising photocatalysts, J. Mater. Chem. A. 4 (2016) 10744–10766. doi:10.1039/C6TA01668E.

[422] S.-F. Ng, M.Y.L. Lau, W.-J. Ong, Engineering Layered Double Hydroxide–Based Photocatalysts Toward Artificial Photosynthesis: State-of-the-Art Progress and Prospects, Sol. RRL. 5 (2021) 2000535. doi:10.1002/SOLR.202000535.

[423] F. Rodriguez-Rivas, A. Pastor, C. Barriga, M. Cruz-Yusta, L. Sánchez,

I. Pavlovic, Zn-Al layered double hydroxides as efficient photocatalysts for NOx abatement, Chem. Eng. J. 346 (2018) 151–158. doi:10.1016/j.cej.2018.04.022.

[424] W. Huo, T. Cao, X. Liu, W. Xu, B. Dong, Y. Zhang, F. Dong, Anion intercalated layered-double-hydroxide structure for efficient photocatalytic NO remove, Green Energy Environ. 4 (2019) 270–277. doi:10.1016/j.gee.2018.11.001.

[425] X. Lv, J. Zhang, X. Dong, J. Pan, W. Zhang, W. Wang, G. Jiang, F. Dong, Layered double hydroxide nanosheets as efficient photocatalysts for NO removal: Band structure engineering and surface hydroxyl ions activation, Appl. Catal. B Environ. 277 (2020) 119200. doi:10.1016/j.apcatb.2020.119200.

[426] F. Rodriguez-Rivas, A. Pastor, G. de Miguel, M. Cruz-Yusta, I. Pavlovic, L. Sánchez, Cr^{3+} substituted Zn-Al layered double hydroxides as UV–Vis light photocatalysts for NO gas removal from the urban environment, Sci. Total Environ. 706 (2020) 136009. doi:10.1016/j.scitotenv.2019.136009.

[427] A. Nehdi, N. Frini-Srasra, G. de Miguel, I. Pavlovic, L. Sánchez, J.Fragoso, Use of LDH- chromate adsorption co-product as an air purification photocatalyst, Chemosphere. 286 (2022). doi:10.1016/j.chemosphere.2021.131812.

Capítulo 3.

Resultados y discusión

3.1. Carbendazim-clay complexes for its potential use as antimicrobial additives in mortars.

ELSEVIER

Building and Environment
Volume 183, October 2020, 107214

Carbendazim-clay complexes for its potential use as antimicrobial additives in mortars

Adrián Pastor [a], Beatriz Gámiz [b] ✉, Manuel Cruz-Yusta [a], Luis Sánchez [a], Ivana Pavlovic [a]

[a] Departamento de Química Inorgánica, Instituto Universitario de Investigación en Química Fina y Nanoquímica IUIQFN, Universidad de Córdoba, Campus de Rabanales, E-14071, Córdoba, Spain
[b] Instituto de Recursos Naturales y Agrobiología, Consejo Superior de Investigaciones Científicas (IRNAS-CSIC), Avda. Reina Mercedes nº10, 41010, Sevilla, Spain

Received 2 June 2020, Revised 27 July 2020, Accepted 17 August 2020, Available online 19 August 2020.

https://doi.org/10.1016/j.buildenv.2020.107214

Highlights

- CL20 was the best clay to adsorb the CBZ biocide, using the cosolvent DMF (25% v/v).
- Adsorption complexes showed good fungicidal action when Cs was >50 mg g^{-1}
- Lime mortars with CL20-CBZ achieved a biocidal effect lasting after the leaching test.
- The released amount of CBZ from the mortar was lower when it was anchored to CL20.

ABSTRACT

Mortars containing biocidal chemicals are widely applied as they show resistance to microbiological growth, thus preventing the aging of heritage materials. However, factors such as ultraviolet radiation, the weather etc. could greatly affect the biocidal activity of the active principles in mortars. The aim of this study was to optimize the preparation of several complexes of the biocide carbendazim (CBZ) with clays: natural Wyoming montmorillonite SWy-1 and two commercial organoclays, Cloisite® 10 and Cloisite® 20, and to test their antimicrobial activity for their potential application in restoration mortars. The optimized material here proposed would minimize the amount of active principle needed avoiding its leaching and consequently reducing its environmental impact with a maximum heritage compatibility.

Prepared organoclay-CBZ adsorption complexes were inoculated with microorganisms (algae and fungus) to assess the antimicrobial activity. In this sense, one of the CL20-CBZ adsorption complexes which showed the best algicidal and fungicidal activity was used to prepare the antimicrobial mortar, and subsequently compared to those with pure CBZ as a antimicrobial additive. Furthermore, the mortars specimens were subjected to a standardized leaching test to check the effectiveness of the antimicrobial activity. After the leaching tests, the antimicrobial action of mortar containing only CBZ was lower compared to CL20-CBZ which had a good antimicrobial effect. We can conclude from these results that the heritage lime mortars could be easily prepared and have good efficiency against microbial contamination.

Keywords: *Adsorption, Biocide, Carbendazim, Clays, Leaching, Mortar*

GRAPHICAL ABSTRACT

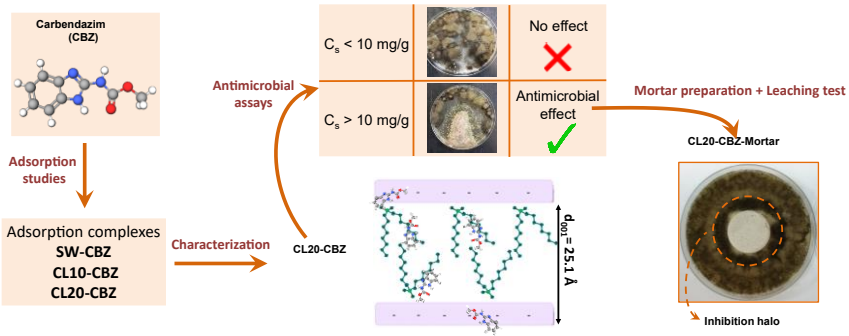

3.1.1. Introduction

Most of the cultural heritage in our cities, such as monuments and facades, are built with plaster, lime mortars or stones of different nature (limestone, dolomite, marble, etc.) [1]. With time, they suffer alterations, which are very heterogeneous and complex in nature, since the materials and techniques used for their preparation are very diverse. The phenomena of alteration and deterioration are produced either by the normal aging of the materials, or induced by environmental agents such as humidity, temperature, light, CO_2 concentration or biological factors [2–4].

Among these deterioration factors, microbial activity is one of the most important and aggressive. The microflora of the external surface of the stone is a complex ecosystem formed by fungi, algae, bacteria, lichens and even protozoa [5]. These microorganisms induce biological processes promoting deterioration to monuments, one of the least studied mechanisms of heritage biodeteroration [6]. Moreover, this deterioration phenomenon is being accelerated due to the increase in environmental urban pollution and also the absence of preventive conservation systems [7].

One way to address the problem is by incorporating biocidal compounds as one of the raw materials used in the building and restoration tasks concerning the cultural heritage. According to the 98/8/EC, 1 (BDP) European Directive on biocide products (chemicals used to eliminate the growth of undesirable biological species) these can be classified into four groups: preservatives, pest control, disinfectants and other biocidal products [8]. Of importance, the biocidal product must have high efficacy against biological agents, no interference with the constituent materials of the monument, low toxicity and low risk of

environmental contamination [9]. Nowadays, there is a wide variety of commercial biocide compounds whose function and effectiveness depends on their chemical composition and field of application [10,11].

Restoration mortars are perhaps the most frequently used building material in the intervention tasks on historical and archaeological constructions, because their composition can be formulated in a similar manner to those of pristine materials, thus minimizing the apparition of aesthetical or mechanical/degradation failures [12]. The development of an additive with biocidal properties which could be properly incorporated into a mortar formulation, is an interesting and simple way to avoid or minimize the deterioration of historical buildings by microorganisms [13]. Most commercial biocides are not suitable for use in mortars, because they exhibit some residual activity or instability at the high pH values found in mortars. Among the different biocide compounds, the pesticide carbendazim (CBZ) could be an attractive option due to its low cost and low water solubility (8 mg L^{-1}), the latter being a key factor in avoiding leaching from mortar cladding into outdoor environments. In fact, CBZ is a fungicide with broad spectra to control a range of diseases and is one of the most frequently used as a preservative in agriculture (corn, tomatoes, fruit, etc.) [14].

Moreover, the expected durability of the biocide application for mortar must be longer than that of other biocidal applications (cleaning gels, containers, etc.), thus, the biocide additive must be retained in the mortar for as long time as possible. Actually, an extended duration of biocidal activity can be achieved by incorporating an active agent into an adequate carrier. Thus, the biocide could be released more gradually, its activity being extended. Also, carriers shield the biocidal compound from any harmful effects of environmental exposure, making its handling

easier, safer and with better environmental performance. For instance, recently Scarfato et al. [15] proposed a novel carrier based on a natural halloysite for the biocide Biotin T, effective in prolonging the activity of the chemical for 2 years.

The use of clay minerals as adsorbents of pesticides has been extensively studied in the field of agricultural and environmental sciences. Mainly, the 2:1-type phyllosilicates, which contain a layer of octahedral alumina and two linked tetrahedral silicate layers, such as smectites, are good adsorbents for cationic and polar organic compounds, as a consequence of their hydrophilic and negatively charged surfaces [16]. Nevertheless, the affinity of these materials towards anionic or hydrophobic compounds can be improved by a simple modification of their surfaces after the incorporation of organic cations in their interlayer space through an exchange reaction, forming a new material generally called organoclay [17–19]. Quaternary ammonium surfactants which are found as cations in nature, are one of the most common modifiers used in the preparation of organoclays [20,21]. They usually contain short aliphatic chains or benzyl groups that are incorporated along with at least one long aliphatic chain (C12–C18) resulting in a higher interlayer space which is capable of housing the organic compounds, among other pesticides [20]. Consequently, smectites can be modified to improve their affinity for a particular pesticide [16,22]. Furthermore, quaternary ammonium surfactants have been approved by the European Biocide Directive as an additive for commercial biocides in the context of the monuments' cultural heritage conservation [23].

Hence, these materials, smectites and organoclays, have been used as supports for the slow release of pesticides, in such a way that the active ingredient is not in an immediately available form, controlling the

amount of pesticides and therefore avoiding undesirable leaching losses thus reducing their environmental impact [24,25]. In this work, we hypothesized that they can be good carriers for the control release of the biocides in mortars, due to the peculiarity of their structures and their compatibility as a component in mortars [26–29]. There are studies dealing with the controlled release of biocides from paints [30–33], but few regarding the release from mortars. In this study, we present new results obtained in the development of a long-lasting biocidal additive using carbendazim as a broad spectrum biocide, using the reference Wyoming montmorillonite, SWy-1 and two commercial organoclays, Cloisite® 10 and Cloisite® 20, as its encapsulation and protection system. The biocidal activity of a restoration mortar with CBZ-clay complex and free CBZ was also evaluated. The information provided would be beneficial as an alternative of the current commercial biocides in the context of using less amount of active compound ensuring their bioefficacy and avoiding its leaching with a maximum heritage compatibility.

3.1.2. Materials and methods

3.1.2.1 Biocide

Carbendazim (CBZ) is a benzimidazole biocide with a molecular weight of 191.21 g mol^{-1}, water solubility of 8 mg L^{-1} and pKa of 4.2 (weak base). Pure analytical CBZ (purity = 99.5 %), purchased from Sigma-Aldrich (Spain), was used to prepare the external standards for its analysis, preparation of the composites and for sorption experiments. The chemical structure is represented in **Fig. S1**.

3.1.2.2. Adsorbents

Three layered materials were assayed as adsorbents for carbendazim. The reference used was Na-rich Wyoming montmorillonite (SWy-1) from The Clay Minerals Society (Purdue University), labeled as SW, had a basal spacing d_{001} of 15.1 Å, cationic exchange capacity (CEC) of 76.4 meq/100g, with principal exchange cations Na^{+} and Ca^{2+} and surface area of 11.5 m^2 g^{-1}. Two commercial organoclays, Cloisite® 10 and Cloisite® 20, which were generously provided by BYK Additives & Instruments, are labeled as CL10 and CL20, respectively. These two are organobentonites modified with dimethyl, benzyl, hydrogenated alkyl tallow quaternary ammonium and with dimethyl-bis (hydrogenated alkyl tallow) quaternary ammonium cations, respectively. The schematic structures of the interlayer cations are shown in **Fig. S2**.

3.1.2.3. Preparation of biocide-sorbent complexes

Carbendazim-sorbent complexes were prepared by adding, in duplicate, 30 mg of each layered sorbent to solutions of CBZ at different concentrations. Methanol (MeOH) and dimethylformamide (DMF) 25 % (v/v) in water were used as solutions. The volume and pH of the solution and the CBZ concentration were variable, and in this way, the optimization sorption process was planned. The initial conditions assayed are compiled in **Table 2**. The suspensions were equilibrated for 24 h at 20 ± 2 ºC until centrifugation (10 min, 10000 rpm). The supernatants were removed, filtered (0.45 µm) and the concentration of CBZ was determined by high-performance liquid chromatography (HPLC). The solids, CBZ-complexes, were dried overnight at 70 ºC for the characterization and bioassays experiments. Samples without adsorbents were also shaken for 24 h and served as controls. The amount of CBZ adsorbed on the layered materials was calculated by the difference between the initial (Ci) and final concentration after the equilibration time (Ce) biocide concentrations as follows:

$$Cs = [(Ci\text{-}Ce) \times V]/m$$

where Cs is the adsorbed amount of CBZ (mg g^{-1}), Ci is the initial concentration of CBZ (mg L^{-1}), Ce is the concentration of CBZ after the equilibration (mg L^{-1}), V is the volume of the assayed solution (L), and m is the mass of the adsorbent (g).

3.1.2.4. Biocide analysis by HPLC

Carbendazim concentration in samples was determined by high performance liquid chromatography (HPLC) using a Perkin Elmer Flexar chromatograph coupled to a UV diode-array detector. The analytical conditions were: Brownlee Analytical C18 column (150 mm length × 4.6 mm internal diameter and 5 µm); eluent mixture, 35:65 acetonitrile/water at a flow rate of 1 mL min^{-1}; 25 µL injection volume and UV detection at 280 nm. Data acquisition and the processing system were carried out with Chromera software. External calibration curves with four standard solutions between 26.2 and 261.5 µM were used in the calculations.

3.1.2.5. Characterization of the biocide-adsorbent complexes

The basal spacings (d_{001}) of layered complexes were determined with a Discover diffractometer (Bruker) with CuKα radiation, and the step size and step counting time used were 0.02° (2θ) and 0.65 s respectively. Attenuated total reflectance infrared (ATR-FTIR) spectra were recorded on a Perkin Elmer Dos spectrometer using 20 scans from 450 to 4000 cm^{-1} with a nominal resolution of 4 cm^{-1}. Zetasizer Nano ZSP (Malvern Instruments) was used to measure zeta-potential at 25 ^{o}C and at two pH values (4.0 and 6.6). Adsorption isotherms of N_2 on samples were measured at 77 K, using a Micromeritics ASAP2020 gas adsorption analyzer, to obtain the specific surface area (SSA) by applying the Brauner-Emmet-Teller (BET) method. TG-curves of the complexes were recorded on a Setaram Setsys Evolution 16/18 apparatus, in air atmosphere using a heating rate of 10 °C min^{-1} until reaching the final temperature of 600 ºC.

3.1.2.6. Biocidal assays

The bioactivity of clay-supported and free carbendazim as well as the untreated clays was tested by means of antimicrobial assays to determine their fungicidal and algaecide bioefficacy. For the biocidal assays, 100 mg of the sample were used: 15 mg of the biocide agent or the CBZ-complexes were dispersed in 85 mg of dolomite, a standard filler in building materials. This amount of each sample was placed in Petri dishes containing an inoculated strain of algae (*Stichococcus bacillaris*, UTEX 2542) or fungus (*Aspergilius Niger*, ATCC 16404) contained a specific agar for each microorganism. The Petri dishes were incubated at 22 ± 2 ° C for 7-14 days (*Aspergilius Niger*) or 30 days (*Stichococcus bacillaris*). At the end of the incubation, the antimicrobial properties of the samples were analyzed visually for the presence/absence of microorganisms. The same procedure was used to assess the antimicrobial activity of the mortars by placing the mortar specimens (with or without active principle) onto inoculated Petri dish. Based on the obtained results, the CL20-CBZ adsorption complex was selected as an additive for the mortar preparation

3.1.2.7. Mortar specimens with biocide additives

Lime mortars specimens (height = 5 mm) were prepared using a water-to-mortar ratio of 0.19. The mortar dosage is shown in **Table 1**. In order to prepare biocidal mortars, two powdered biocidal additives were added to the initial composition, the active ingredient (CBZ) dosage being 0.1 % w/w over the mortar. The selected additives were pure CBZ, and the prepared adsorption complex CL20-CBZ. The specimens were placed in a silicone mould and were kept at 20 ± 2 ºC for one week. After that, the

specimens were removed from the moulds and left to cure in a curing chamber (20 ± 2 °C and 65 ± 5 % relative humidity) for 21 days. As the high pH of the mortars prevented the growth of microorganisms even without any biocide in their composition, it was necessary to age all the mortar samples in a CO_2 chamber for a month (1% CO_2; 21 ± 2 ºC; 60 ± 10 % relative humidity) in order to carbonate the mortar surface. The chosen time was established after carrying out the fungicidal and algicidal activity assays on a reference mortar (i.e. without antimicrobial additives) aged for several periods in the CO_2 chamber. Finally, the aged mortars were subjected to biocidal activity assays and leaching tests.

Table 1. Composition for biocide and reference mortars[a]

Component	Dosage (% wt)
Aggregates	80 - 90
Lime	10 - 20
Pozzolan	0-1
Additives	0.0025 - 0.25

[a] Real dosage is protected by Grupo Puma S.L. manufacturer rights

3.1.2.8. Leaching tests

The ability of the mortars to keep the biocidal properties was checked after performing a standardized leaching test. The procedure is detailed in EA NEN 7375:2004 (Netherlands normalization institute standard, 2004) and is used to simulate the leaching of inorganic components from moulded and monolithic materials. The round mortar specimens (h = 5 mm, d = 25 mm) were placed in a sealed tank containing

180 mL of distilled water and the eluate was replenished at different times (0.25, 2.25, 4, 9, 16, 36, and 64 days). At the beginning (0.25 and 2.25 days) and at the end (64 days) of the leaching test, 2 mL were filtered (0.45 µm) and analyzed by using HPLC-UV to obtain the CBZ concentration. Once the leaching test was finished, the mortar specimens were dried and used for biocidal assays.

3.1.3. Results and discussion

3.1.3.1. Preliminary study of biocide adsorption on adsorbents

The amount of CBZ adsorbed by the layered compound at different ratios and solvent proportion is shown in **Table 2**. Adsorption values, Cs, were higher for a solution/adsorbent mass ratio equal to 1000. Slight adsorption was measured only when the methanol solvent was used while the adsorption was pH-dependent. In this way, the organic-modified layered materials, CL10 and CL20 displayed greater affinity at pH 6.6 instead of pH 4.0 (**Table 2**), which can be attributed to the hydrophobic environment provided by the organic modifiers, since at this pH (6.6), CBZ was predominantly present in the solution as a neutral form [35]. Alternatively, under the same conditions but at pH 4.0, the amount of CBZ adsorbed on SW was Cs = 24.6 mg g^{-1} while there was no adsorption at pH of 6.6. This result was indicative of the importance of the pH for ionizable compounds, which is the case of CBZ. The fungicide is a weak base with a p*K*a of 4.2 meaning that during the adsorption experiment at pH of 4.0 (**Table 2**) was partially protonated showing affinity for the negatively charged surface of SW, according to the zeta-potential measured (**Table S1**). CBZ could be also adsorbed by ion

exchange in the interlayer space [36,37], as will be confirmed by XRD technique. This has been well-documented for the sorption of other basic pesticides in their sorption on montmorillonites and soils [36,38,39]. The greatest adsorption of CBZ on SW was registered when DMF (25%) was the background solution, with the same trend as in the case of MeOH (25%), at pH 4.0. On the other hand, the organic adsorbents displayed the highest adsorption values at pH 6.6 (**Table 2**). This fact can be explained by the high solubility of CBZ in DMF (5 g L^{-1}) [40], which provides a higher number of free biocide molecules in the solution, facilitating contact with the clay surface.

Table 2. Solvent, absorbents, pH and concentration values used in the preparation of the CBZ-complexes compounds.

Solvent	pH[a]	CBZ solution concentration (mg L^{-1})	Solution/adsorbent ratio (mL per 0.03 g)	Cs[b] (mg g^{-1})		
				SW	CL10	CL20
25% MetOH	6.6	33	50	0	1.2	1.3
			667	0	0	0
			1000	0	10.4	11.6
			4000	0	0	0
	4.0	40	1000	24.6	0	0
25% DMF	6.6	181	1000	0	58.2	79.0
	4.0	181	1000	52.5	0	0

[a] pH adjusted with HCl or NaOH as requested

[b] Amount of CBZ in adsorbents assayed after 24 h equilibration.

3.1.3.2. Characterization of the selected CBZ-complexes

XRD characterization. The XRD patterns of CBZ, unmodified SW, CL10 and CL20 and the CBZ-complexes are shown in **Fig. 1**. The layered

materials exhibited the classical patterns characteristic of this type of materials, the diffraction peak of the basal plane, d_{001} appearing for SW and the Cloisites (**Fig. 1**), representative of a crystalline layered structure. After the incorporation of CBZ into the complexes, structural differences were observed. The incorporation of CBZ in SW slightly decreased the d_{001} value from 13.3 to 12.8 Å, **Fig. 1A**. This could be due to the strong interaction between the N-H groups of the biocide and the negative layer charges of SW, possibly maintaining the layers closer together [41], which is also in good agreement with the adsorption mechanism proposed above. It has been observed that for certain organic cations, the amino groups could be keyed into the ditrigonal cavities of the clay mineral, which hampered the expansion of the layers [19].

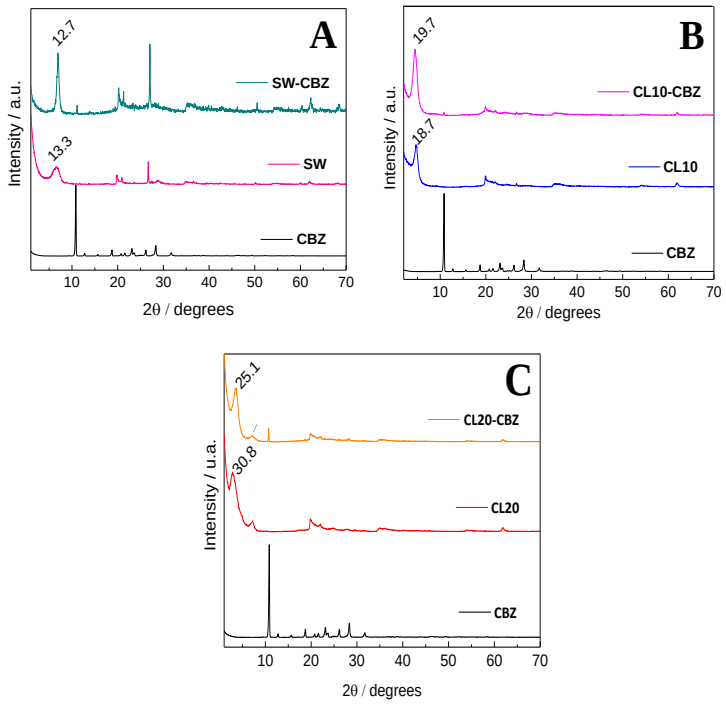

Fig. 1. X-ray diffraction patterns of CBZ, unmodified SW, CL10 and CL20 and the CBZ-complexes.

However, for CL10, the position of the basal reflection (d_{001}) is shifted to higher 2θ values which indicates an increase in the distance between the layers (from 18.7 Å to 19.7 Å) (**Fig. 1B**) probably because of the CBZ incorporation into the adsorbed alkyl chains of the modifier, a phenomenon known as "adsolubilitation" [42]. This expansion of basal spacing reveals that the host-guest interaction has taken place between clay layers. Conversely, for the CL20 sample, quite a substantial decrease in the basal spacing occurred (from 30.8 Å to 25.1 Å) when CBZ was incorporated (**Fig. 1C**). In this case, a very high basal spacing of the CL20 was caused by the organic modifier type, which possesses two alkyl tallows leading to a more paraffinic structure. Thus, the initial interactions between the alkyl chains of the modifier molecules have probably been altered by means of the organic solvent (DMF) used during the adsorption test, giving rise to a lower interlayer distance by the re-arrangement of the alkyl chains in the interlayer space [43]. Notwithstanding, the adsorption of CBZ in this case probably also occurs through a partitioning mechanism, formerly reported for this type of host-guest interactions [18,44,45].

FTIR Spectroscopy. The FTIR spectra of SW, CL10 and CL20 treated with CBZ, together with those of the blank clay samples and the pure biocide, were recorded to ascertain the presence of CBZ in the prepared complexes (**Fig. 2**). Band assignation was performed according to Bellamy [46]. In CBZ, the most important band recorded at 3325 cm^{-1} was assigned to the N-H stretching vibrations. Additionally, those appearing in the range of 2500-3000 cm^{-1} were attributed to the -CH stretch aromatic group. In addition, the band recorded at 1700 cm^{-1} was assigned to the carbonyl –C=O stretching vibration from the ester group -$COOCH_3$,

whereas the bands at 1625 cm^{-1} and 1585 cm^{-1} also corresponded with the bending of –N-H groups with the contribution of the carbonyl group, but were assigned as a part of carboxylate. Peaks at 1430 and 1600 cm^{-1} were attributed to C=C stretching of aromatic carbon bonds, which can overlap with the stretching -C=N bands, as well as the band recorded at 1392 cm^{-1} which was assigned to -C-N vibration. Regarding the layered materials, they exhibit their representative bands which were previously recorded for the montmorillonites samples (SW, CL10 and CL20).

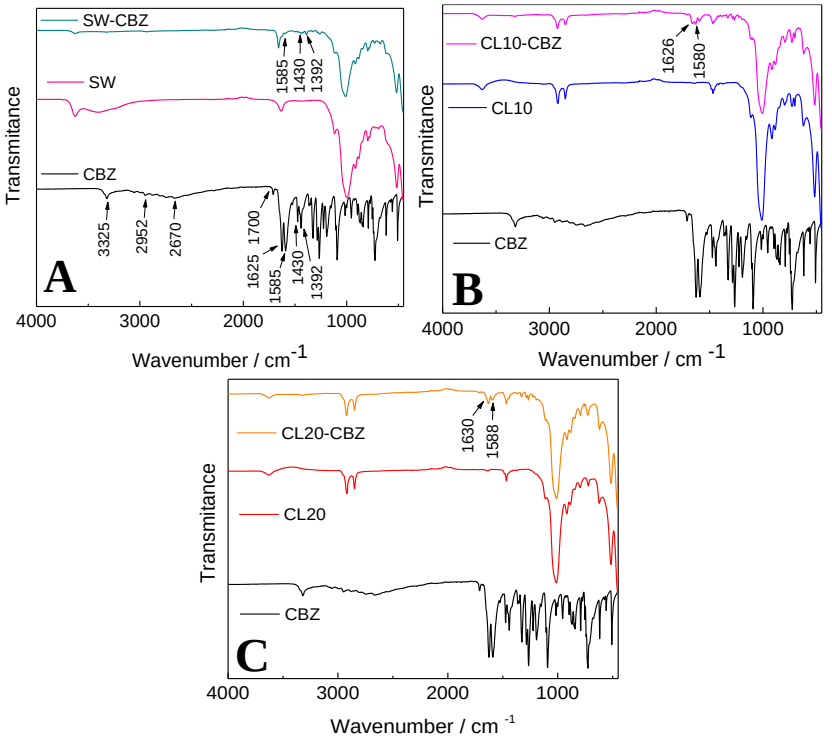

Fig. 2. The FTIR spectra of CBZ, SW, CL10 and CL20 treated with CBZ, indicating the main characteristic bands.

The presence of CBZ in the complexes was corroborated since the bands described above for the compound were detected in the samples.

Specifically, the bands belonging to C=C and -C=N stretching ranging between 1625 cm^{-1} and 1585 cm^{-1}, were more noticeable for the cases of CL10 and CL20 in comparison to SW (**Fig. 2**).

*Thermogravimetric analysis***.** The thermal stability of the CBZ and the complexes was also evaluated and the TGA curves are shown in **Fig. 3**. The mass losses are compiled in **Table S2**. The thermogravimetric analysis of the samples showed accordance with the data reported for the thermal decomposition of layered materials [47,48].

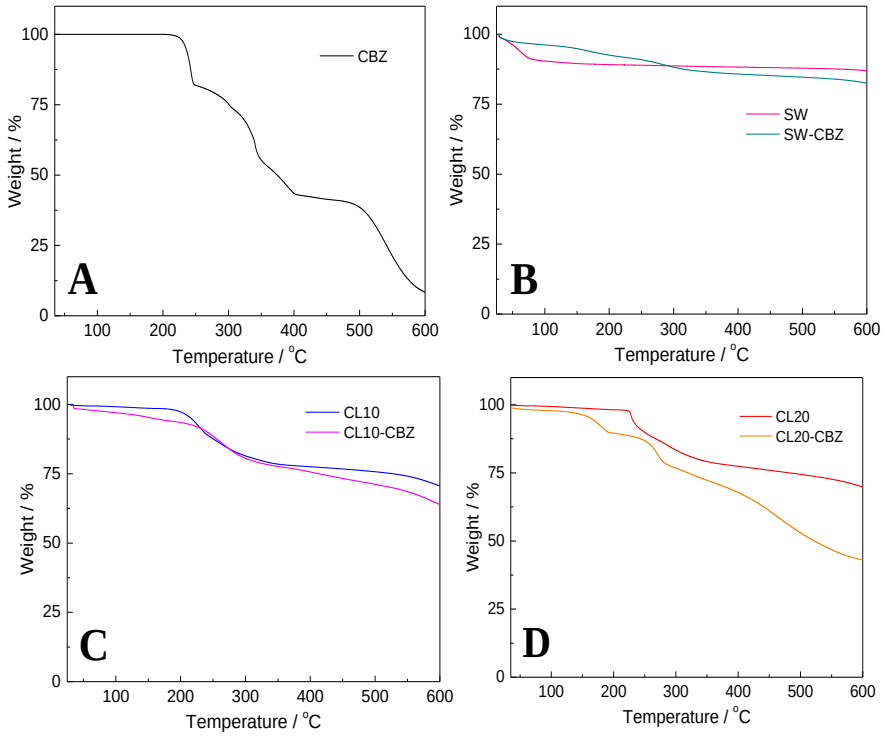

Fig. 3. Thermogravimetric analysis (TG) of CBZ and complexes prepared with SW, CL10 and CL20.

They are characterized by an initial mass loss due to the dehydration corresponding to the physisorbed water [19,48], as is shown

for SW with a mass loss of 9.9 % around 100 ºC (**Table S2**). The dehydroxylation of the clay minerals usually occurs at temperatures higher than 700 ºC [49]. Therefore it was not possible in our case to detect this step since the analyses were done at temperatures lower than 600 ºC [50]. For the organoclays, the mass losses occurring between 200-600 ºC are attributed to the loss of the organic cation, phase which can occur in several steps [49,51], as is shown in the case of CL20 (**Fig. 3**). The presence of CBZ in the different complexes had a different effect on the thermal stability. For instance, for CL10-CBZ, the second step was delayed in comparison with the pristine clay, suggesting some interactions of CBZ with the alkyl tallow of the CL10 (**Fig. 3**). A similar effect was also observed for CL20-CBZ, since various steps were registered in the range of 180-600 ºC, a most likely consequence of the different interactions between CBZ and the organoclays (**Fig. 3**), which also justified the re-arrangement of the alkyl chains by the presence of CBZ in the interlayer space according to DRX data. Interestingly, CBZ started to decompose at lower temperatures in the complexes in comparison to the free biocide. This fact has been also observed for the adsorption of CBZ on alumina particles [52]. The authors explained that lower thermal energy is required for the degrading of the adsorbed CBZ molecules, compared to those necessary for decomposing CBZ crystal lattice and its transformation into individual molecules.

Specific surface area. In general, all adsorbents showed low specific areas, following this order: CL20 (9.55 $m^2 g^{-1}$) < SW (11.5 $m^2 g^{-1}$) < CL10 (36.30 $m^2 g^{-1}$). There was no correlation with adsorption capacity of the adsorbent and SSA values. This is a consequence of the fact that the SSA values are not a crucial factor defining the adsorption capacity of

these layered materials, since N_2 is not able to access all the adsorption sites [18]. Thus, we can conclude here that the portioning mechanism has a key role here, meaning that the hydrophobic interactions are predominated.

3.1.3.3. Biocidal assays of CBZ-complexes powder samples

A preliminary biocidal assay was performed to assess the antimicrobial effect of the pure adsorbents (clays). The existence of antimicrobial effect was considered positive by the presence of a halo surrounding the powder placed on the dishes, determined by the visualization of the samples. Different antimicrobial behaviour was found for the different clays. None of them were able to preserve the fungal growth at 7 or 14 days of incubation (**Fig. 4**). The CL10 adsorbent was able to inhibit any algal growth and the CL20 exerted a protection halo preventing this growth. It is known that alkylammonium salts are used as biocide compounds [53], therefore, this observed antifungal activity could be associated to the modifier, since the montmorillonite SW did not show this feature. Moreover, it suggested that the alkylammonium groups were more bioavailable in CL10 as compared with CL20, in spite of the greater interlayer space of CL20 compared to CL10.

Subsequently, the fungicidal and algicidal activities of the CBZ-complexes were evaluated, with the aim of assessing the activity of a dry mix powder (using dolomite as filler) which could potentially be used as a biocide additive in mortar. Following the composition compiled in **Table 2**, the assays of biocidal activity were observed for the samples with low (**Fig. 5**) and high content (**Figs. 6** and **7**) of carbendazim, Cs. The samples were denoted SW-xx, CL10-xx and CL20-xx, where xx means the Cs value

measured for each CBZ-clay complex/dolomite mixture powder sample (**Table 2**).

Microorganism	Sample				
	Incubation days	Blank	SW	CL10	CL20
Aspergilius Niger	7				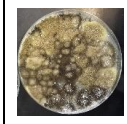
	14				
Stichococcus bacillaris	28	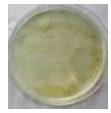		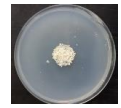	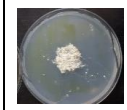

Fig. 4. Preliminary bioassay showing the algaeicidal and fungicidal activity of layered SW, CL10 and CL20 at different incubation times.

In the case of the antifungal effect on *Aspergilius Niger*, **Fig. 5** shows that samples with Cs around 1.0 mg g^{-1} were ineffective. The samples with Cs around 11.0 mg g^{-1} were able to stop the fungi growth within the first 7 days but not after 14 days. Only the sample SW-25, due to its higher Cs value, was effective as an antifungal compound (**Fig 5**). In **Fig. 6**, it was observed that all CBZ-complexes, once the Cs values are higher than 50 mg g^{-1}, exhibited an antifungal effect during every period of the microorganism incubation. Moreover, a bacterial contamination appeared on CL10-58 and CL20-79 samples due to the sample manipulation. Thus, it could be possible that the CBZ effect against bacteria is less effective in comparison to *Aspergillus Niger*.

Incubation days	Sample					
	CBZ	SW-25	CL10-1	CL10-10	CL20-1	CL20-11
7					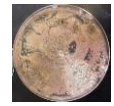	
14						

Fig. 5. Petri dishes photographs showing the fungicide activity of CBZ-complexes containing CBZ at low biocide content on the growth of Aspergilius Niger.

Incubation days	Sample			
	CBZ	SW-52	CL10-58	CL20-79
7				
14				

Fig. 6. Petri dishes photographs showing the fungicide activity of CBZ-complexes containing CBZ at high biocide content on the growth of Aspergilius Niger.

Following the fungi grown assays, the high content CBZ samples were studied as anti-algae ingredients against *Stichococcus Bacillaris*, **Fig. 7**. In this case, the best response as algaecide was found for powder samples when comprised of pure CBZ. However, a certain activity in a wider halo is also observed for CL10-58 and CL20-79 CBZ-complexes, being this inexistent for the SW-52 sample. By observing the algaecide response of the three CBZ-clays complexes, and that illustrated in **Fig. 4**, it seems that the anti-algae effect of CL organoclays is due to their chemical composition (including the structural alkylammonium groups) and not to

the adsorbed CBZ, the latter probably in too low an adsorbed amount to produce an effective algaecide response.

Incubation days	Sample			
	CBZ	SW-52	CL10-58	CL20-79
28		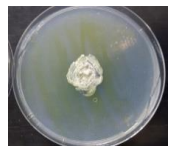		

Fig. 7. Petri dishes photographs showing the algaecide activity of CBZ-complexes containing CBZ at high biocide content on the growth of Stichococcus bacillaris.

It is worth noting the good biocide response exhibited by the CBZ-complexes when compared to the pure CBZ sample (**Figs. 5** and **6**), considering that the amount of carbendazim present in the dolomite mixtures of SW, CL10 and CL20 samples was around 93 % wt lower than those of the dolomite mixture of CBZ. This is indicative of the favourable dispersion of the biocide in the substrate itself giving rise to efficient responses substantially lowering the amount of biocide needed, which serves to reduce potential secondary environmental problems associated with the use of biocides [54].

3.1.3.4. Biocide mortars

The biocide-mortar activity was performed on lime-based mortars, which are mainly used in the rehabilitation tasks on cultural heritage buildings, in which the presence of microorganisms on their facade leads to serious external damages.

Among the three CBZ-complexes studied, the CL20-79 sample showed the best response to both fungicidal and algicidal activity. This sample was chosen as an additive to prepare a mortar with antimicrobial

activity. Firstly, the antimicrobial activity of the mortar without any CBZ or CBZ-complex additives was studied as a blank, because the mortar high pH could also have biocidal properties. Thus, the mortar specimens were studied before and after accelerated aging, for 30 and 60 day periods. A halo protection towards the growth of *Stichococcus Bacillaris* microorganism was observed for the sample mortar before aging, although the halo evanesced after 30 and 60 days of aging (**Fig. 8**). In this sense, the mortar carbonation process should have completed in 30 days (giving rise to the mortar surface pH decrease), as it reported in a similar study using clay additives in lime mortars [55]. Therefore, 30 days aged samples are of interest to clearly discern the antimicrobial activity of the biocide additive.

Microorganism	0 days	30 days	60 days
Aspergilius Niger	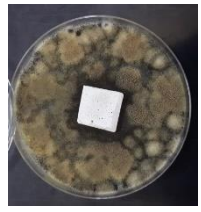	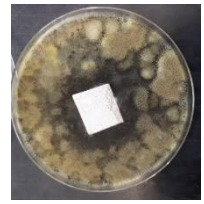	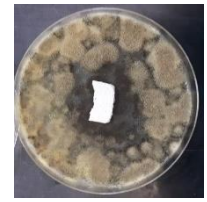
Stichococcus bacillaris	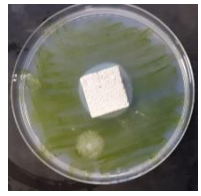		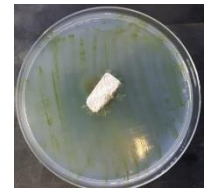

Fig. 8. Petri dishes photographs of reference mortars tested after different accelerating ageing times.

Fig. 9 illustrates the antimicrobial effect exhibited by CBZ-Mortar and CL20-79-Mortar. In order to carry out a comparative study and to evaluate the effectiveness of supporting biocides in clays, both samples of

mortars were prepared with the same charge of carbendazim, 70 mg per kg of mortar. The first observation concerns the leaching effect on mortars. Before leaching, both samples exhibit a powerful fungicidal and algicidal activity. However, after the leaching test, and due to the carbendazim release from the mortar, the antimicrobial effect clearly decreased. Moreover, the leaching test could also induced a decrease of surface pH of the mortars, so the microbial growth could be favoured. Of importance, the halo protection remained greater in the CL20-79-Mortar which would indicate that the stronger carbendazim bonding to the clay adsorbate preserved its release into the environment to a greater extent in comparison with the CBZ-Mortar. In fact, the released amount of CBZ was measured at the beginning and at the end of the performed leaching tests (**Table 3**), the results indicating a lower amount of released active for the CL20-79-Mortar. Thus, taking into account the total moles leached for every mortar sample, 17.8 % less of CBZ is released from CL20-79-Mortar in comparison with the CBZ-Mortar. The best leaching data observed for the adsorption complex are explained by the stronger interactions between the CBZ molecules and the organic modifier, slowing down the release of CBZ molecules into the environment.

Microorganism	Incubation days	Leaching test	Sample	
			CBZ	CL20-79
Aspergilius Niger	14	NO		
	7	YES	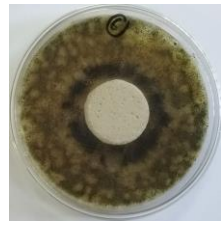	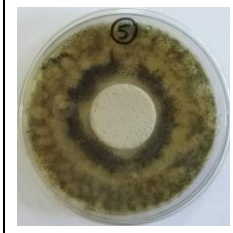
	14		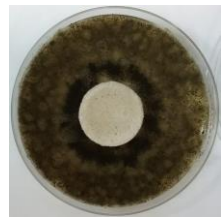	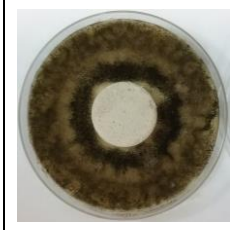
Stichococcus bacillaris	28	NO		
		YES		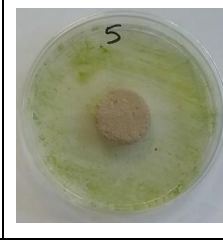

Fig. 9. Petri dishes photographs of biocidal mortars tested before and after the leaching test

Table 3. Amount of CBZ leached during the standardized leaching test of the mortars.

Time (h)	$(C\ C_0^{-1}) \times 100$ (%)	
	CL20-79	CBZ
6	2.52	3.52
54	2.70	2.88
1536	0.42	0.47

3.1.4. Conclusions

We have prepared different complexes of the biocide carbendazim based on layered clay minerals natural Wyoming montmorillonite SWy-1 and two commercial organoclays, Cloisite® 10 and Cloisite® 20. The characterization of the samples showed the presence of the biocide in all the prepared composites. XRD and TGA techniques confirmed that the part of the CBZ was adsorbed in the interlayers of the clay minerals studied here. The bioassays showed that the CBZ-clay complexes displayed appreciable fungicidal activities when Cs was higher than 50 mg g^{-1}, whereas the CL20-CBZ complex showed the best fungicidal and algaecidal effect. The use of clays as biocides supports significantly decreased the amount of active necessary to obtain mixed powders with a positive antimicrobial response and its corresponding environmental benefits. Furthermore, the CL20-CBZ adsorption complex was used as an additive in a typical lime mortar, providing a positive biocidal effect. Finally, the endurance of the biocidal action present in the mortar was checked after 64 days of leaching tests. In this sense, the amounts of leached biocide were lower for CL20-CBZ-Mortar compared to CBZ-mortar. The fact that carbendazim was attached to the clay, and not only

mixed with the mortar components, would enhance the preservation of the active principle over time. Because of the antimicrobial activity developed by clays-complexes containing only low amounts principle active and their preservation on time, the prepared complexes are highly interesting for its potential application as biocide additives for building materials.

3.1.5. Acknowledgements

Spanish government (MINECO, RTC-2015-3916-6) and Junta de Andalucía government (PAI Groups FQM-214 and FQM-175) financed this work. A. Pastor acknowledges a contract (FPU16/05041) from the Ministerio de Educación, Cultura y Deporte (MECD) to research at the University of Córdoba (Spain). The authors also acknowledge the support of Grupo Puma S.L.

3.1.6. References

[1] S. Thirumalini, S.K. Sekar, B. Bhuvaneshwari, R. Nagesh, Bio-inorganic composites as repair mortar for heritage structures, J. Struct. Eng. 42 (2015) 294–304.

[2] T. Rosado, M. Gil, A.T. Caldeira, M.D.R. Martins, C.B. Dias, L. Carvalho, J. Mirão, A.E. Candeias, Material characterization and biodegradation assessment of mural paintings: Renaissance frescoes from Santo Aleixo Church, Southern Portugal, Int. J. Archit. Herit. 8 (2014) 835–852. doi:10.1080/15583058.2012.751466.

[3] T.H. Tran, A. Govin, R. Guyonnet, P. Grosseau, C. Lors, E. Garcia-Diaz, D. Damidot, O. Devès, B. Ruot, Influence of the intrinsic characteristics of mortars on biofouling by Klebsormidium flaccidum, Int. Biodeterior. Biodegrad. 70 (2012) 31–39. doi:10.1016/j.ibiod.2011.10.017.

[4] A. De Turris, L. Ocando, M.F. Romero, M. Fernández, ¿Pueden los Microorganismos Impactar los Materiales de Construcción? A review, Gac. Técnica. (2013) 23–33.

[5] S. Scheerer, Microbial biodeterioration of outdoor stonemonuments. Assessment method and control strategies, Cardiff University, 2008.

[6] A.A. Gorbushina, Life on the rocks, Environ. Microbiol. 9 (2007) 1613–1631. doi:10.1111/j.1462-2920.2007.01301.x.

[7] R. Černý, A. Kunca, V. Tydlitát, J. Drchalová, P. Rovnaníková, Effect of pozzolanic admixtures on mechanical, thermal and hygric properties of lime plasters, Constr. Build. Mater. 20 (2006) 849–857. doi:10.1016/j.conbuildmat.2005.07.002.

[8] E. Union, Directive 98/8/EC of the European Parliament and of the Council of 16 February 1998 Concerning the Placing of Biocidal Products on the Market, (2004) 301–365. doi:10.1002/352760197x.app1.

[9] H. Singer, S. Jaus, I. Hanke, A. Lück, J. Hollender, A.C. Alder, Determination of biocides and pesticides by on-line solid phase extraction coupled with mass spectrometry and their behaviour in wastewater and surface water, Environ. Pollut. 158 (2010) 3054–3064. doi:10.1016/j.envpol.2010.06.013.

[10] M.. Nugari, O. Salvadori, Biocides and treatment of stone: limitations and future prospects. Art, biology, and conservation: biodeterioration of works of art, The Metropolitan Museum of Art, 518-535, 2003.

[11] M. Sameño, El biodeterioro en edificios del patrimonio cultural. Metodología de evaluación de tratamientos biocidas, Universidad de Sevilla, 2018.

[12] P.R. Rossi-Doria, Mortars for restoration: Basic requirements and quality control, Mater. Struct. 19 (1986) 445–448. doi:10.1007/BF02472148.

[13] S. Martinez-Ramirez, F. Puertas Maroto, M.T. Blanco Varela, Morteros de reparación basados en cal. Ensayos de envejecimiento acelerado, Mater. Construcción. 45 (1995) 35–45. http://materconstrucc.revistas.csic.es.

[14] C. Bai, S. Zhang, L. Huang, H. Wang, W. Wang, Q. Ye, Starch-based hydrogel loading with carbendazim for controlled-release and water absorption, Carbohydr. Polym. 125 (2015) 376–383. doi:10.1016/j.carbpol.2015.03.004.

[15] P. Scarfato, E. Avallone, L. Incarnato, L. Di Maio, Development and evaluation of halloysite nanotube-based carrier for biocide activity in construction materials protection, Appl. Clay Sci. 132–133 (2016) 336–342. doi:10.1016/j.clay.2016.06.027.

[16] J. Cornejo, R. Celis, I. Pavlovic, M.A. Ulibarri, Interactions of pesticides with clays and layered double hydroxides: a review, Clay Miner. 43 (2008) 155–175. doi:10.1180/claymin.2008.043.2.01.

[17] W.F. Jaynes, S.A. Boyd, Clay mineral type and organic compound sorption by hexadecyltrimethlyammonium-exchanged clays, Soil Sci. Soc. Am. J. 55 (1991) 43–48.

[18] B. Gámiz, M.C. Hermosín, J. Cornejo, R. Celis, Hexadimethrine-montmorillonite nanocomposite: Characterization and application as a pesticide adsorbent, Appl. Surf. Sci. 332 (2015) 606–613. doi:10.1016/j.apsusc.2015.01.179.

[19] B. Gámiz, R. Celis, M.C. Hermosín, J. Cornejo, C.T. Johnston, Preparation and characterization of spermine-exchanged montmorillonite and interaction with the herbicide fluometuron, Appl. Clay Sci. 58 (2012) 8–15. doi:10.1016/j.clay.2012.02.005.

[20] B. Sarkar, Y. Xi, M. Megharaj, G. Krishanamurti, M. Bowman, H. Rose, R. Naidu, Bioreactive Organoclay : A New Technology for Environmental Remediation, Crit. Rev. Environ. Sci. Technol. (2012) 37–41. doi:doi/abs/10.1080/10643389.2010.518524.

[21] H. He, Y. Ma, J. Zhu, P. Yuan, Y. Qing, Organoclays prepared from montmorillonites with different cation exchange capacity and surfactant configuration, Appl. Clay Sci. 48 (2010) 67–72. doi:10.1016/j.clay.2009.11.024.

[22] G. Lagaly, Pesticide–clay interactions and formulations, Appl. Clay Sci. 18 (2001) 205–209. doi:10.1016/S0169-1317(01)00043-6.

[23] A. Marco, S. Santos, J. Caetano, M. Pintado, E. Vieira, P.R. Moreira, Basil essential oil as an alternative to commercial biocides against fungi associated with black stains in mural painting, Build. Environ. 167 (2020) 106459. doi:10.1016/j.buildenv.2019.106459.

[24] M. Carrizosa, M. Calderon, M. Hermosin, J. Cornejo, Organosmectites as sorbent and carrier of the herbicide bentazone, Sci. Total Environ. 247 (2000) 285–93.

[25] C. Trigo, R. Celis, M.C. Hermosín, J. Cornejo, Organoclay-based formulations to reduce the environmental impact of the herbicide diuron in olive groves, Soil Sci. Soc. Am. J. 73 (2009) 1652–1657. doi:10.2136/sssaj2008.0349.

[26] S. Andrejkovičová, C. Alves, A. Velosa, F. Rocha, Bentonite as a natural additive for lime and lime–metakaolin mortars used for restoration of adobe buildings, Cem. Concr. Compos. 60 (2015) 99–110. doi:10.1016/j.cemconcomp.2015.04.005.

[27] S. Andrejkovičová, A.L. Velosa, E. Ferraz, F. Rocha, Influence of clay minerals addition on mechanical properties of air lime–metakaolin mortars, Constr. Build. Mater. 65 (2014) 132–139. doi:10.1016/j.conbuildmat.2014.04.118.

[28] C. He, Thermal stability and pozzolanic activity of raw and calcined mixed-layer mica/smectite, Appl. Clay Sci. 17 (2000) 141–161. doi:10.1016/S0169-1317(00)00011-9.

[29] F. Winnefeld, K.G. Böttger, How clayey fines in aggregates influence the properties of lime mortars, Mater. Struct. 39 (2007) 433–443. doi:10.1617/s11527-005-9023-6.

[30] M.M. Urbanczyk, K. Bester, U.E. Bollmann, Multi-layered approach

to determine diffusion coefficients through polymer films: Estimating the biocide release from paints, Build. Environ. 148 (2019) 294–298. doi:10.1016/j.buildenv.2018.11.011.

[31] N. Bandow, M.D. Aitken, A. Geburtig, U. Kalbe, C. Piechotta, U. Schoknecht, F.-G. Simon, I. Stephan, Using Environmental Simulations to Test the Release of Hazardous Substances from Polymer-Based Products: Are Realism and Pragmatism Mutually Exclusive Objectives?, Materials (Basel). 13 (2020) 2709. doi:10.3390/ma13122709.

[32] R. Arreche, P. Vázquez, Green biocides to control biodeterioration in materials science and the example of preserving World Heritage Monuments, Curr. Opin. Green Sustain. Chem. 25 (2020) 100359. doi:10.1016/j.cogsc.2020.100359.

[33] U. Schoknecht, J. Gruycheva, H. Mathies, H. Bergmann, M. Burkhardt, Leaching of biocides used in façade coatings under laboratory test conditions, Environ. Sci. Technol. 43 (2009) 9321–9328. doi:10.1021/es9019832.

[34] Netherlands normalization institute standard, NEN7375, 2004. The Determination of the Availability of Inorganic Components for Leaching. Netherlands Normalization Institute Standard, Netherlands., n.d.

[35] N. Ni, T. Sanghvi, S.H. Yalkowsky, Solubilization and preformulation of carbendazim, Int. J. Pharm. 244 (2002) 99–104. doi:10.1016/S0378-5173(02)00318-6.

[36] G. Dios, E. Romero, F. Sánchez-Rasero, Carbendazim adsorption on montmorillonite, peat and soils, J. Soil Sci. 43 (1992) 99–111. doi:10.1111/j.1365-2389.1992.tb00122.x.

[37] T. Paszko, Effect of pH on the adsorption of carbendazim in Polish mineral soils, Sci. Total Environ. 435–436 (2012) 222–229. doi:10.1016/j.scitotenv.2012.07.013.

[38] R. Celis, J. Cornejo, M.C. Hermosín, W.C. Koskinen, Sorption-desorption of atrazine and simazine by model soil colloidal components, Soil Sci. Soc. Am. J. 61 (1997) 436–443. doi:10.2136/sssaj1997.03615995006100020010x.

[39] D. a Laird, P.Y. Yen, W.C. Koskinen, T.R. Steinheimer, R.H. Dowdy, Sorption of atrazine on Soil Clay Components., Environ. Sci.

Technol. 28 (1994) 1054–61. doi:10.1021/es00055a014.

[40] W.H.O. WHO, WHO_PCS_DS_96.89.pdf, 1996.

[41] J.M. Serratosa, J. Rausell-Colom, J. Sanz, Charge density and its distribution in phyllosilicates: Effect on the arrangement and reactivity o adsorbed species, J. Mol. Catal. 27 (1984) 225–234.

[42] E. Klumpp, C. Contreras-Ortega, P. Klahre, F.J. Tino, S. Yapar, C. Portillo, S. Stegen, F. Queirolo, M.J. Schwuger, Sorption of 2,4-dichlorophenol on modified hydrotalcites, Colloids Surfaces A Physicochem. Eng. Asp. 230 (2003) 111–116. doi:10.1016/j.colsurfa.2003.09.018.

[43] G. Lagaly, Inorganic Layer Compounds, Naturwissenenschaften. 68 (1981) 82–88.

[44] D. Chaara, F. Bruna, M.A. Ulibarri, K. Draoui, C. Barriga, I. Pavlovic, Organo/layered double hydroxide nanohybrids used to remove non ionic pesticides, J. Hazard. Mater. 196 (2011) 350–359. doi:10.1016/j.jhazmat.2011.09.034.

[45] S.A. Boyd, M.A.X.M. Mortland, G.T. Chiou, Sorption characteristics of organic compounds on hexadecyltrimethylammonium-smectite, Soil Sci. Soc. Am. J. 657 (1988) 652–657.

[46] L.J. Bellamy, The Infrared Spectra of Complex Molecules, 3 rd, London, n.d.

[47] S. Yariv, The role of charcoal on DTA curves of organo-clay complexes: an overview, Appl. Clay Sci. 24 (2004) 225–236. doi:10.1016/j.clay.2003.04.002.

[48] I. Lapides, M. Borisover, S. Yariv, Thermal analyis of hexadecyltrimethylammonium–montmorillonites, J. Therm. Anal. Calorim. 105 (2011) 921–929. doi:10.1007/s10973-011-1304-4.

[49] Y. Xi, W. Martens, H. He, R.L. Frost, Thermogravimetric analysis of organoclays intercalated with the surfactant octadecyltrimethylammonium bromide, J. Therm. Anal. Calorim. 81 (2005) 91–97. doi:10.1007/s10973-005-0750-2.

[50] J.M. Cervantes-Uc, J. V. Cauich-Rodríguez, H. Vázquez-Torres, L.F. Garfias-Mesías, D.R. Paul, Thermal degradation of commercially available organoclays studied by TGA-FTIR, Thermochim. Acta. 457 (2007) 92–102. doi:10.1016/j.tca.2007.03.008.

[51] M. Borisover, N. Bukhanovsky, I. Lapides, S. Yariv, The potential of thermally treated organobentonites to adsorb organic compounds from water, Appl. Clay Sci. 67–68 (2012) 151–157. doi:10.1016/j.clay.2011.11.005.

[52] B.D. Mattos, W.L.E. Magalhães, Design and preparation of carbendazim-loaded alumina nanoparticles as a controlled-release biocide for wood protection, Int. Biodeterior. Biodegrad. 123 (2017) 174–181. doi:10.1016/j.ibiod.2017.06.019.

[53] B. Gutarowska, B. Brycki, K. Majchrzycka, A. Brochocka, New bioactive polymer filtering material composed of nonwoven polypropylene containing alkylammonium microbiocides on a perlite carrier, Polimery/Polymers. 55 (2010) 568–574. doi:10.14314/polimery.2010.568.

[54] D. Hernández-Moreno, M. Blázquez, O. Andreu-Sánchez, A. Bermejo-Nogales, M.L. Fernández-Cruz, Acute hazard of biocides for the aquatic environmental compartment from a life-cycle perspective, Sci. Total Environ. 658 (2019) 416–423. doi:10.1016/j.scitotenv.2018.12.186.

[55] S. Martínez-Ramírez, F. Puertas, M.T.B. Varela, Carbonation process and properties of a new lime mortar with added sepiolite, Cem. Concr. Res. 25 (1995) 39–50. doi:10.1016/0008-8846(94)00110-K.

Appendix I: Supplementary Information

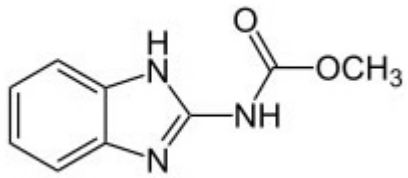

Fig. S1. Chemical structure of carbendazim .

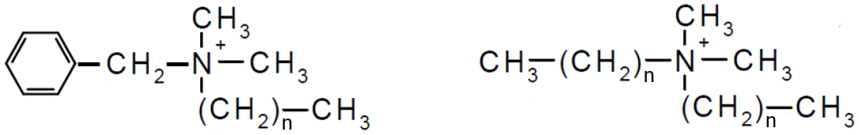

Fig. S2. Chemical structure of organic modifier cation of CL10 (left) and CL20 (right).

Table S1. Zeta potential values (mV) measured for SW, CL10 and CL20 at different pH values.

Adsorbent	Z potential; pH = 6.6 (mV)	Z potential; pH = 4.0 (mV)
SW	- 20.4	- 18.8
CL10	+ 20.7	+ 28.7
CL20	+ 20.0	+ 29.6

Table S2. Steps and mass losses of CBZ, adsorbents and complexes registered in TGA measurements.

	Step	Mass loss (%)
CBZ	217.5 ºC → 248.0 ºC	15.72
	248.0 ºC → 344.7 ºC	26.61
	344.7 ºC → 401.2 ºC	12.80
	401.2 ºC → 496.8 ºC	4.13
	496.8 ºC → 600.0 ºC	31.82
SW	25.0 ºC → 82.7 ºC	9.90
	82.7 ºC → 600.0 ºC	3.90
SW-CBZ	25.0 ºC → 295.0 ºC	12.15
	295.0 ºC → 600.0 ºC	5.18
CL10	177.8 ºC → 237.5 ºC	8.27
	237.5 ºC → 340.2 ºC	10.76
	340.2 ºC → 600.0 ºC	8.34
CL10-CBZ	25.0 ºC → 219.7 ºC	7.70
	219.7 ºC → 334.6 ºC	14.13
	334.6 ºC → 600.0 ºC	14.14
CL20	222.0 ºC → 347.0 ºC	17.70
	347.0 ºC → 600.0 ºC	9.35
CL20-CBZ	25.0 ºC → 149.1 ºC	3.24
	149.1 ºC → 188.4 ºC	6.67
	188.4 ºC → 251.3 ºC	3.06
	251.3 ºC → 281.8 ºC	8.84
	281.8 ºC → 600.0 ºC	35.14

3.2. ZnO on rice husk: a sustainable photocatalyst for urban air purification.

ELSEVIER

Chemical Engineering Journal

Volume 368, 15 July 2019, Pages 659-667

ZnO on rice husk: A sustainable photocatalyst for urban air purification

Adrián Pastor, José Balbuena, Manuel Cruz-Yusta, Ivana Pavlovic, Luis Sánchez

Departamento de Química Inorgánica, Instituto Universitario de Investigación en Química Fina y Nanoquímica IUNAN, Universidad de Córdoba, Campus de Rabanales, E-14071 Córdoba, Spain

Received 20 October 2018, Revised 28 February 2019, Accepted 2 March 2019, Available online 4 March 2019.

https://doi.org/10.1016/j.cej.2019.03.012

Highlights

- RHA support influences morphological and physical characteristics of deposited ZnO.
- ZnO@SiO_2 based photocatalysts exhibit outstanding De-NO_X performance.
- De-NOx selectivity values above 90% are found.
- The photocatalyst is prepared by a cost-effective and easily scalable methodology.
- The photocatalyst can be used repeatedly in simulated real life conditions.

ABSTRACT

A cost-effective and sustainable De-NO_X photocatalyst is prepared using zinc acetate and rice husk. ZnO@SiO_2 samples are obtained from the calcination of a homogenised precursor mixture at 600 ^oC. ZnO nanoparticles (70 – 180 nm) grow aggregated in spheres and well dispersed (40 – 53 m^2g^{-1} surface area) covering the silicon skeleton. The corresponding band gap for ZnO@SiO_2 photocatalysts was estimated at 3.1 – 3.2 eV. When the samples are irradiated by sunlight in a nitrogen oxide atmosphere the NO → HNO_2 → NO_2 → NO_3^- photochemical oxidation takes place. In comparison to unsupported ZnO and TiO_2-P25, ZnO@SiO_2 samples exhibit high NO_X removal values (70%) and outstanding selectivity (> 90%), the latter related to the sensitivity of zinc oxide towards NO_2 gas. This new photocatalyst is easily recyclable and reusable.

Keywords: *Zinc oxide, Photocatalyst, Nitrogen oxides*

GRAPHICAL ABSTRACT

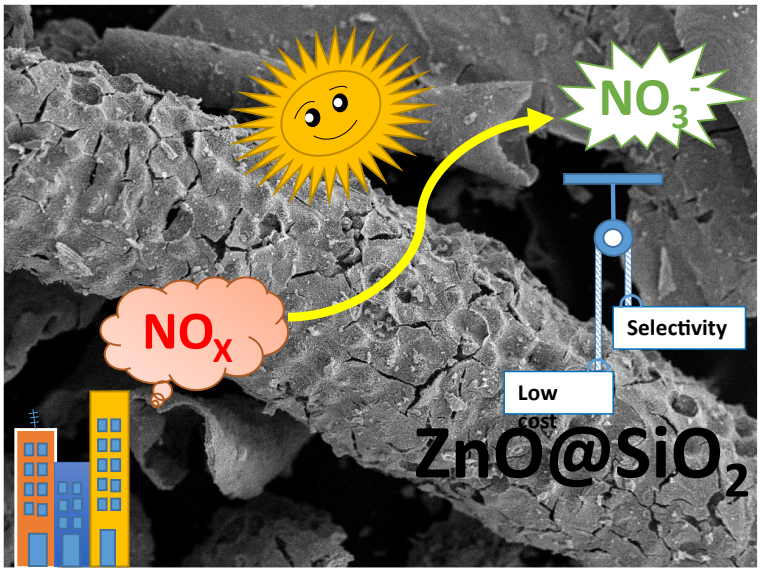

3.2.1. Introduction

Semiconductor (SC) photocatalysts have been widely studied as suitable materials for environmental remediation. A multitude of compounds, based mainly on TiO_2, ZnO, CdS, Fe_2O_3 and WO_3, were reported for the photocatalytic degradation of a variety of water, air and solid pollutants [1, 2]. In the recent years, an increasing interest has arisen in the study of the photochemical oxidation (PCO) of nitrogen oxide gases as a sustainable tool to combat urban air pollution [3].

Because of their toxicity, the presence of nitrogen oxides, commonly referred as NO_X - nitric oxide (NO) and nitrogen dioxide (NO_2) - , in the urban environment is a high risk for human health [4]. Thus, environmental agencies in the USA and European Community limit the hourly NO_X air concentration to 0.1 ppm and 0.2 ppm, respectively. However, these limits are difficult to be attained because the NO_X emissions rates from older vehicles worsen as time goes on [5]. In fact, nowadays higher NO_X levels are measured in very populated cities all over the world and thousands of early deaths worldwide are associated with these NO_X emissions [6, 7]. Today´s research works have demonstrated the potential applicability of semiconductors in directly removing large amounts of NO_X gases (De-NO_X action) from the urban centres in our cities. In fact, at present, depolluting building materials, using TiO_2 as a photocatalytic additive, are integrated in some advanced buildings in an attempt to achieve effective NO_X de-pollution in urban areas [8]. In this sense, many researchers pay attention to the preparation of modified titania with enhanced De-NO_X photocatalytic performance [9-13].

However, it´s necessary to point out that TiO_2 has just been proposed to be classified as possibly causing cancer when inhaled [14]. This could limit some of its applications and, therefore, a rapid advance in

the study and development of new De-NO_X photocatalysts is desired. g-C_3N_4, N-$(BiO)_2CO_3$, BiOBr, Bi/$ZnWO_4$, or Ni-Bi_2O_3 among others, were reported as alternative materials towards the photochemical NO abatement [15-20]. In this work we study the De-NO_X ability of ZnO, which is not considered to be a threat to consumers health [21]. Even though ZnO is a preferred photocatalyst because of its high photosensitivity, mechanical-thermal stability and tuneable morphology, only a few studies have been recently reported for this specific environmental application. Some of them are devoted to enhancing titanium dioxide De-NO_X efficiency through the preparation of TiO_2/ZnO composites [22, 23]. In the case of a pure ZnO photocatalyst, whose preparation proceeded by using amine derivatives or ionic liquids, the NO conversion photo-efficiency was equal to or lower than 50% [24-28]. On the other hand, the preparation of ZnO spheres by a carbon template via the one-step process is highly interesting, the resulting compound showing the highest photocatalytic activity [28]. Herein we propose a very simple procedure that allows us to obtain a ZnO efficient photocatalyst by using rice husk ash (RHA) as a support, a strategy successfully employed in the preparation of metals and metal oxides (photo)catalysts [29-32]. Rice husk (RH) is an agricultural waste product, the ash of which contains about 92–95% silica (SiO_2) [29], and when used to synthesize silica nanoparticles, offers additional advantages, including greener raw materials, lower costs, and higher sustainability [30]. The physicochemical characterization and photocatalytic activity of different ZnO@SiO_2 samples are presented. Remarkably, as the main novelty, De-NO_X ZnO based photocatalysts are prepared using a cost-effective and large-scale synthetic procedure and exhibiting the highest NO photo-chemical conversion efficiency and selectivity values reported. Due to the high selectivity values found, the

use of photocatalysis proves to be sustainable as a NO abatement process.

3.2.2. Materials and methods

3.2.2.1 Preparation of ZnO supported photocatalyst

The complete characterization of RHA support is provided in **Supplementary Information** (**SI**; **Figures S1 – S4** and **Table S1**). With the aim of obtaining a cost-effective and large-scale synthesis procedure in mind, the methodology used for the preparation of a photocatalyst was as simple as possible. Zinc acetate is a very cheap salt that is successfully used in the synthesis of ZnO-based materials [33]. $Zn(OAc)_2{\cdot}_2H_2O$ (99,0%, Sigma-Aldrich) and RH were used as precursor components, in the 0.65 weight ratio. This ratio was selected following that previously reported as optimum in the preparation of a catalyst on RHA as a support [34], focussing the attention of this preliminary work in the preparative methodology. Two methods were chosen in order to enhance the contact between the precursor components:

i) Liquid to solid deposition. 30.73 g of $Zn(OAc)_2{\cdot}_2H_2O$ was dissolved in 150 mL of milliQ water. Subsequently, 20 g of RH was added to the vessel. After 30 min of magnetic stirring, the paste was dried at 80 ^oC for 4 days. Later, the product was calcined at 600 ^oC for 2 and 4 hours. The photocatalyst samples obtained were denominated as dZn@RHA-2 and dZn@RHA-4, respectively.

ii) Mechanical milling. A mixture of 30.73 g of $Zn(OAc)_2{\cdot}_2H_2O$ and 20 g of RH was milled using a planetary mill (45 min, 300 rpm). The collected product was calcined at 600 ^oC for 2 and 4 hours. The

photocatalyst samples obtained were denominated as mZn@RHA-2 and mZn@RHA-4, respectively.

3.2.2.2. Sample characterization

Energy Dispersive X-ray Fluorescence analysis (XRF) was done in a ZSX Primus IV (Rigaku) equipment. The carbon content elemental analysis was determined by using an Eurovector EA 3000 elemental instrument. Crystalline phases were identified by using X-ray diffraction (XRD). The XRD patterns were recorded in a Bruker D8 Discover A25 diffractometer. The crystal size of the samples was determined by means of the Scherrer equation. This equation was calculated with DIFFRACT.EVA V3.1 software. The morphology of the samples was examined by scanning electron microscopy (SEM). SEM images were obtained with a Jeol JMS-6400 microscope. Particle size distribution was estimated using a Visiolog 6.1 software. Nitrogen absorption isotherms were obtained at 77.4 K on an ASAP 2020 instrument from Micromeritics, from which the specific surface areas were calculated using the multipoint Brunauer–Emmett–Teller (BET) and Barrett-Joyner-Halenda (BJH) methods. Diffuse reflectance (DR) spectra were recorded using a Varian Cary 1E spectrophotometer. Thermogravimetry (TGA) was carried out with a Mettler Toledo in air atmosphere (flow: 100 mL min^{-1}) from room temperature to 600 ^{o}C (heating rate of 10 ^{o}C min^{-1}).

Additional information is provided in **SI**.

3.2.2.3. Photocatalytic activity tests

The photocatalytic activity of the materials towards the oxidation of NO was studied using a protocol similar to the standardised test method developed for the characterisation of air-purification performance, ISO 22197-1 [35]. However, some of the specifications described in this standard were modified in order to obtain better performance with the samples of this study. Thus, the tests were carried out on a 50 mm × 50 mm sample holder placed in a laminar flow reactor [35]. Artificial sunlight irradiation (Solarbox 3000e RH light irradiation box) was obtained with an Xe lamp with controlled irradiance (25 and 580 Wm^{-2} for UV and visible, respectively). For each De-NO_X test, 1.0 g of the sample supported on the sampler holder inside the reactor was used. As a pollutant, a mixture of air/NO was sent to the photoreactor with a NO concentration of 150 ppb (obtained by mixing synthetic air and pure NO). This concentration was chosen because it is representative of NO concentrations found during intense photochemical pollution periods in urban environments [6], having already been successfully adopted in previous research works [15, 36, 37]. The gas mixture was supplied by using a flow rate of 0.30 L min^{-1} and fixing the relative humidity at 50 ± 5%. The measurement of the concentration of NO, NO_X and NO_2 gases was carried out using a chemiluminescence analyser (model Environnement AC32M). Each test was repeated three times to obtain average concentration values. The calculated standard deviations were ± 0.3 ppb for NO concentration and ± 1.0 ppb for NO_2 and NO_X concentrations. The photocatalytic efficiency was evaluated following the NO conversion (%), NO_2 released (%) and NO_X conversion (%) parameters (defined in SI).

3.2.3. Results and discussion

3.2.3.1. Photocatalyst characterisation

ZnO@SiO_2 supported photocatalysts were obtained after the calcination of the $Zn(OAc)_2$/RH precursor mixtures. The chemical composition of samples is provided in **Table S2**. The XRD patterns obtained for the four samples are shown in **Fig. 1**. Only peaks ascribable to hkl reflections of hexagonal structure of ZnO (wurtzite) were detected. The diffraction peaks at 31.5°, 34.2°, 36.1°, 47.3°, 56.4°, 62.7°, 66.1°, 67.7° and 68.9° two theta degrees can be attributed to (100), (002), (101), (102), (110), (103), (200), (112) and (201) crystal planes, respectively [38]. Apart from its amorphous character, the negligible presence of the silica halo expected at 22º (**Fig. S5**) [39] would be indicative of good zinc oxide covering on the silica support. For comparison purposes, ZnO without the use of RH was also prepared using the same calcination procedure.

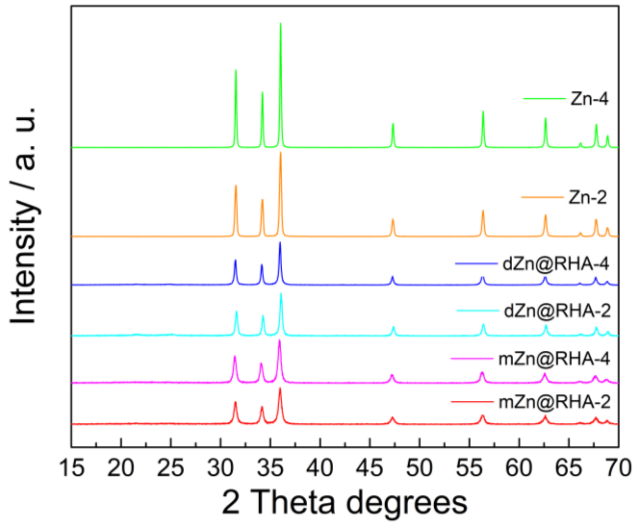

Fig. 1. XRD patterns for dZn@RHA, mZn@RHA and Zn samples.

The ZnO samples thus obtained after 2 and 4 hours of calcination were labelled as Zn-2 and Zn-4, respectively. Their corresponding XRD patterns also show the formation of pure zinc oxide. In the case of silica supported samples, the intensity of diffraction peaks is significantly lower than that observed for Zn-2 and Zn-4 samples. Thus, the smallest crystallite size values were estimated for the ZnO@SiO_2 samples, **Table 1**.

Table 1. The surface analysis parameters and crystallite size for zinc oxide samples.

Sample	BET surface area ($m^2 \cdot g^{-1}$)	BJH* pore volume ($cm^3 \cdot g^{-1}$)	BJH* mesoporous volume ($cm^3 \cdot g^{-1}$)	BJH* average pore diameter (nm)	BJH* surface area ($m^2 \cdot g^{-1}$)	BJH* mesoporous surface area ($m^2 \cdot g^{-1}$)	Crystallite size (nm)
dZn@RHA-2	49,3	0,11	0,08	8,99	48,5	42,3	23,6
dZn@RHA-4	53,5	0,13	0,1	9,00	56,2	49,5	25,0
mZn@RHA-2	40,3	0,11	0,08	9,00	47,1	41,5	32,7
mZn@RHA-4	50,7	0,10	0,07	8,66	45,1	38,8	36,9
Zn-2	4,5	0,01	0,01	17,15	3,3	2,5	62,0
Zn-4	2,8	0,01	0,01	21,02	1,8	1,4	72,1

* Determined from the N_2 desorption isotherm

The SEM images for dZn@RHA samples, **Fig. 2**, show ZnO particles growing dispersed on the cob-shaped skeleton, being aggregated in spheres of different sizes. The milling process breaks this skeleton but

similar particle aggregation is observed for mZn@RHA samples, **Fig. 3** (**a-d**). In both cases, the wurtzite particle size is around 70-180 nm (**Fig. S6a**). For the whole set of samples, the silica support (**Supplementary Information**) appears completely covered by ZnO particles, as expected from XRD patterns. The extended heating period of up to 4 hours had no significant influence on the morphology of the ZnO crystals. The silica skeleton acts as a support but also as a template influencing the growth of the wurtzite crystals. Thus, without the use of RH, the ZnO is constituted by independent larger amorphous nanoparticles of 140-280 nm, **Figs. 3** (**e,f**) and **S6b**.

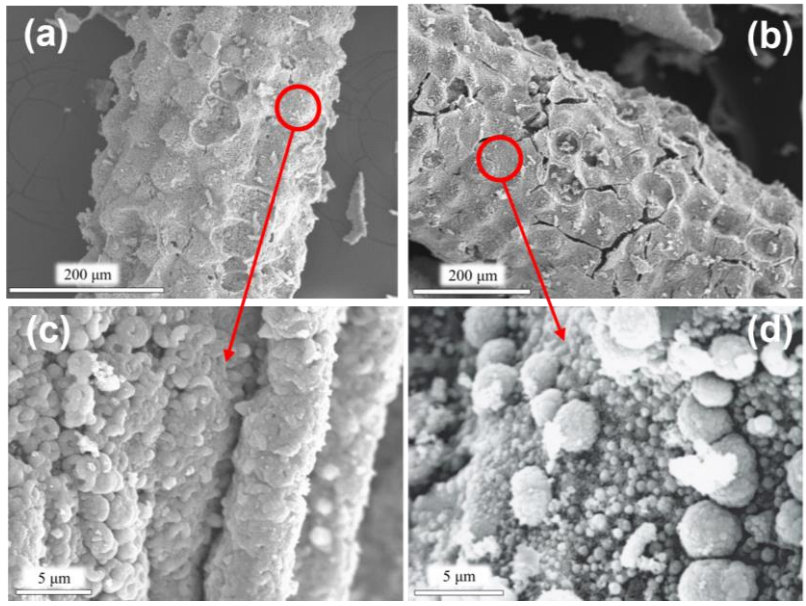

Fig. 2. XRD patterns for dZn@RHA, mZn@RHA and Zn samples.

The differences observed in ZnO crystallite size and morphology, with and without the use of RH, could be explained by assuming the following crystal growth mechanism. Since the RH decomposes at a lower temperature than the zinc acetate precursor (**Fig. S1**), ZnO crystallizes

once the amorphous silica is formed. By considering the appearance of the Zener pinning process [40], the growth of the first ZnO crystals must be restricted by the presence of silica as an inert phase, which is believed to result in tiny discrete particles located in the interface regions between the emergent ZnO nanocrystals. These reduce the radius of the crystallite surfaces, thus increasing the energy required for growth. This would explain the limited size of ZnO crystals and nanoparticles in Zn@RHA samples (**Fig. S6**; **Table 1**).

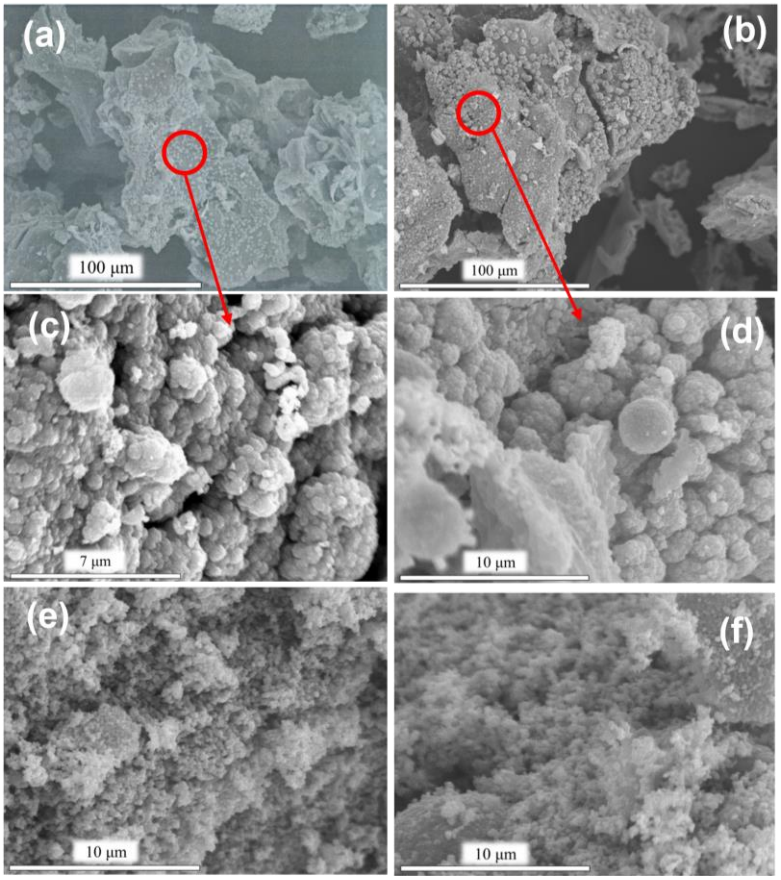

Fig. 3. SEM images for mZn@RHA-2 (a, c), mZn@RHA-4 (b, d), Zn-2 (e) and Zn-4 (f) samples.

Because of the derived dependence on the photocatalytic activity, the preparation of ZnO with a large surface area has been studied extensively [41]. The ZnO exhibits very complex and diversified morphologies, and the manipulation of a desirable structure for the rational tailoring of surface to volume ratios was largely reported. Thus, as way of example, large surface area ZnO photocatalysts were prepared such as spherical shape nanocrytals, flower-like, mesoporous, nanostar, nanofibers, tetrapods, nanorod arrays, porous nanopyramids, porous nanosheets, hollow spheres, nanotube arrays and porous films morphologies. Various preparative methods were employed such as capping agent, spray pyrolysis, the solution combustion route, the biotemplate-assisted approach, electrospinning, thermal evaporation, the solution-phase approach, the polyol solution route or chemical deposition [41]. Here we explore the influence of RH on the preparation of ZnO with increased surface area. Thus, in order to establish the surface area and porous structure of the photocatalysts, the corresponding N_2 adsorption-desorption isotherms were measured.

In comparison with the bare RHA support (**Fi, S4**), the pore structure changes considerably once ZnO growth covers silica support, **Fig, 4**. The isotherms of ZnO@SiO_2 composites exhibited almost the same shape, being similar to BET classification type II. These porous materials are constituted mainly by mesopores in a wide range of sizes (**Fig, 4** insets). **Table 1** summarizes the main surface properties of the ZnO@SiO_2 and ZnO samples. The pronounced hysteresis loop observed in the 0.45-0.95 P/P_0 range for the RHA sample (**Fig, S4**) is almost closed. These pores are progressively blocked and covered by the ZnO crystals on the surface, thus explaining the significant decrease of N_2 adsorption on ZnO@SiO_2, as observed for other metal oxides catalysts supported on RHA [42].

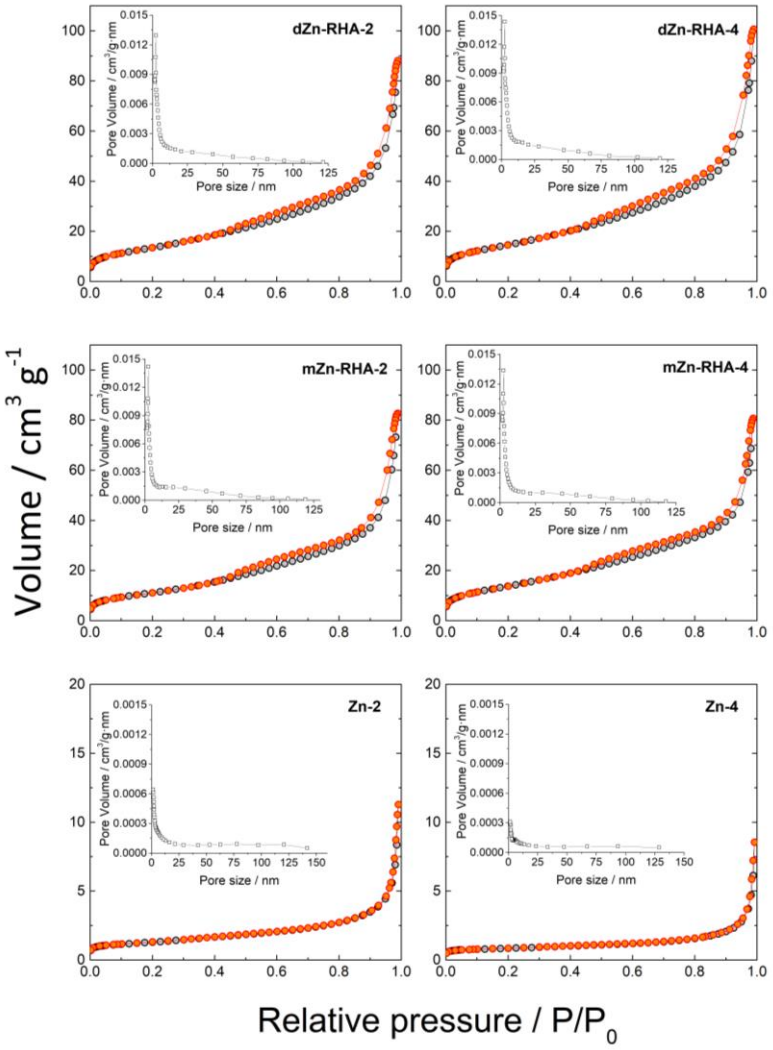

Fig. 4. N_2 adsorption-desorption isotherm and pore size distribution for dZn@RHA, Zn@RHA and Zn samples.

The new porous structure formed by wurtzite covering the silica skeleton exhibits a surface area of around 40 - 53 $m^2 g^{-1}$, being larger for samples obtained after 4 hours of calcination. In spite of the loss of surface area found from RHA to ZnO@SiO_2 samples, which was four times lower, the use of a silica skeleton as a support is of high interest. Thus,

without the use of RHA the isotherms show a collapsed microstructure for samples Zn-2 and Zn-4, exhibiting negligible surface area values lower than 5 m^2g^{-1} (**Fig. 4**; **Table 1**). From the results commented above, the beneficial effect of RHA as a template, which allows smaller and well dispersed ZnO particles, can be concluded.

The optical properties of the six samples were studied by a UV-visible diffuse reflectance spectroscopy (**Fig. S7**). The acquired diffuse reflectance spectra were converted to the Kubelka–Munk function, $[F(R_\infty)h\nu]^2$. The band gap energies of the samples are estimated from the tangent lines in the plots of the Kubelka–Munk function vs. the energy of exciting light, as shown in **Fig. 5**. As expected, as SiO_2 is as a good insulator material (8 eV; band gap energy) [43], significant changes were not observed for the composites. The estimated band-gap values were in line with those reported for pure ZnO [28, 44, 45]. Depending on the morphology and particle size of the samples (**Table 1**), they ranged between 3.1 and 3.2 eV. As previously reported [38] a slight decrease in band-gap values was observed with the crystallite size increase for ZnO@SiO_2 samples.

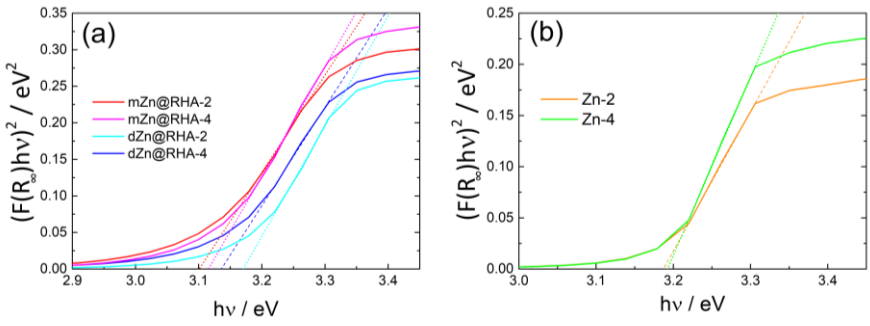

Fig. 5. Kubelka-Munk transformed reflectance spectra for Zn@RHA (a) and Zn (b) samples.

3.2.3.2. De-NO_X photocatalytic tests

The photochemical ability of ZnO@SiO_2 samples to abate the atmospheric concentration of nitrogen oxides gases was studied. The photochemical De-NO_X process proved to be efficient when NO_X gases were removed from the air through their complete oxidation to nitrite/nitrate (NO_2^-/NO_3^-) species. This is not a simple process as it involves several intermediate species [3, 46]. Briefly, it can be summarised as follow:

$$SC + hv \Rightarrow e^- + h^+ \quad (1)$$

$$H_2O + h^+ \Rightarrow H^+ + OH\bullet \quad (2)$$

$$NO + 2\,OH\bullet \Rightarrow NO_2 + H_2O \quad (3)$$

$$NO_2 + OH\bullet \Rightarrow NO_3^- + H^+ \quad (4)$$

$$NO + NO_2 + H_2O \Rightarrow 2\,HNO_2 \quad (5)$$

$$O_2 + e^- \Rightarrow \bullet O_2^- \quad (6)$$

$$NO_X + \bullet O_2^- \Rightarrow NO_3^- \quad (7)$$

Therefore, when sunlight shines on ZnO nanoparticles (semiconductor, SC) the electron in the valence band (VB) acquires the necessary energy to migrate to the conduction band (CB), (reaction 1). The pairs of mobile charges (e^- and h^+) that reach the surface of the semiconductor particles react with the adsorbed water and oxygen molecules (2,6). Thus, the formation of reactive oxygen species (ROS) – as previously reported for ZnO systems [25, 26] – and the progressive oxidation of nitrogen oxide gases is initiated (3,4,5,7) [24-26, 28]. During this process, the presence of the intermediate NO_2 gas must be reduced as much as possible (3) because NO_2 is far more dangerous than NO [47].

Fig. 6 shows the evolution of the nitrogen oxide concentration profiles recorded for the ZnO@SiO_2 samples as a function of light irradiation time. In the absence of light irradiation, in the first ten minutes of the test, the concentration of gases stayed constant confirming that neither NO gas adsorption nor any reaction on the ZnO particle surface occurred.

The photochemical oxidation (PCO) process began on the ZnO active sites once the lamp was switched on, as inferred from the sudden decrease observed for NO concentration. This PCO process was kept constant during the 30 min of light irradiation and stopped when the light was turned off, then the NO concentration returned to its initial value. Following this experiment, the decrease in NO concentration values measured during the light irradiation period was related to the amount of removed NO. For comparison purposes, the commercial Aeroxide® TiO_2 P25 (Evonik) was also studied, a material broadly used worldwide as a reference in photocatalysis. In fact, this material is quite similar to the studied samples in reference to band- gap energy, crystal size and surface area (3.18 eV ; 23-44 nm; 48.6 m^2g^{-1}) [48].

As expected, the NO conversion value was related to the surface area exhibited by the samples, around 75% for ZnO@SiO_2 samples and TiO_2 P25, and decreasing around 50% for pure ZnO samples, **Figs. 6a** and **7**. As previously mentioned, it is worth remarking on the subsequent appearance of the highly toxic NO_2 gas whose amount differs between samples. As is known for other modified titania photocatalysts, and different benchmark TiO_2 samples, the emission of NO_2 increases continuously under light irradiation in the case of the TiO_2-P25 sample, **Fig. 6b** [48].

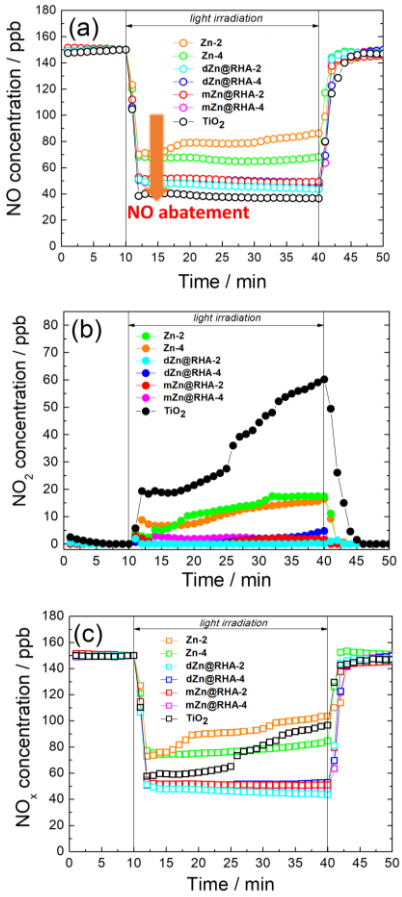

Fig. 6. Nitrogen oxides concentration profiles obtained during the photo-degradation of gaseous NO under light irradiation on dZn@RHA, mZn@RHA and Zn samples.

Thus, the highest slope observed for TiO_2-P25 would indicate that the theoretical full oxidation of NO towards nitrites/nitrates lowers with the irradiation time, thus explaining the noticeably increased amount of NO_2 molecules released during the experiment. This emission was somewhat inhibited in pure ZnO samples. However, it is remarkable that in ZnO@SiO_2 samples the amount of NO_2 concentration measured is negligible. By considering a sustainable process, the photocatalytic De-NO_X process must address not only the highest NO conversion values, but

also the aim of achieving the highest De-NO_X selectivity. The selectivity system parameter, *S*, expresses the ratio of degraded NO fully converted into harmless nitrite/nitrate rather than into toxic nitrogen dioxide, being determined according to the equation:

$$S\ (\%) = \frac{([\mathrm{NOx}]_{\mathrm{in}} - [\mathrm{NOx}]_{\mathrm{out}})/[\mathrm{NOx}]_{\mathrm{in}}}{([\mathrm{NO}]_{\mathrm{in}} - [\mathrm{NO}]_{\mathrm{out}})/[\mathrm{NO}]_{\mathrm{in}}} \times 100 \qquad (8)$$

Therefore, the highest S values mean the highest amount of nitrogen oxides removed from air. For a better comprehension of the results obtained, **Fig. 7** shows the conversion/emission nitrogen oxide values together with the photocatalytic NO_X abatement selectivity (*S*), in the case of ZnO@SiO_2 and should be compared with those obtained for common photocatalysts: ZnO and TiO_2-P25 samples. The outstanding results with S values above 90% measured for ZnO@SiO_2 samples, allowed a high amount of the whole NO_X gases, around 70%, to be removed. To our knowledge, these high selectivity values are scarcely reported and only for some TiO_2 advanced photocatalysts [11, 13, 49-52]. In fact, due to its poor selectivity, the NO_X removal observed for TiO_2 P25 is limited to 35%. In agreement with our findings, low NO_2 release was reported for a ZnO thin film De-NO_X photocatalyst [23] associated with the sensitivity of this oxide to NO_2 gas [53]. On the other hand, *S* values of ZnO@SiO_2 samples are higher than those of ZnO (samples Zn-2 and Zn-4). The influence of the SiO_2 support on the ZnO crystalline growth allows microstructures with higher surface area and pore volume to be obtained, making the accessibility of reactant molecules to the active sites easier and therefore, facilitating the oxidation of NO and NO_2 molecules. In this sense, the best performance for the $NO \rightarrow HNO_2 \rightarrow NO_2 \rightarrow NO_3^-$ oxidation

process (reactions 3 to 7) was easily achieved by the ZnO@SiO_2 photocatalysts. Additionally, the nitrogen oxide gases abatement performance of the last advanced De-NO_x photocatalysts is compared in **Table S3**. From this table it is usually observed that the photocatalysts with higher NO efficiency values exhibited low De-NO_x selectivity and the vice-versa. The NO_x abatement performance of our ZnO@SiO_2 sample is among the best reported in the last few years for De-NO_x photocatalysts as shown in **Table S3**, showing very high NO/NO_x and S values, in similarity to BiOCl [54].

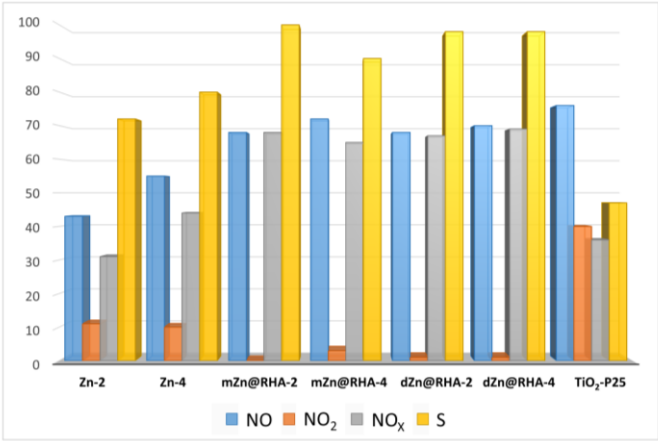

Fig. 7. NO conversion (%, blue), NO_2 released (%, orange), NO_X conversion (%, grey) and Selectivity values (%, yellow) for dZn-RHA, mZn-RHA, Zn and TiO2-P25 samples. (For interpretation of the references to colour in this figure legend, the reader is referred to the web version of this article).

In order to confirm the mechanism proposed, which implies the selective formation and deposition of nitrite/nitrate onto the surface of the ZnO@SiO_2 sample, additional evidences were obtained. FTIR measurement was used to qualitatively detect nitrogen oxide species on the surface before and after photocatalytic reactions, **Fig. 8a**. No bands

concerning N–O vibration modes were observed for the pristine sample. However, new absorption bands at 1258, 1327, 1375, 1518 and 1702 cm^{-1} appeared once the sample was subjected to the photocatalytic reaction, confirming the generation of nitrite/nitrate species during the PCO process. The bands located at 1518 and 1370 cm^{-1} correspond to stretching vibrations of nitrate species [55-57], whereas that at 1327 cm^{-1} is ascribed to nitrite ones [57, 58]. The assignation of the band located at 1258 cm^{-1} could be ambiguously done for both nitrate [57, 59] and nitrite [55, 60] species. Finally, the band at 1710 cm^{-1} can be tentatively assigned to the adsorbed NO_2 [59]. A more detailed assignment of IR bands attributed to N−O stretching vibrations of surface nitrate (NO_3^-) and nitrite (NO_2^-) species is a difficult task, since ν(N−O) of different NO_3^- and NO_2^- species fall in the same 1700−1000 cm^{-1} interval and their IR bands are strongly overlapped [55].

On the other hand, to shed light on differences found in De-NO_X selectivity values, new evidence was obtained from preliminary NO_2 adsorption studies carried out on ZnO@SiO_2, ZnO and TiO_2-P25 samples. Thus, a mixture of air/NO_2 was sent to the reactor with a NO_2 concentration around 150 ppb, obtained by mixing synthetic air and pure NO_2 (flow rate of 0.30 L min^{-1}; R.H. at 50 ± 5). In the absence of light irradiation, NO_2 gas was passed over the samples and substantial differences were observed in the evolution of the concentration profile with time, **Fig. 8b**. The NO_2 concentration profile for TiO_2-P25 is similar to that of a blank test (without the presence of a catalyst). In both cases, the NO_2 concentration remained constant at the initial inlet value during the time of the experiment, and therefore, there was no interaction between the gas and the catalyst or chamber surface. However, in the case of zinc oxide samples, lower concentration values for NO_2 are measured during

the first 30 minutes indicating that gas molecules are probably being adsorbed on their surface. This adsorption is higher for the dZn@RHA-4 sample because of its larger surface area compared to that of Zn-4. As aforementioned, the high De-NO_X selectivity found for $ZnO@SiO_2$ samples would be explained based on their ability to adsorb the recently formed NO_2 gas molecule (reaction 3), facilitating its oxidation to nitrate before being released into the atmosphere. In the other hand, even though ZnO has the same band-gap energy as TiO_2-anatase (3.2 eV), its conduction band (CB) is situated at a slightly higher energy level, which implies an increase in the reduction ability of the CB electrons to form superoxide radicals $\bullet O_2^-$ [10, 61].

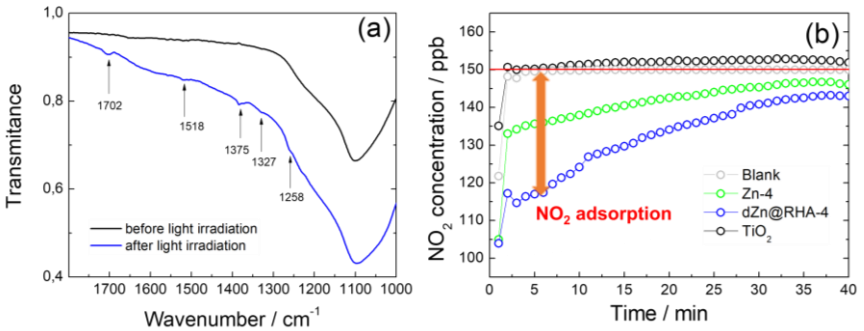

Fig. 8. (a) IR spectra obtained for dZn@RHA-4 sample before and after light irradiation. (b) NO2 concentration profiles obtained in dark condition for Zn-4, dZn@RHA-4 and TiO_2 samples. Red line marks the NO_2 inlet concentration. (For interpretation of the references to colour in this figure legend, the reader is referred to the web version of this article.)

This would also favour the oxidation of the NO_2 adsorbed molecules. Therefore, it can be summarized that the higher sensitivity of $ZnO@SiO_2$ samples to NO_2 gas greatly enhances the completion of NO $\rightarrow$ HNO_2 $\rightarrow$ NO_2 $\rightarrow$ NO_3- photochemical oxidation process. Thus, the amount of NO_2 toxic molecules which rose into the atmosphere during the

photocatalytic reaction is negligible, making the use of De-NO_X photocatalysts sustainable.

Finally, the potential practical application of these photocatalysts was qualitatively characterized by the evaluation of their reusability on large experiments. **Fig. 9** shows the diurnal mean values of NO concentration measured at an urban roadside in a highly populated city [6]. Because of the road traffic the NO concentration increases during the daytime, rapidly after sunrise and reaching its maximum level (≈ 180 ppbs) between 6.00 and 12.00 in the morning. It would seem of interest that De-NO_X photocatalysts could serve to abate this main NO_X peak concentration level. In this sense, the dZn@RHA-4 sample was subjected to four consecutive NO photocatalytic removal experiments run in periods of 6 hours under similar NO concentrations. The data collected (**Fig. 9**) suggest that most of the pollution peak is abated, around 110 ppbs of NO being removed by the photocatalytic action (from a NO inlet concentration of 150 ppb). The photocatalytic efficiency decreased slightly in the next three cycles, probably due to the nitrite/nitrate deposition masking the photoactive sites, thus hindering the photochemical performance, this loss of efficiency being similar to that obtained during a 24 hour light irradiation test (**Fig. S8**). In fact, after the repeated photocatalytic test cycles, the mechanism proposed is again validated by the presence of nitrite/nitrate species in the corresponding FTIR spectra (**Fig. S9**). Thus, after the fourth run, the sample was washed with water (filtered, collected and dried) in order to eliminate nitrite/nitrate species. (as confirmed by FTIR, **Fig. S9**). Even though there was a small amount of decay compared to the 4^{th} run (probably because the washing/drying procedure must be optimized in order to avoid particle aggregations), the efficiency exhibited in the next two runs (5^{th} and 6^{th}) was similar,

indicating good reusability. Moreover, the selectivity (data not shown) was maintained around 85%. This qualitative study shows that ZnO@SiO_2 photocatalysts would be highly useful in the abatement of the NO urban pollution. The photocatalysts were prepared by cost-effective and easily scalable methodologies. As the De-NO_x performance was similar enough for the four samples studied, avoiding the use of liquid solutions and decreasing the amount of energy used during the calcination process it is the preferred method for a potential industrialization of this synthetic procedure. Thus, the production of a mZn@RHA-2 sample would be preferred in which 20 g are easily obtained in only 3 hours of preparation at lab scale, indicating its favourable scalability.

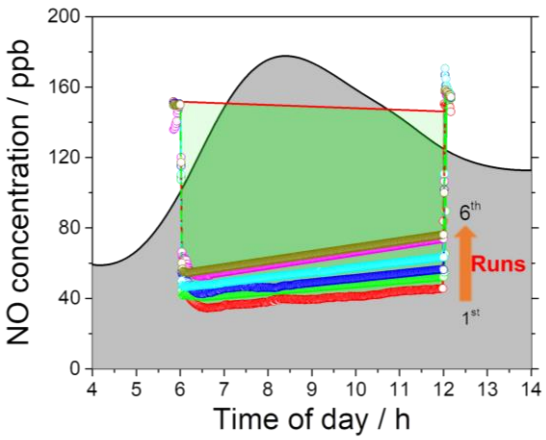

Fig. 9. Diurnal distribution pattern of NO gas at urban roadside (grey shading) and NO concentration profile obtained for dZn@RHA-4 sample (o) at different runs during 6 h of light irradiation (NO inlet concentration: 150 ppb). The sample was washed and dried after the 4th run.

3.2.4. Conclusions

A cost-effective and easily scalable methodology was reported in the preparation of a ZnO photocatalyst. By using simple procedures, liquid to solid deposition or mechanical milling, homogenous zinc acetate/rice husk mixtures were obtained by calcination at 600 ^{o}C thus obtaining ZnO@SiO_2 samples. The ZnO particles, aggregated in spheres of different sizes, grow dispersed on the silica skeleton which also acts as a template. In comparison to pure zinc oxide obtained under the same experimental conditions, the use of a silica support enables a lower particle size, 70 – 180 nm, and the highest surface area, 40 – 53 m^2g^{-1} to be obtained. Concerning the light absorption ability, 3.1 – 3.2 eV band gap was estimated for ZnO@SiO_2 samples.

When they are activated by sunlight, the ZnO@SiO_2 samples act as catalysts in the NO photochemical oxidation. The PCO process occurs through the NO $\rightarrow$ HNO_2 $\rightarrow$ NO_2 $\rightarrow$ NO_3^- oxidation steps, as confirmed by the presence of nitrite/nitrate species on the catalyst´s surface after the light induced reaction. High NO conversion values up to 75% are reached because of the high surface area exhibited by ZnO nanoparticles when grown on the silica skeleton, being limited to 50% for unsupported zinc oxide. It is worth mentioning the excellent De-NO_X selectivity values measured with ZnO@SiO_2 photocatalyts, above 90%, which allows removing approximately 70% of the NO_X gases. In comparison, due to its poor selectivity, the NO_X removal observed for the benchmark product TiO_2 P25 was limited to 35%. Thus, by using ZnO@SiO_2 samples the amount of NO_2 gases, which rose into the atmosphere during the photocatalytic reaction, is negligible. This minimal appearance of the NO_2 toxic molecules makes the use of De-NO_X photocatalysts sustainable. The low emission of NO_2 molecules is associated with the sensitivity of zinc

oxide towards this gas. In fact, the preliminary adsorption essays indicated that NO_2 gas is removed in the dark, in the presence of the ZnO@SiO_2 sample. Moreover, this highly selective and sustainable photocatalyst exhibits high efficiency and recovery when operated under experimental conditions similar to NO_X urban pollution periods (150 ppb NO; 6 hours), thus being proposed as a potential photocatalyst for air remediation. Because of their outstanding results of selectivity, further study will be addressed in the near future to ensure that the photocatalytic process works even more effectively. In this sense, metal doping would be an interesting strategy (preventing the recombination of the charge carriers), as we know that doped ZnO surpasses the photocatalytic efficiency of an un-doped one [62].

3.2.5. Acknowledgements

The Spanish (MINECO; MAT2017-88284-P) and Junta de Andalucía governments (PAI Groups FQM-214 and FQM-175) financed this work. Adrián Pastor acknowledges a grant from the Ministerio de Educación, Cultura y Deporte (FPU16/05041) to research at the University of Córdoba (Spain).

3.2.6. References

[1] R. Vinu, G. Madras, Environmental remediation by photocatalysis, J. Indian Inst. Sci. 90 (2012) 189-230.

[2] X. Li, J. Yu, M. Jaroniec, Hierarchical photocatalysts, Chem. Soc. Rev. 45 (2016) 2603-2636. doi: 10.1039/C5CS00838G

[3] J. Balbuena, M. Cruz-Yusta, L. Sánchez, Nanomaterials to Combat NO_X Pollution, J. Nanosci. Nanotechnol. 15 (2015) 6373-6385. doi: 10.1166/jnn.2015.10871

[4] M.W. Frampton, I.A. Greaves, NO_X - NO_X: Who's There?, Am. J. Respir. Crit. Care. Med. 179 (2009) 1077-1078. doi: 10.1164/rccm.200903-0485ED

[5] Y. Chen, J. Borken-Kleefeld, NOX Emissions from Diesel Passenger Cars Worsen with Age, Environ. Sci. Technol. 50 (2016) 3327-3332. doi: 10.1021/acs.est.5b04704

[6] S.K. Pandey, K.-H. Kim, S.-Y. Chung, S.J. Cho, M.Y. Kim, Z.-H. Shon, Long-term study of NO_X behavior at urban roadside and background locations in Seoul, Korea, Atmos. Environ. 42 (2008) 607-622. doi: 10.1016/j.atmosenv.2007.10.015

[7] H. Nie, M. Ou, Q. Zhong, S. Zhang, L. Yu, Efficient visible-light photocatalytic oxidation of gaseous NO with graphitic carbon nitride ($g–C_3N_4$) activated by the alkaline hydrothermal treatment and mechanism analysis, J. Hazard. Mater. 300 (2015) 598-606. doi: 10.1016/j.jhazmat.2015.07.066

[8] J. Chen, C.S. Poon, Photocatalytic construction and building materials: From fundamentals to applications, Build. Environ. 44 (2009) 1899-1906. doi: 10.1016/j.buildenv.2009.01.002

[9] S. Karapati, T. Giannakopoulou, N. Todorova, N. Boukos, I. Papailias, D. Dimotikali, C. Trapalis, Novel 'Pickering' modified TiO_2 photocatalysts with high De-NO_x efficiency, Catal. Today 287 (2017) 45-51. doi: 10.1016/j.cattod.2017.01.044

[10] T. Giannakopoulou, I. Papailias, N. Todorova, N. Boukos, Y. Liu, J. Yu, C. Trapalis, Tailoring the energy band gap and edges' potentials of g-C_3N_4/TiO_2 composite photocatalysts for NO_x removal, Chem. Eng. J. 310 (2017) 571-580. doi: 10.1016/j.cej.2015.12.102

[11] B. Tan, X. Zhang, Y. Li, H. Chen, X. Ye, Y. Wang, J. Ye, Anatase TiO_2 Mesocrystals: Green Synthesis, In Situ Conversion to Porous Single Crystals, and Self-Doping Ti^{3+} for Enhanced Visible Light Driven Photocatalytic Removal of NO, Chem. Eur. J. 23 (2017) 5478-5487. doi: 10.1002/chem.201605294

[12] N.C.T. Martins, J. Ângelo, A.V. Girão, T. Trindade, L. Andrade, A. Mendes, N-doped carbon quantum dots/TiO_2 composite with improved photocatalytic activity, Appl. Catal. B: Environ. 193 (2016) 67-74. doi: 10.1016/j.apcatb.2016.04.016

[13] J. Balbuena, J.M. Calatayud, M. Cruz-Yusta, P. Pardo, F. Martin, J. Alarcon, L. Sanchez, Mesocrystalline anatase nanoparticles synthesized using a simple hydrothermal approach with enhanced light harvesting for gas-phase reaction, Dalton Trans. (2018). doi: 10.1039/C8DT00721G

[14] E.C. Agency, ANNEX 2 – Comments and response to comments on CLH proposal on titanium dioxide, 2017.

[15] J. Balbuena, M. Cruz-Yusta, A. Pastor, L. Sánchez, α-Fe_2O_3/SiO_2 composites for the enhanced photocatalytic NO oxidation, J. Alloys Compd. 735 (2018) 1553-1561. doi: 10.1016/j.jallcom.2017.11.259

[16] J. Luo, G. Dong, Y. Zhu, Z. Yang, C. Wang, Switching of semiconducting behavior from n-type to p-type induced high photocatalytic NO removal activity in g-C_3N_4, Appl. Catal. B: Environ. 214 (2017) 46-56. doi: 10.1016/j.apcatb.2017.05.016

[17] F. Dong, T. Xiong, Z. Zhao, Y. Sun, M. Fu, Ammonia induced formation of N-doped $(BiO)_2CO_3$ hierarchical microspheres: the effect of hydrothermal temperature on the morphology and photocatalytic activity, CrystEngComm 15 (2013) 10522-10532. doi: 10.1039/c3ce41634h

[18] Z. Ai, W. Ho, S. Lee, L. Zhang, Efficient Photocatalytic Removal of NO in Indoor Air with Hierarchical Bismuth Oxybromide Nanoplate Microspheres under Visible Light, Environ. Sci. Technol. 43 (2009) 4143-4150. doi: 10.1021/es9004366

[19] Y. Gao, Y. Huang, Y. Li, Q. Zhang, J.-j. Cao, W. Ho, S.C. Lee, Plasmonic Bi/$ZnWO_4$ Microspheres with Improved Photocatalytic Activity on NO Removal under Visible Light, ACS Sustain. Chem. Eng. 4 (2016) 6912-6920. doi: 10.1021/acssuschemeng.6b01852

[20] S. Zhu, L. Lu, Z. Zhao, T. Wang, X. Liu, H. Zhang, F. Dong, Y. Zhang, Mesoporous Ni-Doped δ-Bi_2O_3 Microspheres for Enhanced Solar-Driven Photocatalysis: A Combined Experimental and Theoretical Investigation, J. Phys. Chem. C 121 (2017) 9394-9401. doi: 10.1021/acs.jpcc.7b01608

[21] K.-B. Kim, Y.W. Kim, S.K. Lim, T.H. Roh, D.Y. Bang, S.M. Choi, D.S. Lim, Y.J. Kim, S.-H. Baek, M.-K. Kim, H.-S. Seo, M.-H. Kim, H.S. Kim, J.Y. Lee, S. Kacew, B.-M. Lee, Risk assessment of zinc oxide, a cosmetic ingredient used as a UV filter of sunscreens, J. Toxicol. Environ. Health B 20 (2017) 155-182. doi: 10.1080/10937404.2017.1290516

[22] C.C. Pei, W.W.-F. Leung, Enhanced photocatalytic activity of electrospun TiO_2/ZnO nanofibers with optimal anatase/rutile ratio, Catal. Commun. 37 (2013) 100-104. doi: 10.1016/j.catcom.2013.03.029

[23] N. Todorova, T. Giannakopoulou, K. Pomoni, J. Yu, T. Vaimakis, C. Trapalis, Photocatalytic NO_x oxidation over modified ZnO/TiO_2 thin films, Catal. Today 252 (2015) 41-46. doi: 10.1016/j.cattod.2014.11.008

[24] E. Kowsari, S. Abdpour, Investigation performance of rod-like ZnO/CdO composites, synthesized in ionic liquid medium as photocatalytic for degradation of air pollutants (SO_2 and NO_X), Optik 127 (2016) 11567-11576. doi: 10.1016/j.ijleo.2016.09.084

[25] E. Kowsari, S. Abdpour, In-situ functionalization of mesoporous hexagonal ZnO synthesized in task specific ionic liquid as a photocatalyst for elimination of SO_2, NO_x, and CO, J. Solid State Chem. 256 (2017) 141-150. doi: 10.1016/j.jssc.2017.08.038

[26] E. Kowsari, B. Bazri, Synthesis of rose-like ZnO hierarchical nanostructures in the presence of ionic liquid/Mg^{2+} for air purification and their shape-dependent photodegradation of SO_2, NO_x, and CO, Appl. Catal. A: Gen. 475 (2014) 325-334. doi: 10.1016/j.apcata.2014.01.046

[27] Y. Huang, C. Guo, L. Huang, Q. Dong, S. Yin, T. Sato, Photocatalytic oxidation of NO_x gases using ZnO with superstructure by a low temperature soft solution process, Int. J. Nanotechnol. 10 (2012) 30-37. doi: 10.1504/IJNT.2013.050878

[28] Y. Wei, Y. Huang, J. Wu, M. Wang, C. Guo, D. Qiang, S. Yin, T. Sato, Synthesis of hierarchically structured ZnO spheres by facile

methods and their photocatalytic deNO_x properties, J. Hazard. Mater. 248-249 (2013) 202-210. doi: 10.1016/j.jhazmat.2013.01.012

[29] F. Adam, J.N. Appaturi, R. Thankappan, M.A.M. Nawi, Silica–tin nanotubes prepared from rice husk ash by sol–gel method: Characterization and its photocatalytic activity, Appl. Surf. Sci. 257 (2010) 811-816. doi: 10.1016/j.apsusc.2010.07.070

[30] Y. Li, J.Y. Lan, J. Liu, J. Yu, Z. Luo, W. Wang, L. Sun, Synthesis of Gold Nanoparticles on Rice Husk Silica for Catalysis Applications, Ind. Eng. Chem. Res. 54 (2015) 5656-5663. doi: 10.1021/acs.iecr.5b00216

[31] A. Jaroenworaluck, N. Pijarn, N. Kosachan, R. Stevens, Nanocomposite TiO_2–SiO_2 gel for UV absorption, Chem. Eng. J. 181–182 (2012) 45-55. doi: 10.1016/j.cej.2011.08.028

[32] H. Chen, L. Zhao, Y. Xiang, Y. He, G. Song, X. Wang, F. Liang, A novel Zn–TiO_2/C@SiO_2 nanoporous material on rice husk for photocatalytic applications under visible light, Desalination and Water Treatment 57 (2016) 9660-9670. doi: 10.1080/19443994.2015.1035339

[33] C. Tian, Q. Zhang, A. Wu, M. Jiang, Z. Liang, B. Jiang, H. Fu, Cost-effective large-scale synthesis of ZnO photocatalyst with excellent performance for dye photodegradation, Chem. Commun. 48 (2012) 2858-2860. doi: 10.1039/c2cc16434e

[34] P. Sujaridworakun, S. Jinawath, W. Panpa, A. Nakajima, M. Yoshimura, Hydrothermal Synthesis of TiO_2/SiO_2 Hybrid Photocatalyst from Rice Husk Ash, Key Eng. Mater. 352 (2007) 281-285. doi: 10.4028/0-87849-454-5.281

[35] ISO, Fine ceramics (advanced ceramics, advanced technical ceramics) -- Test method for air-purification performance of semiconducting photocatalytic materials -- Part 1: Removal of nitric oxide, in: ISO 22197-1:2007, International Organization for Standardization, 2007.

[36] F. Rodriguez-Rivas, A. Pastor, C. Barriga, M. Cruz-Yusta, L. Sánchez, I. Pavlovic, Zn-Al layered double hydroxides as efficient photocatalysts for NO_x abatement, Chem. Eng. J. 346 (2018) 151-158. doi: 10.1016/j.cej.2018.04.022

[37] M.E. Monge, B. D'Anna, C. George, Nitrogen dioxide removal and nitrous acid formation on titanium oxide surfaces—an air quality remediation process?, Phys. Chem. Chem. Phys. 12 (2010) 8991-8998. doi: 10.1039/b925785c

[38] T.S.T. da Silva Gelson, T.G. Carvalho Kele, F. Lopes Osmando, S. Gomes Eliziana, R. Malagutti Andréa, R. Mastelaro Valmor, C. Ribeiro, A.J.L. Mourão Henrique, Synthesis of ZnO Nanoparticles Assisted by N Sources and their Application in the Photodegradation of Organic Contaminants, ChemCatChem 9 (2017) 3795-3804. doi: 10.1002/cctc.201700756

[39] L. Shi, P. Zhu, R. Yang, X. Zhang, J. Yao, F. Chen, X. Gao, P. Ai, N. Tsubaki, Functional rice husk as reductant and support to prepare as-burnt Cu-ZnO based catalysts applied in low-temperature methanol synthesis, Catal. Commun. 89 (2017) 1-3. doi: 10.1016/j.catcom.2016.10.011

[40] L.A. O'Dell, S.L.P. Savin, A.V. Chadwick, M.E. Smith, Structural studies of silica- and alumina-pinned nanocrystalline SnO_2, Nanotechnology 16 (2005) 1836. doi: 10.1088/0957-4484/16/9/070

[41] S.G. Kumar, K.S.R.K. Rao, Zinc oxide based photocatalysis: Tailoring surface-bulk structure and related interfacial charge carrier dynamics for better environmental applications, RSC Adv. 5(5) (2015) 3306-3351. doi: 10.1039/c4ra13299h

[42] A.E. Ahmed, F. Adam, The benzylation of benzene using aluminium, gallium and iron incorporated silica from rice husk ash, Microporous Mesoporous Mater. 118 (2009) 35-43. doi: 10.1016/j.micromeso.2008.08.024

[43] S. Vives, C. Meunier, Optical properties of copper modified sol–gel SiO2 thin films, Mater. Lett. 91 (2013) 165-169. doi: 10.1016/j.matlet.2012.09.081

[44] S. Kaviya, E. Prasad, Eco-friendly synthesis of ZnO nanopencils in aqueous medium: a study of photocatalytic degradation of methylene blue under direct sunlight, RSC Adv. 6 (2016) 33821-33827. doi: 10.1039/c6ra04306b

[45] A.K. Zak, M.E. Abrishami, W.H.A. Majid, R. Yousefi, S.M. Hosseini, Effects of annealing temperature on some structural and optical properties of ZnO nanoparticles prepared by a modified sol–gel

combustion method, Ceram. Int. 37 (2011) 393-398. doi: 10.1016/j.ceramint.2010.08.017

[46] S. Devahasdin, C. Fan Jr, K. Li, D.H. Chen, TiO_2 photocatalytic oxidation of nitric oxide: transient behavior and reaction kinetics, J. Photochem. Photobiol. A 156 (2003) 161-170. doi: 10.1016/S1010-6030(03)00005-4

[47] R.J. Lewis, N.I. Sax, Sax's Dangerous Properties of Industrial Materials, 12th ed., Van Nostrand Reinhold, New York, 2012.

[48] M.J. Hernández Rodríguez, E. Pulido Melián, O. González Díaz, J. Araña, M. Macías, A. González Orive, J.M. Doña Rodríguez, Comparison of supported TiO_2 catalysts in the photocatalytic degradation of NO_X, J. Mol. Catal. A: Chem. 413 (2016) 56-66. doi: 10.1016/j.molcata.2015.12.007

[49] J. Ma, H. Wu, Y. Liu, H. He, Photocatalytic Removal of NO_X over Visible Light Responsive Oxygen-Deficient TiO_2, J. Phys. Chem. C 118 (2014) 7434-7441. doi: 10.1021/jp500116n

[50] N. Todorova, T. Giannakopoulou, S. Karapati, D. Petridis, T. Vaimakis, C. Trapalis, Composite TiO_2/clays materials for photocatalytic NO_X oxidation, Appl. Surf. Sci. 319 (2014) 113-120. doi: 10.1016/j.apsusc.2014.07.020

[51] A. Trapalis, N. Todorova, T. Giannakopoulou, N. Boukos, T. Speliotis, D. Dimotikali, J. Yu, TiO_2/graphene composite photocatalysts for NO_X removal: A comparison of surfactant-stabilized graphene and reduced graphene oxide, Appl. Catal. B: Environ. 180 (2016) 637-647. doi: 10.1016/j.apcatb.2015.07.009

[52] A.V. Katsanaki, A.G. Kontos, T. Maggos, M. Pelaez, V. Likodimos, E.A. Pavlatou, D.D. Dionysiou, P. Falaras, Photocatalytic oxidation of nitrogen oxides on N-F-doped titania thin films, Appl. Catal. B: Environ. 140–141 (2013) 619-625. doi: 10.1016/j.apcatb.2013.04.070

[53] S. Öztürk, N. Kılınç, N. Taşaltin, Z.Z. Öztürk, A comparative study on the NO_2 gas sensing properties of ZnO thin films, nanowires and nanorods, Thin Solid Films 520 (2011) 932-938. doi: 10.1016/j.tsf.2011.04.177

[54] H. Li, H. Shang, X. Cao, Z. Yang, Z. Ai, L. Zhang, Oxygen vacancies mediated complete visible light NO oxidation via side-on bridging

superoxide radicals, Environ. Sci. Technol. 52 (2018) 8659-8665. doi: 10.1021/acs.est.8b01849

[55] R.V. Mikhaylov, A.A. Lisachenko, B.N. Shelimov, V.B. Kazansky, G. Martra, S. Coluccia, FTIR and TPD Study of the Room Temperature Interaction of a NO–Oxygen Mixture and of NO_2 with Titanium Dioxide, J. Phys. Chem. C 117 (2013) 10345-10352. doi: 10.1021/jp311593s

[56] R. Sugrañez, J. Balbuena, M. Cruz-Yusta, F. Martín, J. Morales, L. Sánchez, Efficient behaviour of hematite towards the photocatalytic degradation of NO_X gases, Appl. Catal. B: Environ. 165 (2015) 529-536. doi: 10.1016/j.apcatb.2014.10.025

[57] K.I. Hadjiivanov, Identification of neutral and charged N_xO_Y surface species by IR spectroscopy, Catal. Rev. Sci. Eng. 42 (2000) 71-144. doi: 10.1081/CR-100100260

[58] J. Sá, J.A. Anderson, FTIR study of aqueous nitrate reduction over Pd/TiO_2, Appl. Catal. B: Environ. 77 (2008) 409-417. doi: 10.1016/j.apcatb.2007.08.013

[59] B. Zhao, R. Ran, X. Wu, D. Weng, X. Wu, C. Huang, Comparative study of Mn/TiO_2 and Mn/ZrO_2 catalysts for NO oxidation, Catal. Commun. 56 (2014) 36-40. doi: 10.1016/j.catcom.2014.07.003

[60] Y. Duan, M. Zhang, L. Wang, F. Wang, L. Yang, X. Li, C. Wang, Plasmonic $Ag\text{-}TiO_{2-x}$ nanocomposites for the photocatalytic removal of NO under visible light with high selectivity: The role of oxygen vacancies, Appl. Catal. B: Environ. 204 (2017) 67-77. doi: 10.1016/j.apcatb.2016.11.023

[61] A.L. Linsebigler, G. Lu, J.T. Yates, Photocatalysis on TiO_2 Surfaces: Principles, Mechanisms, and Selected Results, Chem. Rev. 95 (1995) 735-758. doi: 10.1021/cr00035a013

[62] T. Giannakopoulou, I. Papailias, N. Todorova, N. Boukos, Y. Liu, J. Yu, C. Trapalis, Tailoring the energy band gap and edges' potentials of $g\text{-}C_3N_4/TiO_2$ composite photocatalysts for NO_x removal, Chem. Eng. J. 310 (2017) 571-580. doi: 10.1016/j.watres.2015.09.045

Appendix II: Supplementary Information

Experimental

Characterization of RHA support

Prior to the photocatalyst´s preparation, the characterization of the expected ashes to be used as a support was performed. Firstly, the rice husk (RH; from Herba Ricemills, S.L.U.) was washed to remove dirt by boiling in deionized water for 2 h under continuous stirring, then filtered and dried in an oven at 70 ^{o}C for 24 h. A temperature of 600 ^{o}C was selected to achieve the complete calcination process of the rice husk (**Figure S1**; RH´s thermogravimetric pattern). The sample was calcined for periods of 2 and 4 hours, obtaining the corresponding RHA-2 and RHA-4 silica ashes. The temperature time had no effect on the morphological or mineralogical composition. The RHA sample consists of sub-millimetre particles adopting a cob-shaped cellulose skeleton (**Figure S2**). The X-ray diffraction patterns exhibited a broad peak centred at 22^{o} (**Figure S3a**) corresponding to amorphous SiO_2 [1].

Infrared spectra (IR) were obtained with a FT-MIR Tensor 27 (Bruker) collecting 100 scans from 450 to 4000 cm^{-1} with a resolution of 4 cm^{-1}. Si-O vibration modes were only detected in the corresponding IR spectra (**Figure S3b**). Three bands stand out: about 472 cm^{-1}, due to the deformation vibration Si-O-Si; 820 cm^{-1}, corresponding to rings of atomic groups Si-O-Si; 1110 cm^{-1}, coming from the valence vibrations Si-O (SiO_4). In this last band we can distinguish a small shoulder at 1230 cm^{-1}, which is due to the small amount of silica that is still polymerized in the structure.

Therefore, after calcination the carbon content was removed and the product obtained consisted mainly of silica (>93% of Si, **Table S1**). On the other hand, the porous structure was somewhat altered when the

calcination period was extended. Both RHA-2 and RHA-4 samples exhibited a similar N_2 adsorption-desorption isotherm identified as a type (IV) isotherm with a type H1 hysteresis loop (**Figure S4**), the slight slope of the isotherm in the 0.2–0.9 P/P_0 range being indicative of the presence of mesopores [1, 2]. A larger surface area was developed when the calcination period was prolonged from 2 to 4 h, and values of 157 and 194 m^2g^{-1} were measured for samples RHA-2 and RHA-4, respectively.

Sample characterization

The XRD patterns were recorded in a Bruker D8 Discover A25 diffractometer equipped with CuKα1 radiation, germanium primary monochromator and lynx-eye detector. The diffractogram was run with a step size of 0.016 2θ° and a counting time of 19,2 s. The crystal size of the samples was determined by means of the Scherrer equation, $D=(k\lambda/\beta\cos\theta)$, where D is the particle size in nanometres, λ is 1.54056 A° (which is the wavelength of the CuKα1 radiation), the constant k is 0.94, β is the peak width at half-maximum intensity and θ is the peak position. Energy-Dispersive X-Ray Spectroscopy analysis (EDX) was obtained with a Jeol JMS-6400 microscope. Diffuse reflectance (DR) spectra were recorded at a scan rate of 150 nm min^{-1} from 200 to 800 nm in 0.5 nm steps.

Photocatalytic activity tests

In order to discuss about the photocatalytic efficiency, the following parameters were defined:

$$\text{NO conversion (\%)} = \{([NO]_{in} - [NO]_{out})/[NO]_{in}\} \times 100 \quad (1)$$

$$NO_2 \text{ released (\%)} = ([NO_2]_{out}/[NO]_{in}) \times 100 \quad (2)$$

$$NO_X \text{ conversion } (\%) = \{([NO_X]_{in} - [NO_X]_{out})/[NO_X]_{in}\} \times 100 \quad (3)$$

where $[NO_X] = [NO] + [NO_2]$.

References

[1] A.E. Ahmed, F. Adam, The benzylation of benzene using aluminium, gallium and iron incorporated silica from rice husk ash, Microporous Mesoporous Mater. 118 (2009) 35–43. doi:10.1016/J.MICROMESO.2008.08.024.

[2] F.W. Chang, W.Y. Kuo, H.C. Yang, Preparation of Cr_2O_3 promoted copper catalysts on rice husk ash by incipient wetness impregnation, Appl. Catal. A Gen. 288 (2005) 53–61. doi:10.1016/J.APCATA.2005.04.046.

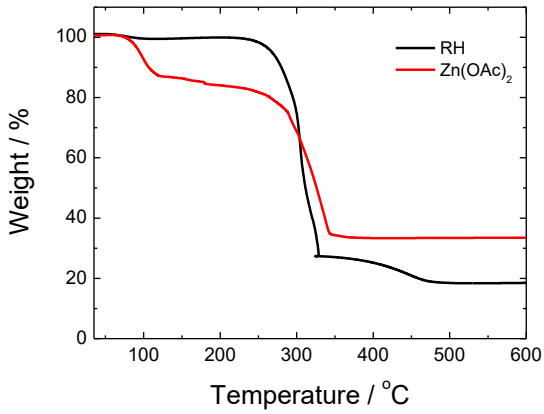

Figure S1. TGA pattern obtained for RH and Zn(OAc)2 samples.

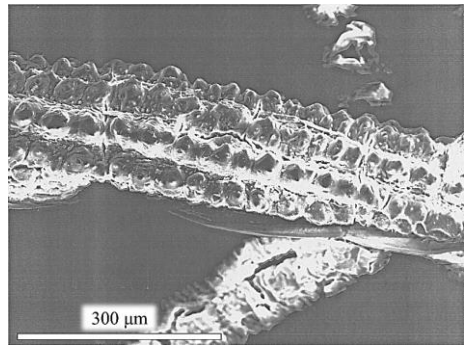

Figure S2. SEM image for RHA sample.

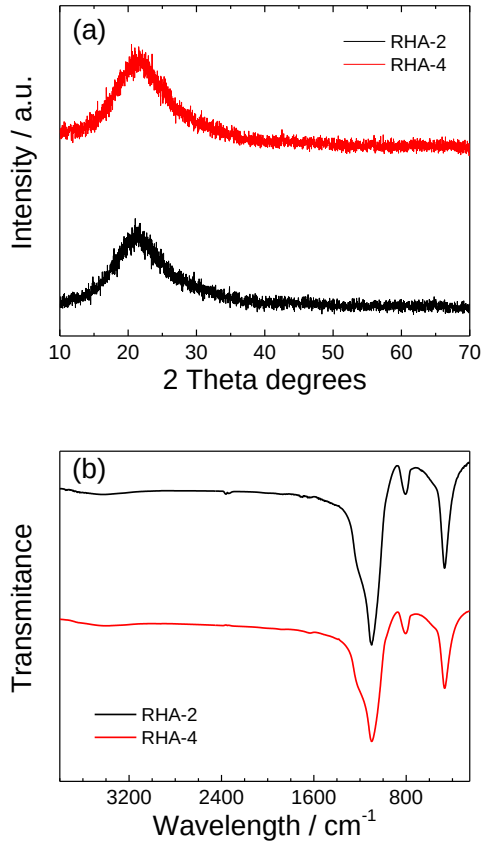

Figure S3. (a) XRD pattern and (b) IR spectra obtained for RHA sample after 2 and 4 hours of calcination.

Table S1. EDX compositional analysis for RHA-2 sample.

Sample	Element / % Atomic							
	Si	**Zn**	**Mg**	**Ca**	**K**	**Cl**	**S**	**P**
RHA	93,61	0,81	0,81	2,87	1,00	1,10	0,70	0,48

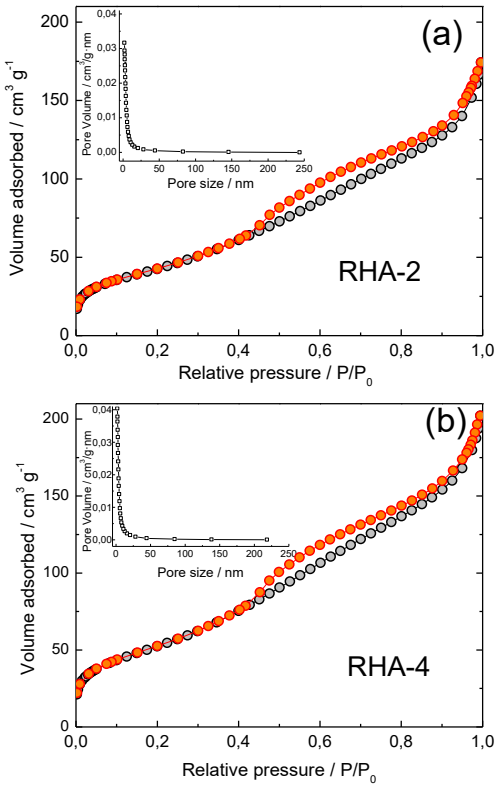

Figure S4. N_2 adsorption-desorption isotherm and pore size distribution for RHA samples obtained after (a) 2 and (b) 4 hours of calcination.

Table S2. XRF compositional analysis and carbon content for Zn@RHA and Zn samples.

Sample	Element / % weight								
	Zn	**Si**	**Mg**	**Ca**	**K**	**Cl**	**S**	**P**	**C**
dZn@RHA-2	40,99	8,58	0,17	0,15	0,08	0,04	0,05	0,02	0,84
dZn@RHA-4	43,01	8,58	0,13	0,14	0,08	0,06	0,06	0,03	0,42
mZn@RHA-2	42,01	8,67	0,05	0,09	0,06	0,09	0,04	0,02	0,77
mZn@RHA-4	40,01	7,44	0,06	0,09	0,07	0,06	0,04	0,02	1,49
Zn-2	61,73	0	0	0	0	0	0	0	0,84
Zn-4	63,34	0	0	0	0	0	0	0	0,42

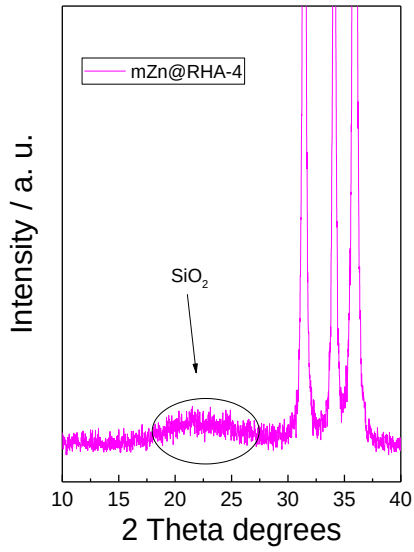

Figure S5. Zoom in the XRD pattern obtained for mZn@RHA-4 sample.

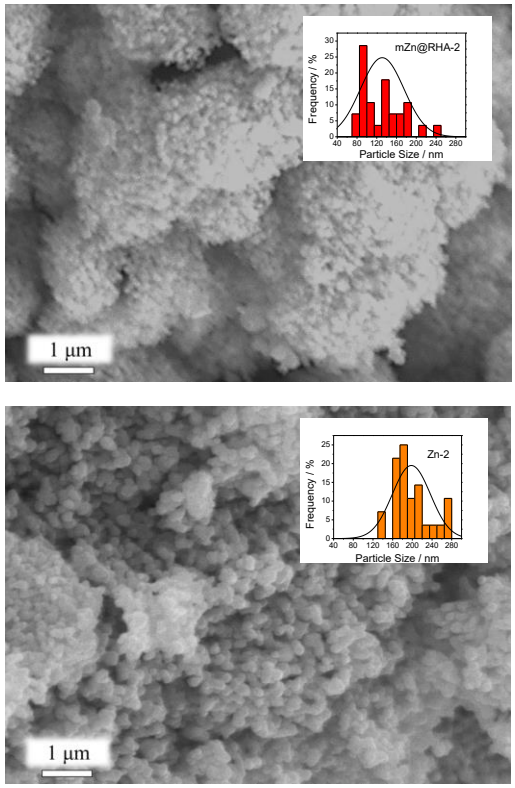

Figure S6. SEM images and particle size distribution for (a) mZn@RHA-2 and (b) Zn-2 samples.

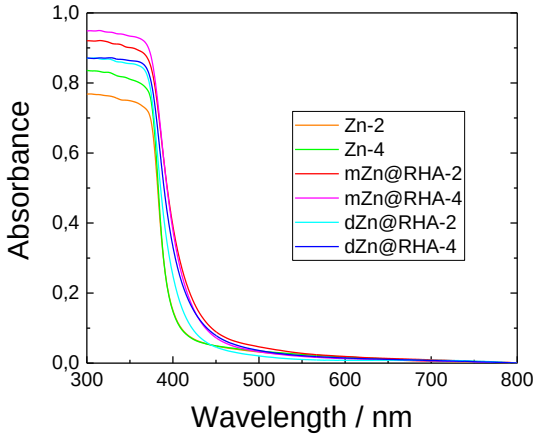

Figure S7. The absorption spectra for Zn@RHA and Zn samples.

Table S3. Photocatalytic efficiency for the removal of NO_X gases of different advanced De-NO_x compounds.

Sample	NO inlet concentration (ppb)	Light irradiation time (min)	NO conversion (%)	NO_X conversion (%)	*Selectivity (%)
ZnO@SiO_2 (this work)	150	30	70	69	98
ZnO spheres [a]	1000	--	68	---	---
CQD/$ZnFe_2O_4$ [b]	400	30	38	37	97
ZnAl-LDH [c]	150 600	60 60	55 50	50 45	91 90
$Cu_{0.08}In_{0.25}ZnS_{1.41}$ [d]	600	30	48	--	--
TiO_2 [e]	400	30	65	55	84
TiO_2/HT [f]	1000	30	45	38	85
Fe-TiO_2 [g]	400	--	58	38	65
TiO_2/graphene [h]	1000	30	53	45	85
TiO_2 mesocrystalline [i]	500	300	59	50	89
Ti^{3+}-TiO_2 mesocrystal [j]	600	40	55	53	97
$LaFeO_3$-$SrTiO_3$ [k]	400	30	40	29	72
p-g-C_3N_4 [l]	600	50	80	28	34
C_3N_4/graphene-$InVO_4$ [m]	600	30	65	---	---
Bi@$Bi_2O_2SiO_3$ [n]	450	30	50	48	96
BiOCl [o]	500	30	70	69	99
$SrCO_3$-BiOI [p]	----	30	48	48	100
Bi_2MoO_6 [q]	600	35	55	51	92

* Selectivity values were calculated from the cited articles by using the equation (8) the in manuscript.

The photocatalysts were selected from the best of the different Zn, Ti, C_3N_4 and Bi based compounds.

Because these are UV and/or Vis active photocatalysts, the light intensity was not considered as a comparative item, thus different light irradiation lamps are used for each one. The NO inlet concentration and light irradiation time also differ among the studies, 600 ppb and 30 min being the most frequently used standard. Thus, with the aim of the conclusions of the comparative results being reliable, the NO/NO_X conversion and *S* values were described in percentages. The comparative is validated by the crossed references. Thus, the photocatalytic efficiencies (in %) don´t seem to be significantly altered by the time of light irradiation, as observed for TiO_2 mesocrystalline samples, nor by the NO inlet concentration, as the case of ZnAl-LDH systems.

For both NO conversion and *S* values, the performance of $ZnO@SiO_2$ samples is among the best reported in the last few years for De-NO_X photocatalysts.

[a] Y. Wei, J. Wu, M. Wang, C. Guo, Q. Dong, S. Yin, T. Sato, Synthesis of hierarchically tructured ZnO spheres by facile methods and their photocatalytic deNO_x properties, J. Hazard. Mater 248–249 (2013) 202-210.

[b] Y. Huang, Y. Liang, Y. Rao, D. Zhu, J. Cao, Z. Shen, W. Ho, S.C. Lee, Environment-Friendly Carbon Quantum Dots/$ZnFe_2O_4$ Photocatalysts: Characterization, Biocompatibility, and Mechanisms for NO Removal, Environ. Sci. Technol. 51 (2017) 2924–2933.

[c] F. Rodriguez-Rivas, A. Pastor, C. Barriga, M. Cruz-Yusta, L. Sánchez, I. Pavlovic, Zn-Al layered double hydroxides as efficient photocatalysts for NOx abatement, Chem. Eng. J. 346 (2018) 151–158.

[d] Y. Ye, Z. Zang, T. Zhou, F. Dong, S. Lu, X. Tang, W. Wei, Y. Zhang, Theoretical and experimental investigation of highly photocatalytic performance of CuInZnS nanoporous structure for removing the NO gas, J. Catal. 357 (2018) 100-107.

[e] J. Ma, H. Wu, Y. Liu, H. He, Photocatalytic Removal of NO_x over Visible Light Responsive Oxygen-Deficient TiO_2, J. Phys. Chem. C, 118 (2014) 7434-7441.

[f] N. Todorova, T. Giannakopoulou, S. Karapati, D. Petridis, T. Vaimakis, A. Trapalis, Composite TiO_2/clays materials for photocatalytic NO_x oxidation, Appl. Surf. Sci., 319 (2014) 113-120.

[g] J. Ma, H. He, F. Liu, Effect of Fe on the photocatalytic removal of NO_x over visible light responsive Fe/TiO_2 catalysts, Appl. Catal. B: Environ. 179 (2015) 21-28.

[h] A. Trapalis, N. Todorova, T. Giannakopoulou, N. Boukos, T. Speliotis, D.; Dimotikali, J. Yu, TiO_2/graphene composite photocatalysts for NO_x removal: A comparison of surfactant-stabilized graphene and reduced graphene oxide Appl. Catal. B: Environ. 180 (2016) 637-647.

[i] J. Balbuena, J.M. Calatayud, M. Cruz-Yusta, P. Pardo, F. Martín, J. Alarcón, L. Sánchez, Mesocrystalline anatase nanoparticles synthesized using a simple hydrothermal approach with enhanced light harvesting for gas-phase reaction, Dalton Trans. 47 (2018) 6590.

[j] B. Tan, X. Zhang, Y. Li, H. Chen, Xi. Ye, Y. Wang, J. Ye, Anatase TiO_2 Mesocrystals: Green Synthesis, In Situ Conversion to Porous Single Crystals, and Self-Doping Ti^{3+} for Enhanced Visible Light Driven Photocatalytic Removal of NO, Chem. Eur. J. 23 (2017) 5478 –5487.

[k] Q. Zhang, Y. Huang, S. Peng, Y. Zhang, Z. Shen, J-j. Cao, W. Ho, S. Cheng, L. David, Y.H. Pui, Perovskite $LaFeO_3$-$SrTiO_3$ Composite for Synergistically Enhanced NO Removal under Visible Light Excitation, Appl. Catal. B: Environ. 204 (2017) 346-357.

[l] J. Luo, G. Dong, Y. Zhu, Z. Yang, Chuanyi Wang, Switching of semiconducting behavior from n-type to p-type induced high photocatalytic NO removal activity in g-C_3N_4, Appl. Catal. B: Environ. 214 (2017) 46-56.

[m] J. Hu, D. Chen, N. Li, Q. Xu, H. Li, J. He, J. Lu, Fabrication of graphitic-C_3N_4 quantum dots/graphene-$InVO_4$ aerogel hybrids with enhanced photocatalytic NO removal under visible-light irradiation, Appl. Catal. B: Environ. 236 (2018) 45-52.

[n] X. Li, W. Zhang, J. Li, G. Jiang, Y. Zhou, S. Lee, Fan Dong, Transformation pathway and toxic intermediates inhibition of photocatalytic NO removal on designed Bi metal@defective $Bi_2O_2SiO_3$, Appl. Catal. B: Environ. 241 (2019) 187-195.

[o] H. Li, H. Shang, X. Cao, Z. Yang, Z. Ai, L. Zhang, Oxygen Vacancies Mediated Complete Visible Light NO Oxidation via Side-On Bridging Superoxide Radicals*, Environ. Sci. Technol. 52* (2018) 8659–8665.

[p] H. Wang, Y. Sun, G. Jiang, Y. Zhang, H. Huang, Z. Wu, S. C. Lee, F. Dong, Unraveling the Mechanisms of Visible Light Photocatalytic NO Purification on Earth-Abundant Insulator-Based Core–Shell Heterojunctions, Environ. Sci. Technol. 52 (2018) 1479–1487.

[q] X. Ding, W. Ho, J. Shang, Li. Zhang, Self doping promoted photocatalytic removal of no under visible light with Bi_2MoO_6: Indispensable role of superoxide ions, Appl. Catal. B: Environ. 182 (2016) 316-325.

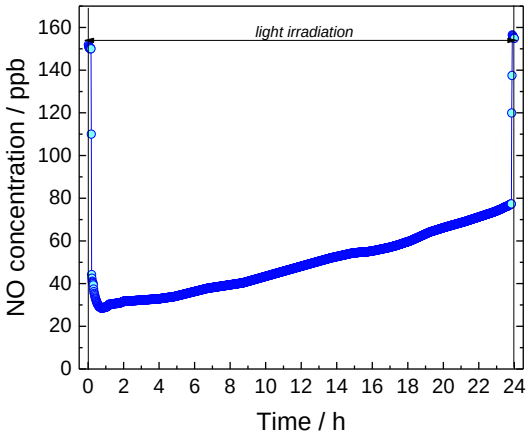

Figure S8. Concentration profile obtained during the photo-degradation of gaseous NO under 24 hours of light irradiation on dZn@RHA-4 sample.

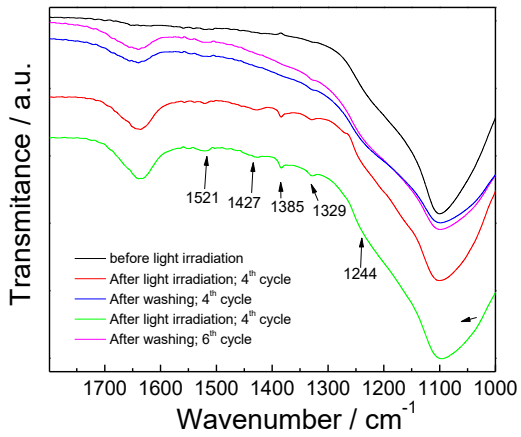

Figure S9. IR spectra obtained for dZn@RHA-4 sample before and after the repeated photocatalytic test cycles, and the corresponding washing products.

3.3. Effects of Fe^{3+} substitution on Zn-Al layered double hydroxides for enhanced NO photochemical abatement.

ELSEVIER

Chemical Engineering Journal

Volume 387, 1 May 2020, 124110

Effects of Fe^{3+} substitution on Zn-Al layered double hydroxides for enhanced NO photochemical abatement

Adrián Pastor [a], Fredy Rodriguez-Rivas [a, b], Gustavo de Miguel [c], Manuel Cruz-Yusta [a], Francisco Martin [d], Ivana Pavlovic [a] ✉, Luis Sánchez [a] ✉

[a] Departamento de Química Inorgánica, Instituto Universitario de Nanoquímica IUNAN, Universidad de Córdoba, Campus de Rabanales, E-14014 Córdoba, Spain

[b] Departamento de Química, Facultad de Química y Farmacia, Universidad Nacional Autónoma de Honduras (UNAH), Tegucigalpa, Honduras

[c] Departamento de Química Física y Termodinámica Aplicada, Instituto Universitario de Nanoquímica IUNAN, Universidad de Córdoba, Campus de Rabanales, E-14014 Córdoba, Spain

[d] Departamento de Ingeniería Química, Facultad de Ciencias, Universidad de Málaga, Campus de Teatinos, E-29071 Málaga, Spain

Received 25 September 2019, Revised 19 December 2019, Accepted 11 January 2020, Available online 13 January 2020.

https://doi.org/10.1016/j.cej.2020.124110

Highlights

- ZnAlFe-CO_3 LHDs are effective UV–Vis light De-NO_X photocatalysts.
- The Al^{3+} by Fe^{3+} ion replacement increases the surface area and Vis light absorption.
- The Fe centres decrease the e^-/h^+ recombination enhancing the ROS species production.
- The observed De-NO_X performance is remarkable.

ABSTRACT

In this work the ability of ZnAlFe-CO_3 layered double hydroxides (LDHs) as highly efficient UV–Vis light photocatalysts for the photochemical oxidation of NO gas was studied. LDHs with 3.5 to 4.1 M^{2+}/M^{3+} and 0.33 to 1.55 Fe/Al ratios were prepared by a coprecipitation method. The samples were characterized by different techniques such as XRD, XPS, FT-IR, ICP-MS, TG, SBET, SEM and Diffuse reflectance (DR). The increased presence of the Fe^{3+} ions gave rise to changes in the structure, morphology and optical properties of the LDHs. The prepared ZnAlFe-CO_3 systems exhibited increased surface area and enhanced visible-light absorbance. The photochemical NO abatement resulted in outstanding conversion efficiency (56%) and selectivity (93%) for the iron containing samples, due to a decrease of the e^-/h^+ recombination, higher generation of $\cdot O_2^-$ and ·OH radicals and their NO_2 adsorption ability.

Keywords: *LDH, Hydrotalcite, Photocatalyst, Nitrogen oxides*

GRAPHICAL ABSTRACT

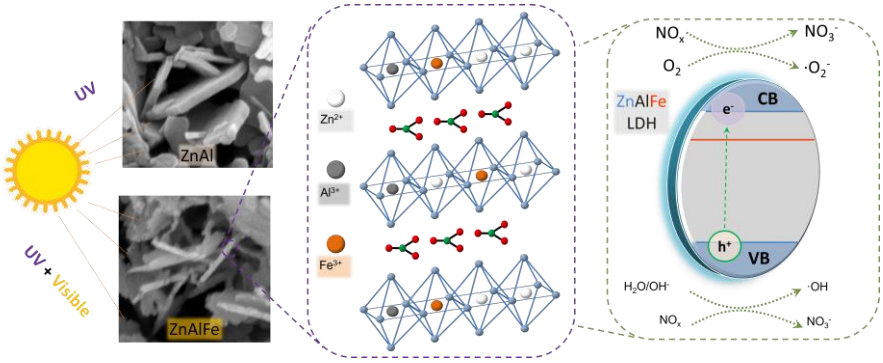

3.3.1. Introduction

The pollution in urban atmosphere is a major concern for modern society being one of the most serious environmental problems. Among the primary air pollutants, the presence of nitrogen oxides gases (NO_X = NO + NO_2) is highly relevant because they cause several adverse and harmful effects [1]. The transport sector contributes to about 30–40% of the emitted NO_X, of which 80% comes from diesel-powered vehicles [2,3]. As the emissions from diesel cars worsen with age [4], and because of the increase in road traffic, the recommended maximum amount of breathable NO_X is still often exceeded, especially in large cities [5,6].

In recent years, with the aim to confront this environmental problem, photocatalysis has been proposed as a viable technology to remedy NO_x pollution (De-NO_X action) at ppb-ppm levels in surrounding air [7]. Thus, photocatalytic De-NO_X removal is carried out in the presence of sunlight, atmospheric oxygen and water, all being abundant and already present in working ambient [8,9]. The feasibility of this remediation technology is demonstrated in many field tests [10,11] and corroborated by a great variety of commercial products available on the market, using TiO_2 as a photocatalyst due to its stable chemical properties.

However, the large implementation of this promising air purification technique requires tackling some of the drawbacks observed for TiO_2, such as its inability to exploit the visible light radiation, the low De-NO_x selectivity causing emissions of the higher toxic NO_2 molecules in the atmosphere [12–14], and its potential toxicity when inhaled [15]. In this sense, a large variety of semiconductor photocatalysts have been proposed as an alternative to titanium dioxide, with $Cu_{0.08}In_{0.25}ZnS_{1.41}$ [16], $LaFeO_3$-$SrTiO_3$ [17], p-g-C_3N_4 [18], C_3N_4/graphene-$InVO_4$ [19], Bi@$Bi_2O_2SiO_3$

[20], BiOCl [21], $SrCO_3$-BiOI [22], Bi_2MoO_6 [23], $Bi/ZnWO_4$ [24], α-Fe_2O_3 [25], WO_3/ZnO [26], ZnO@SiO_2 [27]; Bi@Bi_2GeO_5 [28], among the latest advanced De-NO_x compounds reported.

In this field of research we have just proposed the use of layered double hydroxides (LDH) as promising De-NO_x photocatalysts for the first time [29]. LDHs are layered materials with the general formula $[M_{1-x}^{II}M_x^{III}(OH)_2]^{x+}\ X_{x/n}^{n-}\cdot mH_2O$, where M(II) and M(III) are divalent and trivalent cations and X is the interlayer anion. This structure is similar to that of brucite, $Mg(OH)_2$, where a fraction of M (II) ions is replaced by M(III) ones. The excess of positive charge in the layers is balanced by intercalating anions and water molecules in the interlayer space. Metal ions and interlayer anions may vary over a wide range, while a metal ratio M(II)/M(III) could be in the range $0.1 < x < 0.33$ [30]. Recently, LDHs were considered as novel photocatalysts in processes such as aerobic degradation of pollutants [31], photocatalytic water splitting [32] and CO_2 photoreduction [33]. The unique structure, uniform distribution of different metal cations in the brucite layer, surface hydroxyl groups, flexible tunability, a variety of intercalated anions in their interlayer spaces, swelling properties, oxo-bridged linkage, high chemical stability and easy preparation are some of the encouraging advantages of the use of this group of materials as photocatalysts [34].

In the field of De-NOx photochemical processing, and considering the high efficiency and selectivity of a Zn based photocatalyst [26,27], our first approach in the use of LDH was related to the ZnAl-CO_3 system [29]. This photocatalyst, working under UV light, exhibited high NO removal efficiencies and impressive selectivity to the De-NO_x process. However new advances are necessary in the search of photocatalysts to be used in applications for De-NO_x remediation of urban atmosphere, where the

availability of UV light is sometimes limited due to the urban architecture, geographical location and gloomy weather conditions [7]. Thus, the visible light activation of a $DeNO_x$ photocatalyst is mandatory. To this aim, the present work treats the effect that gradual Fe^{3+} for Al^{3+} replacement has on improving LDH De-NO_x performance, i.e. on shifting their photocatalytic activity to the visible range and the enhanced NO2 adsorption. Moreover, by using EPR and PL techniques, the enhanced photocatalytic mechanism of NO_X removal by using ZnAlFe-CO_3 LDH was explained.

3.3.2. Materials and methods

$Zn(NO_3)_2{\cdot}6H_2O$, $Al(NO_3){\cdot}9H_2O$ and $Fe(NO_3){\cdot}9H_2O$ were purchased from PanReac AppliChem. 5,5-dimethyl-l-pyrroline-N-oxide (DMPO) was acquired from Sigma Aldrich. All the chemicals were at least 98–99% pure and demineralized water was used in the experimental section.

3.3.2.1 Synthesis of LDHs

The coprecipitation method was used to synthetize ZnAlFe-LDHs with different Fe/Al ratios. 100 mL of 0.015 M solution of Zn $(NO_3)_2{\cdot}6H_2O$, $Al(NO_3){\cdot}9H_2O$ and $Fe(NO_3){\cdot}9H2O$ (Zn/(Fe+Al) = 4; Fe/Al = 0, 0.3, 0.6, 0.9, 1.2, 1.5) was added drop-wise into 100 mL of 0.01 M Na_2CO_3 solution under stirring at room temperature. The constant pH = 10 was kept by dropping a 2.0 M NaOH solution during the coprecipitation reaction. The slurry obtained was then stirred for 3 h, centrifuged, washed with distilled water to be neutral (pH = 7.0), and dried in an oven at 60 °C. The LDHs

prepared were labelled as ZAF0, ZAF0.3, ZAF0.6, ZAF0.9, ZAF1.2 and ZAF1.5, the number denoting the initial Fe/Al ratio.

3.3.2.2. Characterization of the photocatalysts

X-ray diffraction (XRD) patterns of powdered samples were collected on a Bruker D8 Discovery instrument using Cu Kα radiation (λ =1.5405 Å) at the step size and step counting time of 0.02° (2θ) and 0.65 s, respectively. Infrared spectra (IR) analyses from 450 to 4000 cm^{-1} were carried out on transmission mode in a FT-MIR Bruker Tensor 27 with a resolution of 1 cm^{-1}. Nitrogen adsorption–desorption isotherms were recorded at 77.4 k in an ASAP 2020 apparatus (Micromeritics). Prior to the sorption measurements, samples were degassed at 105 °C under vacuum for 3 h. Specific surface areas were estimated from the N_2 adsorption isotherms, using the multipoint Brunauer–Emmett–Teller (BET) method over the relative equilibrium pressure interval $0.05 < P/P_0 < 0.30$. Scanning electron microscopy (SEM) images were obtained with a Helios Nanolab 650 microscope. Analyses of chemical compositions of LDHs were performed with induced coupled plasma mass spectroscopy (ICP-MS; Perkin Elmer Nexion X) after dissolving the samples in 0.1 M HCl. The water content of LDH was calculated from the thermogravimetric (TG) analysis which was obtained by using a Mettler Toledo apparatus in air atmosphere (flow: 100 mL min^{-1}) at a heating rate of 10 °C min^{-1}.

Diffuse reflectance (DR) spectra were collected from 200 to 800 nm in a Varian Cary 1E spectrophotometer, at a rate of 30 nm min^{-1} and a step of 0.5 nm. X-ray photoelectron spectra (XPS) were recorded using non-monochromated MgK radiation (hv = 1253.6 eV) and a hemispherical analyser operating at a constant pass energy of 29.35 eV (Physical

Electronics PHI 5700 spectrometer): The X-ray generator operated at 15 kV and 300 W. The pressure in the analysis chamber was about 10−7 Pa. Binding energies were corrected against those for C 1s peak of adventitious carbon fixed at 284.8 eV. The XPS peaks were curve-fitted by the software MultiPak version 9.3 using a convolution of independent Gaussian and Lorentzian contributions (the so-called Voigt profile). The steady-state photoluminescence (PL) emission spectra were collected on a FLS920 Fluorimeter (Edinburgh Instrument Ltd, Livingston, UK). Electron paramagnetic resonance (EPR) spectra were recorded in an EMXmicro (Bruker) spectrometer at room temperature. LDH powder was dispersed in a solution (water or methanol for detecting •OH or $\bullet O_2^-$, respectively) with 45 mM DMPO as the spin-trap agent and irradiated for 15 min with artificial sunlight (Xe Lamp).

3.3.2.3. Photocatalytic activity tests

The experimental conditions to carry out the photocatalytic tests, were based on ISO 22197-1, a method used to characterize the air purification measurement. The performance of LDHs in photo-oxidizing NO gas was assessed in a laminar flow reactor which contained a 50 × 50 mm sample holder. The reactor was placed inside a light sealed irradiation box (Solarbox 3000e RH) equipped with a Xe lamp with controlled irradiance. LDHs were irradiated with artificial sunlight (irradiances of 25 and 580 Wm^{-2} for UV and visible light) using 500 mg of sample powder in each test. Synthetic air and pure NO were mixed to create a simulated polluted urban atmosphere of 150 ppb [35] and sent to the reactor (flow rate gas = 0.30 l min^{-1}). Air was previously passed through a gas-washing bottle filled with demineralized water in order to maintain the relative

humidity at 50 ± 5%. The concentration of NO, NO_X and NO_2 gases from the reactor was continuously measured in a chemiluminescence analyzer (model Environment AC32M). Before and after the irradiation period of each test, the air/NO gas mixture was passed over the sample in the dark for 15 min to discard the existence of NO_X adsorption. Besides, there was no NO photolysis when the photocatalytic test was carried out in the absence of the sample. Each test was done three times in order to calculate the average concentration values. The calculated standard deviations were ± 0.3 ppb for NO concentration and ± 1.0 ppb for NO_2 and NO_X concentrations. The photocatalytic activity of the samples was studied regarding the following facets:

$$NO\ conversion\ (\%) = \frac{([NO]_{\mathrm{in}} - [NO]_{out})}{[NO]_{in}} \times 100 \qquad (1)$$

$$NOx\ conversion\ (\%) = \frac{([NOx]_{in} - [NOx]_{out})}{[NO]_{in}} \times 100 \qquad (2)$$

$$Selectivity;\ S\ (\%) = \frac{([NOx]_{in} - [NOx]_{out})/[NOx]_{in}}{([NO]_{in} - [NO]_{out})/[NO]_{in}} \times 100 \qquad (3)$$

where $[NO]_{in}$, $[NO_X]_{in}$ and $[NO]_{out}$, $[NO_X]_{out}$ represent the measured inlet and outlet concentrations, respectively, and $[NO_X] = [NO] + [NO_2]$.

3.3.3. Results and discussion

3.3.3.1. Phase and composition

The XRD patterns corresponding to the ZnAl-LDH and ZnAlFe-LDH samples are shown in **Fig. 1.** All the recorded XRD patterns are characteristic of layered double hydroxides, with higher intensity peaks (a basal diffraction plane with its corresponding harmonics, (*0 0 l*) at 2Θ values below 30°, and with broader and lower intensity (*h k l*) peaks above this value [36]. The basal spacing of around d_{003} = 7.6 Å obtained for all samples indicates that the carbonate anion is situated in the interlayer of LDH [37]. In comparison with the ZnAl-CO_3 LDH system previously reported [29], the XRD reflection peaks in the ZnAlFe-LDH samples are small and broad, suggesting that gradual substitution of Al^{3+} by Fe^{3+} provokes a decrease in the size of the crystalline domains of the samples. XRD patterns also show that the replacement of Al^{3+} for Fe^{3+} ions in the samples provokes a slight shift of the *0 0 l* reflections towards higher two theta degrees, thus indicating that the value of the lattice parameter c decreases (**Table S1**). This presence of Fe^{3+} increases the effective layer charge and thus increases the attraction between positive layers and interlayer anions. Moreover, the slightly larger ionic radius of Fe^{3+} (0.69 Å) with respect to Al^{3+} (0.67 Å) causes a slight increase in the lattice parameter *a*.

In **Fig. 1**, it is observed that XRD patterns of the ZnAlFe-LDH samples are similar in the 0.33–1.22 Fe/Al ratio range, confirming the crystallization of only a pure LDH phase. However, when increasing this ratio to 1.55 significant changes are observed in the XRD pattern of the ZAF1.5 sample (**Fig. 1**). Now a new low intensity reflection appears at around 17 two-tetha degrees and the (*0 1 2*) plane becomes higher in

intensity and slightly shifts two-theta degrees higher. Both reflections could be tentatively assigned to the presence of the $Fe_2CO_3(OH)_2$ phase (ICDD card n° 01-076-6357) [38]. **Figure S1** (in **Supplementary Information**) comparatively shows the C 1s, O 1s, Fe 2p, and Zn LMM normalized XPS spectra of the ZAF1.2 and ZAF1.5 samples. In addition to the peak of adventitious C (284.8 eV), the intensity of the peak at 289 eV associated with $CO_3^{2-}(OH^-)$ [39] is higher for the sample ZAF1.5, which corroborates that by XRD. All the rest of the samples showed a peak at 289 eV with an intensity similar to that shown for sample ZAF1.2 (**Fig. S1**). O1s peak at 531.4 eV was attributed to CO_3^{2-} and OH^- [39–41]. **Figure S1** also shows the pattern of the Zn LMM Auger bands, with the main peak at around 988 eV kinetic energy (498 eV binding energy) corresponding to the $Zn_5(CO_3^{2-})_2(OH^-)_6$ [39]. As shown by the pattern of the Al 2p (not shown) and Fe 3p regions and their binding energies (**Fig. S1**), the oxidation states were Al^{3+} and Fe^{3+}, respectively.

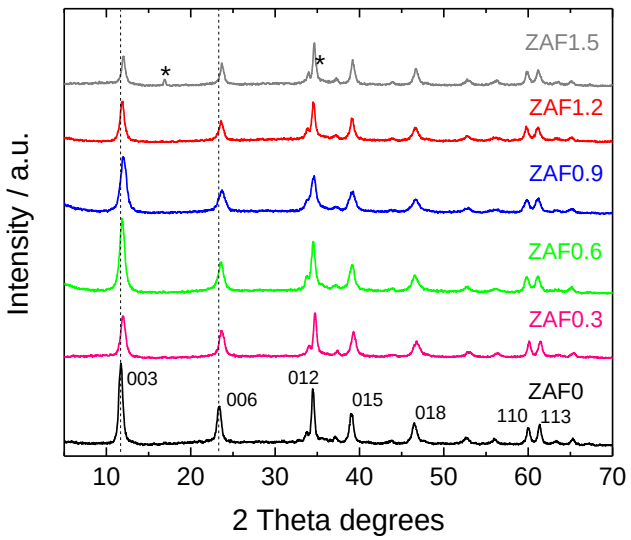

Fig. 1. XRD patterns for the ZnAl-LDH and ZnAlFe-LDH samples (*: $Fe_2CO_3(OH)_2$).

The Fourier Transform Infrared (FT-IR) spectra of the samples ZAF0 and ZAF0.6, by way of example, is included in **Fig. S2** and is characteristic of LDH compounds [36]. The most representative features are: a broad band around 3500 cm^{-1} corresponding to the hydroxyl groups vibrations, a band at 1634 cm^{-1} due to the bending mode of water molecules and the splited band around 1400 cm^{-1} (at 1366 cm^{-1} and 1507 cm^{-1}) of the carbonate v_3 antisymmetric vibration mode. This splitting is a consequence of the symmetry lowering from D_{3h} to C_{2v}, for the free carbonate and the interlayered LDH carbonate, respectively, due to its interaction with the OH^- groups and H_2O molecules. This splitting is more pronounced for ZnAlFe LDH phases [36] which confirms the Fe presence in LDH brucite-layers (**Fig. S2**). The decrease of symmetry, also gives rise to the activation of carbonate v_1 mode, infrared inactive in the free carbonate, with the corresponding band around 1075 cm^{-1}, together with the bending vibrations of OH groups in the 850–1000 cm^{-1} range. However, this range of IR spectrum is more complex because the carbonate bands could be overlapped with OH groups and metal–oxygen vibrational bands, as is the case in the ZAF sample [36,42,43].

Table 1 shows the data corresponding to the chemical analysis of the pure LDH samples. In the case of the ZAF0, the Zn/Al molar ratio is similar to that of the starting solution used to prepare the LDH material. However, as the amount of iron increases, the Zn^{2+}/M^{3+} molar ratio decreases, indicating the difficulty to preserve the M^{2+}/M^{3+} ratio constant during the building of the LDH framework. The Zn/(Al + Fe) atomic ratio, together with the number of water molecules (those calculated from the first weight loss in the TG curve), were used to propose the chemical formulae of the samples. It was assumed that the carbonate anions

compensate all positive charge caused by the presence of M^{3+} ions in the layers.

Table 1. Chemical and physical properties for the pure LDH samples: metal content and ratio; proposed formulae; BET surface and band gap energy value.

Sample	% Atomic			Atomic ratio		Proposed Formula	S_{BET}	Band gap (eV)
	Zn	Al	Fe	Zn/Al+Fe	Fe/Al		(m^2g	
ZAF0	63.16	15.34	--	4.11	--	$[Zn_{0.81}Al_{0.19}(OH)_2](CO_3)_{0.1}\cdot 0.67H_2O$	57.9	3.52
ZAF0.3	63.62	12.49	3.9	3.88	0.31	$[Zn_{0.80}Al_{0.15}Fe_{0.05}(OH)_2](CO_3)_{0.1}\cdot 0.48H_2O$	63.5	3.21
ZAF0.6	63.62	10.30	6.51	3.78	0.63	$[Zn_{0.79}Al_{0.13}Fe_{0.08}(OH)_2](CO_3)_{0.11}.0.50H_2O$	72.6	3.13
ZAF0.9	61.02	8.96	8.34	3.53	0.93	$[Zn_{0.78}Al_{0.11}Fe_{0.10}(OH)_2](CO_3)_{0.11}.0.62H_2O$	79.3	2.84
ZAF1.2	62.25	7.74	9.47	3.61	1.22	$[Zn_{0.78}Al_{0.10}Fe_{0.12}(OH)_2](CO_3)_{0.11}.0.68H_2O$	87.8	2.62

3.3.3.2. Morphology and porous structure of photocatalysts

The method of synthesis here used involves obtaining poorly crystalline samples. Thus for the ZAF0 sample, without iron, the typical hexagonal sheet-like structure expected for ZnAl-CO_3 LDHs was not completely formed, and the particles appear as rounded pseudo hexagonal sheets, as observed in the SEM images shown in **Fig. 2**. The crystallization becomes poorer with the presence and increase of the amount of iron in the chemical formulae, the sheets being mixed with aggregates of smaller amorphous particles. In the same way, the presence of iron seems to restrain the pillaring of LDH. In fact, the thickness of the platelets clearly decreases from 34 nm for the ZAF0 to 13 nm observed for the ZAF0.9 and ZAF1.2 samples, **Fig. S3**.

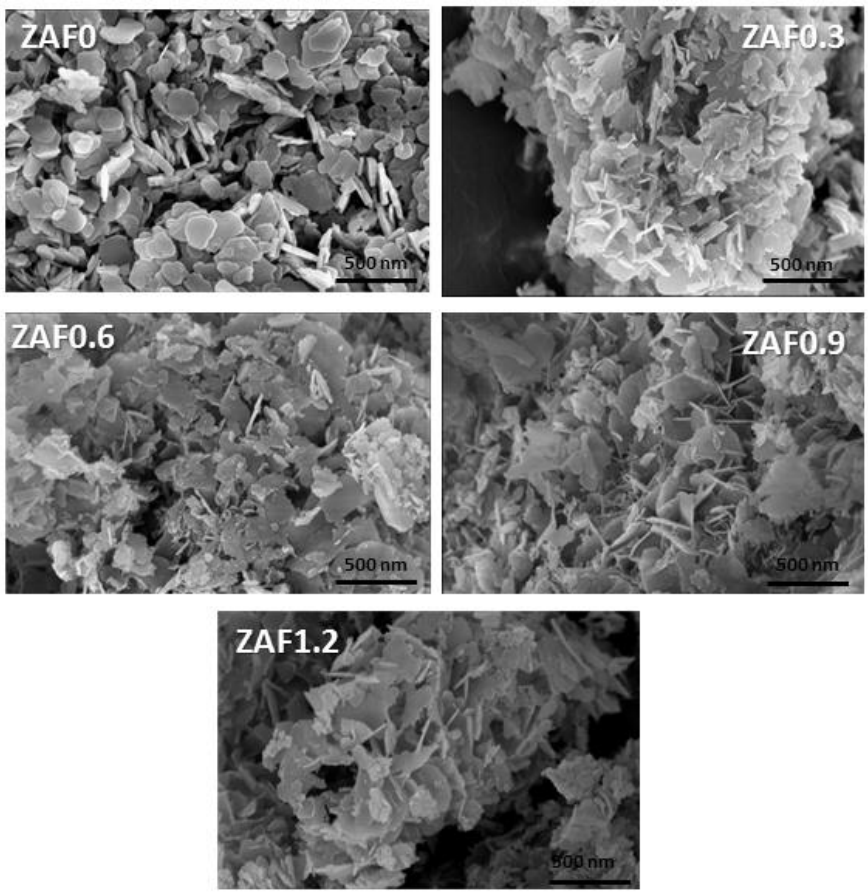

Fig. 2. SEM images for the ZnAl-LDH and ZnAlFe-LDH samples.

Subsequently, the surface area and porous structure were elucidated from the corresponding N_2 adsorption-desorption isotherm of the different samples, **Fig. 3**. The isotherm shape which corresponds to a type II, according to IUPAC classification [44] and characteristic of the adsorption on macro and non-porous materials, is similar to that reported for ZnAl LDHs [29,45]. At high relative pressure, $P/P_0 > 0.85$, the isotherms exhibit a H1 hysteresis loop, suggesting the presence of mesopores. The H1 loop is characteristic of agglomerates arranged in a fairly uniform way, indicating relatively high pore size uniformity and facile pore connectivity

[45]. In fact, a slight broadening of the hysteresis loop occurs when the amount of Fe in the LDH samples is increased, in agreement with the non-uniform particle size distribution observed by SEM. Specific surface areas determined by BET method are given in **Table 1** and were higher for Fe substituted samples, increasing with the iron content, which is in agreement with their lower crystallinity, as was confirmed by XRD (**Fig. 1**) and SEM characterization (**Fig. 2**).

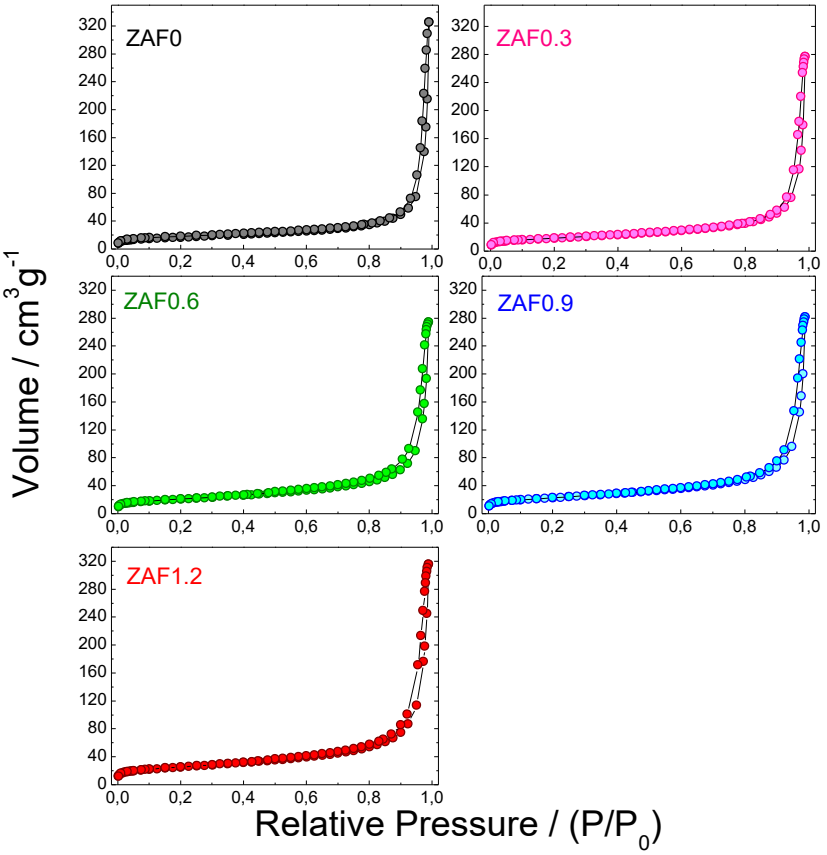

Fig. 3. N_2 adsorption-desorption isotherms for the ZnAl-LDH and ZnAlFe-LDH samples.

3.3.3.3. Optical properties

The corresponding UV–Vis spectra of the samples are shown in **Fig. 4a**. The absorption spectrum obtained for the ZAF0 sample is as expected for Zn-Al LHDs [46,47]. As Al^{3+} ions are replaced by Fe^{3+}, the absorbance increases and new bands characteristics of Zn-Fe LDHs appear at 280, 414 and 480 nm, assigned to ligand-to-metal charge transfer (O → Fe) for Fe^{3+} species octahedrally coordinated within the brucite-like sheets [48–51]. The incorporation of iron ions in the LDH structure results in the enhancement of the visible light absorption, in agreement with the appearance of a reddish colour in the samples (**Fig. S4**).

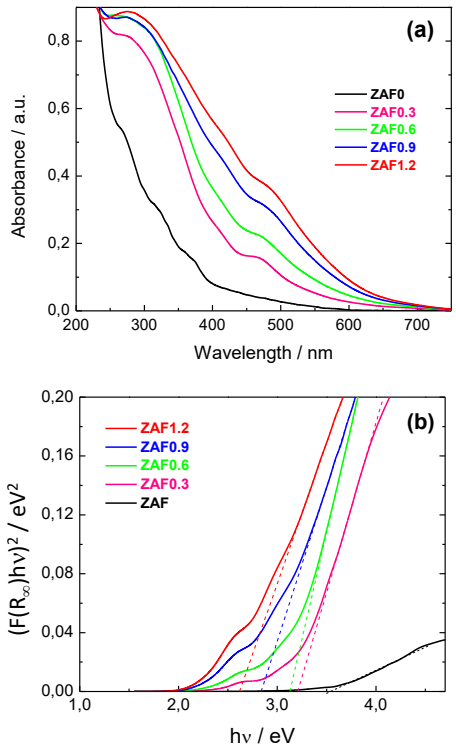

Fig. 4. The UV–Vis absorption spectra (a) and the Kubelka-Munk transformed reflectance spectra (b) for ZnAl-LDH and ZnAlFe-LDH samples.

The acquired diffused reflectance spectra were converted to the Kubelka–Munk function $[F(R_\infty)hv]^2$ with the objective to determine the value of the optical band gap (E_g). The band gap energies of the samples are estimated from the tangent lines in the plots of the modified Kubelka–Munk function vs. the energy of exciting light [47], as shown in **Fig. 4b**. The calculated band-gap energy for the ZAF0 was 3.52 eV (**Table 1**), this value decreasing as the iron content increased in the LDH compound. Thus for the ZAF1.2 sample, those with the higher content in Fe, a value of 2.62 eV is measured, similar to that previously reported for Zn-Fe LDHs materials [37,39].

3.3.3.4. Photocatalytic NO removal

The photochemical abatement of NO gas using ZnAlFe-LDH photocatalysts was studied. As previously reported by our group, ZnAl-LDHs are able to activate the complete oxidation of NO molecules to nitrate species under sunlight irradiation [29]. Thus, once the LDH particles absorb light, an electron transfer from the valence band (VB) to the conduction band (CB) occurs. The pairs of mobile charges (e^- and h^+) reaching the surface of the semiconductor particles [45,49] produce, as we will discuss later, reactive oxygen species (ROS) from the adsorbed water molecules, initiating the progressive oxidation of NO gas [7,25,52,53]. The occurrence of this NO photochemical removal process is simply confirmed through the observation of the evolution of the nitrogen oxide gases concentration recorded for the ZnAl-LDH and ZnAlFe-LDH samples as a function of sunlight irradiation time, **Fig. 5a**. In the absence of light for the first 15 min, the inlet NO concentration remained constant

indicating no physico-chemical interaction with the photocatalyst. However, a sudden decrease of NO concentration occurred just when the lamp was turned on. Under light irradiation, the NO removal rapidly increased on time (60 min) and reached a constant value, indicating the achievement of a stable photo-oxidation activity. The photochemical process stopped when illumination was shut down. Interesting differences were found for the NO abatement ability measured in the ZnAl-LDH and ZnAlFe-LDH samples. The presence of Fe in the LDH compound enhanced the NO abatement in 4–11%. The increased efficiency observed for the enriched iron samples is related with their higher surface area, which facilitates the contact between the reactant molecules and the metallic photo-active centres. Morevover, the amount of Fe^{3+} present in the LDH sample is highly relevant to the photochemical activity measured under only visible light ($\lambda > 510$ nm), **Fig. 5b**, in correlation with the changes in the band gap values measured (**Table 1**). Subsequently, a minor amount of NO molecules (10–17 ppbs) are removed from the reaction chamber, which is reasonable considering that the presence of Fe is 7 to 15 times lower than that of Zn in the LDH formulae. Interestingly, in spite of the minor presence of Fe, the efficiency in the NO abatement clearly increases with the content of iron. This is indicative that, under visible light, the iron centres are responsible for the light absorption and the photochemical oxidation process. In fact, in the absence of iron (ZAF0 sample), the NO abatement was not detected (**Fig. 5b**). Therefore, the replacement of Al^{3+} by Fe^{3+} ions converts the LDH into a De-NO_x visible light photocatalyst.

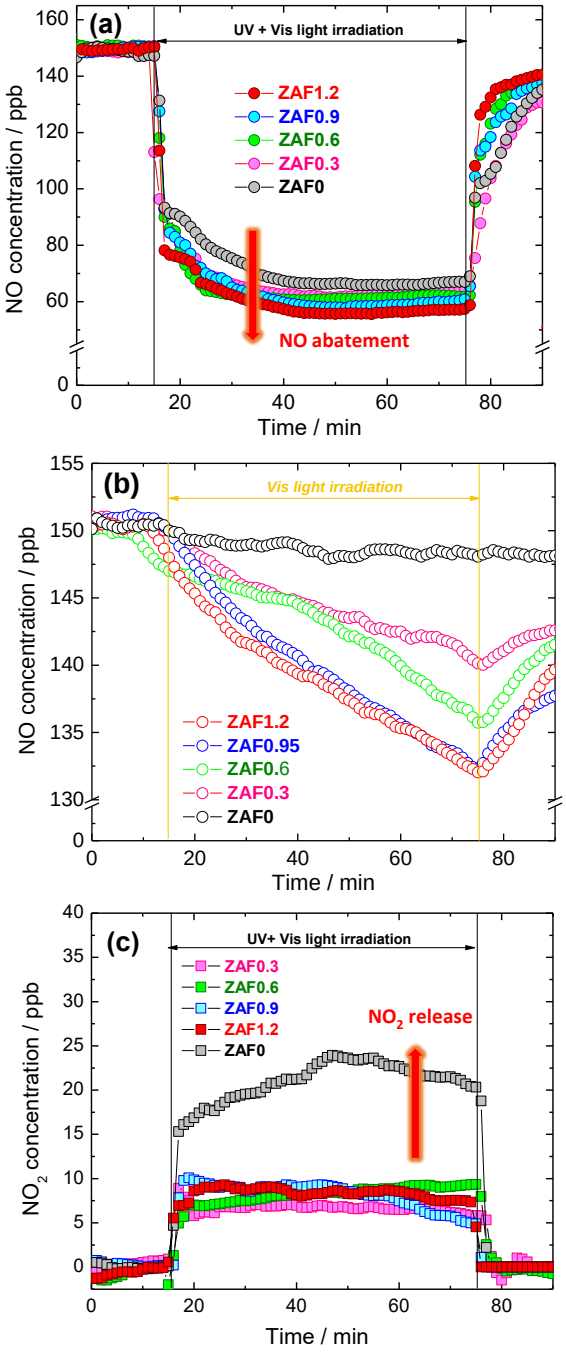

Fig. 5. Nitrogen oxides concentration profiles obtained during the photo-degradation of gaseous NO under light irradiation on the ZnAl-LDH and ZnAlFe-LDH samples.

Apart from the enhanced NO removal, the ZnAlFe-LDH samples are of interest because of their higher De-NO_x selectivity values. During the NO photochemical oxidation, the NO_2 gas appears as an intermediate, undesired specie because it is much more dangerous than NO [12]. The De-NO_x selectivity term [54], *S*, defines the ratio of degraded NO that is ultimately converted into harmless nitrate rather than into toxic nitrogen dioxide. In **Fig. 5c**, it can be observed that the amount of NO_2 raised molecules when using ZnAlFe-LDH photocatalysts, is nearly half that obtained by using ZnAl-LDH. As previously reported by our group [29], in similarity to ZnO systems [27,55], the ZnAl-LDH exhibits outstanding De-NO_x selectivity due to the sensitivity to NO_2 gas. Thus, the preliminary NO_2 adsorption studies carried out on the ZAF0 and ZAF0.3 samples in the dark, **Fig. S5**, show that lower concentration values for NO_2 are measured during the first 30 min, in comparison to that of a blank test (without the presence of a catalyst) in which the gas concentration remained constant. This is indicative that, during the De-NO_x process, the NO_2 gas molecules are probably being adsorbed on the surface of LDHs, facilitating their oxidation to nitrate before being released into the atmosphere. In **Fig. S5**, both samples ZAF0 and ZAF0.3 exhibited a similar NO_2 gas adsorption profile in agreement with their similar values of Zn content and specific surface area. However, the release of NO_2 is doubled when the De-NO_x reaction is performed with the ZAF0 sample, **Fig. 5c**. This would be indicative that physical as well as electronic govern the photochemical oxidation, as discussed below.

For practical considerations, **Fig. 6a** shows the NO and NO_X conversion and the *S* values measured from De-NO_X tests performed on phototacalysts and compared with those for Aeroxide® TiO_2 P25 (Evonik), a material broadly used worldwide as a reference in photocatalytic De-

NO_X processes. The photocatalyst reusability is represented in **Fig. 6b**. Due to their excellent *S* values around 92%, the ZnAlFe-LDH photocatalysts possess a higher ability to remove the NO_x oxides with an efficiency of about 30%, higher than that of the non-substituted ZnAl-LDH. These values are in line with the NO conversion (45–70%) and selectivity (84–98%) values recently reported for De-NO_x photocatalysts [13,21,23,27,56–58]. The measured values stand out from that of the TiO_2 P25 benchmark product, obtained under identical experimental conditions. As inferred from the nitrogen oxides concentration profiles obtained during the photo-degradation of gaseous NO on TiO_2 P25, **Fig. S6a**, this photocatalyst exhibited poor ability to avoid the release of NO_2 gas during the photochemical test [59]. The TiO_2 P25 did not show sensitivity to adsorb NO_2 gas [27], which would imply that the newly formed NO_2 molecules are released into the atmosphere before being oxidized. Therefore, its low De-NO_x selectivity (40%) is detrimental for favourable NO_x removal efficiency. Moreover, no photochemical activity was measured for TiO_2 P25 under visible light irradiation, **Fig. S6b**. **Fig. 6b** shows the diurnal mean values of NO concentration, reaching its maximum level (≈180 ppb) between 6.00 and 12.00 in the morning, measured at an urban roadside in a highly populated city [35]. It is of interest to know how the ZnAlFe-LDH could serve to abate this main NO_X peak concentration level. Thus, the ZAF1.2 sample was subjected to three consecutive NO photocatalytic removal experiments run in periods of 6 h under similar NO concentrations (NO inlet concentration of 150 ppb). The data collected (**Fig. 6b**) suggest that half of the pollution peak is abated, decreasing the photocatalytic efficiency by around 6% in the first three cycles due to the deposition of the nitrite/nitrate species during the photochemical oxidation process [27,29]. With the aim of eliminating these species, the

sample was washed with milli-Q water (filtered, collected and dried) after the third run. Subsequently, the efficiency was recovered in the next two runs (1st and 2nd after washing) indicating good regeneration and reusability for this type of photocatalyst. Therefore, the ZnAlFe-LDH can be considered as a useful photocatalyst in the abatement of the NO urban pollution.

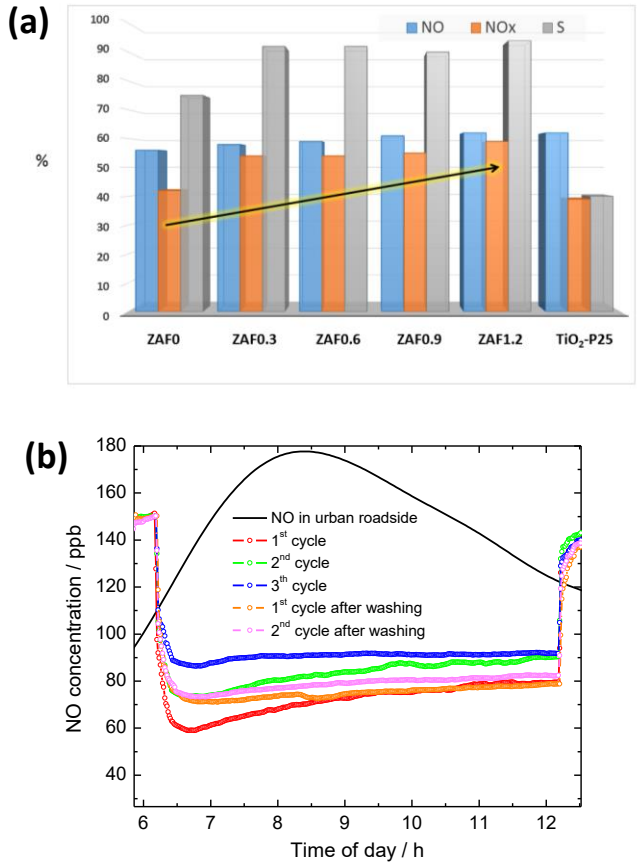

Fig. 6. (a) NO conversion, NO_X conversion and Selectivity values (%) for the ZnAl-LDH, ZnAlFe-LDH and TiO_2-P25 samples. (b) The diurnal distribution pattern of NO gas at urban roadsides and the NO concentration profile obtained for the ZAF1.2 sample (o) at different runs during 6 h of light irradiation. The sample was washed and dried after the 3rd run.

3.3.3.5. Charge separation and oxidation mechanism

Recently, our research group reported on the ability of ZnAl-LDH to photochemically remove the NO_X from air by its conversion into nitrate ions [29]. In the presence of oxygen and water molecules, the photocatalytic oxidation mechanism is briefly summarized in the NO $\rightarrow$ HNO_2 $\rightarrow$ NO_2 $\rightarrow$ NO_3^- sequential steps [29], assisting the reactive oxygen species (ROS), hydroxyl and/or superoxide radicals, as strong oxidants. The efficiency and active species involved in this mechanism when using the ZnAlFe-LDH photocatalyst are studied.

Photoluminescence (PL) spectroscopy is commonly used to study the photocharge generation, transfer and separation efficiency of photocatalysts, including LDH compounds [60]. **Fig. 7a** shows the PL signal corresponding to the ZnAl-LDH [61] and ZnAlFe-LDH photocatalysts. Under appropriate light illumination, the electrons in the valence band of ZnAl-LDH are promoted to the conduction band, leaving a hole in the valence band. The electrons in the conduction band are taken up by the Al atoms while the surface OH groups accept the photogenerated holes, which minimizes the e^-/h^+ recombination. These photogenerated charges initiate the formation of radical reactive species [62–64]. The high PL intensity measured for the non-substituted ZnAl-LDH is indicative of the high radiative recombination rate of the electrons and holes in the semiconductor, which competes with the reaction of the photogenerated charges with oxygen and water molecules to form the reactive oxygen species [19]. However, the PL signal is strongly attenuated by the presence of the iron centres in all the ZnAlFe-LDH samples. This behaviour clearly indicates that a new deactivation pathway for the photocharges is now available due to the presence of the iron centres. It is well-known

that iron doping introduces energy levels into the band gap of the ZnAl-LDH semiconductor which may act as electron scavengers [46]. Moreover, the MMCT (metal to metal charge transfer) electron transition through the oxo-bridged binuclear M^{III}–O–M^{II} linkages constructed in LDHs has been previously reported for catalysts absorbing visible light [64–66]. In a similar way, the absence of any PL signal in the ZnAlFe-LDH samples could reveal that the photogenerated charge is mainly transferred from the zinc to the iron centres even at low percentages of this metal. The MMCT electron transition will result in the production of superoxide anion radical, which is one of the main oxidative species in the NO $\rightarrow$ NO_3^- process. This effect should produce an enhancement of the catalytic reaction rates, which is in agreement with the enhanced performance commented above.

On the other hand, to shed light on the reactive species evolved in the photochemical reaction over the ZnAl-LDH and ZnAlFe-LDH samples, EPR measurements were conducted using DMPO as the spin trapping agent under sunlight excitation, **Fig. 7b** and **c**. No signal was detected when the photocatalyst suspension was in the dark. The strong characteristic signals of $\cdot O_2^-$ were detected in a methanolic dispersion of the ZnAl-LDH and ZnAlFe-LDH samples (**Fig. 7b**), whereas peaks of ·OH where observed in the corresponding aqueous dispersion (**Fig. 7c**). The high intensity of both signals is indicative of the important role played by these radical species in the photocatalytic NO oxidation. The four characteristic peaks for the DMPO-$\cdot O_2^-$ adduct were observed in the case of the ZnAl-LDH sample [67]. The presence of Fe^{3+} ions induces changes in the shape, and a sextet peaks appear in the signal measured for the ZnAlFe-LDH samples, resembling those observed for Zn-Fe based compounds [68,69].

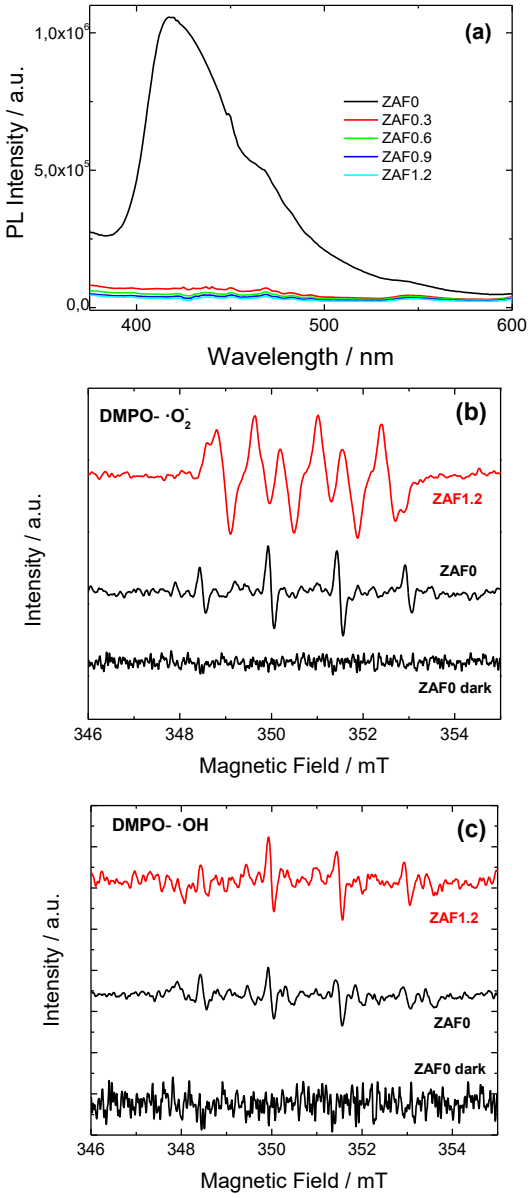

Fig. 6. (a) Photoluminescence (PL) spectra (excitation wavelength = 300 nm) of the different samples. DMPO spin-trapping EPR spectra of the ZAF0 and ZAF1.2 samples under UV–Vis light irradiation for 15 min in (b) methanol solution for $\cdot O_2^-$ and (c) aqueous solution for ·OH.

The intensity of the signal increases with the Fe content (**Fig S7**). In agreement with the commented MMCT transition mechanism, ZnAlFe-LDH samples displayed much stronger $\cdot O_2^-$ signals indicating that more radicals are produced by Fe substitution. For all the samples, the signal of DMPO-·OH adduct was constituted by quartet peaks featuring a 1:2:2:1 intensity ratio. The results commented above confirm the generation of reactive species and their involvement in NO and NO_2 photochemical oxidation, this being enhanced for the ZnAlFe-LDH photocatalyst.

3.3.4. Conclusions

ZnAlFe-CO^3 LHDs were studied as UV–Vis light photocatalysts for the photochemical oxidation of NO gas. The LHDs were prepared by the coprecipitation method, the Al^{3+} ion being gradually replaced by Fe^{3+} in the 0.33 to 1.55 Fe/Al ratio range. All the samples crystallized as pure LDH phase except Fe/Al = 1.55. The increased presence of Fe^{3+} ions caused different structural and morphological effects. As the iron content increased, the M^{2+}/M^{3+} ratio and the *c* lattice parameter decreased. Moreover, those samples enriched in iron exhibited the poorest crystallized particles. Consequently, the specific surface area resulted higher for the samples containing iron, and values ranging from 58 to 88 m^2g^{-1} were determined for the ZAF0 and ZAF1.2 samples, respectively. Concerning the optical properties, the incorporation of iron ions in the LDH structure resulted in the enhancement of the visible light absorption.

The ZnAlFe-LDH photocatalysts were able to activate the photochemical oxidation of NO molecules under UV–Vis irradiation. The photochemical abatement of NO gas is 4%–11%, increasing with the presence of Fe in the LDH compound. This enhanced photochemical

efficiency is related to their higher surface area and the better sunlight harvesting, as the iron centres are responsible for the visible light catalysis. The LDHs samples exhibited ability to adsorb NO_2 gas molecules explaining the outstanding De-NO_x selectivity values measured (≈92%), *S* being higher for the iron containing samples. Moreover, the studied photocatalysts are reusable, maintaining good NO removal for an extended period. PL and EPR measurements also served to understand how the electronic properties also assist to the high efficiency found in the removal of NO_X gases. The high radiative recombination rate of the photocharges observed for the non-substituted ZnAl-LDH clearly decreased in iron containing samples, indicating that the presence of the iron centres in the LDH framework must promote a new deactivation pathway for the photocharges. The EPR measurements confirmed the participation of the $\cdot O_2^-$ and ·OH reactive species in the photochemical processes involving in the ZnAl-LDH and ZnAlFe-LDH samples. The decay of the PL signal together with the stronger $\cdot O_2^-$ signal observed with the increase of iron content in ZnAlFe-LDH samples suggests a MMCT electron transition through the oxo-bridged M^{III}–O–M^{II} linkages in the LDH framework.

In summary, the Fe^{3+} substitution on the ZnAl-LDH induced changes in the physical and electronic properties producing an enhancement of the accessibility to the reactant molecules, of the light harvesting, of the reaction rates and the availability of the reactive species, all of them increasing the efficiency and selectivity of NO photochemical abatement.

3.3.5. Acknowledgements

This work was partly financed by the Junta de Andalucía, Spain (PAI Groups FQM-214 and FQM-175) and Spanish Government (MAT2017-88284-P and CTQ2017-84221-R). Rodriguez-Rivas acknowledges a grant from the Fundación Carolina, Colombia to research at the University of Córdoba (Spain). Adrián Pastor acknowledges a grant from the Ministerio de Educación, Cultura y Deporte, Spain (FPU16/05041) to research at the University of Córdoba (Spain).

3.3.6. References

[1] Michael C. Newman, William H. Clements, Ecotoxicology: A Comprehensive Treatment, CRC Press, Boca Raton, Florida, 2008.

[2] B. Yang, K.M. Zhang, W.D. Xu, S. Zhang, S. Batterman, R.W. Baldauf, P. Deshmukh, R. Snow, Y. Wu, Q. Zhang, Z. Li, X. Wu, On-Road Chemical Transformation as an Important Mechanism of NO_2 Formation, Environ. Sci. Technol. 52 (2018) 4574–4582. doi:10.1021/acs.est.7b05648.

[3] R. Zouzelka, J. Rathousky, Photocatalytic abatement of NOx pollutants in the air using commercial functional coating with porous morphology, Appl. Catal. B Environ. 217 (2017) 466–476. doi:10.1016/j.apcatb.2017.06.009.

[4] Y. Chen, J. Borken-Kleefeld, NOx Emissions from Diesel Passenger Cars Worsen with Age, Environ. Sci. Technol. 50 (2016) 3327–3332. doi:10.1021/acs.est.5b04704.

[5] M.W. Frampton, I.A. Greaves, NOx - NOx: Who's there?, Am. J. Respir. Crit. Care Med. 179 (2009) 1077–1078. doi:10.1164/rccm.200903-0485ED.

[6] M.L. Williams, D.C. Carslaw, New Directions: Science and policy – Out of step on NO_x and NO_2?, Atmos. Environ. 45 (2011) 3911–3912. doi:10.1016/j.atmosenv.2011.04.067.

[7] J. Balbuena, M. Cruz-Yusta, L. Sánchez, Nanomaterials to Combat NO_x Pollution, J. Nanosci. Nanotechnol. 15 (2015) 6373–6385.

doi:10.1166/jnn.2015.10871.

[8] H. Chen, C.E. Nanayakkara, V.H. Grassian, Titanium Dioxide Photocatalysis in Atmospheric Chemistry, Chem. Rev. 112 (2012) 5919–5948. doi:10.1021/cr3002092.

[9] A. Folli, S.B. Campbell, J.A. Anderson, D.E. MacPhee, Role of TiO_2 surface hydration on NO oxidation photo-activity, J. Photochem. Photobiol. A Chem. 220 (2011) 85–93. doi:10.1016/j.jphotochem.2011.03.017.

[10] G.L. Guerrini, Photocatalytic performances in a city tunnel in Rome: NO_x monitoring results, Constr. Build. Mater. 27 (2012) 165–175. doi:10.1016/j.conbuildmat.2011.07.065.

[11] T. Maggos, J.G. Bartzis, M. Liakou, C. Gobin, Photocatalytic degradation of NO_x gases using TiO_2 -containing paint: A real scale study, J. Hazard. Mater. 146 (2007) 668–673. doi:10.1016/j.jhazmat.2007.04.079.

[12] R.J. Lewis, N.I. Sax, Sax's dangerous properties of industrial materials, twelfth, New York, 2012.

[13] J. Ma, H. Wu, Y. Liu, H. He, Photocatalytic removal of NO_x over visible light responsive oxygen-deficient TiO_2, J. Phys. Chem. C. 118 (2014) 7434–7441. doi:10.1021/jp500116n.

[14] J. Balbuena, M. Cruz-Yusta, A. Pastor, L. Sánchez, α-Fe_2O_3 /SiO_2 composites for the enhanced photocatalytic NO oxidation, J. Alloys Compd. 735 (2017) 1553–1561. doi:10.1016/j.jallcom.2017.11.259.

[15] E.C. Agency, ANNEX 2, Comments and response to comments on CLH proposal on titanium dioxide, 2017. https://echa.europa.eu/documents/10162/4fd87a5d-e671-43e4-a3b8-30e51a723107.

[16] Y. Ye, Z. Zang, T. Zhou, F. Dong, S. Lu, X. Tang, W. Wei, Y. Zhang, Theoretical and experimental investigation of highly photocatalytic performance of CuInZnS nanoporous structure for removing the NO gas, J. Catal. 357 (2018) 100–107. doi:10.1016/j.jcat.2017.11.002.

[17] Q. Zhang, Y. Huang, S. Peng, Y. Zhang, Z. Shen, J. Cao, W. Ho, S.C. Lee, D.Y.H. Pui, Perovskite $LaFeO_3$ -$SrTiO_3$ composite for synergistically enhanced NO removal under visible light excitation, Appl. Catal. B Environ. 204 (2017) 346–357.

doi:10.1016/j.apcatb.2016.11.052.

[18] J. Luo, G. Dong, Y. Zhu, Z. Yang, C. Wang, Switching of semiconducting behavior from n-type to p-type induced high photocatalytic NO removal activity in g-C_3N_4, Appl. Catal. B Environ. 214 (2017) 46–56. doi:10.1016/j.apcatb.2017.05.016.

[19] J. Hu, D. Chen, N. Li, Q. Xu, H. Li, J. He, J. Lu, Fabrication of graphitic-C_3N_4 quantum dots/graphene-$InVO_4$ aerogel hybrids with enhanced photocatalytic NO removal under visible-light irradiation, Appl. Catal. B Environ. 236 (2018) 45–52. doi:10.1016/j.apcatb.2018.04.080.

[20] X. Li, W. Zhang, J. Li, G. Jiang, Y. Zhou, S.C. Lee, F. Dong, Transformation pathway and toxic intermediates inhibition of photocatalytic NO removal on designed Bi metal@defective $Bi_2O_2SiO_3$, Appl. Catal. B Environ. 241 (2019) 187–195. doi:10.1016/j.apcatb.2018.09.032.

[21] H. Li, H. Shang, X. Cao, Z. Yang, Z. Ai, L. Zhang, Oxygen Vacancies Mediated Complete Visible Light NO Oxidation via Side-On Bridging Superoxide Radicals, Environ. Sci. Technol. 52 (2018) 8659–8665. doi:10.1021/acs.est.8b01849.

[22] H. Wang, Y. Sun, G. Jiang, Y. Zhang, H. Huang, Z. Wu, S.C. Lee, F. Dong, Unraveling the Mechanisms of Visible Light Photocatalytic NO Purification on Earth-Abundant Insulator-Based Core-Shell Heterojunctions, Environ. Sci. Technol. 52 (2018) 1479–1487. doi:10.1021/acs.est.7b05457.

[23] X. Ding, W. Ho, J. Shang, L. Zhang, Self doping promoted photocatalytic removal of no under visible light with bi2moo6: Indispensable role of superoxide ions, Appl. Catal. B Environ. 182 (2016) 316–325. doi:10.1016/j.apcatb.2015.09.046.

[24] Y. Gao, Y. Huang, Y. Li, Q. Zhang, J. Cao, W. Ho, S.C. Lee, Plasmonic Bi/$ZnWO_4$ Microspheres with Improved Photocatalytic Activity on NO Removal under Visible Light, ACS Sustain. Chem. Eng. 4 (2016) 6912–6920. doi:10.1021/acssuschemeng.6b01852.

[25] R. Sugrañez, J. Balbuena, M. Cruz-yusta, F. Martín, J. Morales, L. Sánchez, Efficient behaviour of hematite towards the photocatalytic degradation of NO_x gases, Appl. Catal. B Environ. 165 (2015) 529–536. doi:10.1016/j.apcatb.2014.10.025.

[26] A. Gasparotto, G. Carraro, C. Maccato, C. Sada, J. Balbuena, M. Cruz-Yusta, L. Sánchez, N. Vodišek, U. Lavrencic Štangar, D. Barreca, WO_3 -decorated ZnO nanostructures for light-activated applications, CrystEngComm. 20 (2018) 1282–1290. doi:10.1039/C7CE02148H.

[27] A. Pastor, J. Balbuena, M. Cruz-Yusta, I. Pavlovic, L. Sánchez, ZnO on rice husk: A sustainable photocatalyst for urban air purification, Chem. Eng. J. 368 (2019) 659–667. doi:10.1016/j.cej.2019.03.012.

[28] X. Li, W. Zhang, W. Cui, J. Li, Y. Sun, G. Jiang, H. Huang, Y. Zhang, F. Dong, Reactant activation and photocatalysis mechanisms on Bi-metal@Bi_2GeO_5 with oxygen vacancies: A combined experimental and theoretical investigation, Chem. Eng. J. 370 (2019) 1366–1375. doi:10.1016/j.cej.2019.04.003.

[29] F. Rodriguez-Rivas, A. Pastor, C. Barriga, M. Cruz-Yusta, L. Sánchez, I. Pavlovic, Zn-Al layered double hydroxides as efficient photocatalysts for NOx abatement, Chem. Eng. J. 346 (2018) 151–158. doi:10.1016/j.cej.2018.04.022.

[30] C. Forano, T. Hibino, F. Leroux, C. Taviot-Guého, Layered Double Hydroxides, in: F. Bergaya, B.K.G. Theng, G.B.T.-D. in C.S. Lagaly (Eds.), Handb. Clay Sci., Elsevier, 2006: pp. 1021–1095. doi:https://doi.org/10.1016/S1572-4352(05)01039-1.

[31] M. Shao, J. Han, M. Wei, D.G. Evans, X. Duan, The synthesis of hierarchical Zn-Ti layered double hydroxide for efficient visible-light photocatalysis, Chem. Eng. J. 168 (2011) 519–524. doi:10.1016/j.cej.2011.01.016.

[32] C.G. Silva, Y. Bouizi, V. Fornés, H. García, Layered double hydroxides as highly efficient photocatalysts for visible light oxygen generation from water, J. Am. Chem. Soc. 131 (2009) 13833–13839. doi:10.1021/ja905467v.

[33] N. Ahmed, Y. Shibata, T. Taniguchi, Y. Izumi, Photocatalytic conversion of carbon dioxide into methanol using zinc-copper-M(III) (M = aluminum, gallium) layered double hydroxides, J. Catal. 279 (2011) 123–135. doi:10.1016/j.jcat.2011.01.004.

[34] L. Mohapatra, K. Parida, A review on the recent progress, challenges and perspective of layered double hydroxides as promising photocatalysts, J. Mater. Chem. A. 4 (2016) 10744–10766. doi:10.1039/c6ta01668e.

[35] K.H. Kim, S.K. Pandey, H.T. Nguyen, S.Y. Chung, S.J. Cho, M.Y. Kim, J.M. Oh, Y. Sunwoo, Long-term behavior of particulate matters at urban roadside and background locations in Seoul, Korea, Transp. Res. Part D Transp. Environ. 15 (2008) 168–174. doi:10.1016/j.trd.2009.12.001.

[36] V. Rives, Layered Double Hydroxides: Present and Future, Nova Science Publishers Inc, New York, 2001.

[37] A.V. F. Cavani, F. Trifirò, Hydrotalcite-type anionic clays: preparation, properties and applications, Catal. Today. 11 (1991) 173–301.

[38] L. Zheng, N.S. Matin, J. Landon, G.A. Thomas, K. Liu, CO_2 loading-dependent corrosion of carbon steel and formation of corrosion products in anoxic 30 wt.% monoethanolamine-based solutions, Corros. Sci. 102 (2016) 44–54. doi:10.1016/j.corsci.2015.09.015.

[39] J. Winiarski, W. Tylus, K. Winiarska, I. Szczygieł, B. Szczygieł, XPS and FT-IR Characterization of Selected Synthetic Corrosion Products of Zinc Expected in Neutral Environment Containing Chloride Ions, J. Spectrosc. 2018 (2018). doi:10.1155/2018/2079278.

[40] B.R. Strohmeier, W.T. Evans, D.M. Schrall, Preparation and surface characterization of zincated aluminium memory-disc substrates, J. Mater. Sci. 28 (1993) 1563–1572. doi:10.1007/BF00363350.

[41] J. Duchoslav, R. Steinberger, M. Arndt, D. Stifter, XPS study of zinc hydroxide as a potential corrosion product of zinc: Rapid X-ray induced conversion into zinc oxide, Corros. Sci. 82 (2014) 356–361. doi:10.1016/j.corsci.2014.01.037.

[42] J.M. García-García, M.E. Pérez-Bernal, R.J. Ruano-Casero, V. Rives, Chromium and yttrium-doped magnesium aluminum oxides prepared from layered double hydroxides, Solid State Sci. 9 (2007) 1115–1125. doi:10.1016/j.solidstatesciences.2007.07.029.

[43] N. Gutmann, B. Müller, Insertion of the Dinuclear Dihydroxo-Bridged Cr(III) Aquo Complex into the Layered Double Hydroxides of Hydrotalcite-Type, J. Solid State Chem. 122 (1996) 214–220. doi:10.1006/jssc.1996.0104.

[44] K.S.W. Sing, Reporting physisorption data for gas/solid systems with special reference to the determination of surface area and

porosity (Recommendations 1984), Pure Appl. Chem. 57 (1985) 603–619. doi:10.1351/pac198557040603.

[45] D. Carriazo, M. Del Arco, E. García-López, G. Marc, C. Martín, L. Palmisano, V. Rives, Zn,Al hydrotalcites calcined at different temperatures: Preparation, characterization and photocatalytic activity in gas-solid regime, J. Mol. Catal. A Chem. 342–343 (2011) 83–90. doi:10.1016/j.molcata.2011.04.015.

[46] K.M. Parida, L. Mohapatra, Carbonate intercalated Zn/Fe layered double hydroxide: A novel photocatalyst for the enhanced photo degradation of azo dyes, Chem. Eng. J. 179 (2012) 131–139. doi:10.1016/j.cej.2011.10.070.

[47] A.A.A. Ahmed, Z.A. Talib, M.Z. Bin Hussein, A. Zakaria, Zn-Al layered double hydroxide prepared at different molar ratios: Preparation, characterization, optical and dielectric properties, J. Solid State Chem. 191 (2012) 271–278. doi:10.1016/j.jssc.2012.03.013.

[48] E.M. Seftel, M. Puscasu, M. Mertens, P. Cool, G. Carja, Photo-responsive behavior of γ-Fe_2O_3 NPs embedded into ZnAlFe-LDH matrices and their catalytic efficiency in wastewater remediation, Catal. Today. 252 (2015) 7–13. doi:10.1016/j.cattod.2014.11.039.

[49] K. Morimoto, K. Tamura, S. Anraku, T. Sato, M. Suzuki, H. Yamada, Synthesis of Zn-Fe layered double hydroxides via an oxidation process and structural analysis of products, J. Solid State Chem. 228 (2015) 221–225. doi:10.1016/j.jssc.2015.04.045.

[50] A.C. Heredia, M.I. Oliva, B. Agñ, C.I. Zandalazini, S.G. Marchetti, E.R. Herrero, M.E. Crivello, Synthesis, characterization and magnetic behavior of Mg-Fe-Al mixed oxides based on layered double hydroxide, J. Magn. Magn. Mater. 342 (2013) 38–46. doi:10.1016/j.jmmm.2013.04.057.

[51] G. Carja, E. Husanu, C. Gherasim, H. Iovu, Layered double hydroxides reconstructed in $NiSO_4$ aqueous solution as highly efficient photocatalysts for degrading two industrial dyes, Appl. Catal. B Environ. 107 (2011) 253–259. doi:10.1016/j.apcatb.2011.07.020.

[52] S.M. Xu, T. Pan, Y.B. Dou, H. Yan, S.T. Zhang, F.Y. Ning, W.Y. Shi, M. Wei, Theoretical and Experimental Study on $M^{II}M^{III}$-Layered Double Hydroxides as Efficient Photocatalysts toward Oxygen Evolution from Water, J. Phys. Chem. C. 119 (2015) 18823–18834.

doi:10.1021/acs.jpcc.5b01819.

[53] S.J. Xia, F.X. Liu, Z.M. Ni, J.L. Xue, P.P. Qian, Layered double hydroxides as efficient photocatalysts for visible-light degradation of Rhodamine B, J. Colloid Interface Sci. 405 (2013) 195–200. doi:10.1016/j.jcis.2013.05.064.

[54] J.Z. Bloh, A. Folli, D.E. Macphee, Photocatalytic NO_x abatement: Why the selectivity matters, RSC Adv. 4 (2014) 45726–45734. doi:10.1039/c4ra07916g.

[55] S. Öztürk, N. Kilinç, N. Taşaltin, Z.Z. Öztürk, A comparative study on the NO_2 gas sensing properties of ZnO thin films, nanowires and nanorods, Thin Solid Films. 520 (2011) 932–938. doi:10.1016/j.tsf.2011.04.177.

[56] J. Balbuena, J.M. Calatayud, M. Cruz-Yusta, P. Pardo, F. Martín, J. Alarcón, L. Sánchez, Mesocrystalline anatase nanoparticles synthesized using a simple hydrothermal approach with enhanced light harvesting for gas-phase reaction, Dalt. Trans. 47 (2018) 6590–6597. doi:10.1039/C8DT00721G.

[57] B. Tan, X. Zhang, Y. Li, H. Chen, X. Ye, Y. Wang, J. Ye, Anatase TiO_2 Mesocrystals: Green Synthesis, In Situ Conversion to Porous Single Crystals, and Self-Doping Ti^{3+} for Enhanced Visible Light Driven Photocatalytic Removal of NO, Chem. – A Eur. J. 23 (2017) 5478–5487. doi:10.1002/chem.201605294.

[58] J. Liao, W. Cui, J. Li, J. Sheng, H. Wang, X. Dong, P. Chen, G. Jiang, Z. Wang, F. Dong, Nitrogen defect structure and NO+ intermediate promoted photocatalytic NO removal on H_2 treated g-C_3N_4, Chem. Eng. J. 379 (2020) 122282. doi:10.1016/j.cej.2019.122282.

[59] M.J. Hernández Rodríguez, E. Pulido Melián, O. González Díaz, J. Araña, M. Macías, A. González Orive, J.M. Doña Rodríguez, Comparison of supported TiO_2 catalysts in the photocatalytic degradation of NO_x, J. Mol. Catal. A Chem. 413 (2016) 56–66. doi:10.1016/j.molcata.2015.12.007.

[60] Y. Zhao, X. Jia, G.I.N. Waterhouse, L.Z. Wu, C.H. Tung, D. O'Hare, T. Zhang, Layered Double Hydroxide Nanostructured Photocatalysts for Renewable Energy Production, Adv. Energy Mater. 6 (2016) 1–20. doi:10.1002/aenm.201501974.

[61] K. Xu, Z. Zhang, G. Chen, J. Shen, Photoluminescence of colloids of

pristine ZnAl Layered Double Hydroxides, RSC Adv. 4 (2014) 19218–19220. doi:10.1039/c4ra01987c.

[62] S.A. Khan, S.B. Khan, A.M. Asiri, Toward the design of Zn-Al and Zn-Cr LDH wrapped in activated carbon for the solar assisted de-coloration of organic dyes, RSC Adv. 6 (2016) 83196–83208. doi:10.1039/c6ra10598j.

[63] N. Baliarsingh, K.M. Parida, G.C. Pradhan, Effects of Co, Ni, Cu, and Zn on photophysical and photocatalytic properties of carbonate intercalated M^{II}/Cr LDHs for enhanced photodegradation of methyl orange, Ind. Eng. Chem. Res. 53 (2014) 3834–3841. doi:10.1021/ie403769b.

[64] K. Parida, L. Mohapatra, N. Baliarsingh, Effect of Co^{2+} substitution in the framework of carbonate intercalated Cu/Cr LDH on structural, electronic, optical, and photocatalytic properties, J. Phys. Chem. C. 116 (2012) 22417–22424. doi:10.1021/jp307353f.

[65] N. Baliarsingh, L. Mohapatra, K. Parida, Design and development of a visible light harvesting Ni–Zn/Cr–CO_3^{2-} LDH system for hydrogen evolution, J. Mater. Chem. A. 1 (2013) 4236–4243. doi:10.1039/c2ta00933a.

[66] L. Mohapatra, K. Parida, M. Satpathy, Molybdate/tungstate intercalated oxo-bridged Zn/Y LDH for solar light induced photodegradation of organic pollutants, J. Phys. Chem. C. 116 (2012) 13063–13070. doi:10.1021/jp300066g.

[67] Y. Cai, H. Song, Z. An, X. Xiang, X. Shu, J. He, The confined space electron transfer in phosphotungstate intercalated ZnAl-LDHs enhances its photocatalytic performance for oxidation/extraction desulfurization of model oil in air, Green Chem. 20 (2018) 5509–5519. doi:10.1039/c8gc02284d.

[68] Y. Huang, D. Zhu, Q. Zhang, Y. Zhang, J. ji Cao, Z. Shen, W. Ho, S.C. Lee, Synthesis of a $Bi_2O_2CO_3/ZnFe_2O_4$ heterojunction with enhanced photocatalytic activity for visible light irradiation-induced NO removal, Appl. Catal. B Environ. 234 (2018) 70–78. doi:10.1016/j.apcatb.2018.04.039.

[69] Q. Yang, S. Wang, F. Chen, K. Luo, J. Sun, C. Gong, F. Yao, X. Wang, J. Wu, X. Li, D. Wang, G. Zeng, Enhanced visible-light-driven photocatalytic removal of refractory pollutants by Zn/Fe mixed metal oxide derived from layered double hydroxide, Catal.

Commun. 99 (2017) 15–19. doi:10.1016/j.catcom.2017.05.010.

Appendix III: Supplementary Information

Table S1. Cell parameters for the LDH samples.

Sample		Lattice parameters (Å)	
	d_{003}[(a)]	*a*	*c*
ZAF0	7,54	3,08	22,63
ZAF0.3	7,44	3,08	22,33
ZAF0.6	7,54	3,09	22,63
ZAF0.9	7,51	3,10	22,54
ZAF1.2	7,44	3,11	22,34

(a) Calculated form XRD patterns

The unit cell parameters were calculated as reported for LDH compounds by K. parida et al. in *J. Phys. Chem. C 116 (2012) 22417-22424.* The standard deviation in the calculated values was $\pm 10^{-3}$

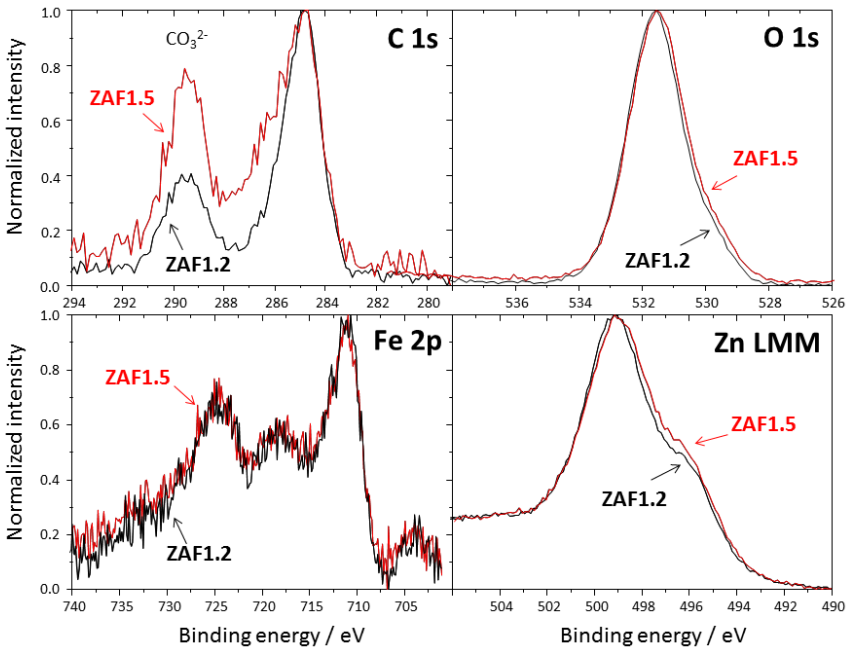

Figure S1. XPS spectra obtained from the ZAF1.2 and ZAF1.5 samples surface: C 1s, O 1s, Fe 2p and Zn LMM regions.

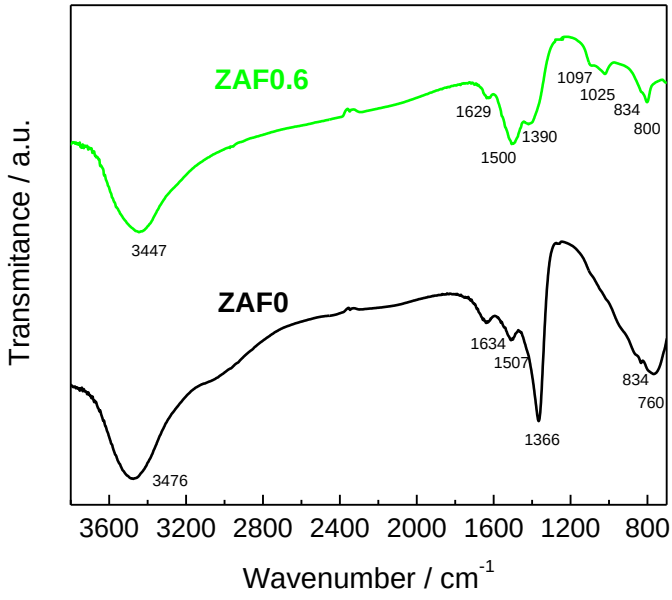

Figure S2. FT-IR spectra obtained for the ZAF0 and ZAF0.6 samples.

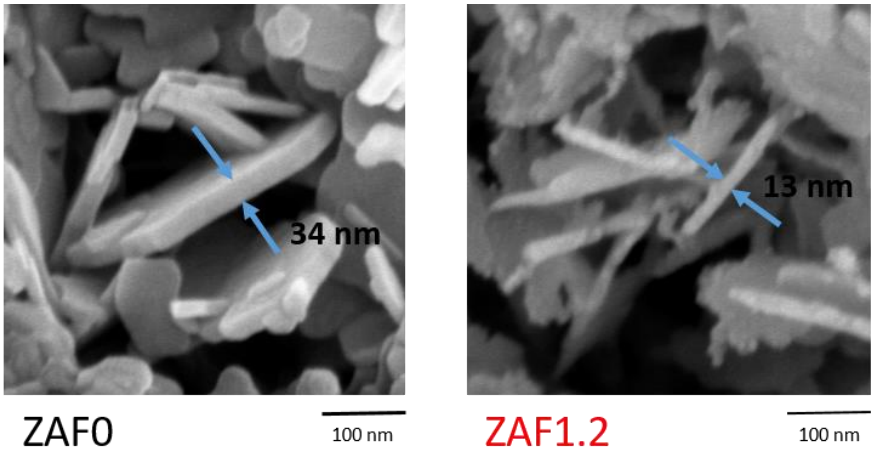

Figure S3. SEM images of the ZAF0 and ZAF1.2 samples.

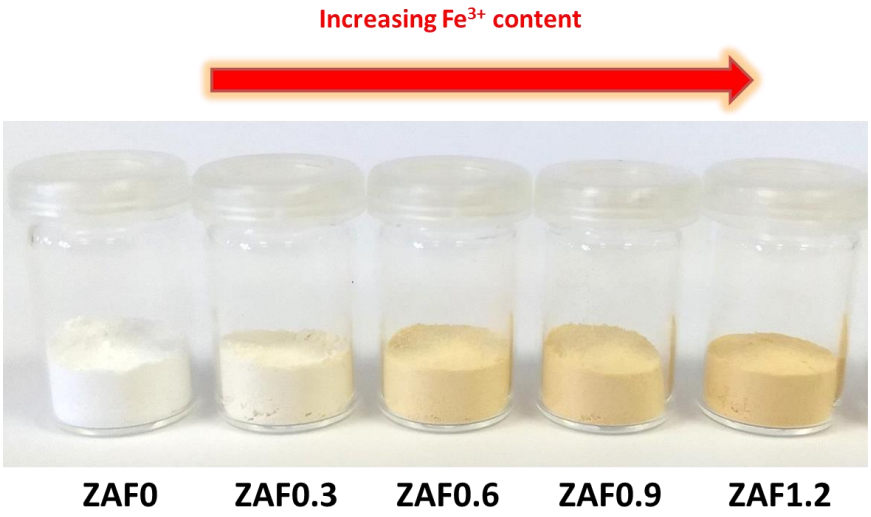

Figure S4. Images of the ZAF sample powders.

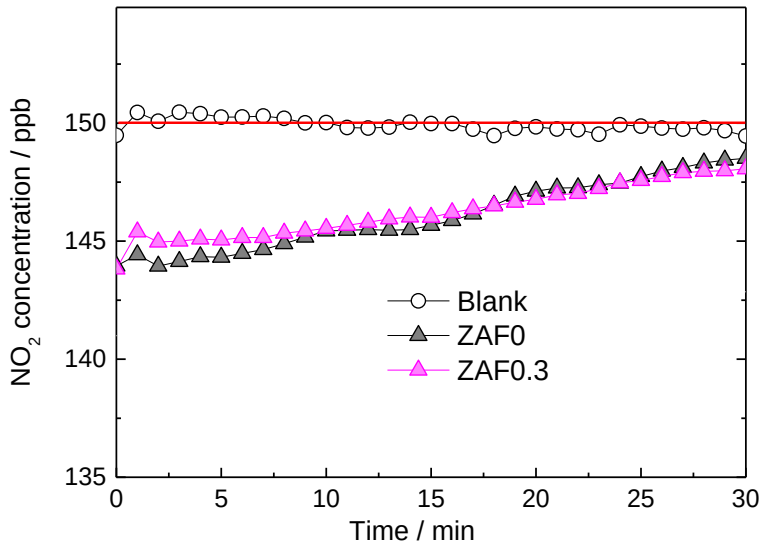

Figure S5. NO_2 concentration profiles obtained in dark condition for the ZAF0 and ZAF0.3 samples. The red line marks the NO_2 inlet concentration.

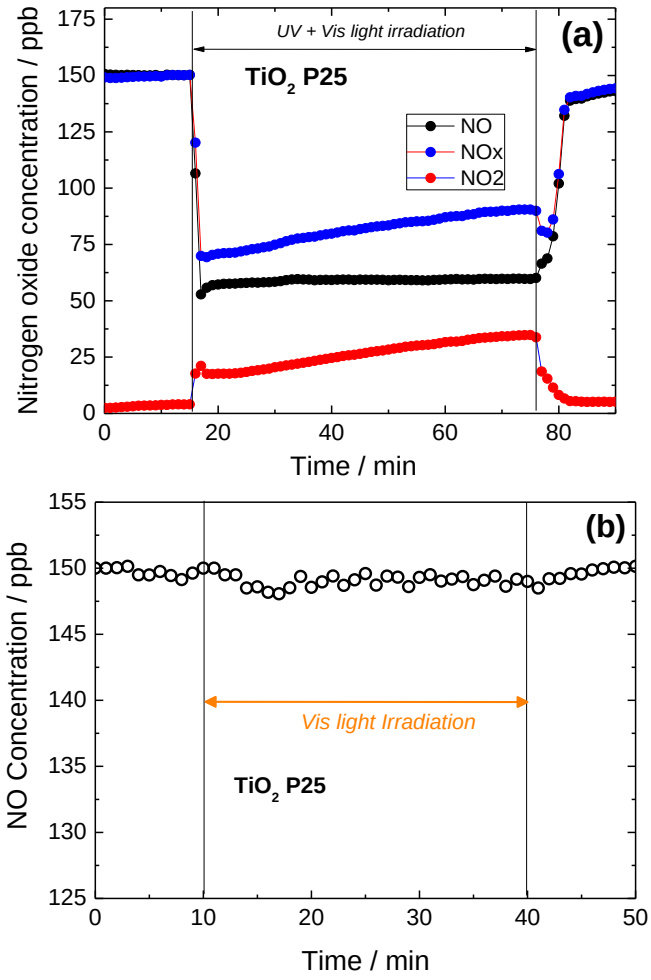

Figure S6. (a) Nitrogen oxides concentration profiles obtained during the photodegradation of gaseous NO under UV-Vis light irradiation on the TiO_2 P25 photocatalyst. (b) Concentration profiles obtained for TiO_2-P25 photocatalyst during the photochemical degradation of gaseous NO under Vis light irradiation ($\lambda > 510$ nm).

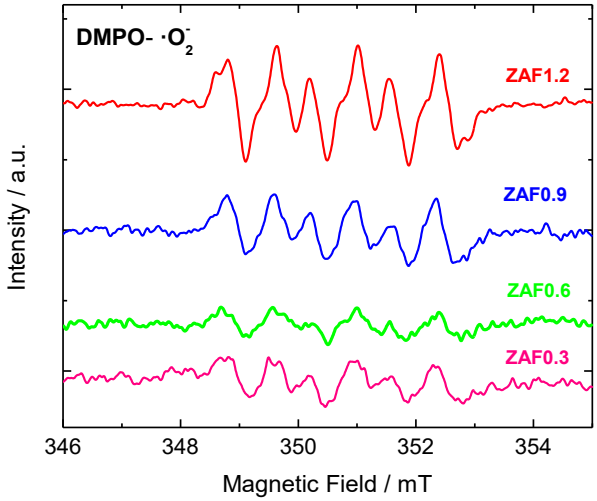

Figure S7. (a) DMPO spin-trapping EPR spectra of the ZnAlFe-LDH samples under UV-Vis light irradiation in a methanol solution for $\bullet O_2^-$.

3.4. Aqueous miscible organic solvent treated NiTi layered double hydroxide De-NO_x photocatalysts.

Chemical Engineering Journal
Volume 429, 1 February 2022, 132361

Aqueous miscible organic solvent treated NiTi layered double hydroxide De-NO_x photocatalysts

Adrián Pastor [a], Chunping Chen [b], Gustavo de Miguel [c], Francisco Martin [d], Manuel Cruz-Yusta [a], Jean-Charles Buffet [b], Dermot O'Hare [b] ✉, Ivana Pavlovic [a], Luis Sánchez [a] ✉

[a] Departamento de Química Inorgánica, Instituto Universitario de Nanoquímica IUNAN, Universidad de Córdoba, Campus de Rabanales, E-14014 Córdoba, España
[b] Chemistry Research Laboratory, Department of Chemistry, University of Oxford, Oxford OX1 3TA, UK
[c] Departamento de Química Física y Termodinámica Aplicada, Instituto Universitario de Nanoquímica IUNAN, Universidad de Córdoba, Campus de Rabanales, E-14014 Córdoba, España
[d] Departamento de Ingeniería Química, Facultad de Ciencias, Universidad de Málaga, Campus de Teatinos, E-29071 Málaga, España

Received 7 July 2021, Revised 3 September 2021, Accepted 5 September 2021, Available online 12 September 2021.
https://doi.org/10.1016/j.cej.2021.132361

Highlights

- LDH nanosheets are synthesized in large scale by a simple AMOST method.
- AMO-LDHs show impressive specific surface area values (up to 492 m^2g^{-1}).
- TiO_2 P25 De-NOx performance is surpassed by AMO-LDHs in 29 %.
- AMO-LDHs show an outstanding $DeNO_x$ selectivity.
- AMO-LDH photocatalysts are highly reusable.

ABSTRACT

New efficient photocatalysts are required to remediate polluted urban atmospheres. We prepared a series of highly dispersed aqueous miscible organic (AMO) solvent treated NiTi layered double hydroxide (Ni_xTi-AMO-LDHs (x = 2,3)) and studied their performance in the photocatalytic abatement of NO_x gases. These photocatalysts can be prepared by a simple and scalable coprecipitation method at room temperature. Ni_xTi-AMO-LDHs (x = 2,3) have been prepared with specific N_2 BET surface areas and pore volumes up to to 492 $m^2 g^{-1}$ and 1.37 $cm^3 g^{-1}$ respectively. Under sunlight simulation, the De-NO_x performance of the conventional LDH and P25 (TiO_2) benchmarks were surpassed by 40% and 17% respectively by the Ni_xTi-AMO-LDHs. The Ni_xTi-AMO-LDHs photocatalyst also exhibited outstanding reusability and unusually low release of the toxic NO_2. The selectivity for the De-NO_x process was investigated by in situ DRIFT measurements, the high surface area and pore volume was observed to play a significant role on the adsorption of the NO_2 and N_2O_4 intermediates. The 2D character of the AMO-LDHs contributed to an enhancement in the production of radical species under illumination and reduction charge carrier recombination.

Keywords: *LDH, Photocatalyst, Nitrogen oxides, AMOST, Nanosheet*

GRAPHICAL ABSTRACT

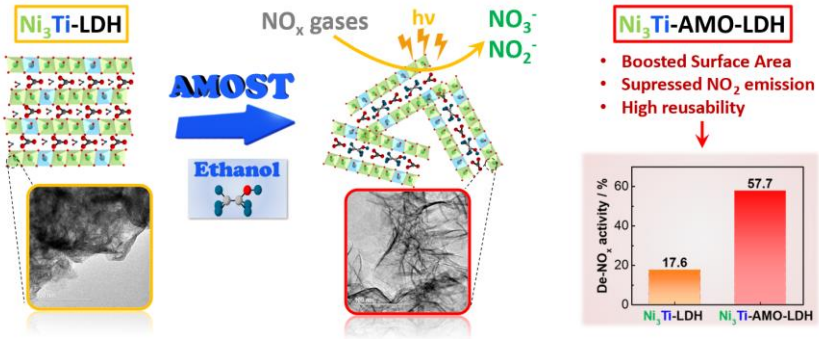

3.4.1. Introduction

Air quality in urban environments is one of the main issues marking current affairs and government policies [1,2]. The greater industrialization together with road traffic emissions are causing an increase in pollution in large cities despite the legislative measures taken [3,4]. Among the existing urban air pollutant gases, the presence of nitrogen oxides (NO_x = NO + NO_2) is of great concern because of their high toxicity and their adverse effects on the environment such as acid rain, tropospheric ozone and particulate matter formation [5,6]. Moreover, their presence in the urban atmosphere causes thousands of early deaths worldwide [7].

In recent years, photocatalysis has been shown to be a promising process to remove NO_x directly from the air (De-NO_x process) [8,9]. In contrast to the traditional catalytic reduction technologies which need high temperatures to obtain a correct De-NO_x efficacy, photocatalysis works under mild conditions (room temperature and ambient pressure) by using abundant and natural resources in the air: oxygen, water and sunlight irradiation [10]. This alternative strategy has already been applied in field trials using materials available in the commercial sector, demonstrating a potential real life application [11–13]. Commercial materials typically contain TiO_2 as a photocatalyst additive since it possesses chemical stability and a high band gap value (3.0 – 3.2 eV). Nevertheless, TiO_2 is also reported to exhibit some drawbacks such as the negligible absorption in the visible spectrum [14], poor De-NO_x selectivity (i.e. NO oxidation towards highly toxic NO_2) [15,16] or even hazardous when the powder is inhaled [17]. Therefore, research has been carried out to design alternative photocatalysts to TiO_2. Several interesting alternative De-NO_x advanced photocatalysts have been proposed lately, such as α-

Fe_2O_3 [18], g-C_3N_4 [19], Fe_3O_4/*mpg*-C_3N_4 (*mpg*: mesoporous graphitic) [20], $BaWO_4$/g-C_3N_4 [21], $Cu_{0.08}In_{0.25}ZnS_{1.41}$ [22], $LaFeO_3$-$SrTiO_3$ [23], FeOOH-Carbon quantum dots [24], WO_3/ZnO [25], ZnO@SiO_2 [26], Bi/$Bi_2O_{2-x}CO_3$ [27], Au/La-Bi_5O_7I [28], $BiSbO_4$ [29] and Bi_2MoO_6 [30], between others.

Herein we have developed a novel approach to using a family of layered double hydroxides (LDHs) as efficient De-NO_x photocatalysts, working under UV light [31] or even visible light [32,33]. LDHs adopt a brucite-like structure, whose general formula may be expressed as $[(M^{z+}_{1-x}M'^{y+}_{x}(OH)_2)]^{w+}(A^{n-})_{w/n}\cdot mH_2O]$, where *z* is typically 2 and *y* can be 3 or 4, A is an *n*-valent anionic moiety, either organic or inorganic [34]. Among the wide variety of research fields using LDHs, photo-induced applications have been highlighted in the recent years owing to the LDH's unique properties such as easy composition variation, synthesis simplicity, uniform distribution of metal cations in the layers and oxo-bridged linkages [35]. As a result, pollutant removal [36], photodetection [37], N_2 fixation [38], CO_2 photoreduction and water splitting [39] have been reported.

Nevertheless, due to their intrinsic hydrophilicity, bulk LDHs prepared using traditional methods undergo extensive layer stacking resulting in stone-like particle aggregates of low surface area and pore volume [40]. This gives rise to a loss of the essential sites for heterogeneous photocatalytic reactions. In order to tackle this issue, bulk preparation of LDHs with particles constituted by only one monolayer or a few layers – 2D-LDHs – can be performed by LDH delamination (Top-Down Method) or from direct synthesis with controlled nucleation (Down-Top Method) [41]. However, the most efficient reported methods at room temperature often require aggressive and hazardous solvents (e.g. formamide), are time consuming (e.g. pre-intercalation of a suitable

anion) and offer very low yields that prevent recovery of significant amount of LDH [41]. Therefore, it is desirable the preparation of 2D-LDHs with a satisfactory combination of mass production ability, high yield, high quality and low costs.

In order to produce large amounts of 2D-LDH samples in a much simpler way, O'Hare and co-workers devised a novel method, Aqueous Miscible Organic Solvent Treatment (AMOST) [42]. The so-formed LDH wet cake is water washed and then redispersed in an aqueous miscible organic solvent prior to the drying step, leading to so called AMO-LDHs that exhibit high dispersion and large pore volumes [40,43]. Thanks to its increased specific surface area, AMO-LDHs have been utilised as catalyst supports [44], catalyst precursors [45], flame retardant additives [46], for CO_2 capture [47] and for the thermochemical conversion of glucose to fructose [48]. However, the use of the pristine AMO product as a photocatalyst remains unexplored. Of importance, when compared to several methods reported to prepare 2D photocatalysts, AMOST procedure does not use toxic dispersants. As most of them usually contain nitrogen in their formula, the emission of NO_x gases during the photocatalysis occurs (the contrary to the desired De-NO_x process).

In this work, for the first time, we have successfully implemented the AMOST prepared 2D-LDH for its use as photocatalysts. Herein, we have studied the use of Ni_xTi-AMO-LDHs as a photocatalyst for air purification, focusing the study on the removal of NO_x gases from air. We have prepared both conventional Ni(II)/Ti(IV)-LDHs and Ni(II)/Ti(IV)-AMO-LDHs containing CO_3^{2-} as the interlayer anion (**Scheme S1**). There are relatively few reports of convenient and scalable methods to synthesise pure Ni_xTi LDH nanosheets (**Table S1**). The physicochemical properties and the photocatalytic performance of the synthesised Ni_xTi LDHs were

characterised and discussed based on parameters influencing the AMOST (i.e. metal ratio, redispersion time and temperature). We found the AMOST process increased the LDH nanosheets dispersion and the specific surface area up an unprecedented value of 492 $m^2\ g^{-1}$ (**Table S1**). Of importance, the 2D character of samples helps to mitigate the electron/hole recombination favouring the production of radical species.

3.4.2. Materials and methods

3.4.2.1 Chemicals

$Ni(NO_3)_2{\cdot}6H_2O$, titanium isopropoxide (named as TiO^iPr_4), Na_2CO_3, NaOH, HCl, Ethanol (EtOH) and 5,5-dimethyl-l-pyrroline-N-oxide (DMPO) were purchased from Sigma Aldrich. Methanol was purchased from PanReac AppliChem.

3.4.2.2 Photocatalysts preparation

3.4.2.2.1. Synthesis of conventional Ni_xTi-LDHs (x = 2, 3).

An adapted method was followed to synthesise conventional Ni_xTi-LDHs (i.e. water-treated LDHs, named as LDH-W) using the coprecipitation method [42]. 25 mmol of TiO^iPr_4 were slowly added dropwise into a 3-neck round-bottom flask containing 100 mmol of concentrated HCl under N_2 atmosphere. The yellowish solution thus obtained was added into a 75 mmol of $Ni(NO_3)_2$ aqueous solution to get a metal source with Ni:Ti = 3:1. Next, the metal source was dropped into a Na_2CO_3 aqueous solution (25 mmol) while stirring for 1 hour. During the reaction, a pH = 10 value was accurately maintained by using NaOH 4M

added from an auto-titrator (Syrris, Atlas Syringe Pump). Subsequently, the mixture was stirred at room temperature for 16 h, filtered and washed with deionised water until pH = 7. Finally, the Ni_3Ti-W sample was obtained after drying the product at 30 °C in a vacuum oven overnight (**Scheme S1**). Around 8 g of green solid sample, Ni_3Ti-LDH-W, was obtained (yield ~ 68%). A similar procedure was carried out to produce Ni_2Ti-W by using HCl (133.32 mmol), TiO^iPr_4 (33.33 mmol), $Ni(NO_3)_2$ (66.66 mmol) and Na_2CO_3 (33.33 mmol).

3.4.2.2.2. Synthesis of Ni_xTi-AMO-LDHs (x = 2, 3).

For the AMO-LDH samples, the synthesis protocol is modified after the aging stage. Following a modified published procedure [43], the collected LDH product is washed with demineralised water and subsequently with 500 mL of ethanol (**Scheme S1**). The obtained wet solid was dispersed in ethanol (300 mL) and stirred at room temperature for 4 h. Finally, the LDH was filtered, washed with 200 mL of ethanol and dried in a vacuum oven at 30 °C overnight. These AMO-LDH samples were labelled as Ni_3Ti-E4 (Ni:Ti = 3:1) and Ni_2Ti-E4 (Ni:Ti = 2:1), where E refers to the solvent (ethanol) and 4 refers to the redispersion time (4 h).

3.4.2.2.3. Variation the AMOST parameters

The redispersion time effect was studied over the samples with Ni:Ti = 3:1. Four additional AMO-LDH samples were synthesised for which the following redispersion times in ethanol were applied: 2, 6, 24 and 48 h. The samples were labelled as Ni_3Ti-E2, Ni_3Ti-E6, Ni_3Ti-E24 and Ni_3Ti-E48, respectively. Moreover, the temperature during the redispersion step was

studied using the sample Ni_3Ti-E6 at 0 °C (Ni_3Ti-E6-0) or 50 °C (Ni_3Ti-E6-50).

3.4.2.3. Characterization of the photocatalysts

The obtained samples were characterized using the following techniques: X-ray diffraction (XRD), X-ray photoelectron spectra (XPS), Infrared (FT-IR) and UV-Vis spectroscopy; Nitrogen adsorption–desorption isotherms; Transmission electron microscopy (TEM); ICP mass spectrometry, Thermogravimetric analysis coupled with mass spectrometry (TGA-MS); Time-Resolved Photoluminescence (TRPL); Electron paramagnetic resonance (EPR).

A detailed information is provided in "**Electronic Supplementary Information**" (**SI**).

3.3.2.4. Photocatalytic activity evaluation

The ISO 22197-1 method (utilised to characterise the air purification measurement) was applied to perform the NO gas abatement photocatalytic tests. The capability of the photocatalysts to induce NO photo-oxidation was assessed in a laminar flow reactor containing a 50x50 mm quartz sample holder with 300 mg of powdered sample. The reactor was placed inside a light sealed irradiation box (Solarbox 3000e RH with Xe lamp and controlled irradiance). Samples were irradiated during the tests with artificial sunlight (irradiances of 25 and 580 W m^{-2} for UV and visible light, respectively). For each test, a flow consisted of zero air and NO (NO concentration = 500 ppb; flow rate gas = 0.37 L min^{-1}) was continuously sent to the photoreactor. The relative humidity was set to 50 ± 5% by passing the air flow through a gas-washing bottle filled with

demineralised water. A chemiluminescence analyser (Environment AC32M) measured the concentration of NO, NO_x and NO_2 gases from the reactor. Before the irradiation period, adsorption−desorption equilibrium among photocatalysts was achieved upon passing the air/NO flow in the dark for 10 minutes. A photocatalytic test blank (without sample) was carried to discard NO photolysis. Tests were repeated three times and the average concentration values were calculated. The obtained standard deviations were ± 0.3 ppb for NO concentration and ± 1.0 ppb for NO_2 and NO_x concentrations. The photocatalytic performance of the samples was studied regarding the NO, NO_x and S indexes (**SI**).

3.4.3. Results and discussion

3.4.3.1. Composition and structure

Fig. 1A and **Fig. S1** show the X-ray diffraction (XRD) patterns for the synthesised Ni_xTi-CO_3 LDH samples. The XRD data exhibit the characteristic Bragg diffraction from an LDH with *R*3*m* rhombohedral symmetry (JCPDS 15-0087). Specifically, the Bragg reflections at 2θ ~ 11° and 23° correspond to the (*003*) and (*006*) basal planes respectively, while the rest of the Bragg peaks belongs to (*012*), (*015*), (*018*), (*110*) and (*113*) planes [49]. The basal spacing d_{003} was calculated to be 7.9 Å for the Ni_xTi-W samples (**Table 1**), very similar to those reported for Ni_xTi LDHs [50,51]. This value is consistent with the presence of CO_3^{2-} as interlayer anion.

The Bragg reflections are almost unaltered after the AMOST (Ni_xTi-E samples, **Fig. 1A**), indicating that the LDH structure is preserved [52]. Based on previous reports, the AMO solvents (i.e. ethanol) may partially enter the interlayer galleries, replacing the co-intercalated water molecules and reducing the hydrogen bonding between layers [52]. Thus,

the degree of LDH layer delamination slightly increases and the layer stacking is decreased, leading to the broadness and decrease of peak intensity of the basal XRD reflections [42,53], **Fig. 1A**. As a consequence, the interlayer distance (d_{003}) of Ni_xTi AMO-LDHs increased up to ~ 8 Å (**Table 1**), this value being higher in Ni_3Ti-E4 than in Ni_2Ti-E4.

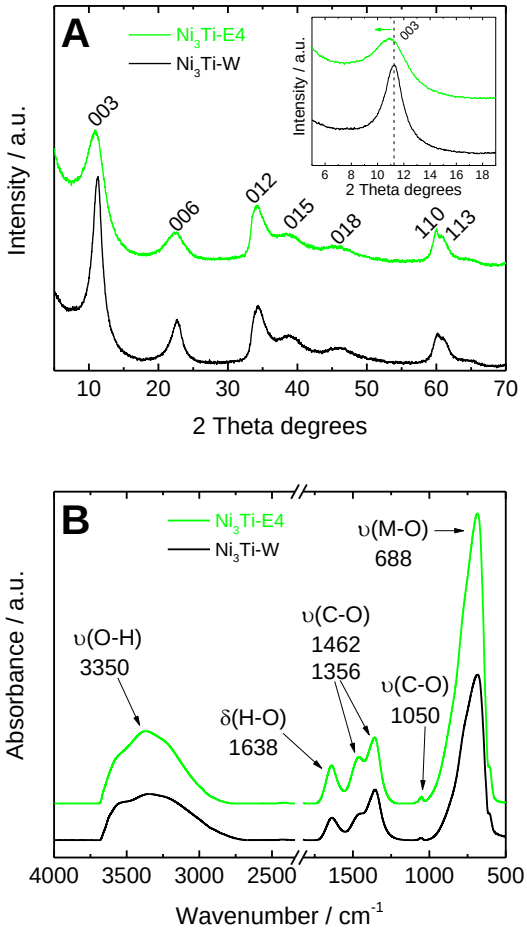

Fig. 1. (A) XRD patterns and (B) ATR spectra for Ni_3Ti samples.

Table 1. Lattice parameters and basal spacing for the synthesised Ni_xTi LDH samples.

Sample	d_{003} (Å)	Lattice parameters (Å)		Crystal domain size (Å)	
		a	*c*	*c*-axis	*ab* plane
Ni_2Ti-W	7.89	3.07	23.67	43.6	123.5
Ni_2Ti-E4	8.01	3.08	24.02	35.2	119.7
Ni_3Ti-W	7.86	3.07	23.58	47.3	117.7
Ni_3Ti-E2	7.87	3.07	23.61	32.4	127.5
Ni_3Ti-E4	8.10	3.08	24.30	30.4	108.2
Ni_3Ti-E6	8.09	3.08	24.28	28.6	108.3
Ni_3Ti-E6-0	8.09	3.08	24.28	27.4	100.7
Ni_3Ti-E6-50	8.09	3.08	24.28	27.7	100.7
Ni_3Ti-E24	8.02	3.08	24.06	31.8	121.0
Ni_3Ti-E48	8.08	3.08	24.23	31.2	104.1

The effects of redispersion time during AMOST was studied for the Ni_3Ti-LDH samples. Samples were obtained after 2, 4, 6, 24 and 48 h of redispersion in ethanol (**Fig. S1B**). The Ni_3Ti-E6 sample exhibits the lowest intensity and broadest (*00l*) Bragg reflections, indicating the lowest extent of layer stacking. For redispersion times in excess of 2 h the interlayer spacing increases to a similar value ca. 8.09 Å, suggesting the incorporation of ethanol molecules into the LDH gallery. Redispersion temperature did not seem to be a crucial factor to boost the degree of platelet delamination (**Fig S1C**).

The calculated crystal domain size, using the FWHM of the *003* Bragg reflection from the Ni_xTi AMO-LDHs (**Table 1**), showed a significant diminution of the domain length from 47.3 to 28.6 Å with increasing dispersion time from 0 to 6 h in ethanol, indicating a less layer stacking degree of the sheets. In this regard, the least crystal domain size is reached in the Ni_3Ti-E6 sample. Conversely, the crystal domain size along

in the ab plane remained nearly constant for all the samples. When the redispersion time was longer than 6 h, the d_{003} parameter remained almost unaltered, which would suggest that the optimal dispersion time in the AMOST was 6 h.

ATR spectra show the characteristic bands for LDH materials (**Fig. 1B**) [54]. Specifically, a broad band at ca. 3350 cm^{-1} is ascribed to the stretching mode of hydrogen-bonded OH arising from hydroxyl groups in the layer and the water molecules in the interlayer spacing. The bending mode of the interlayer water molecules is seen at 1638 cm^{-1}, **Fig. 1B**. The vibration mode ν_3 of the interlayer carbonate anions appears split into two bands at 1462 and 1356 cm^{-1}. Indeed, this interlayer restricted symmetry makes the ν_1 carbonate mode to show a band at 1050 cm^{-1}. The spectra were similar for all the samples. Additionally, for samples on which water molecules are almost completely replaced by ethanol molecules (Ni_2Ti-E4 and Ni_3Ti-E6 samples, **Table 2**), new low intensity bands appeared at 2974 and 1093 cm^{-1} and the band at 1050 cm^{-1} noticeably increased, **Fig. S2**. In order to reveal the origin of these bands and discard possible impurity phases, the ATR spectra of other related compounds TiO_2, $Ni(OH)_2$ (most common impurities) and ethanol were recorded (**Fig. S3**). The comparison of the spectra indicates that these new bands should correspond to the presence of ethanol molecules adsorbed/incorporated in AMO-LDH. Slight shifts in the wavenumber of these bands might be a consequence of the different vibration behaviour between free ethanol and that incorporated into the AMO-LDH galleries.

Table 2. Chemical properties for the synthesised Ni_xTi LDH samples: metal content and ratio; formula and band gap energy value.

Sample	% Atomic		Atomic ratio	Formula	Band gap (eV)
	Ni	Ti	Ni/Ti		
Ni_2Ti-W	0.55	0.23	2.37	$[Ni_{0.71}Ti_{0.3}\ (OH)_2](CO_3)_{0.3} \cdot 0.91\ H_2O$	2.56
Ni_2Ti-E4	0.55	0.22	2.47	$[Ni_{0.71}Ti_{0.29}\ (OH)_2](CO_3)_{0.29} \cdot 0.09\ H_2O \cdot$ 0.37 EtOH	2.94
Ni_3Ti-W	0.65	0.21	3.14	$[Ni_{0.77}Ti_{0.23}\ (OH)_2](CO_3)_{0.23} \cdot 0.92\ H_2O$	2.54
Ni_3Ti-E2	0.65	0.21	3.04	$[Ni_{0.75}Ti_{0.25}\ (OH)_2](CO_3)_{0.25} \cdot 0.19\ H_2O \cdot$ 0.27 EtOH	2.96
Ni_3Ti-E4	0.63	0.21	2.96	$[Ni_{0.75}Ti_{0.25}\ (OH)_2](CO_3)_{0.25} \cdot 0.17\ H_2O \cdot$ 0.31 EtOH	2.91
Ni_3Ti-E6	0.60	0.18	3.26	$[Ni_{0.77}Ti_{0.23}\ (OH)_2](CO_3)_{0.23} \cdot 0.01\ H_2O \cdot$ 0.38 EtOH	2.94
Ni_3Ti-E6-0	0.61	0.18	3.31	$[Ni_{0.78}Ti_{0.23}\ (OH)_2](CO_3)_{0.23} \cdot 0.04\ H_2O \cdot$ 0.40 EtOH	2.96
Ni_3Ti-E6-50	0.60	0.18	3.30	$[Ni_{0.77}Ti_{0.23}\ (OH)_2](CO_3)_{0.23} \cdot 0.04\ H_2O \cdot$ 0.39 EtOH	2.96
Ni_3Ti-E24	0.57	0.18	3.18	$[Ni_{0.76}Ti_{0.24}\ (OH)_2](CO_3)_{0.24} \cdot 0.08\ H_2O \cdot$ 0.35 EtOH	2.92
Ni_3Ti-E48	0.65	0.21	3.14	$[Ni_{0.76}Ti_{0.24}\ (OH)_2](CO_3)_{0.24} \cdot 0.14\ H_2O \cdot$ 0.23 EtOH	2.88

X-ray photoelectron spectroscopy (XPS) was used to analyse the Ni_xTi-LDH surface in order to probe the oxidation states of Ti and Ni. C 1s signal at 284.8 eV, was used as internal charge shift correction. No significant differences between samples were found in their XPS spectra. As way of example, the X-ray photoemissions of Ni_3Ti-W are shown in **Fig. S2**. The Ni $2p_{3/2}$ signal at 855.6 eV corresponds to Ni^{2+} hydroxide (**Fig. S4A**). **Fig. S4B** shows the high resolution Ti 2p region. The Ti $2p_{3/2}$ signal has been deconvoluted in two resonances set at 459.2 and 457.7 eV, and the corresponding to Ti $2p_{1/2}$ at 464.7 eV and 463 eV respectively, which have been proposed to correspond to the contributions from Ti^{4+} ions in tetrahedral and octahedral coordination, respectively [55]. This is indicative that at the surface, some Ti^{4+} ions may have migrated out of the

LDH layer network, possibly due to the high electrical charge of Ti^{4+}. No evidence for any Ti^{3+} species was found in the samples, although these have been reported in Ni_xTi-LDHs synthesised by other methods [56]. The C 1s XPS region shows contributions corresponding to the adventitious hydrocarbon, –CO, and –COO– groups at 284.8, 286 and 288.6 eV respectively (**Fig. S4C**). Finally, the O1s peak has been deconvoluted in three peaks at 529.5, 531.1 and 532.5 eV, which have been assigned to lattice oxygen in metal oxides (M-O-M), hydroxyl groups (M-O-H) and adsorbed water (H-O-H), respectively (**Fig. S2D**) [57].

All samples showed similar TGA profiles, characteristic of LDHs [50]. The derivative of the TGA curves are depicted in order to investigate the mass losses in more details (**Fig. S5**). Ni_3Ti-W exhibits two mass loss events at 107 and 285 °C (P1 and P2 peaks, respectively). The first one is ascribed to the removal of adsorbed and interlayer water, while the second one is due to both carbonate decomposition and dehydroxylation of LDH [58]. For Ni_2Ti-W, both mass losses appeared shifted to lower temperature than the Ni_3Ti-W sample (**Fig. S5B**), which could be a consequence of some structural disorder in the LDH network due to its higher Ti^{4+} cations content. When the AMOST was applied (Ni_xTi-E samples), the P1 event occurred at a lower temperature suggesting the presence of both ethanol and water molecules. Moreover, the temperature onset of the P1 event shifted depending on the AMOST redispersion time (**Fig S5D**), appearing at the lowest temperatures for the Ni_3Ti-E4 and Ni_3Ti-E6 samples. Beyond 6 h of redispersion time in the AMOST, the P1 event shifted to higher temperature, indicating that the optimal ethanol substitution was achieved at 6 h. The lower desorption temperatures at the P1 event are indicative of weaker interactions between sorbates and metal hydroxide layers, and the higher dispersion

of the platelets. Similarly, the P2 event also underwent similar behaviour in the AMO samples.

LDH composition was calculated by using the data from TGA and ICP-MS techniques (in all cases carbonate anions were assumed to balance the layer positive charge, **Table 2**). Good agreement was found between the experimental values and the theoretical metal ratios in the initial solution. TGA-MS studies corroborates that water molecules in LDH structure are partially replaced by ethanol when the AMOST was performed (**Fig. S6**). Water signal (m/z =18) decreased (**Fig S6A**) and the ethanol signal appeared in Ni_3Ti-E samples (**Fig S6B**). The P1 events from the derivative curves of the samples were deconvoluted to calculate the amounts water and ethanol (**Fig S6C, D**) present. The estimated quantities of ethanol in the samples (**Table 2**) correlated well with the interlayer stacking and crystal domain size inferred from the XRD data. Thus, those samples with a higher ethanol content (Ni_3Ti-E6 samples) exhibit the highest interlayer distance (d_{003}) and, because of the delamination effect, lower crystal domain size.

3.4.3.2. Morphology and textural properties of photocatalysts

Different morphologies were found for the Ni_3Ti-W and Ni_3Ti-E samples (**Figs. 2** and **S7**). Ni_3Ti-W sample (**Fig. 2A**, **S7A** and **S8A**) consisted of irregular particles with severe aggregation produced by the strong interactions between the metal hydroxide layers, interlayer anions and water molecules. In contrast, flower-type particles constituted by corrugated nanosheets were observed after the AMOST (**Fig. S7B**, **C**, **D**, **E** and **F**).

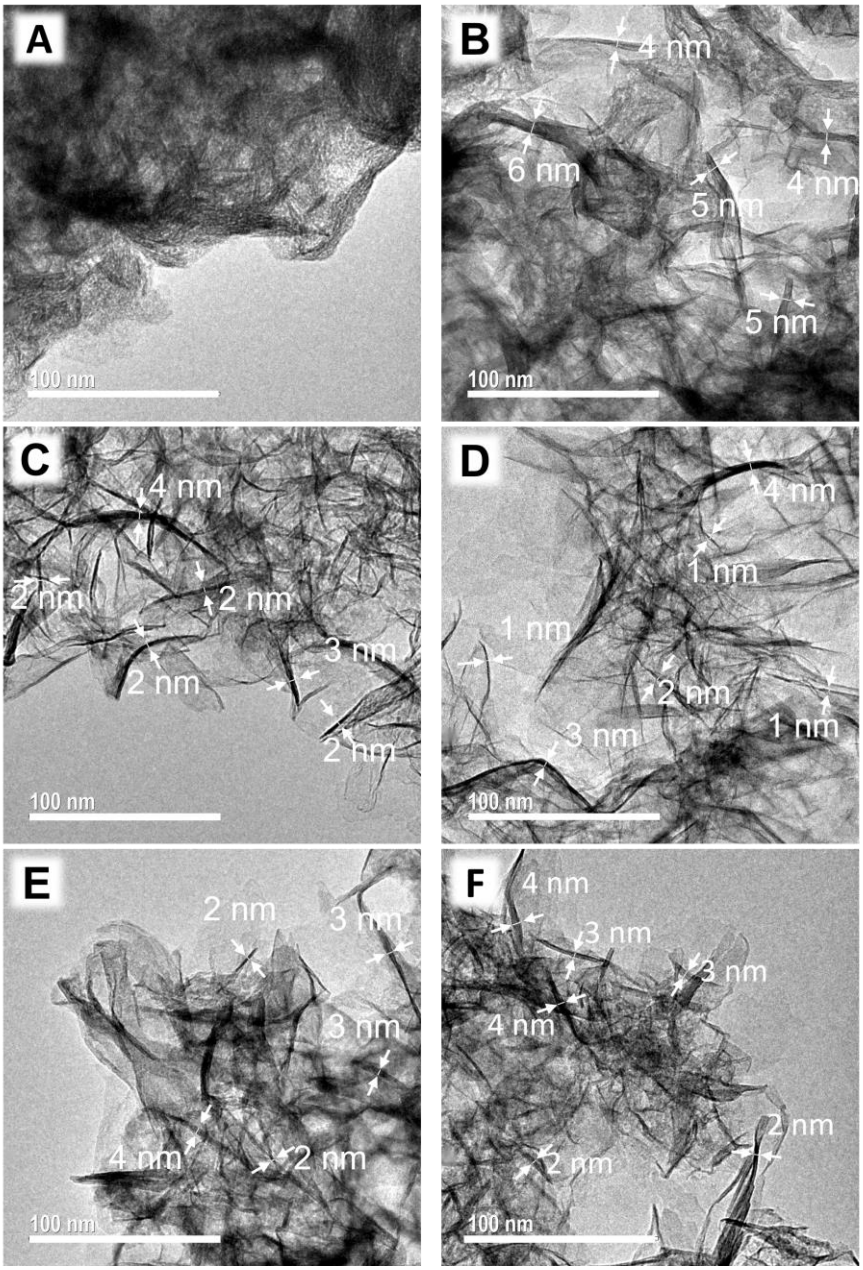

Fig. 2. TEM images of: (A) Ni_3Ti-W; Ni_3Ti with different redispersion times in the AMOST: (B) 2 h, (C) 4 h, (D) 6 h, (E) 24 h, (F) 48 h.

The highest dispersion of nanosheets is observed for treatment times longer than 2 h. For the Ni_3Ti-E samples optimal delamination was observed at 6 h. Thus, the observed thickness of nanosheets decreased from 4 – 5 nm of sample Ni_3Ti-E2 to 1 – 3 nm of sample Ni_3Ti-E6. The morphology transformation is attributed to the AMOST effect, specifically the ethanol displacing bound water from the LDH surface and reducing the propensity of hydrogen bonding. Some insertion of ethanol molecules into the LDH interlayer spacing also takes place [40], the net effect being a boost of the metal hydroxide layers exfoliation. Similar observations were found with Ni_2Ti-E samples (**Fig. S8**). The temperature on the redispersion step made no appreciable differences to the sample dispersion Ni_3Ti-E6 (**Fig. S9**).

In order to learn more about the pore structure and surface areas of the samples, they were investigated by N_2 adsorption-desorption measurements (**Fig. 3**, **S10**, **S11** and **S12**). According to IUPAC classification, the isotherm shape of Ni_3Ti-W and Ni_2Ti-W samples were characteristic of a type II isotherm with a H2-type hysteresis, which indicates the presence of narrow-neck porosity with wide bodies. These pore types should be a consequence of the huge interparticle aggregation, as observed by TEM. This microstructure was altered in the AMO samples. Now, a IV type isotherm with a H3 hysteresis loop is observed for all of them (**Figs. 3B**, **S10** and **S11B**), this is in agreement with those reported for other AMO-LDHs [43]. This pore structure is associated to slit-shaped pores arising from the sheet-like morphology as observed in TEM images.

The redispersion time effect had a clear influence in the specific surface area and pore volumes. The corresponding values measured for Ni_3Ti-E2, Ni_3Ti-E4, Ni_3Ti-E6, Ni_3Ti-E24 and Ni_3Ti-E48 samples are shown in **Fig. 3C**. The maximum values are reached after ethanol dispersion for 6 h

(492 m^2 g^{-1} and 1.37 cm^3 g^{-1}, respectively). This is consistent with the TEM observations that showed a higher amount of thin nanosheets in Ni_3Ti-E6 sample. The Ni:Ti ratio seemed to affect the AMOST effectiveness (**Table S2**), ethanol was less effective at dispersing Ni_2Ti platelets compared to Ni_3Ti platelets, the N_2 BET surface area increased by 0.25 and 3 times for Ni_2Ti-E4 and Ni_3Ti-E4, respectively. It is thought the greater layer charge density has made it more difficult for the ethanol to delaminate the platelets as confirmed by the XRD data. Ni_3Ti-E6 showed the highest surface area and pore volume demonstrating that room temperature is the optimum choice to obtain the highest degree of delamination (**Table S2**).

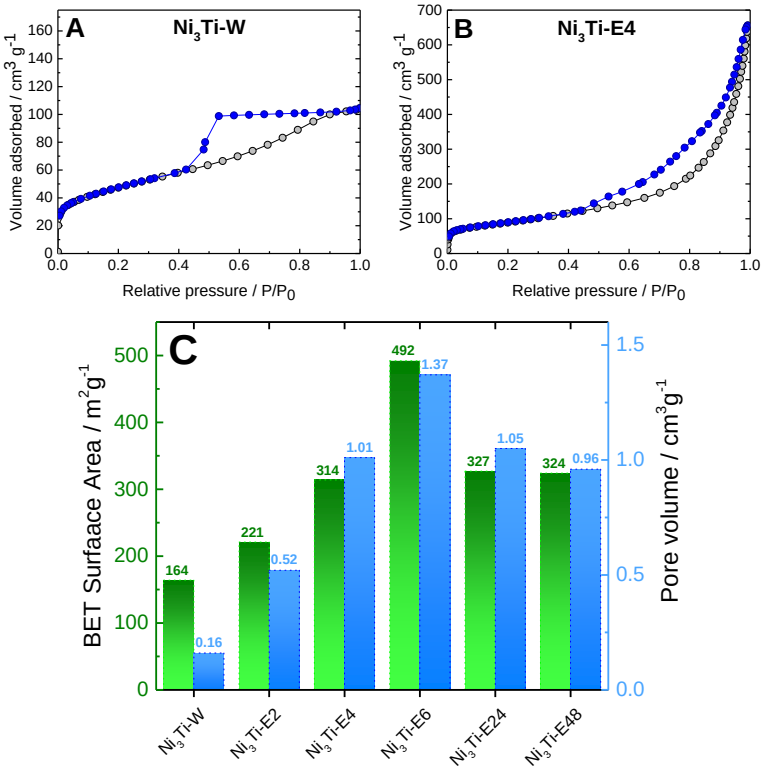

Fig. 3. (A, B) N_2 adsorption-desorption isotherms of Ni_3Ti samples. (C) BET surface area and pore volume for Ni_3Ti with different redispersion times in the AMOST.

By analysing the pore size distribution for different redispersion times, it was found that the specific surface area boost came from the increase of the mesoporous and macroporous pore regime (**Fig. S13**). Specifically, pores in the region 6 – 13 nm and 20 – 40 nm were generated for all Ni_3Ti-E samples, except for Ni_3Ti-E2, suggesting that the delamination, by the AMOST process, has not totally been completed for this sample. The Ni_3Ti-E6 porosity increased in the 4 – 5 nm pore size region. Because its higher degree of delamination, the significance of this small pore diameter could be associated to occurrence of a high number of slit-shaped pores between the exfoliated nanosheets. In fact, both the porosity in the 4 – 13 nm range and the pore volume increased with the specific surface area (**Fig. S13A**).

3.4.3.3. Optical properties

The diffuse reflectance UV–Vis absorption spectra of Ni_3Ti-W and Ni_3Ti-E4 samples are plotted in **Fig. 4A**. Two clear absorbances were observed: bands between 200 and ~ 400 nm were ascribed to the ligand-to-metal charge transfer for Ti^{4+} in an octahedral environment, while the broad band in the region of 600-800 nm can be assigned to *d-d* transitions for the Ni^{2+} located in the layers [59]. This absorbance in the visible spectrum region gives rise to a characteristic green colour observed for the Ni_xTi LDH-W samples (**Fig S14**). Remarkably, the sample absorbance in this region was decreased when the AMOST was performed, probably caused by the enhanced LDH particle dispersion (**Figs. S15A**, **B**). Band gap values were calculated by plotting the transformed Kubelka-Munk function versus the photon energy (**Figs. 4B** and **S15C**, **D**). The Ni_3Ti-W sample showed an estimated band gap of around 2.5 eV (**Table 2**), a similar value to that reported for previously reported NiTi-LDHs [56,59].

This value increased to ~ 0.4 eV for all the Ni_xTi AMO-LDH samples. Analogous results were observed for the Ni_3Ti samples following different redispersion times (**Fig. S15C**). After the redispersion process the Ni_3Ti-LDH nanosheets are typically only a few layers thick. Similar to that observed for 2D layered semiconductors, the electronic band structure changes with the number of layers; band gap increasing with decreasing thickness because of confinement effects [60].

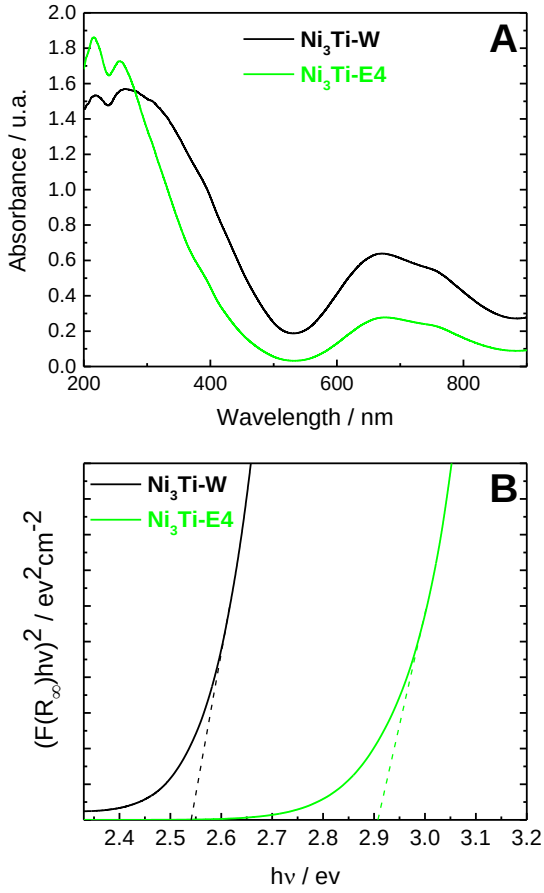

Fig. 4. (A) UV–Vis absorption spectra and (B) Kubelka-Munk transformed function plots for Ni_3Ti-W and Ni_3Ti-E4 samples.

3.4.3.4. De-NO_x performance assessment

The synthesised compounds along with the benchmark TiO_2 P25, used as standard for comparison purposes, were subjected to photocatalytic tests to evaluate their activity for the NO gas removal. **Figure 5A** shows the NO_x gases concentration values recorded for the Ni_3Ti-E4 photocatalyst in a typical De-NO_x test. During the first 10 minutes, under dark conditions, the simulated polluted atmosphere is flowed through the photoreactor and the concentration of the gases remains constant. Upon light irradiation the NO gas concentration rapidly drops due to the onset of photocatalytic processes. On the surface of the sample, reactive oxygen species (ROS) are produced and these are responsible of the photochemical oxidation of the NO [8,61,62], which may be briefly summarised as follows: $NO \rightarrow NO_2^- \rightarrow NO_2 \rightarrow NO_3^-$. This process is fully selective when all nitrogen gases are removed as nitrite and/or nitrate species. After 60 minutes of light irradiation, the lamp is turned off and the photocatalytic process stops. After 10 minutes the gas concentration recovers the original values. The De-NO and De-NO_x performances for the Ni_3Ti-W and Ni_3Ti-AMO-LDH samples with different ethanol redispersion times is depicted in **Figs. 5B**, **C**. We observed that the photocatalytic performance is closely related with the specific surface areas of the samples. Ni_3Ti-W showed the lowest conversion figures (De-NO_x activity $\sim$ 18%), much lower than the AMO samples (De-NO_x activity > 50%). AMOST promotes delamination, increase in specific surface area, leading to an increase in exposure of the reactant gases to the photocatalytic centres on the LDH surface. The Ni:Ti ratio does not seem to be an important factor in determining photocatalytic activity, Ni_2Ti-E4 and Ni_3Ti-E4 both with surface areas $\sim$ 312 $m^2\ g^{-1}$ exhibit similar De-NO

activity (**Fig. S16A**). Ni_3Ti-E6 samples, having the highest surface area, exhibited outstanding De-NO conversion of about 63%, and superior to that observed for the TiO_2 P25 (57%) reference sample (**Figs. 5B** and **S16B**).

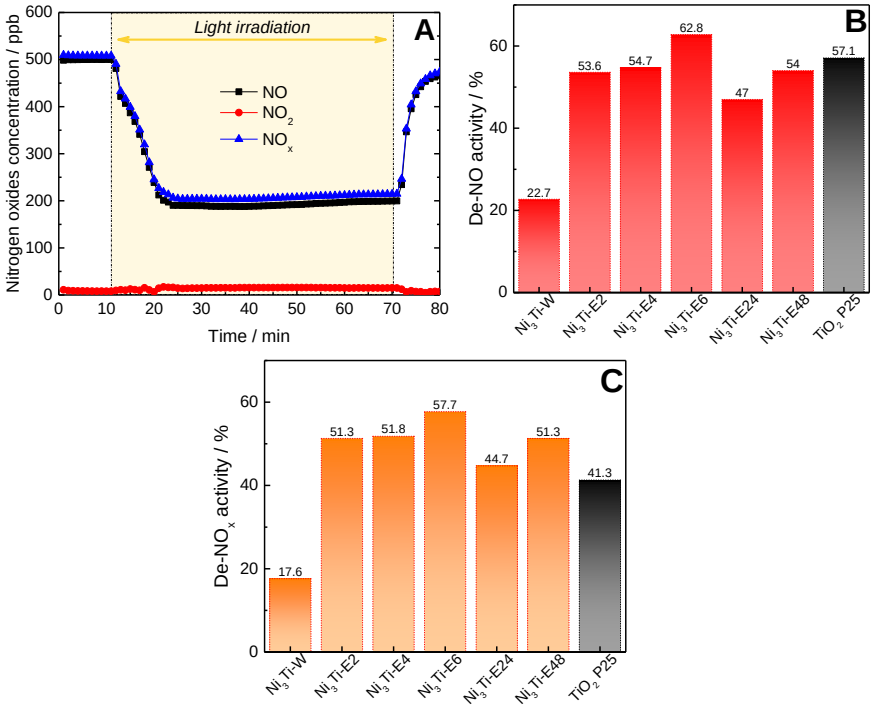

Fig. 5. (A) Nitrogen oxides concentration profile obtained during the photocatalytic NO removal test on Ni_3Ti-E4 sample; (B) calculated De-NO and (C) De-NOx indexes for Ni_3Ti with different redispersion times in the AMOST and TiO_2 P25.

More interestingly, the Ni_xTi-AMO-LDH samples stand out in their ability not to emit NO_2 gas, an intermediate appearing in the sequential photochemical oxidation of NO. This is a key factor for successfully applying these materials within an urban environment because NO_2 is much more hazardous [63]. In order to assess this, the estimated selectivity (*S*) index is shown in **Fig. S17**. Most Ni_xTi-AMO-LDHs showed *S*

values of ~ 94%, higher than LDH-W (~ 80%) and TiO_2 P25 (72%). This result would be related with an enhanced adsorption ability towards NO_2 for the Ni_xTi-AMO-LDHs due to their larger specific surface areas. In this regard, the NO_2 adsorption tests in darkness (**Fig. S18**) showed that, from an inlet value of 150 ppb of NO_2, a significant amount (~ 47%) is removed over 1 hour by Ni_3Ti-E6. Conversely, lower amounts of NO_2 gas are adsorbed by Ni_3Ti-W and TiO_2 P25 (20 and 3%, respectively). This could be due to a superior ability for Ni_xTi-AMO-LDHs to adsorb NO_2 on the surface and then facilitate complete photocatalytic oxidation. In this sense, it has been previously reported that mesoporous networks lead to easy accessibility of active reactive sites to the reactant molecules [64], acting as a sink on which the nitrogen oxide gases molecules are trapped [65]. Therefore, the higher mesopore volume of Ni_3Ti-E6, compared to Ni_3Ti-W, could serve to restrain the NO_2 molecules.

As a consequence, complete removal of NO_x performed by each photocatalyst (De-NO_x activity, **Fig 5C**) is related with its selectivity towards the Photocatalytic Oxidation (PCO) process. Thus, Ni_3Ti-E6 samples exhibit De-NO_x values around 57%, 29% higher than the one shown using TiO_2 P25, being comparable or even superior to those previously reported LDH De-NO_x photocatalysts (42%, NiMgAl-LDH; [66] 50%, ZnAl-LDH [31]; 50%, ZnAlCr-LDH [32]; 59%, ZnAlFe-LDH [33]. Moreover, the reusability of the Ni_3Ti-E6 and TiO_2 P25 photocatalysts was evaluated (**Fig. S19**). After six runs (6 hours of light irradiation), the De-NO_x activity of Ni_3Ti-E6 photocatalyst remained almost constant, producing outstanding De-NO_x performance (~ 58%). Because its high surface area (492 $m^2\,g^{-1}$), there are clearly a vast number of available active sites on photocatalyst´s surface to confront the oxidation of a huge amount of NO_x molecules. Thus, after each run, there are still enough

active sites that remain unreacted to keep the De-NO_x performance constant. Therefore, the characteristic nitrate passivation of the surface is delayed, whose later appearance should be easily removed by using a simple water washing procedure [31–33]. However, the photocatalytic activity of TiO_2 P25 was significantly reduced (~ 44%). Remarkably, the NO_2 emission was around 8 times lower for the AMO photocatalyst than for the TiO_2 P25 (**Fig. S19 C**, **D**). In summary, the NO removal efficiency and Selectivity values found for AMO photocatalysts are in line with those recently reported for advanced De-NO_x photocatalysts, **Table S3**.

3.4.3.5. Photocatalytic mechanism assessment

Several experiments were performed to get an insight into the photocatalytic mechanism expected for the Ni_xTi AMO-LDHs. Picosecond time-resolved photoluminescence decays (TRPL) were measured for Ni_3Ti-W and Ni_3Ti-E photocatalysts. **Fig. 6A** displays the time profiles at 470 nm with the best bi-exponential fits for both photocatalysts. For the samples studied, the deactivation kinetics for the excited state develop within the same time range with time constant of 6.4 and 284 ns for Ni_3TiW, 6.5 and 260 ns for Ni_3Ti-E2, and 5.13 and 562 ns for Ni_3Ti-E6 photocatalysts. The recombination kinetics of the electrons in the Ni_3Ti-E6 samples was slightly slower, which might enhance the photocatalytic activity of this compound. In parallel, EPR measurements were used to probe the reactive species involved in the photochemical process. For methanolic DMPO solutions, under light irradiation, the characteristic sextet of peaks for the trapped $\cdot O_2^-$ radical is observed for the three samples, **Fig. 6B**. The intensity of the signal increases in the order Ni_3Ti-E6 > Ni_3Ti-E2 > Ni_3Ti-W, being higher with the delamination degree of the sample.

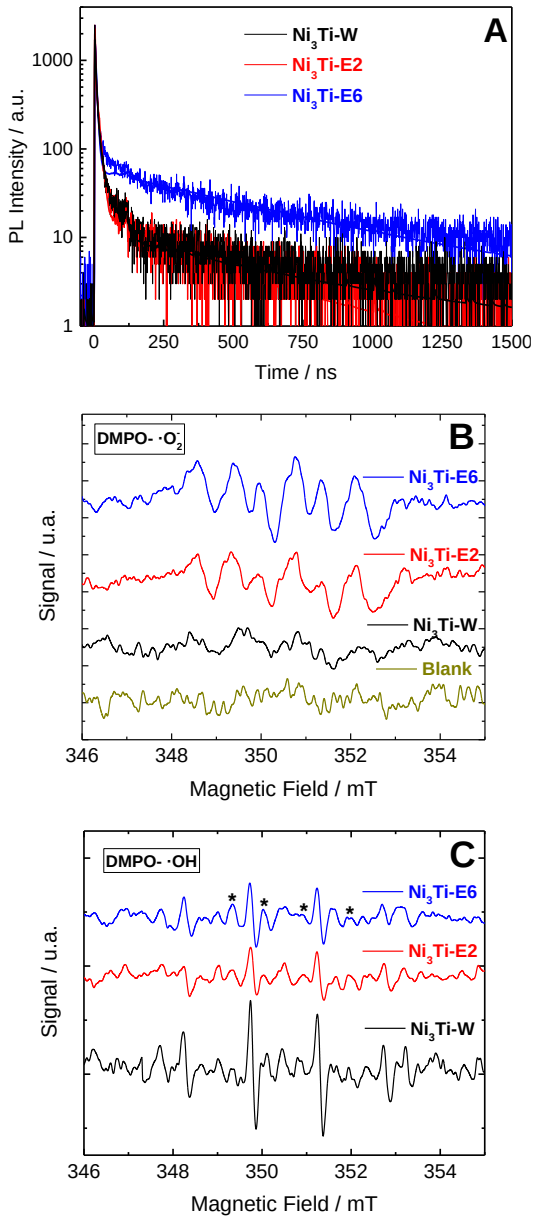

Fig. 6. (A) Time decay of the photoluminescence signals and (B, C) DMPO spin-trapping EPR spectra for the Ni_3Ti-W, Ni_3Ti-E2 and Ni_3Ti-E6 photocatalysts.

For aqueous solutions, the quartet of peaks DMPO-·OH adduct is clearly observed for the Ni_3Ti-W sample (**Fig. 6C**). However, the signal

obtained for the case Ni_xTi-E photocatalysts is more complex. Even though the mentioned quartet is shown, there are additional peaks (marked with asterisk) which precludes the existence of DMPO-·O_2^- adduct, which would be originated from the existence of ethanol molecules in the samples. The higher amount of superoxide detected for Ni_3Ti-E6 sample together with the slower recombination kinetics observed would be in agreement with a higher availability of electrons on the semiconductor surface. As previously reported, the 2D character of this photocatalyst facilitates the electron conduction through the surface lessening the e^-/h^+ recombination [38].

In situ DRIFTS measurements were carried out with the aim to monitor the photocatalytic removal of NO. Initially, the samples were subjected to pre-treatment and NO adsorption processes. The background spectrum was recorded before NO flow through the reaction chamber. **Fig. 7A** shows the spectra obtained under dark conditions for samples Ni_3Ti-W and Ni_3Ti-E6, once the background had been subtracted, after 10 minutes of NO flow. Signals corresponding to the appearance of NO_x species are observed. Clear differences between both samples were found. The IR spectra indicate that NO is easily adsorbed onto Ni_3Ti-E6 photocatalyst surface (1070 cm^{-1}, [66,67]), presumably due its very high specific surface area. As a result, NO^- and NO_2^- species (1107 cm^{-1} and 838-873 cm^{-1}, [67,68]) are produced by NO disproportionation in the presence of the hydroxyl LDH groups [69]; (Eqs. (1-3)), which ultimately are oxidised to nitrate (1527 – 1577 cm^{-1}, [70,71]) (Eq. (5)). In addition, in the presence of O_2, NO is partially oxidised to NO_2 which could converted into N_2O_4 (901 cm^{-1} [68]; Eq. (4)). This last identification emphasizes the ability of Ni_3Ti-E6 sample to adsorb most gases. These processes are

scarcely observed in Ni_3Ti-W because its low affinity for NO adsorption. These transformations can be summarised as follows:

$$2\ NO + OH^- \rightarrow HNO_2 + NO^- \quad (1)$$

$$NO + HNO_2 + OH^- \rightarrow NO^- + NO_2 + H_2O \quad (2)$$

$$NO^- + NO_2 \rightarrow NO_2^- + NO \quad (3)$$

$$2\ NO + O_2 \rightarrow 2\ NO_2 \rightarrow N_2O_4 \quad (4)$$

$$NO^- + 2\ NO_2 \rightarrow NO_3^- + 2\ NO \quad (5)$$

Afterwards, the samples were irradiated by light during 60 minutes, and the amount and typology of adsorbed species on surface change significantly. As light reaches the surface of the catalyst, the photoexcited e^- and h^+ (Eq. (6)) react with H_2O and O_2 to produce hydroxyl and superoxide radicals (Eqs. (7-8)), which promote the photochemical oxidation of NO. Thus, the spectra show now a larger number and more intense signals corresponding mainly to nitrite (843-882, 1138, 1294, 1353 and 1434 cm^{-1}, [67,68,71,72]) and nitrate species (924-1054 and 1527-1583 cm^{-1}, [66,67,70,71]), as the resulting products of the NO photo-oxidation (**Fig. 7B**) (Eqs. (10-14)). Consistent with its high De-NO_x photoactivity, the spectra of Ni_3Ti-E6 are differentiated by the highest intensity of these signals, the majority assigned to NO_3^-, the final product of the PCO process. Under light irradiation, the occurrence of NO_2 (1240 cm^{-1}, [67]) accounts from the oxidation of NO by superoxide radicals (Eq. (9)), which in turn dimerizes to N_2O_4 (1397 cm^{-1}, [69]). The identification of NO_2 and N_2O_4 on the surface is in agreement with the higher De-NO_x selectivity of this photocatalyst. Thus, the retention of these molecules on surface facilitates their oxidation, decreasing their emission to the atmosphere. Interestingly, the presence of NO^- bands

persisted under light irradiation, more clearly for the Ni_3Ti-E6 sample. This evidence suggested that, similarly to that observed in the reusability tests and after one hour of light irradiation, many unreacted active sites remained available on photocatalyst´s surface to react with gaseous molecules, playing the hydroxyl LDH groups a key role in anchoring NO molecules as NO^-, role emphasized by the large surface area exhibited by the Ni_3Ti-E6 sample.

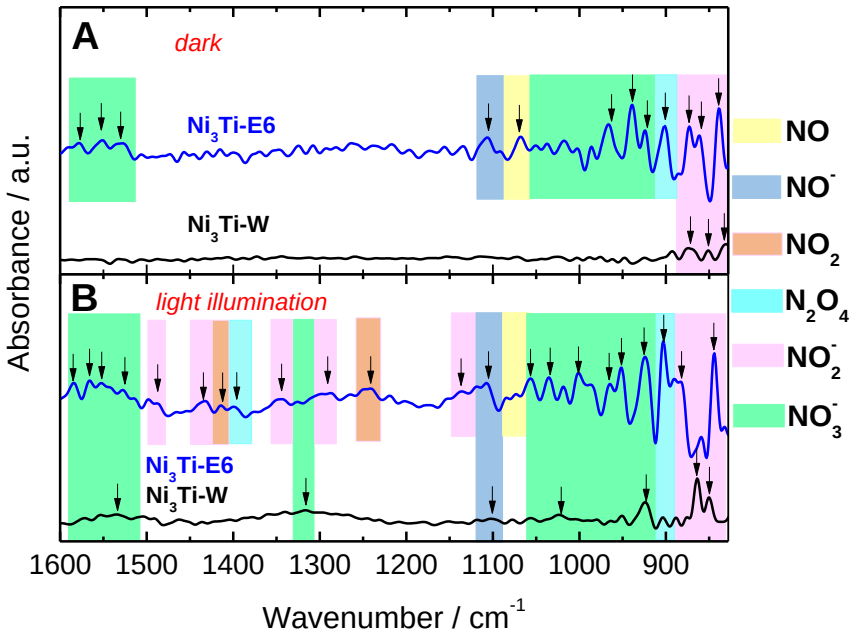

Fig. 7. In situ DRIFTS spectra obtained while NO and O_2 gases are flowing through the Ni_3Ti-W and Ni_3Ti-E6 samples in (A) dark conditions and (B) under light illumination.

Considering the above results, the primary NO oxidation reaction mechanism could be proposed as follows:

$$LDH + hv \rightarrow h^+ + e^- \qquad (6)$$

$$h^+ + H_2O \rightarrow H^+ + \cdot OH \quad (7)$$

$$e^- + O_2 \rightarrow \cdot O_2^- \quad (8)$$

$$2\ NO + \cdot O_2^- \rightarrow 2\ NO_2 + e^- \quad (9)$$

$$NO_2 + e^- \rightarrow NO_2^- \quad (10)$$

$$2\ NO + \cdot O_2^- + e^- \rightarrow 2\ NO_2^- \quad (11)$$

$$NO + \cdot OH \rightarrow HNO_2 \quad (12)$$

$$NO_2^- + 2\ \cdot OH \rightarrow NO_3^- + H_2O \quad (13)$$

$$2\ NO_2^- + \cdot O_2^- \rightarrow 2\ NO_3^- + e^- \quad (14)$$

The in situ DRIFTS spectra provides evidence for the higher efficiency of Ni_3Ti-E6 to promote the photochemical NO oxidation. The ability of Ni_3Ti-E6 to physi/chemisorb NO and NO_2 on the surface facilitates their oxidation to nitrites and nitrates, resulting a high De-NO_x selectivity.

3.4.4. Conclusions

A range of Ni_xTi-AMO-LDHs with different degrees of platelet dispersion were synthesised using the AMOST process. The redispersion time of the Ni_xTi LDHs in ethanol strongly influenced the surface area and pore volumes of the sample. Extensive nanosheets dispersions was observed after 6 h of ethanol dispersion leading to N_2 BET surface areas as high as 492 $m^2\ g^{-1}$.

Ni_xTi-AMO-LDHs were found to be effective photocatalysts, they exhibited much higher De-NO_x performance in comparison to the untreated LDH and the TiO_2 P25 benchmark producing a performance of ~58% under sunlight illumination (40 and 17% higher than conventional

LDH and TiO_2 P25 respectively). Most importantly, the Ni_xTi-AMO-LDHs photocatalysts exhibited stable photocatalytic activity after consecutives cycles, but they showed negligible emission of the toxic intermediate NO_2.

The key role of the specific surface area was revealed: i) the higher number of specific sites of the Ni_xTi-AMO-LDHs photocatalysts provided an enhancement for the adsorption capacity for NO and especially NO_2 and delayed the photocatalyst passivation; ii) the 2D character promotes a lessening of the charge carrier recombination and the increase in the radical species production. Both characteristics, with difference to TiO_2 P25, assist for the enhancement of the De-NO_x photocatalytic process. We conclude that AMO-LDHs provide a platform approach to developing new effective and robust candidates for the photocatalytic NO_x removal.

3.4.5. Acknowledgements

This work was partly financed by the Junta de Andalucía, Spain (PAI Groups FQM-214 and FQM-175) and Spanish Government (MAT2017-88284-P). Adrián Pastor is grateful for the support received by the Ministerio de Educación, Cultura y Deporte (FPU16/05041 contract) to research at Universidad de Córdoba (Spain). C.C. and J.-C. B. thanks SCG Chemicals Co., Ltd. (Thailand) for funding.

3.4.6. References

[1] W.H.O. WHO, 9 out of 10 people worldwide breathe polluted air, but more countries are taking action, (n.d.). https://www.who.int/news-room/detail/02-05-2018-9-out-of-10-people-worldwide-breathe-polluted-air-but-more-countries-are-taking-action (accessed July 5, 2021).

[2] P.J. Landrigan, R. Fuller, N.J.R. Acosta, O. Adeyi, R. Arnold, N. (Nil) Basu, A.B. Baldé, R. Bertollini, S. Bose-O'Reilly, J.I. Boufford, P.N. Breysse, T. Chiles, C. Mahidol, A.M. Coll-Seck, M.L. Cropper, J. Fobil, V. Fuster, M. Greenstone, A. Haines, D. Hanrahan, D. Hunter, M. Khare, A. Krupnick, B. Lanphear, B. Lohani, K. Martin, K. V. Mathiasen, M.A. McTeer, C.J.L. Murray, J.D. Ndahimananjara, F. Perera, J. Potočnik, A.S. Preker, J. Ramesh, J. Rockström, C. Salinas, L.D. Samson, K. Sandilya, P.D. Sly, K.R. Smith, A. Steiner, R.B. Stewart, W.A. Suk, O.C.P. van Schayck, G.N. Yadama, K. Yumkella, M. Zhong, The Lancet Commission on pollution and health, Lancet. 391 (2018) 462–512. doi:10.1016/S0140-6736(17)32345-0.

[3] S.K. Grange, N.J. Farren, A.R. Vaughan, R.A. Rose, D.C. Carslaw, Strong Temperature Dependence for Light-Duty Diesel Vehicle NO_x Emissions, Environ. Sci. Technol. 53 (2019) 6587–6596. doi:10.1021/acs.est.9b01024.

[4] A. Folli, S.B. Campbell, J.A. Anderson, D.E. MacPhee, Role of TiO_2 surface hydration on NO oxidation photo-activity, J. Photochem. Photobiol. A Chem. 220 (2011) 85–93. doi:10.1016/j.jphotochem.2011.03.017.

[5] Q. Di, H. Amini, L. Shi, I. Kloog, R. Silvern, J. Kelly, M.B. Sabath, C. Choirat, P. Koutrakis, A. Lyapustin, Y. Wang, L.J. Mickley, J. Schwartz, Assessing NO_2 Concentration and Model Uncertainty with High Spatiotemporal Resolution across the Contiguous United States Using Ensemble Model Averaging, Environ. Sci. Technol. 54 (2020) 1372–1384. doi:10.1021/acs.est.9b03358.

[6] B.N. Duncan, L.N. Lamsal, A.M. Thompson, Y. Yoshida, Z. Lu, D.G. Streets, M.M. Hurwitz, K.E. Pickering, A space-based, high-resolution view of notable changes in urban NO_x pollution around the world (2005-2014), J. Geophys. Res. Atmos. 121 (2016) 976–996. doi:10.1002/2015JD024121.

[7] 5,000 deaths annually from dieselgate in Europe - International Institute for Applied Systems Analysis, (2017). https://iiasa.ac.at/web/home/about/news/170918-diesel-nox.html (accessed July 5, 2021).

[8] J. Balbuena, M. Cruz-Yusta, L. Sánchez, Nanomaterials to Combat NOx Pollution, J. Nanosci. Nanotechnol. 15 (2015) 6373–6385. doi:10.1166/jnn.2015.10871.

[9] V. Nguyen, J. Che-Chin Yu, C. Huang, J.C.-S. Wu, Recent advances in the development of photocatalytic NOx abatement, in: Curr. Dev. Photocatal. Photocatalytic Mater., Elsevier, 2020: pp. 211–229. doi:10.1016/B978-0-12-819000-5.00014-X.

[10] Q. Guo, C. Zhou, Z. Ma, X. Yang, Fundamentals of TiO_2 Photocatalysis: Concepts, Mechanisms, and Challenges, Adv. Mater. 31 (2019) 1–26. doi:10.1002/adma.201901997.

[11] J.M. Cordero, R. Hingorani, E. Jimenez-Relinque, M. Grande, R. Borge, A. Narros, M. Castellote, NO_x removal efficiency of urban photocatalytic pavements at pilot scale, Sci. Total Environ. 719 (2020) 137459. doi:10.1016/j.scitotenv.2020.137459.

[12] A. Speziale, J.F. González-Sánchez, B. Taşcı, A. Pastor, L. Sánchez, C. Fernández-Acevedo, T. Oroz-Mateo, C. Salazar, I. Navarro-Blasco, J.M. Fernández, J.I. Alvarez, Development of Multifunctional Coatings for Protecting Stones and Lime Mortars of the Architectural Heritage, Int. J. Archit. Herit. 3058 (2020) 1–22. doi:10.1080/15583058.2020.1728594.

[13] G.L. Guerrini, Photocatalytic performances in a city tunnel in Rome: NO_x monitoring results, Constr. Build. Mater. 27 (2012) 165–175. doi:10.1016/j.conbuildmat.2011.07.065.

[14] J. Schneider, M. Matsuoka, M. Takeuchi, J. Zhang, Y. Horiuchi, M. Anpo, D.W. Bahnemann, Understanding TiO_2 Photocatalysis: Mechanisms and Materials, Chem. Rev. 114 (2014) 9919–9986. doi:10.1021/cr5001892.

[15] J.Z. Bloh, A. Folli, D.E. Macphee, Photocatalytic NO_x abatement: Why the selectivity matters, RSC Adv. 4 (2014) 45726–45734. doi:10.1039/c4ra07916g.

[16] J. Balbuena, M. Cruz-Yusta, A. Pastor, L. Sánchez, α-Fe_2O_3/SiO_2 composites for the enhanced photocatalytic NO oxidation, J. Alloys Compd. 735 (2018) 1553–1561. doi:10.1016/j.jallcom.2017.11.259.

[17] European Union law - Document 32020R0217, (n.d.). https://eur-lex.europa.eu/legal-content/EN/TXT/?uri=uriserv:OJ.L_.2020.044.01.0001.01.ENG&toc=OJ:L:2020:044:TOC (accessed July 5, 2021).

[18] J. Balbuena, M. Cruz-Yusta, A.L. Cuevas, F. Martín, A. Pastor, R. Romero, L. Sánchez, Hematite porous architectures as enhanced

air purification photocatalyst, J. Alloys Compd. 797 (2019) 166–173. doi:10.1016/j.jallcom.2019.05.113.

[19] Z. Wang, Y. Huang, M. Chen, X. Shi, Y. Zhang, J. Cao, W. Ho, S.C. Lee, Roles of N-Vacancies over Porous g-C_3N_4 Microtubes during Photocatalytic NO_x Removal, ACS Appl. Mater. Interfaces. 11 (2019) 10651–10662. doi:10.1021/acsami.8b21987.

[20] M. Irfan, M. Sevim, Y. Koçak, M. Balci, Ö. Metin, E. Ozensoy, Enhanced photocatalytic NOx oxidation and storage under visible-light irradiation by anchoring Fe_3O_4 nanoparticles on mesoporous graphitic carbon nitride (mpg-C_3N_4), Appl. Catal. B Environ. 249 (2019) 126–137. doi:10.1016/j.apcatb.2019.02.067.

[21] C. Wang, M. Fu, J. Cao, X. Wu, X. Hu, F. Dong, $BaWO_4$/g-C_3N_4 heterostructure with excellent bifunctional photocatalytic performance, Chem. Eng. J. 385 (2020) 123833. doi:10.1016/j.cej.2019.123833.

[22] Y. Ye, Z. Zang, T. Zhou, F. Dong, S. Lu, X. Tang, W. Wei, Y. Zhang, Theoretical and experimental investigation of highly photocatalytic performance of CuInZnS nanoporous structure for removing the NO gas, J. Catal. 357 (2018) 100–107. doi:10.1016/j.jcat.2017.11.002.

[23] Q. Zhang, Y. Huang, S. Peng, Y. Zhang, Z. Shen, J. Cao, W. Ho, S.C. Lee, D.Y.H. Pui, Perovskite $LaFeO_3$ -$SrTiO_3$ composite for synergistically enhanced NO removal under visible light excitation, Appl. Catal. B Environ. 204 (2017) 346–357. doi:10.1016/j.apcatb.2016.11.052.

[24] Y. Huang, Y. Gao, Q. Zhang, Y. Zhang, J. ji Cao, W. Ho, S.C. Lee, Biocompatible FeOOH-Carbon quantum dots nanocomposites for gaseous NOx removal under visible light: Improved charge separation and High selectivity, J. Hazard. Mater. 354 (2018) 54–62. doi:10.1016/j.jhazmat.2018.04.071.

[25] A. Gasparotto, G. Carraro, C. Maccato, C. Sada, J. Balbuena, M. Cruz-Yusta, L. Sánchez, N. Vodišek, U. Lavrencic Štangar, D. Barreca, WO_3 -decorated ZnO nanostructures for light-activated applications, CrystEngComm. 20 (2018) 1282–1290. doi:10.1039/C7CE02148H.

[26] A. Pastor, J. Balbuena, M. Cruz-Yusta, I. Pavlovic, L. Sánchez, ZnO on rice husk: A sustainable photocatalyst for urban air purification,

Chem. Eng. J. 368 (2019) 659–667. doi:10.1016/j.cej.2019.03.012.

[27] Y. Lu, Y. Huang, Y. Zhang, T. Huang, H. Li, J. ji Cao, W. Ho, Effects of H_2O_2 generation over visible light-responsive $Bi/Bi_2O_{2-x}CO_3$ nanosheets on their photocatalytic NO_x removal performance, Chem. Eng. J. 363 (2019) 374–382. doi:10.1016/j.cej.2019.01.172.

[28] J. Zhang, G. Zhu, S. Li, F. Rao, Q.-U. Hassan, J. Gao, Y. Huang, M. Hojamberdiev, Novel Au/La-Bi_5O_7I Microspheres with Efficient Visible-Light Photocatalytic Activity for NO Removal: Synergistic Effect of Au Nanoparticles, La Doping, and Oxygen Vacancy, ACS Appl. Mater. Interfaces. 11 (2019) 37822–37832. doi:10.1021/acsami.9b14300.

[29] M. Ran, H. Wang, W. Cui, J. Li, P. Chen, Y. Sun, J. Sheng, Y. Zhou, Y. Zhang, F. Dong, Light-Induced Generation and Regeneration of Oxygen Vacancies in $BiSbO_4$ for Sustainable Visible Light Photocatalysis, ACS Appl. Mater. Interfaces. 11 (2019) 47984–47991. doi:10.1021/acsami.9b18154.

[30] S. Wang, X. Ding, N. Yang, G. Zhan, X. Zhang, G. Dong, L. Zhang, H. Chen, Insight into the effect of bromine on facet-dependent surface oxygen vacancies construction and stabilization of Bi_2MoO_6 for efficient photocatalytic NO removal, Appl. Catal. B Environ. 265 (2020) 118585. doi:10.1016/j.apcatb.2019.118585.

[31] F. Rodriguez-Rivas, A. Pastor, C. Barriga, M. Cruz-Yusta, L. Sánchez, I. Pavlovic, Zn-Al layered double hydroxides as efficient photocatalysts for NOx abatement, Chem. Eng. J. 346 (2018) 151–158. doi:10.1016/j.cej.2018.04.022.

[32] F. Rodriguez-Rivas, A. Pastor, G. de Miguel, M. Cruz-Yusta, I. Pavlovic, L. Sánchez, Cr^{3+} substituted Zn-Al layered double hydroxides as UV–Vis light photocatalysts for NO gas removal from the urban environment, Sci. Total Environ. 706 (2020) 136009. doi:10.1016/j.scitotenv.2019.136009.

[33] A. Pastor, F. Rodriguez-Rivas, G. de Miguel, M. Cruz-Yusta, F. Martin, I. Pavlovic, L. Sánchez, Effects of Fe^{3+} substitution on Zn-Al layered double hydroxides for enhanced NO photochemical abatement, Chem. Eng. J. 387 (2020) 124110. doi:10.1016/j.cej.2020.124110.

[34] F. Cavani, F. Trifirò, A. Vaccari, Hydrotalcite-type anionic clays: Preparation, properties and applications., Catal. Today. 11 (1991)

173–301. doi:10.1016/0920-5861(91)80068-K.

[35] L. Mohapatra, K. Parida, A review on the recent progress, challenges and perspective of layered double hydroxides as promising photocatalysts, J. Mater. Chem. A. 4 (2016) 10744–10766. doi:10.1039/c6ta01668e.

[36] G. Zhang, X. Zhang, Y. Meng, G. Pan, Z. Ni, S. Xia, Layered double hydroxides-based photocatalysts and visible-light driven photodegradation of organic pollutants: A review, Chem. Eng. J. 392 (2019) 123684. doi:10.1016/j.cej.2019.123684.

[37] C.-W. Jeon, S.-S. Lee, I.-K. Park, Flexible Visible-Blind Ultraviolet Photodetectors Based on ZnAl-Layered Double Hydroxide Nanosheet Scroll, ACS Appl. Mater. Interfaces. 11 (2019) 35138–35145. doi:10.1021/acsami.9b12082.

[38] Y. Zhao, Y. Zhao, G.I.N. Waterhouse, L. Zheng, X. Cao, F. Teng, L.Z. Wu, C.H. Tung, D. O'Hare, T. Zhang, Layered-Double-Hydroxide Nanosheets as Efficient Visible-Light-Driven Photocatalysts for Dinitrogen Fixation, Adv. Mater. 29 (2017) 1–10. doi:10.1002/adma.201703828.

[39] Y. Zhao, X. Jia, G.I.N. Waterhouse, L.Z. Wu, C.H. Tung, D. O'Hare, T. Zhang, Layered Double Hydroxide Nanostructured Photocatalysts for Renewable Energy Production, Adv. Energy Mater. 6 (2016) 1–20. doi:10.1002/aenm.201501974.

[40] C. Chen, A. Wangriya, J.-C. Buffet, D. O'Hare, Tuneable ultra high specific surface area Mg/Al-CO_3 layered double hydroxides, Dalt. Trans. 44 (2015) 16392–16398. doi:10.1039/C5DT02641E.

[41] Q. Wang, D. O'Hare, Recent Advances in the Synthesis and Application of Layered Double Hydroxide (LDH) Nanosheets, Chem. Rev. 112 (2012) 4124–4155. doi:10.1021/cr200434v.

[42] Q. Wang, D. O'Hare, Large-scale synthesis of highly dispersed layered double hydroxide powders containing delaminated single layer nanosheets, Chem. Commun. 49 (2013) 6301. doi:10.1039/c3cc42918k.

[43] C. Chen, M. Yang, Q. Wang, J.-C. Buffet, D. O'Hare, Synthesis and characterisation of aqueous miscible organic-layered double hydroxides, J. Mater. Chem. A. 2 (2014) 15102–15110. doi:10.1039/C4TA02277G.

[44] J.-C. Buffet, Z.R. Turner, R.T. Cooper, D. O'Hare, Ethylene polymerisation using solid catalysts based on layered double hydroxides, Polym. Chem. 6 (2015) 2493–2503. doi:10.1039/C4PY01742K.

[45] Q. Yan, Y. Nie, R. Yang, Y. Cui, D. O'Hare, Q. Wang, Highly dispersed Cu_yAlO_x mixed oxides as superior low-temperature alkali metal and SO_2 resistant NH_3-SCR catalysts, Appl. Catal. A Gen. 538 (2017) 37–50. doi:10.1016/j.apcata.2017.03.021.

[46] L. Qiu, Y. Gao, C. Zhang, Q. Yan, D. O'Hare, Q. Wang, Synthesis of highly efficient flame retardant polypropylene nanocomposites with surfactant intercalated layered double hydroxides, Dalt. Trans. 47 (2018) 2965–2975. doi:10.1039/c7dt03477f.

[47] S. Shang, A. Hanif, M. Sun, Y. Tian, Y.S. Ok, I.K.M. Yu, D.C.W. Tsang, Q. Gu, J. Shang, Novel M (Mg/Ni/Cu)-Al-CO_3 layered double hydroxides synthesized by aqueous miscible organic solvent treatment (AMOST) method for CO_2 capture, J. Hazard. Mater. 373 (2019) 285–293. doi:10.1016/j.jhazmat.2019.03.077.

[48] I.K.M. Yu, A. Hanif, D.C.W. Tsang, J. Shang, Z. Su, H. Song, Y.S. Ok, C.S. Poon, Tuneable functionalities in layered double hydroxide catalysts for thermochemical conversion of biomass-derived glucose to fructose, Chem. Eng. J. 383 (2020) 122914. doi:10.1016/j.cej.2019.122914.

[49] U. Costantino, F. Marmottini, M. Nocchetti, R. Vivani, New Synthetic Routes to Hydrotalcite-Like Compounds – Characterisation and Properties of the Obtained Materials, Eur. J. Inorg. Chem. 1998 (1998) 1439–1446. doi:10.1002/(SICI)1099-0682(199810)1998:10<1439::AID-EJIC1439>3.0.CO;2-1.

[50] W.H. Zhang, X.D. Guo, J. He, Z.Y. Qian, Preparation of Ni(II)/Ti(IV) layered double hydroxide at high supersaturation, J. Eur. Ceram. Soc. 28 (2008) 1623–1629. doi:10.1016/j.jeurceramsoc.2007.11.016.

[51] G. Lin, L. Zhu, T. Duan, L. Zhang, B. Liu, J. Lei, Efficient capture of iodine by a polysulfide-inserted inorganic NiTi-layered double hydroxides, Chem. Eng. J. 378 (2019) 122181. doi:10.1016/j.cej.2019.122181.

[52] C. Chen, M. Yang, Q. Wang, J.-C. Buffet, D. O'Hare, SI - Synthesis and characterisation of aqueous miscible organic-layered double

hydroxides, J. Mater. Chem. A. 2 (2014) 15102–15110. doi:10.1039/C4TA02277G.

[53] K. Cermelj, K. Ruengkajorn, J.C. Buffet, D. O'Hare, Layered double hydroxide nanosheets via solvothermal delamination, J. Energy Chem. 35 (2019) 88–94. doi:10.1016/j.jechem.2018.11.008.

[54] V. Rives, Layered Double Hydroxides: Present and Future, Nova Science Publishers Inc, New York, 2001.

[55] M.C. Capel-Sanchez, G. Blanco-Brieva, J.M. Campos-Martin, M.P. de Frutos, W. Wen, J.A. Rodriguez, J.L.G. Fierro, Grafting Strategy to Develop Single Site Titanium on an Amorphous Silica Surface, Langmuir. 25 (2009) 7148–7155. doi:10.1021/la900578u.

[56] Y. Zhao, B. Li, Q. Wang, W. Gao, C.J. Wang, M. Wei, D.G. Evans, X. Duan, D. O'Hare, NiTi-Layered double hydroxides nanosheets as efficient photocatalysts for oxygen evolution from water using visible light, Chem. Sci. 5 (2014) 951–958. doi:10.1039/C3SC52546E.

[57] J. Cai, Y. Zhang, Y. Qian, C. Shan, B. Pan, Enhanced Defluoridation Using Novel Millisphere Nanocomposite of La-Doped Li-Al Layered Double Hydroxides Supported by Polymeric Anion Exchanger, Sci. Rep. 8 (2018) 11741. doi:10.1038/s41598-018-29497-1.

[58] X. Wu, R. Wang, Y. Du, X. Li, H. Meng, X. Xie, NO_x removal by selective catalytic reduction with ammonia over hydrotalcite-derived NiTi mixed oxide, New J. Chem. 43 (2019) 2640–2648. doi:10.1039/c8nj05280h.

[59] Y. Zhao, P. Chen, B. Zhang, D.S. Su, S. Zhang, L. Tian, J. Lu, Z. Li, X. Cao, B. Wang, M. Wei, D.G. Evans, X. Duan, Highly dispersed TiO_6 units in a layered double hydroxide for water splitting, Chem. - A Eur. J. 18 (2012) 11949–11958. doi:10.1002/chem.201201065.

[60] Y. Lu, J.H. Warner, Synthesis and Applications of Wide Bandgap 2D Layered Semiconductors Reaching the Green and Blue Wavelengths, ACS Appl. Electron. Mater. 2 (2020) 1777–1814. doi:10.1021/acsaelm.0c00105.

[61] J. Ângelo, L. Andrade, L.M. Madeira, A. Mendes, An overview of photocatalysis phenomena applied to NO_x abatement, J. Environ. Manage. 129 (2013) 522–539. doi:10.1016/j.jenvman.2013.08.006.

[62] W. Cui, J. Li, F. Dong, Y. Sun, G. Jiang, W. Cen, S.C. Lee, Z. Wu,

Highly Efficient Performance and Conversion Pathway of Photocatalytic NO Oxidation on SrO-Clusters@Amorphous Carbon Nitride, Environ. Sci. Technol. 51 (2017) 10682–10690. doi:10.1021/acs.est.7b00974.

[63] R.J.L. N.I. Sax, Sax's Dangerous Properties of Industrial Materials, 12th ed, Van Nostrand Reinhold, New York, 2012.

[64] Y. Wang, H. Huang, J. Gao, G. Lu, Y. Zhao, Y. Xu, L. Jiang, TiO_2–SiO_2 composite fibers with tunable interconnected porous hierarchy fabricated by single-spinneret electrospinning toward enhanced photocatalytic activity, J. Mater. Chem. A. 2 (2014) 12442–12448. doi:10.1039/C4TA01208A.

[65] J. Balbuena, J.M. Calatayud, M. Cruz-Yusta, P. Pardo, F. Martín, J. Alarcón, L. Sánchez, Mesocrystalline anatase nanoparticles synthesized using a simple hydrothermal approach with enhanced light harvesting for gas-phase reaction, Dalt. Trans. 47 (2018) 6590–6597. doi:10.1039/C8DT00721G.

[66] X. Lv, J. Zhang, X. Dong, J. Pan, W. Zhang, W. Wang, G. Jiang, F. Dong, Layered double hydroxide nanosheets as efficient photocatalysts for NO removal: Band structure engineering and surface hydroxyl ions activation, Appl. Catal. B Environ. 277 (2020) 119200. doi:10.1016/j.apcatb.2020.119200.

[67] W. Zhang, X. Dong, Y. Liang, Y. Sun, F. Dong, Ag/AgCl nanoparticles assembled on BiOCl/$Bi_{12}O_{17}Cl_2$ nanosheets: Enhanced plasmonic visible light photocatalysis and in situ DRIFTS investigation, Appl. Surf. Sci. 455 (2018) 236–243. doi:10.1016/j.apsusc.2018.05.171.

[68] P. Chen, H. Liu, Y. Sun, J. Li, W. Cui, L. Wang, W. Zhang, X. Yuan, Z. Wang, Y. Zhang, F. Dong, Bi metal prevents the deactivation of oxygen vacancies in $Bi_2O_2CO_3$ for stable and efficient photocatalytic NO abatement, Appl. Catal. B Environ. 264 (2020) 118545. doi:10.1016/j.apcatb.2019.118545.

[69] J. Liao, W. Cui, J. Li, J. Sheng, H. Wang, X. Dong, P. Chen, G. Jiang, Z. Wang, F. Dong, Nitrogen defect structure and NO+ intermediate promoted photocatalytic NO removal on H_2 treated g-C_3N_4, Chem. Eng. J. 379 (2020) 122282. doi:10.1016/j.cej.2019.122282.

[70] W. Huo, T. Cao, W. Xu, Z. Guo, X. Liu, H.C. Yao, Y. Zhang, F. Dong, Facile construction of $Bi_2Mo_3O_{12}$@$Bi_2O_2CO_3$ heterojunctions for enhanced photocatalytic efficiency toward NO removal and study

of the conversion process, Chinese J. Catal. 41 (2020) 268–275. doi:10.1016/S1872-2067(19)63460-1.

[71] X. Li, W. Zhang, W. Cui, J. Li, Y. Sun, G. Jiang, H. Huang, Y. Zhang, F. Dong, Reactant activation and photocatalysis mechanisms on Bi-metal@Bi_2GeO_5 with oxygen vacancies: A combined experimental and theoretical investigation, Chem. Eng. J. 370 (2019) 1366–1375. doi:10.1016/j.cej.2019.04.003.

[72] W. Huo, W. Xu, T. Cao, X. Liu, Y. Zhang, F. Dong, Carbonate-intercalated defective bismuth tungstate for efficiently photocatalytic NO removal and promotion mechanism study, Appl. Catal. B Environ. 254 (2019) 206–213. doi:10.1016/j.apcatb.2019.04.099.

Appendix IV: Electronic Supplementary Information

Aqueous miscible organic solvent treated NiTi layered double hydroxide De-NO_x photocatalysts

Adrián Pastor[1], Chunping Chen[2], Gustavo de Miguel[3], Francisco Martin[4], Manuel Cruz-Yusta[1], Jean-Charles Buffet[2], Dermot O'Hare[2,*], Ivana Pavlovic[1,] and Luis Sánchez[1,*]

[1] Departamento de Química Inorgánica, Instituto Universitario de Nanoquímica IUNAN, Universidad de Córdoba, Campus de Rabanales, E-14014 Córdoba, Spain.

[2] Chemistry Research Laboratory, Department of Chemistry, University of Oxford, Oxford, OX1 3TA, UK.

[3] Departamento de Química Física y Termodinámica Aplicada, Instituto Universitario de Nanoquímica IUNAN, Universidad de Córdoba, Campus de Rabanales, E-14014 Córdoba, Spain.

[4] Departamento de Ingeniería Química, Facultad de Ciencias, Universidad de Málaga, Campus de Teatinos, E-29071 Málaga, Spain.

Table of contents

Characterization of the samples.

X-ray diffraction (XRD) patterns of powdered samples were collected on a Bruker D8 Discovery instrument using Cu Kα radiation (λ=1.5406 Å). The Scherrer's equation [1] was used to calculate the crystalline domain size of the samples (DIFFRACT.EVA V3.1 software) [2]. In the Scherrer's equation, a K value of 0.9 and 1.84 was taken for the *003* and *110* planes, respectively [2]. The instrumental broadening was previously measured by using a LaB_6 standard (Sigma-Aldrich).

Infrared spectra were obtained on a Vertex 80 Spectrometer, equipped with a high performance DuraSamp1IR II diamond accessory of attenuated total reflection (ATR) mode.

Nitrogen adsorption–desorption isotherms were recorded at 77.4 K in a Micrometric Tristar surface characterization analyzer. Samples were degassed overnight at 90 °C under vacuum prior to analysis. Specific surface areas were measured by nitrogen adsorption and desorption isotherms using the multipoint Brunauer–Emmett–Teller (BET) method over the relative equilibrium pressure interval $0.05 < P/P_0 < 0.30$.

Transmission electron microscopy (TEM) images were obtained with a JEOL 2100 microscope (accelerating voltage = 200 kV). Powder was dispersed in water or ethanol via sonication for 1 h before casting onto carbon-coated grids.

Analyses of chemical compositions of LDHs were performed on ICP mass (Perkin Elmer Nexion X) after dissolving the samples in 0.1 M HCl.

Typical thermogravimetric analyses were performed on a Mettler Toledo equipment from 30 to 800 °C. Thermogravimetric analysis coupled with mass spectrometry (TGA-MS) was performed on a Mettler Toledo

model TGA/DSC 1 in the temperature range 30-500 °C. The thermobalance was connected to the output of a Pfeiffer Vacuum mass spectrometer, model ThermoStar TM GSD 320. The analyses were carried out in 70 µl Al_2O_3 crucibles, with an air flow of 50 mL min^{-1} at a heating rate of 5 °C min^{-1} and 5 mg of sample.

Diffuse reflectance (DR) spectra were measured from 200 to 800 nm on a UV-2600 equipment (Shimadzu).

X-ray photoelectron spectra (XPS) were recorded using a Physical Electronics PHI Versa Probe II spectrometer with a focused beam diameter of 100 µm AlKα (hv= 1486.6 eV), X-ray source radiation (15 kV, 25 W), analysis chamber pressure at 10^{-7} Pa. Hemi-spherical analyzer operating at a constant pass energy of 29.35 eV. Software MultiPak version 9.3 [3] was used to fit the xps peaks with Gaussian/Lorentzian bands (Voigt profile, Shirley Background).

The time-resolved photoluminescence (TRPL) decays were measured at room temperature with a FLS920 Fluorimeter (Edinburgh Instrument Ltd, Livingston, UK).

Electron paramagnetic resonance (EPR) spectra were recorded (EMXmicro, Bruker) at room temperature. Water or methanol LDH dispersions (detection of •OH or $•O_2^-$, respectively) were irradiated for 30 minutes and 45 mM of DMPO (spin-trap agent) was used.

A FTIR spectrometer (Perkin Elmer Frontier), equipped with a Harrick reaction chamber, was used to perform in situ diffuse reflectance infrared Fourier transform (DRIFT) spectroscopy. The DRIFT spectroscopy measurements were employed to monitor the photochemical De-NO_x process and to check the intermediates and products formed on the surface of the photocatalyst. The powdered photocatalyst was placed in

the reaction chamber and treated at room temperature under high purity Ar flow for 10 minutes to remove environmental impurities and then scanned to produce a baseline. Afterwards, under dark conditions, a mixture of 50 mL min^{-1} NO (50 ppm) and 50 mL min^{-1} O_2 was pumped into the chamber being the sample subjected to adsorption reactions during 10 minutes and a new scan was obtained. Subsequently, light was turned on for 60 minutes. The spectrum (accumulation of 12 scans) evolving along with the photocatalytic reaction was obtained every 5 minutes.

The photocatalytic performance of the samples was studied regarding the following indexes:

$$\boldsymbol{NO\ conversion}\ (\%) = \frac{([\boldsymbol{NO}]_{\boldsymbol{in}} - [\boldsymbol{NO}]_{\boldsymbol{out}})}{[\boldsymbol{NO}]_{\boldsymbol{in}}} \times \mathbf{100}$$

$$\boldsymbol{NO_x\ conversion}\ (\%) = \frac{([\boldsymbol{NOx}]_{\boldsymbol{in}} - [\boldsymbol{NOx}]_{\boldsymbol{out}})}{[\boldsymbol{NOx}]_{\boldsymbol{in}}} \times \mathbf{100}$$

$$\boldsymbol{Selectivity};\quad \boldsymbol{S}\ (\%) = \frac{([\boldsymbol{NOx}]_{\boldsymbol{in}} - [\boldsymbol{NOx}]_{\boldsymbol{out}})/[\boldsymbol{NOx}]_{\boldsymbol{in}}}{([\boldsymbol{NO}]_{\boldsymbol{in}} - [\boldsymbol{NO}]_{\boldsymbol{out}})/[\boldsymbol{NO}]_{\boldsymbol{in}}} \times \mathbf{100}$$

where $[NO]_{in}$, $[NO_X]_{in}$ and $[NO]_{out}$, $[NO_X]_{out}$ is the measured inlet and outlet concentrations, respectively, and $[NO_X]=[NO]+[NO_2]$.

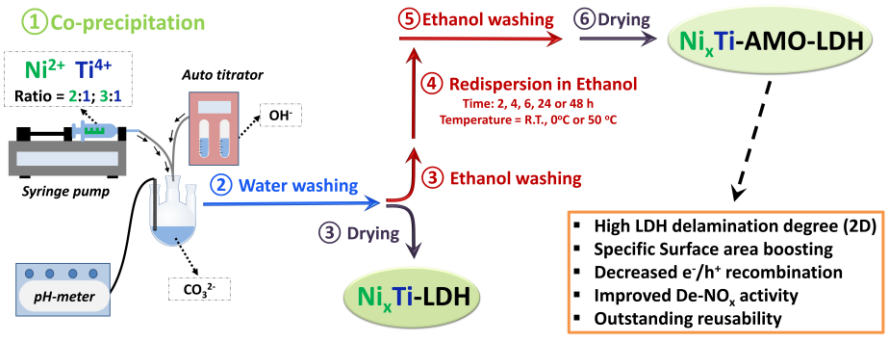

Scheme S1. Description of the procedure for the synthesis of AMO-samples and related main findings.

Table S1. Reported syntheses of NiTi LDHs and comparison with this work.

Application	Attempted synthesis method	Attempted Ni:Ti ratio	Successful synthesis	Interlayer anion	Reported BET Surface Area (m^2g^{-1})	Note	Reference
-	Urea, different reaction times (ranging from 1.5 up to 43 h)	5:1; 5:2 and 3:2	All*	CO_3^{2-}	182 (Ni:Ti = 5:1, synthesis time = 10 h)	*Cyanate anions in the interlayer.	Shu et al., 2006 [4]
-	1) Coprecipitation + reflux 2) Coprecipitation + hydrothermal treatment 3) Urea	2:1; 3:1; 4:1 and 5:1	Method 1 (Ni:Ti = 3:1)	CO_3^{2-}	37	-	Zhang et al., 2008 [5]
Photocatalytic dye degradation	Urea	5:2	All	CO_3^{2-} CNO^-	Not reported	LDH is used as a precursor of layered double oxides (LDO)	Shu, et al., 2009 [6]
Water splitting	Urea	6:1	All*	CO_3^{2-}	187 (Ni:Ti = 6:1)	*Cyanate anions in the interlayer	Lee et al., 2011 [7]
Pentachlorophenol adsorption	Coprecipitation	3:1; 4:1 and 6:1	All*	Dodecylbenzenesulfonate; dodecyl sulfate; Cyanate (CNO^-)	From <3.5 up to 124 (CNO-LDH)	*Possible impurity of amorphous $Ni(OH)_2$	Gao et al., 2011 [8]
Water splitting	Urea	2:1; 3:1; 4:1 and 5:1	Urea (3:1; 4:1 and 5:1)*	CO_3^{2-}	149 (Ni:Ti = 4:1)	*Cyanate anions in the interlayer	Zhao et al., 2012 [9]
Water splitting	Urea	2:1; 3:1; 4:1 and 5:1	All*	CO_3^{2-}	124 (Ni:Ti = 4:1)	*Cyanate anions in the interlayer	Li et al., 2013 [10]
-	Coprecipitation; anion exchange	5:1	All	NO_3^- β-Cyclodextrin	Not reported	-	Hu et al., 2013 [11]

Water splitting	1) Reverse micelles 2) Urea	2:1; 3:1; 4:1 (method 1) 4:1 (method 2)	All*	CO_3^{2-}	From 91 up to 169 (Ni:Ti = 4:1)	*Cyanate anions in the interlayer	Zhao et al., 2014 [12]
Supercapacitors	1) Reverse micelles 2) Urea	4:1	All*	CO_3^{2-}	Not reported	*Cyanate anions in the interlayer	Zhao, et al., 2015 [13]
Acetylene hydrogenation	Urea + reflux	2:1	All	CO_3^{2-}	104	-	Liu et al., 2015 [14]
Photocatalytic antibiotic degradation	Coprecipitation + hydrothermal treatment	2:1	All	NO_3^-	5	-	Abazari et al., 2019 [15]
Iodine sorption	Coprecipitation; anion exchange	3:1	All*	CO_3^{2-} NO_3^- $[S_x]^{2-}$	Not reported	*Sulphate anions in the interlayer when $[S_x]^{2-}$ intercalation is attempted	Lin et al., 2019 [16]
Selective catalytic reduction of NO_x	Urea	2:1; 4:1 and 6:1	All*	NO_3^- and CO_3^{2-}	Not reported	*Cyanate anions in the interlayer. LDH is used as a precursor of Mixed Metal Oxides	Wu et al., 2019 [17]
Photocatalytic NO_x removal	Coprecipitation + AMOST	3:1 and 2:1	All	CO_3^{2-}	From 166 up to 492 (Ni:Ti = 3:1)	-	This paper

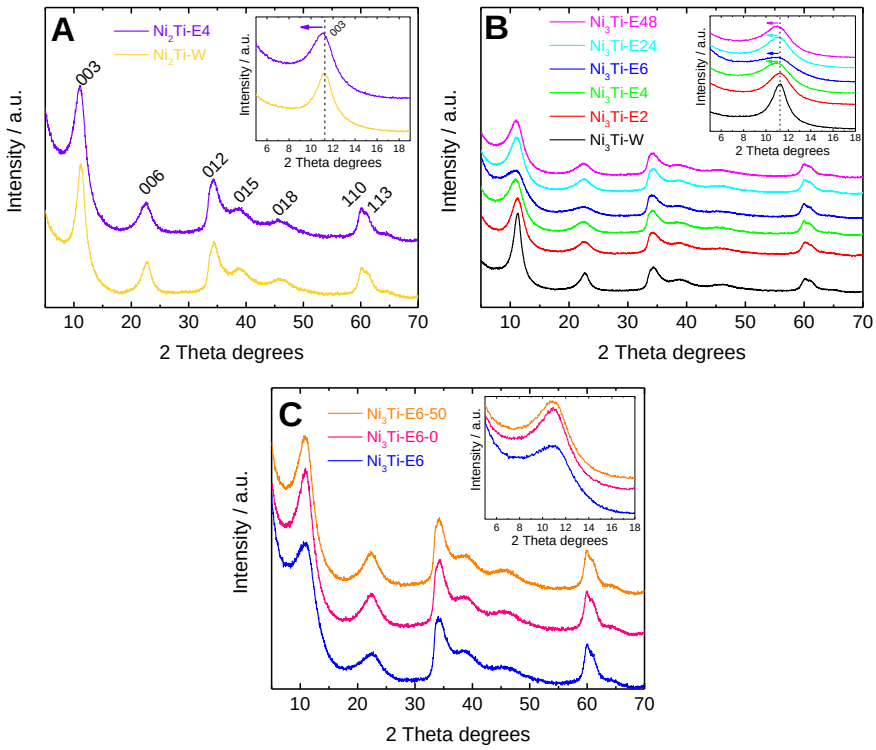

Fig. S1. XRD patterns and inlet for (A) Ni_2Ti samples, (B) Ni_3Ti samples with different redispersion times for the AMOST and (C) Ni_3Ti-E6 samples with different temperatures in the AMOST.

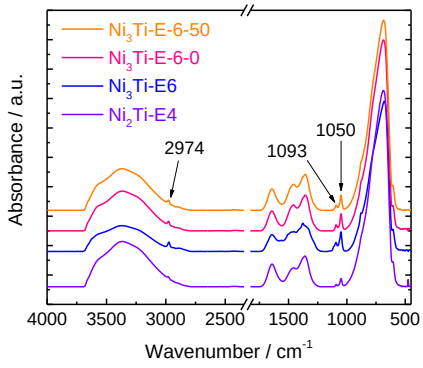

Fig. S2. ATR spectra for Ni_2Ti-E4 and Ni_3Ti-E6 samples with different temperatures in the AMOST.

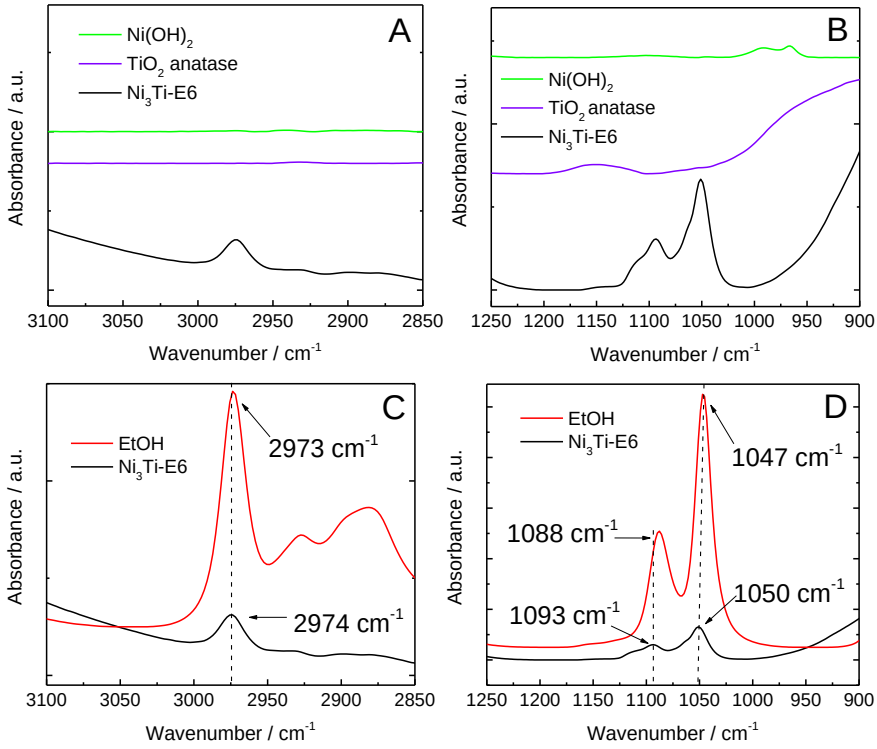

Fig. S3. Comparative ATR spectra for Ni_3Ti-E6 sample: (A, B) comparison with possible impurities; (C, D) comparison with ethanol.

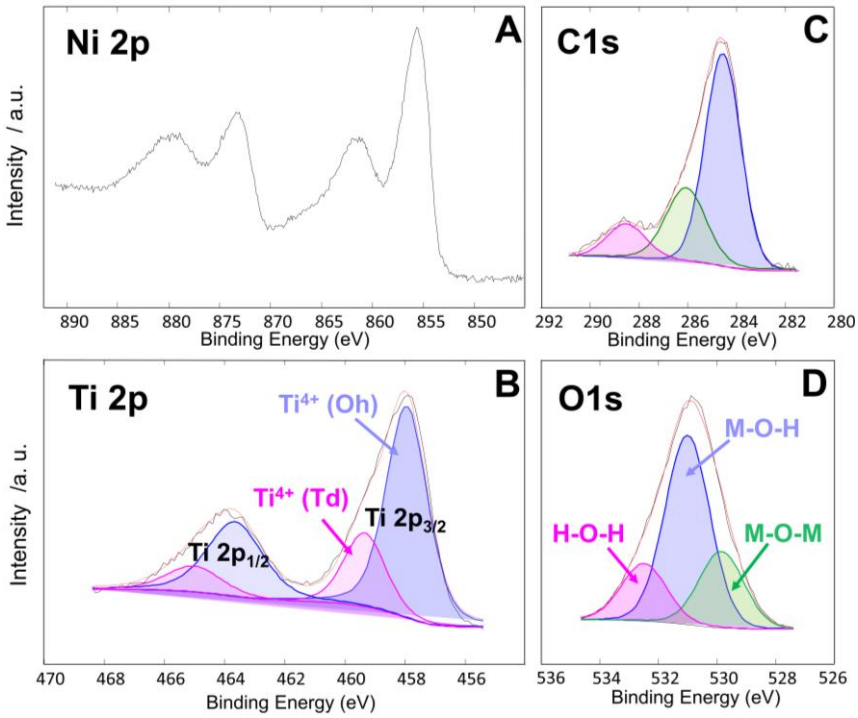

Fig. S4. XPS spectrum of Ni_3Ti-W sample: (A) Ni 2p region; (B) deconvoluted Ti 2p, (C) C 1s and (D) O 1s XPS signals.

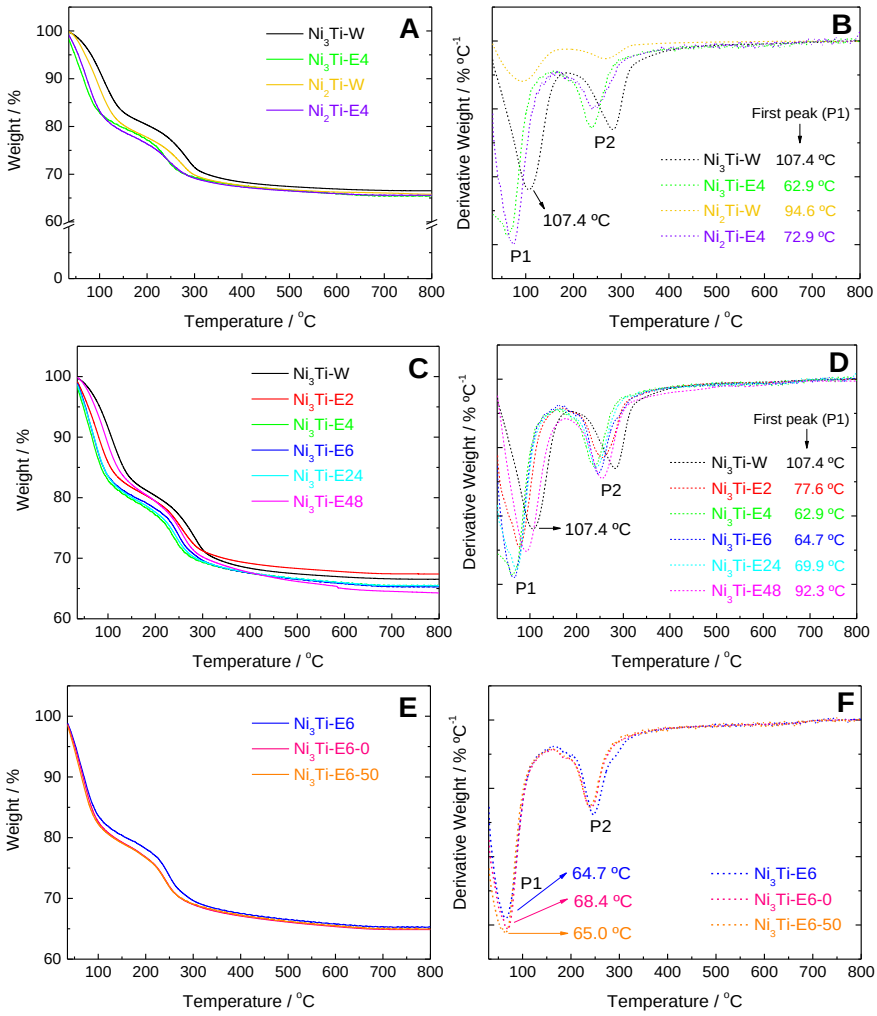

Fig. S5. TGA and derivative curves for: (A, B) Ni_3Ti and Ni_2Ti samples; (C, D) Ni_3Ti with different redispersion times for the AMOST; (E, F) Ni_3Ti-E6 with different temperatures in the AMOST.

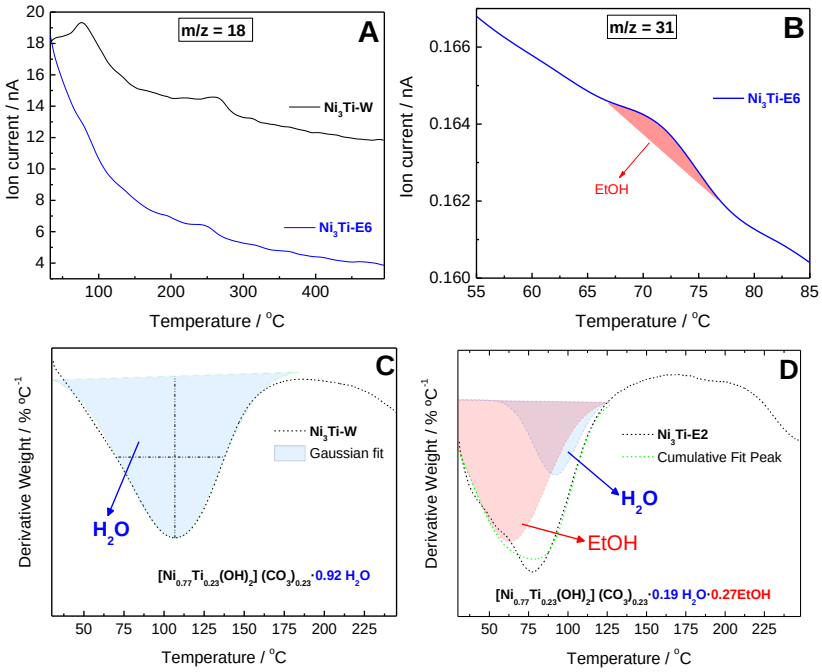

Fig. S6. (A, B) Mass spectra of m/z 18 and 31 for Ni_3Ti-W and Ni_3Ti-E6 samples. (C, D) Deconvolution examples of P1 peaks in the derivative TG curves.

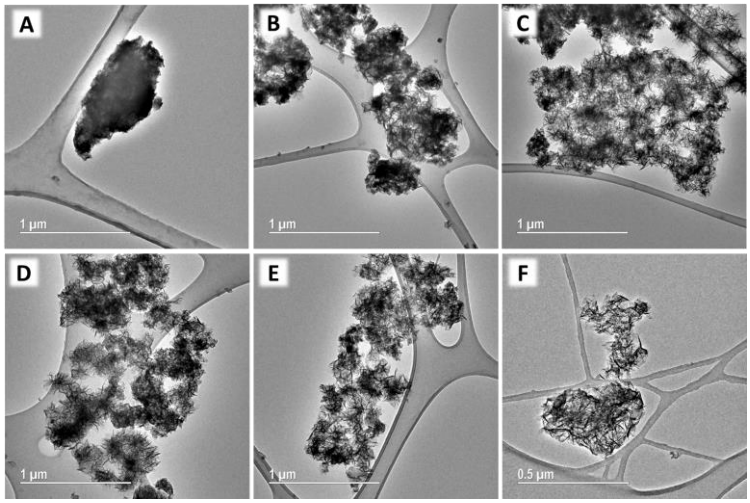

Fig. S7. TEM images of: (A) Ni_3Ti-W; Ni_3Ti with different redispersion times in the AMOST: (B) 2 h, (C) 4 h, (D) 6 h, (E) 24 h and (F) 48 h.

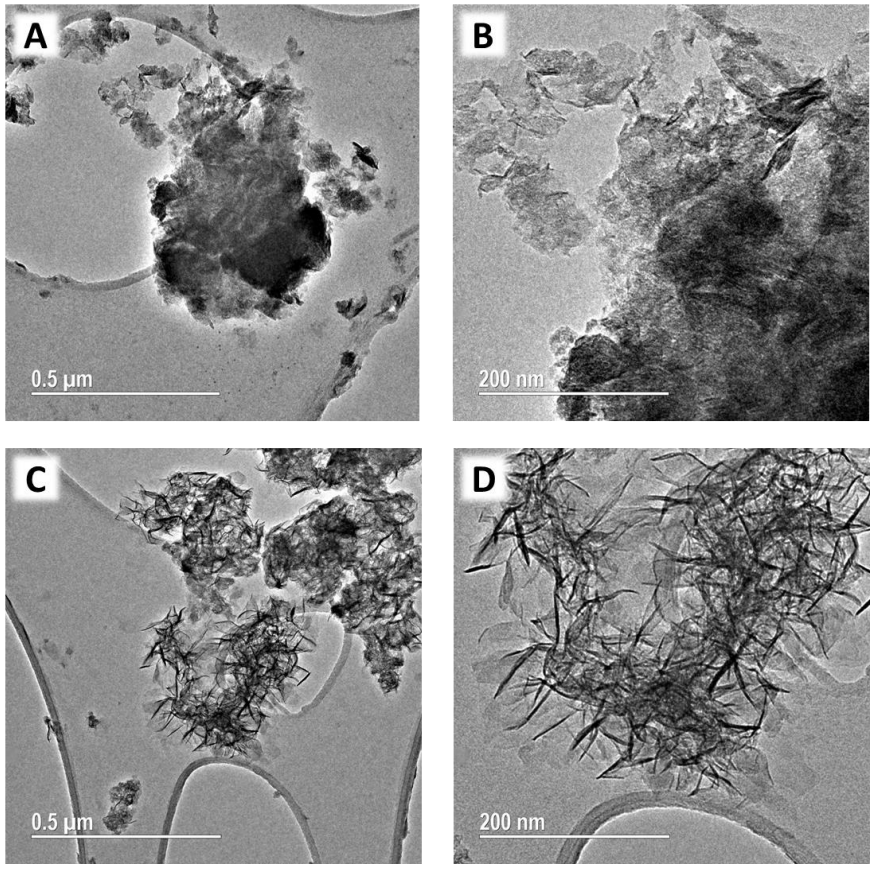

Fig. S8. TEM images of: (A, B) Ni_2Ti-W; (C, D) Ni_2Ti-E4.

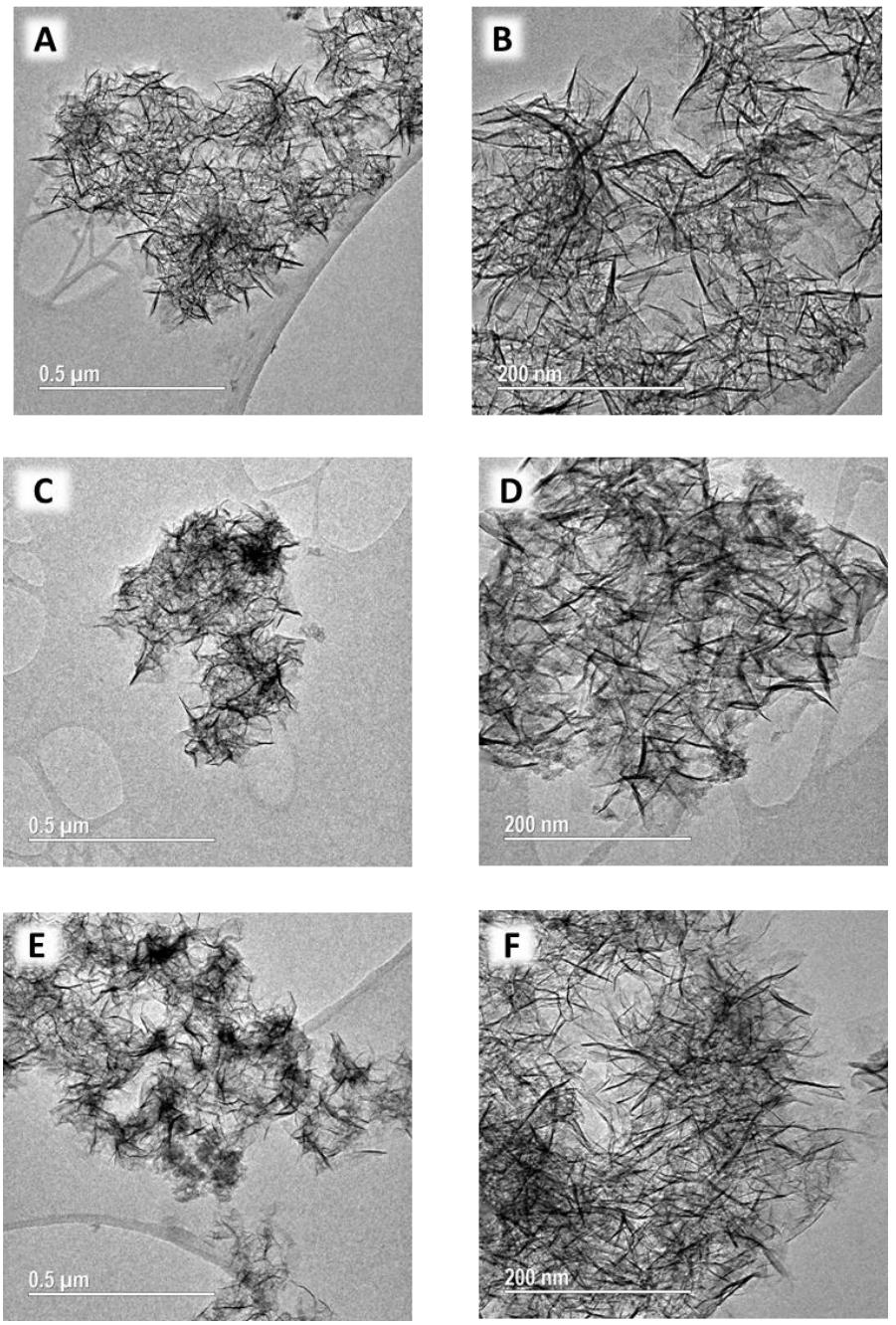

Fig. S9. TEM images of Ni_3Ti-E6 with different temperatures in the AMOST: (A, B) room temperature; (C, D) 0 °C; (E, F) 50 °C.

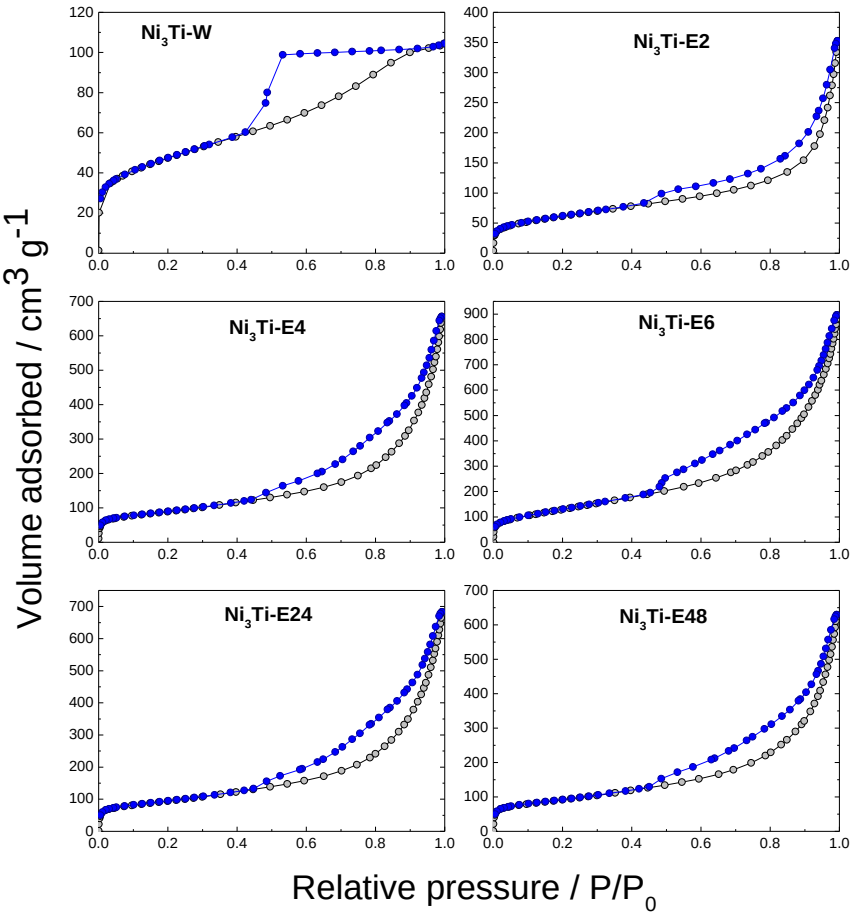

Fig. S10. N_2 adsorption-desorption isotherms of Ni_3Ti samples with different redispersion times in the AMOST.

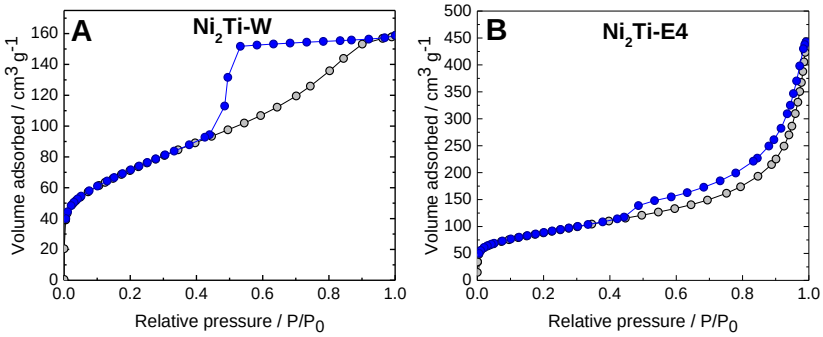

Fig. S11. N_2 adsorption-desorption isotherms of Ni_2Ti samples.

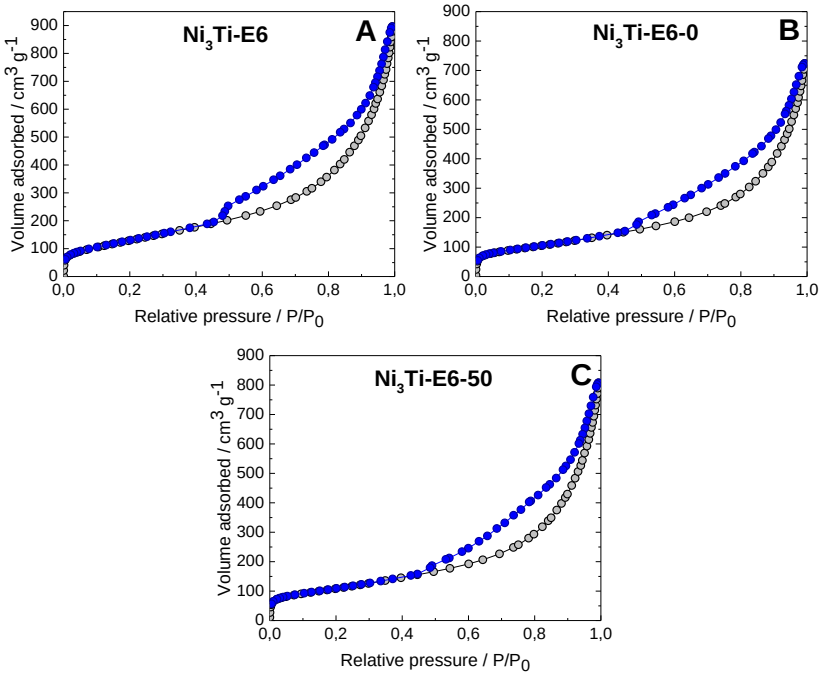

Fig. S12. N_2 adsorption-desorption isotherms of Ni_3Ti-E6 with different temperatures in the AMOST.

Table S2. BET surface area and pore volume calculated for the prepared samples.

Sample	BET surface area[a] / $m^2 g^{-1}$	Pore volume[b] / $cm^3 g^{-1}$
Ni_2Ti-W	254	0.16
Ni_2Ti-E4	311	0.68
Ni_3Ti-W	164	0.16
Ni_3Ti-E2	221	0.52
Ni_3Ti-E4	314	1.01
Ni_3Ti-E6	492	1.37
Ni_3Ti-E6-0	382	1.11
Ni_3Ti-E6-50	395	1.24
Ni_3Ti-E24	327	1.05
Ni_3Ti-E48	324	0.96

[a] Brunauer-Emmett-Teller calculation; [b] total pore volume at $P/P_0 = 0.99$.

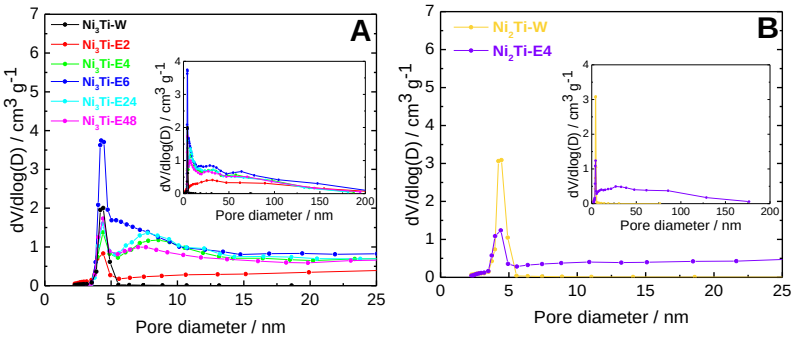

Fig. S13. Pore size distribution for: (A) Ni_3Ti samples with different redispersion times in the AMOST; (B) Ni_2Ti samples.

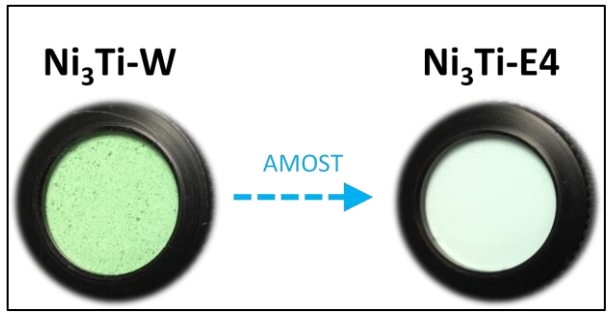

Fig. S14. Photographs of the LDH powders showing the colour change when AMOST is applied to Ni_3Ti samples.

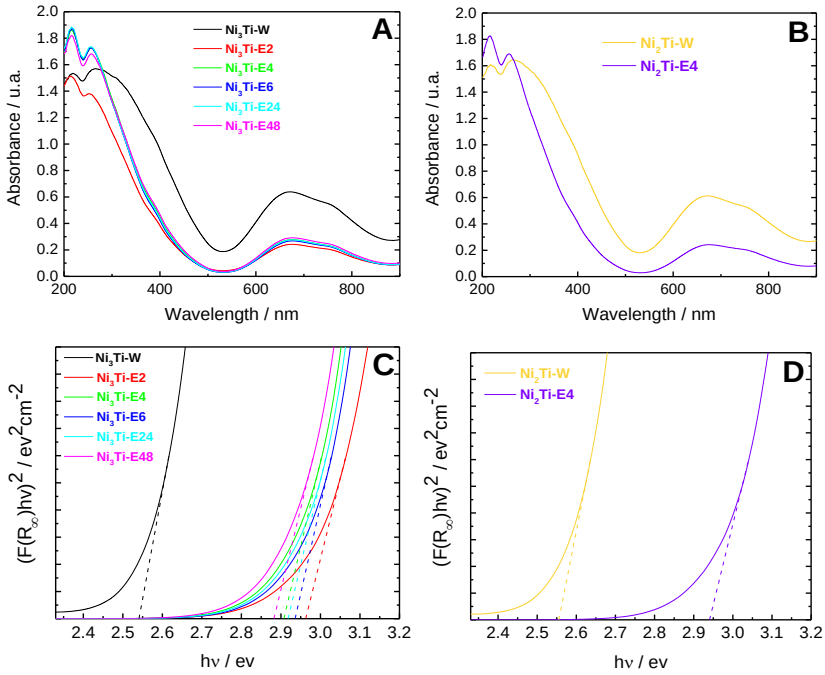

Fig. S15. (A, B) UV–Vis absorption spectra and (C, D) Kubelka-Munk transformed function plots for Ni_3Ti samples with different redispersion times in the AMOST and Ni_2Ti samples.

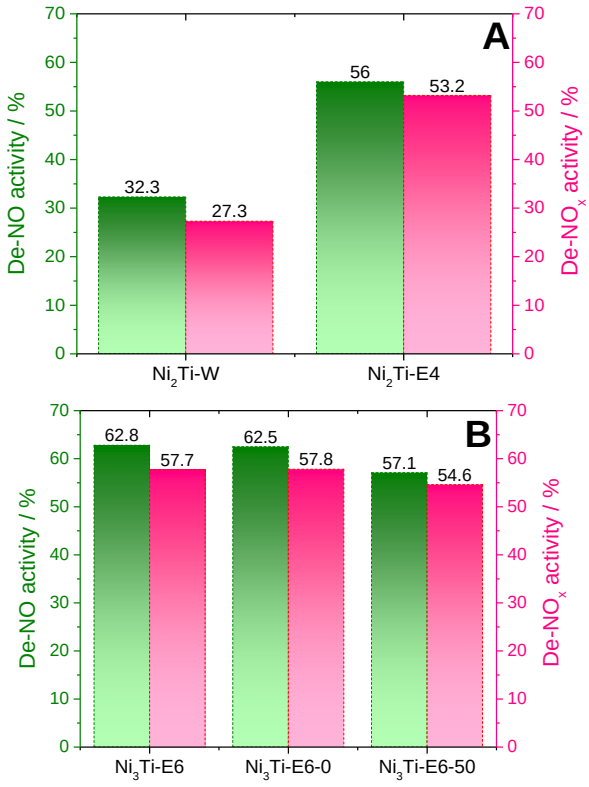

Fig. S16. Calculated De-NO and De-NOx indexes for (A) Ni_2Ti samples and (B) Ni_3Ti-E6 samples with different temperatures in the AMOST.

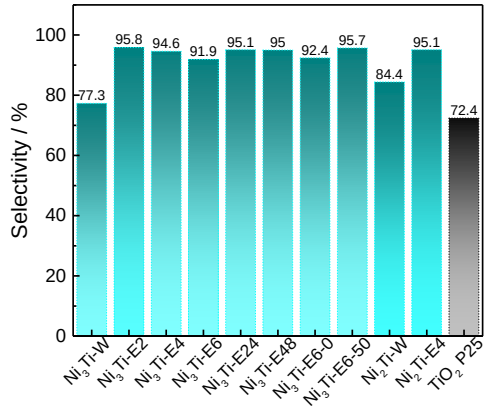

Fig. S17. Selectivity indexes for the De-NO_x reaction corresponding to the studied samples.

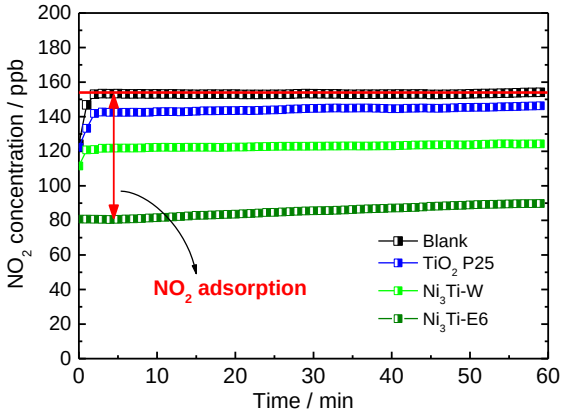

Fig. S18. NO_2 adsorption tests for Ni_3Ti-W, Ni_3Ti-E6 and TiO_2 P25 samples.

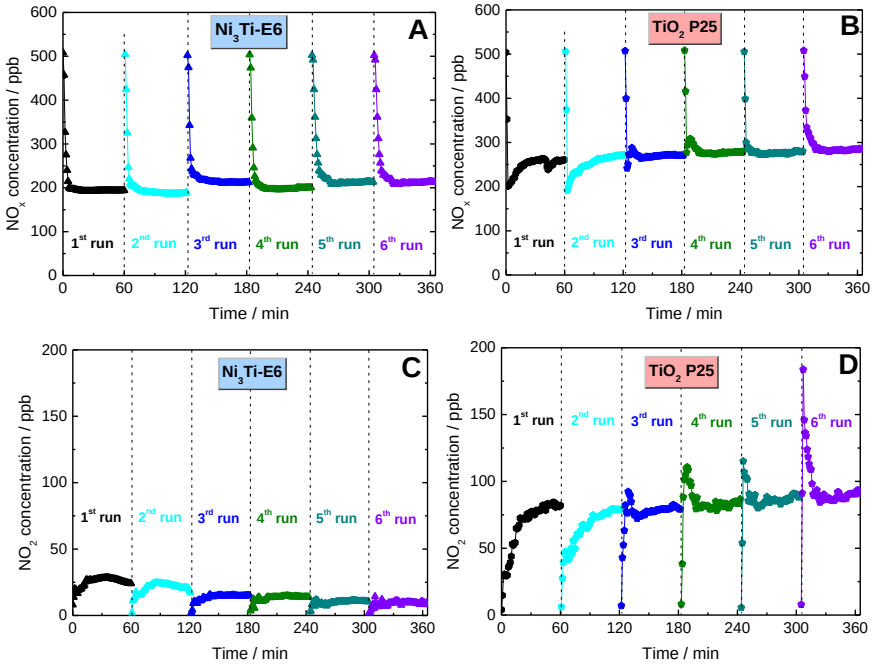

Fig. S19. (A, C) NO_x and (B, D) NO_2 concentration profiles obtained after consecutive photocatalytic assays for Ni_3Ti-E6 and TiO_2 P25 samples.

Table S3. NO removed efficiency and Selectivity values observed for different $DeNO_x$ photocatalysts.

Photocatalyst	NO removed / %	Selectivity / %
BiOCl-OV [18]	70	99
g-C_3N_4/BiOCl/$WO_{2.92}$ [19]	69	93
GQDs/Bi_2WO_6 [20]	73	81
MoS_2/g-C_3N_4 [21]	52	--
ZnO@SiO_2 [22]	70	90
Mg_3AlNi-LDH [23]	42	89
$Zn_4Al_{0.45}Fe_{0.55}$-LDH [24]	59	92
TiO_2-δ/CNTs/N-CQDs [25]	60	98
Mesocrystalline TiO_2 [26]	59	89
TiO_2-P25 (this work)	57	72
Ni_3Ti-AMO-LDH (this work)	63	94

References

[1] B. Post, X-ray diffraction procedures for polycrystalline and amorphous materials. Harold P. Klug and Leroy E. Alexander; New York, 1974, pp. 960., John Wiley & Sons, Ltd, 1975. doi:10.1002/xrs.1300040415.

[2] Bruker, User's Manual, Diffrac.EVA V. 3.1, 2013.

[3] Physical Electronics, Operator's guide, 5800 MultiTechnique ESCA, 2000. https://www.phi.com/assets/documents/manuals/5800-operators-guide.pdf.

[4] X. Shu, W. Zhang, J. He, F. Gao, Y. Zhu, Formation of Ni-Ti-layered double hydroxides using homogeneous precipitation method, Solid

State Sci. 8 (2006) 634–639. doi:10.1016/j.solidstatesciences.2006.02.029.

[5] W.H. Zhang, X.D. Guo, J. He, Z.Y. Qian, Preparation of Ni(II)/Ti(IV) layered double hydroxide at high supersaturation, J. Eur. Ceram. Soc. 28 (2008) 1623–1629. doi:10.1016/j.jeurceramsoc.2007.11.016.

[6] X. Shu, Z. An, L. Wang, J. He, Metal oxide-sensitized TiO_2 and $TiO_{2-x}N_x$ with efficient charge transport conduits, Chem. Commun. (2009) 5901–5903. doi:10.1039/b909301j.

[7] Y. Lee, J.H. Choi, H.J. Jeon, K.M. Choi, J.W. Lee, J.K. Kang, Titanium-embedded layered double hydroxides as highly efficient water oxidation photocatalysts under visible light, Energy Environ. Sci. 4 (2011) 914–920. doi:10.1039/c0ee00285b.

[8] Z. Gao, B. Du, G. Zhang, Y. Gao, Z. Li, H. Zhang, X. Duan, Adsorption of pentachlorophenol from aqueous solution on dodecylbenzenesulfonate modified nickel-titanium layered double hydroxide nanocomposites, Ind. Eng. Chem. Res. 50 (2011) 5334–5345. doi:10.1021/ie101766e.

[9] Y. Zhao, P. Chen, B. Zhang, D.S. Su, S. Zhang, L. Tian, J. Lu, Z. Li, X. Cao, B. Wang, M. Wei, D.G. Evans, X. Duan, Highly dispersed TiO_6 units in a layered double hydroxide for water splitting, Chem. - A Eur. J. 18 (2012) 11949–11958. doi:10.1002/chem.201201065.

[10] B. Li, Y. Zhao, S. Zhang, W. Gao, M. Wei, Visible-Light-Responsive Photocatalysts toward Water Oxidation Based on NiTi-Layered Double Hydroxide/Reduced Graphene Oxide Composite Materials, ACS Appl. Mater. Interfaces. 5 (2013) 10233–10239. doi:10.1021/am402995d.

[11] L.F. Hu, W. Gao, J. He, H. Liu, B. Li, X.M. Zhang, NiTi-layered double hydroxide intercalated with β-CD and CM-β-CD: Interaction between the interlayer guests and the laminates, J. Mol. Struct. 1041 (2013) 151–155. doi:10.1016/j.molstruc.2013.03.019.

[12] Y. Zhao, B. Li, Q. Wang, W. Gao, C.J. Wang, M. Wei, D.G. Evans, X. Duan, D. O'Hare, NiTi-Layered double hydroxides nanosheets as efficient photocatalysts for oxygen evolution from water using visible light, Chem. Sci. 5 (2014) 951–958. doi:10.1039/C3SC52546E.

[13] Y. Zhao, Q. Wang, T. Bian, H. Yu, H. Fan, C. Zhou, L.Z. Wu, C.H. Tung, D. O'Hare, T. Zhang, Ni^{3+} doped monolayer layered double hydroxide nanosheets as efficient electrodes for supercapacitors, Nanoscale. 7 (2015) 7168–7173. doi:10.1039/c5nr01320h.

[14] Y.N. Liu, J.T. Feng, Y.F. He, J.H. Sun, D.Q. Li, Partial hydrogenation of acetylene over a NiTi-layered double hydroxide supported PdAg catalyst, Catal. Sci. Technol. 5 (2015) 1231–1240. doi:10.1039/c4cy01160k.

[15] R. Abazari, A.R. Mahjoub, S. Sanati, Z. Rezvani, Z. Hou, H. Dai, Ni–Ti Layered Double Hydroxide@Graphitic Carbon Nitride Nanosheet: A Novel Nanocomposite with High and Ultrafast Sonophotocatalytic Performance for Degradation of Antibiotics, Inorg. Chem. 58 (2019) 1834–1849. doi:10.1021/acs.inorgchem.8b02575.

[16] G. Lin, L. Zhu, T. Duan, L. Zhang, B. Liu, J. Lei, Efficient capture of iodine by a polysulfide-inserted inorganic NiTi-layered double hydroxides, Chem. Eng. J. 378 (2019) 122181. doi:10.1016/j.cej.2019.122181.

[17] X. Wu, R. Wang, Y. Du, X. Li, H. Meng, X. Xie, NO_x removal by selective catalytic reduction with ammonia over hydrotalcite-derived NiTi mixed oxide, New J. Chem. 43 (2019) 2640–2648. doi:10.1039/c8nj05280h.

[18] H. Li, H. Shang, X. Cao, Z. Yang, Z. Ai, L. Zhang, Oxygen Vacancies Mediated Complete Visible Light NO Oxidation via Side-On Bridging Superoxide Radicals, Environ. Sci. Technol. 52 (2018) 8659–8665. doi:10.1021/acs.est.8b01849.

[19] M. Wang, G. Tan, S. Feng, M. Dang, Y. Wang, B. Zhang, H. Ren, L. Lv, A. Xia, W. Liu, Y. Liu, Defects and internal electric fields synergistically optimized g-C_3N_{4-x}/BiOCl/$WO_{2.92}$ heterojunction for photocatalytic NO deep oxidation, J. Hazard. Mater. 408 (2021) 124897. doi:10.1016/J.JHAZMAT.2020.124897.

[20] Y. Cui, T. Wang, J. Liu, L. Hu, Q. Nie, Z. Tan, H. Yu, Enhanced solar photocatalytic degradation of nitric oxide using graphene quantum dots/bismuth tungstate composite catalysts, Chem. Eng. J. 420 (2021) 129595. doi:10.1016/j.cej.2021.129595.

[21] M.Q. Wen, T. Xiong, Z.G. Zang, W. Wei, X.S. Tang, F. Dong, Synthesis of MoS_2/g-C_3N_4 nanocomposites with enhanced visible-light photocatalytic activity for the removal of nitric oxide (NO),

Opt. Express. 24 (2016) 10205. doi:10.1364/OE.24.010205.

[22] A. Pastor, J. Balbuena, M. Cruz-Yusta, I. Pavlovic, L. Sánchez, ZnO on rice husk: A sustainable photocatalyst for urban air purification, Chem. Eng. J. 368 (2019) 659–667. doi:10.1016/j.cej.2019.03.012.

[23] X. Lv, J. Zhang, X. Dong, J. Pan, W. Zhang, W. Wang, G. Jiang, F. Dong, Layered double hydroxide nanosheets as efficient photocatalysts for NO removal: Band structure engineering and surface hydroxyl ions activation, Appl. Catal. B Environ. 277 (2020) 119200. doi:10.1016/j.apcatb.2020.119200.

[24] A. Pastor, F. Rodriguez-Rivas, G. de Miguel, M. Cruz-Yusta, F. Martin, I. Pavlovic, L. Sánchez, Effects of Fe^{3+} substitution on Zn-Al layered double hydroxides for enhanced NO photochemical abatement, Chem. Eng. J. 387 (2020) 124110. doi:10.1016/j.cej.2020.124110.

[25] Y. Ou, G. Zhu, F. Rao, J. Gao, J. Chang, X. Xie, W. Zhang, Y. Huang, M. Hojamberdiev, Coral-Shaped $TiO_{2-\delta}$ Decorated with Carbon Quantum Dots and Carbon Nanotubes for NO Removal, ACS Appl. Nano Mater. 4 (2021) 7330–7342. doi:10.1021/acsanm.1c01306.

[26] J. Balbuena, J.M. Calatayud, M. Cruz-Yusta, P. Pardo, F. Martín, J. Alarcón, L. Sánchez, Mesocrystalline anatase nanoparticles synthesized using a simple hydrothermal approach with enhanced light harvesting for gas-phase reaction, Dalt. Trans. 47 (2018) 6590–6597. doi:10.1039/C8DT00721G.

Capítulo 4.

Resumen

Actualmente, en la Sociedad surgen dos preocupaciones principales respecto a la conservación del patrimonio y hábitat urbano: i) prevenir el deterioro de este para que siga ejerciendo la funcionalidad para el que fue creado y ii) asegurar su correcta y sana habitabilidad.

En este contexto, la presente tesis doctoral se ha centrado en dos puntos interrelacionados:

i) Por un lado, se han investigado aditivos con propiedades biocidas mejoradas que puedan ser usados en morteros de restauración. Dichos aditivos otorgan al mortero con propiedades biocidas para hacer frente a la contaminación microbiana que afecta a los materiales de construcción utilizados en el patrimonio urbano. Los aditivos fueron preparados mediante el proceso de adsorción de Carbendazima (CBZ), un fungicida que presenta adecuadas propiedades (bajo coste, baja solubilidad en agua) para la aplicación deseada. Se desarrollaron estudios de adsorción de CBZ sobre compuestos tipo arcilla disponibles comercialmente (arcilla natural sin modificar: SWy-1; organo-arcillas: Cloisite® 10 y Cloisite® 20) con el objeto de disminuir la lixiviación de CBZ y mejorar su dispersión en la matriz de la arcilla. Las arcillas fueron seleccionadas como soportes inorgánicos debido a su bajo coste y buenas propiedades de adsorción. Los complejos de adsorción de arcilla-CBZ preparados fueron caracterizados y se evaluaron sus propiedades antimicrobianas frente a dos tipos de microorganismos que se encuentran comúnmente en los materiales pétreos (alga y hongo). Para la preparación del mortero antimicrobiano (en base cal) se utilizó el complejo de adsorción Cloisite® 20-CBZ, que mostró la mejor actividad antimicrobiana. Las propiedades antimicrobianas del mortero con este aditivo también fueron evaluadas y comparadas con el mortero con CBZ como aditivo. Además, las muestras de mortero se sometieron a una

prueba de lixiviación estandarizada para comprobar la eficacia de la actividad antimicrobiana a largo plazo. Después de las pruebas de lixiviación, la acción antimicrobiana del mortero que contenía CBZ fue menor en comparación con Cloisite® 20-CBZ, mostrando un buen efecto antimicrobiano y una lixiviación de CBZ un 20% menor.

Esta investigación se aborda en el **apartado 3.1**., correspondiente a la publicación "***Carbendazim-clay complexes for its potential use as antimicrobial additives in mortars".***

ii) Por otro lado, se ha investigado una serie de compuestos inorgánicos con propiedades fotocatalíticas mejoradas, para su aplicación en la eliminación de los gases NO_x (NO_x = NO + NO_2) presentes en el hábitat urbano (proceso De-NO_x). Estos gases provocan graves efectos negativos en la salud, medio ambiente y en los materiales del patrimonio urbano. Los fotocatalizadores son capaces de oxidar esos gases nocivos a compuestos benignos (nitratos y nitritos) empleando luz solar, oxígeno y agua atmosféricos, a temperatura ambiente. La síntesis de los compuestos estudiados ha implicado métodos muy sencillos, sin el empleo de compuestos tóxicos o de coste elevado, y con los que se obtienen relativamente grandes cantidades de muestra. Estos factores han sido considerados importantes teniendo en mente un potencial escalado industrial, sin provocar gran impacto ambiental.

En un primer trabajo, se prepararon fotocatalizadores de ZnO nano-particulado dispersados sobre una matriz inorgánica de SiO_2 amorfo (ZnO@SiO_2). La síntesis se realizó empleando un residuo agroindustrial muy abundante, la cáscara del arroz, e implicó un método simple de mezclado de precursores y una calcinación convencional a una temperatura relativamente baja (600 ^oC). Las nanopartículas de ZnO (70–180 nm)

crecieron agregadas en esferas y bien dispersas, cubriendo el esqueleto de SiO_2 procedente de la cáscara del arroz. En comparación con el ZnO y el TiO_2-P25, las muestras de ZnO@SiO_2 presentaron valores altos de eliminación De-NO_x (70 %) y una excelente selectividad (> 90 %), esta última relacionada con la sensibilidad del óxido de zinc hacia la adsorción del gas NO_2.

Esta investigación se aborda en el **apartado 3.2**., correspondiente a la publicación "***ZnO on rice husk: A sustainable photocatalyst for urban air purification".***

En el siguiente trabajo, se prepararon fotocatalizadores De-NO_x basados en los Hidróxidos Dobles Laminares (LDHs), mediante el método de coprecipitación, a temperatura ambiente. Los cationes metálicos que constituyeron las láminas de hidróxido fueron Zn^{2+}, Al^{3+} y Fe^{3+}, mientras que el anión interlaminar fue el carbonato. Se estudió el efecto de la sustitución progresiva de Al^{3+} por Fe^{3+} en la red estructural del LDH. La mayor presencia de iones Fe^{3+} originó cambios en la estructura, morfología y propiedades ópticas de los LDH. Los fotocatalizadores preparados presentaron mayores valores de área de superficie específica y una mejorada absorción de luz visible. Los resultados mostraron altos valores De-NO_x (56 %) y de selectividad (93 %) para las muestras que contenían hierro, debido a una disminución de la recombinación e^-/h^+, la mayor generación de especies reactivas de oxígeno, así como la mayor capacidad de adsorción de NO_2.

Esta investigación se aborda en el **apartado 3.3**., correspondiente a la publicación "***Effects of Fe^{3+} substitution on Zn-Al layered double hydroxides for enhanced NO photochemical abatement".***

Finalmente, se sintetizaron LDHs utilizando el método AMOST (Aqueous Miscible Organic Solvent Treatment), para su aplicación como fotocatalizadores De-NO_x. El método de síntesis fue llevado a cabo mediante una sencilla coprecipitación, a temperatura ambiente, con un posterior tratamiento (AMOST) consistente en un lavado y re-dispersión en etanol para obtener las denominadas AMO-LDHs. Los cationes metálicos constituyentes de las láminas fueron Ni^{2+} y Ti^{4+}, mientras que el anión interlaminar fue el carbonato. Se estudiaron varios factores que podrían afectar al procedimiento AMOST: el tiempo de redispersión en etanol, la temperatura durante la re-dispersión y la relación entre los cationes metálicos que forman las láminas. Los compuestos AMO-LDH sintetizados alcanzaron valores de área de superficie específica de hasta 492 $m^2\,g^{-1}$ y volúmenes de poros de 1,37 $cm^3\,g^{-1}$, valores sin precedentes para estos compuestos. El rendimiento De-NO_x de los compuestos AMO-LDH fue elevado, superando al LDH convencional y al TiO_2 P25 en un 40 % y en un 17% respectivamente. Se observó que el elevado valor de área de superficie específica y el volumen de poro jugaban un papel significativo en la adsorción de los intermedios NO_2 y N_2O_4. Además, el carácter 2D de las AMO-LDH contribuyó a una mejora en la producción de especies reactivas de oxígeno y a una reducción de la recombinación de los portadores de carga.

Parte de esta investigación se ha realizado en el grupo del Prof. Dermot O'Hare, University of Oxford, y se aborda en el **apartado 3.4**., correspondiente a la publicación "***Aqueous miscible organic solvent treated NiTi layered double hydroxide De-NO_x photocatalysts".***

Chapter 4.

Summary

Today, society has two main issues with regard to the conservation of heritage buildings and urban habitat: i) preventing its deterioration so that it continues to exercise the functionality for which it was created and ii) ensuring its correct and healthy habitability.

In this context, this doctoral thesis has focused on two interrelated points:

i) Firstly, additives with improved biocidal properties that can be used in restoration mortars have been investigated. These additives give mortar biocidal properties to deal with microbial contamination that affects construction materials used in urban heritage. The additives were prepared through the adsorption process of Carbendazim (CBZ), a fungicide that has adequate properties (low cost and low solubility in water) for the desired application. CBZ adsorption studies were carried out on commercially available clay-type compounds (unmodified natural clay: SWy-1; organo-clays: Cloisite® 10 and Cloisite® 20) in order to decrease the leaching of CBZ and improve its dispersion in the clay matrix. Clays were selected as inorganic supports due to their low cost and good adsorption properties. The clay-CBZ adsorption complexes prepared were characterized and their antimicrobial properties were evaluated against two types of microorganisms commonly found in stone materials (algae and fungus). For the preparation of the antimicrobial mortar (based on lime), the adsorption complex Cloisite® 20-CBZ was used, which showed the best antimicrobial activity. The antimicrobial properties of the mortar with this additive were also evaluated and compared with the mortar with unmodified CBZ as an additive. In addition, the mortar samples were subjected to a standardized leaching test to verify the efficacy of long-term antimicrobial activity. After the leaching tests, the antimicrobial action of

the mortar containing CBZ was lower compared to Cloisite® 20-CBZ, showing good antimicrobial effect and 20% lower CBZ leaching.

This research is addressed in **section 3.1.**, Corresponding to the publication ***"Carbendazim-clay complexes for its potential use as antimicrobial additives in mortars".***

ii) Secondly, a series of inorganic compounds with superior photocatalytic properties have been investigated, for their application in the elimination of NO_x gases (NO_x = NO + NO_2) existing in the urban atmosphere (De-NO_x process). These gases cause serious negative effects on health, the environment and the materials of urban heritage sites. Photocatalysts are capable of oxidizing these harmful gases to benign compounds (nitrates and nitrites) at room temperature using sunlight, atmospheric oxygen and water. The synthesis of the compounds studied involves the use of very simple methods, without the use of toxic or expensive compounds, and with which relatively large amounts of sample are obtained. These factors have been considered important with respect to a potential industrial scale production, without causing great environmental impact.

In initial work, nano-particulate ZnO photocatalysts dispersed on an inorganic matrix of amorphous SiO_2 (ZnO@SiO_2) were prepared. The synthesis was carried out using a very abundant agro-industrial residue, rice husk, and involved a simple method of mixing the precursors and a conventional calcination at a relatively low temperature (600 °C). The ZnO nanoparticles (70-180 nm) grew aggregated in spheres and were well dispersed, covering the SiO_2 skeleton derived from the rice husk. Compared to ZnO and TiO_2-P25, the ZnO@SiO_2 samples presented high De-NO_x

removal values (70%) and excellent selectivity (> 90%), the latter related to the sensitivity of zinc oxide towards NO_2 gas adsorption.

This research is addressed in **section 3.2.**, corresponding to the publication ***"ZnO on rice husk: A sustainable photocatalyst for urban air purification"***.

In the subsequent work, De-NO_x photocatalysts based on Layered Double Hydroxides (LDHs) were prepared, by the coprecipitation method, at room temperature. The metal cations that constituted the hydroxide sheets were Zn^{2+}, Al^{3+} and Fe^{3+}, while the interlaminar anion was carbonate. The effect of the progressive substitution of Al^{3+} by Fe^{3+} in the structural network of LDH was studied. The greater presence of Fe^{3+} ions caused changes in the structure, morphology and optical properties of LDH. The photocatalysts prepared showed higher values of specific surface area and an improved absorption of visible light. The results showed high De-NO_x (56%) and selectivity (93%) values for the samples containing iron, due to a decrease in electro/hole recombination, the increased generation of reactive oxygen species, as well as a higher NO_2 adsorption capacity.

This research is addressed in **section 3.3.**, corresponding to the publication ***"Effects of Fe^{3+} substitution on Zn-Al layered double hydroxides for enhanced NO photochemical abatement"***.

Finally, LDHs were synthesized using the AMOST (Aqueous Miscible Organic Solvent Treatment) method, for their application as De-NO_x photocatalysts. The synthesis method was carried out by means of a simple co-precipitation, at room temperature, with a subsequent (AMOST) treatment consisting of washing and re-dispersion in ethanol to obtain the so-called AMO-LDHs. The constituent metal cations of the hydroxide sheets

were Ni^{2+} and Ti^{4+}, while the interlaminar anion was carbonate. Several factors that could affect the AMOST procedure were studied: the redispersion time in ethanol, the temperature during re-dispersion and the ratio between the metal cations that form the sheets. The synthesized AMO-LDH compounds reached specific surface area values of up to 492 m^2 g^{-1} and pore volumes of 1.37 cm^3 g^{-1}, unprecedented values for these compounds. The De-NO_x yield of AMO-LDH compounds was high, surpassing conventional LDH and TiO_2 P25 by 40% and 17% respectively. The high specific surface area and pore volume were found to play a significant role in the adsorption of intermediates NO_2 and N_2O_4. Furthermore, the 2D character of AMO-LDH contributed to an improvement in the production of reactive oxygen species and a reduction in charge carrier recombination.

Part of this research has been carried out in the group of Prof. Dermot O'Hare, University of Oxford, and is addressed in **section 3.4.**, Corresponding to the publication ***"Aqueous miscible organic solvent treated NiTi layered double hydroxide De-NO_x photocatalysts".***

Capítulo 5.

Conclusiones

La investigación realizada en la presente Tesis Doctoral ha dado lugar a las conclusiones generales que se exponen a continuación:

I) En relación con la preparación de nuevos aditivos con propiedades biocidas para evitar la contaminación microbiana de los materiales pétreos del Patrimonio urbano:

- Mediante un simple método de adsorción a temperatura ambiente, el biocida Carbendazima (CBZ) ha sido soportado en varias arcillas comerciales.
- Modificando los parámetros de la adsorción, se han preparado complejos de adsorción arcilla-CBZ con gran cantidad de CBZ adsorbida.
- Uno de los complejos de adsorción, basado en una organo-arcilla, mostró adecuadas propiedades fungicidas y alguicidas.
- Los morteros en base cal aditivados con dicho complejo de adsorción lograron una lixiviación del biocida reducida y unas propiedades biocidas mejoradas.

II) Respecto a la preparación de nuevos fotocatalizadores funcionales para la descontaminación de la atmósfera del hábitat urbano:

- Mediante un procedimiento sencillo de calcinación, la ceniza de la cáscara del arroz se ha empleado de forma exitosa como soporte inorgánico y como agente de plantilla para la preparación nanopartículas de ZnO.
- Dichos fotocatalizadores han mostrado un rendimiento De-NO_x y selectividad excelentes, siendo reutilizables por periodos de irradiación prolongados. El rendimiento observado fue mayor que el del TiO_2 P25 comercial.

- Una serie de Hidróxidos Dobles Laminares (ZnAlFe-LDH), con un contenido variado de Fe^{3+} en la red estructural, han sido sintetizados mediante una sencilla coprecipitación, a temperatura ambiente, y aplicados como fotocatalizadores De-NO_x.
- El LDH con mayor contenido de Fe^{3+} resultó en unas propiedades De-NO_x mejoradas en condiciones de iluminación solar simulada y bajo irradiación del espectro Visible, gracias al área superficial específica mejorada y a la creación de nuevas vías de desactivación de las fotocargas.
- Por primera vez, un AMO-LDH (AMO-NiTi-LDH) ha sido aplicado como fotocatalizador, específicamente en la eliminación de gases NO_x.
- Los excepcionales valores de área de superficie específica y volumen de poro de los AMO-LDH, así como su carácter 2D (nanoláminas), resultaron en una excelente mejora del rendimiento fotocatalítico De-NO_x, superando los valores del TiO_2 P25 comercial.

Las conclusiones que se han expuesto ponen de manifiesto la potencial aplicación de estos nuevos compuestos para prevenir la contaminación microbiana de los materiales del Patrimonio urbano, así como la reducción de la contaminación de NO_x en el hábitat urbano.

Chapter 5.

Conclusions

The research carried out in this Doctoral Thesis has led to the general conclusions that are set out below:

I) In respect of the preparation of new additives with biocidal properties to avoid microbial contamination of the stone materials of the urban heritage:

- The Carbendazim biocide (CBZ) has been supported on commercial clays (modified with different amounts of quaternary ammonium salts) by simple adsorption processes taking place at room temperature.
- The modification of the parameters that govern the adsorption process have made it possible to prepare organoclay-CBZ complexes with a high amount of adsorbed CBZ.
- One of the organoclay-CBZ adsorption complexes prepared showed adequate fungicidal and algicidal properties.
- Lime-based mortars that include the organoclay-CBZ complex in their formulation, show reduced leaching of the biocidal additive as well as improved biocidal properties.

II) Regarding the preparation of new functional photocatalysts for the depollution of the atmosphere in the urban habitat:

- The possibility of preparing inorganic compounds that act as new alternative photocatalysts to TiO_2 in the depollution of NO_x gases present in the urban atmosphere has been demonstrated.
- By means of a simple calcination procedure, the rice husk ash has been used successfully as an inorganic support and as a template agent for

the preparation of ZnO nanoparticles, obtaining the ZnO@SiO_2 photocatalyst.

- The ZnO@SiO_2 photocatalyst has shown excellent De-NO_x performance and selectivities, being active and reusable in prolonged irradiation periods. The observed De-NO_x performance was higher than that of commercial TiO_2 P25.
- A series of Layered Double Hydroxides based on the ZnAlFe-CO_3 formula, with a variable content of Fe^{3+} in the lattice, have been synthesized by a simple co-precipitation method at room temperature, and studied as De-NO_x photocatalysts.
- The LDH photocatalyst with a higher Fe^{3+} content develops improved De-NO_x properties, when irradiated with both simulated solar lighting (UV-Vis) as well as with Visible light. This occurs thanks to the increase in the improved specific surface area and the modification of the electronic structure, allowing new ways of deactivating the photocharges generated.
- For the first time, a two-dimensional LDH obtained by the AMOST process (AMO-NiTi-LDH) has been studied as a photocatalyst in the NO_x gas removal process.
- It has been shown that the modification of the parameters that govern the AMOST procedure allow the preparation of LDHs compounds with a very high level of particle dispersion and two-dimensional (2D) nano-sheets of very restricted thickness.
- The exceptional values of specific surface area and pore volume of AMO-LDH, as well as its 2D character (nanosheets), turned out to be key parameters for the development of an excellent De-NO_x photocatalytic performance, exceeding the values of commercial TiO_2

P25, as well as other advanced De-NO_x photocatalysts previously described.

The conclusions that have been presented show the potential application of these new compounds to prevent microbial contamination of urban heritage materials, as well as the reduction of NO_x pollution in urban habitat.

Anexo I.

Producción científica

I.I. Publicaciones en Revistas Científicas

a) Publicaciones derivadas de la Tesis Doctoral. Indicios de calidad:

1) Título: ZnO on rice husk: A sustainable photocatalyst for urban air purification. *Clic aquí para ver sección 3.2.*

Autores: Adrián Pastor, José Balbuena, Manuel Cruz, Ivana Pavlovic, Luis Sánchez

Revista: Chemical Engineering Journal

Código ISSN: 1385-8947

Año: 2019; **volumen:** 368; **páginas:** 659-667

Editorial: Elsevier

DOI: 10.1016/j.cej.2019.03.012

Clic aquí para visitar la versión web del artículo

Base de datos en la que está indexada: Journal Citation Reports

Índice de impacto de la revista: 10.652

Lugar que ocupa/Nº revistas del área temática:

Engineering, Environmental: 2/53 Q1

Engineering, Chemical: 4/143 Q1

---

2) Título: Carbendazim-clay complexes for its potential use as antimicrobial additives in mortars. *Clic aquí para ver sección 3.1.*

Autores: Adrián Pastor, Beatriz Gámiz, Manuel Cruz, Luis Sánchez, Ivana Pavlovic

Revista: Building and Environment

Código ISSN: 0360-1323

Año: 2020; **volumen:** 183; **número de referencia:** 107214

Editorial: Elsevier

DOI: 10.1016/j.buildenv.2020.107214

Clic aquí para visitar la versión web del artículo

Base de datos en la que está indexada: Journal Citation Reports

Índice de impacto de la revista: 6.456

Lugar que ocupa/Nº revistas del área temática:

Engineering, Civil: 6/136 Q1

Construction & Building Technology: 6/66 Q1

Engineering, Environmental: 12/54 Q1

---

3) Título: Effects of Fe^{3+} substitution on Zn-Al layered double hydroxides for enhanced NO photochemical abatement. *Clic aquí para ver sección 3.3.*

Autores: Adrián Pastor, Fredy Rodríguez, Gustavo de Miguel, Manuel Cruz, Francisco Martin, Ivana Pavlovic, Luis Sánchez

Revista: Chemical Engineering Journal

Código ISSN: 1385-8947

Año: 2020; **volumen:** 387; **número de referencia:** 124110

Editorial: Elsevier

DOI: 10.1016/j.cej.2020.124110

Clic aquí para visitar la versión web del artículo

Base de datos en la que está indexada: Journal Citation Reports

Índice de impacto de la revista: 13.273

Lugar que ocupa/Nº revistas del área temática:

Engineering, Environmental: 2/54 Q1

Engineering, Chemical: 4/143 Q1

---

4) Título: Aqueous miscible organic solvent treated NiTi layered double hydroxide De-NO_x photocatalysts. *Clic aquí para ver sección 3.4.*

Autores: Adrián Pastor, Chunping Chen, Gustavo de Miguel, Francisco Martin, Manuel Cruz-Yusta, Jean-Charles Buffet, Dermot O'Hare, Ivana Pavlovic, Luis Sánchez

Revista: Chemical Engineering Journal

Código ISSN: 1385-8947

Año: 2021; **volumen:** 429; **número de referencia:** 132361

Editorial: Elsevier

DOI: 10.1016/j.cej.2021.132361

Clic aquí para visitar la versión web del artículo

Base de datos en la que está indexada: Journal Citation Reports

Índice de impacto de la revista (*2020): 13.273

Lugar que ocupa/Nº revistas del área temática (*2020):

Engineering, Environmental: 2/54 Q1

Engineering, Chemical: 4/143 Q1

---

b) Otras publicaciones derivadas de la formación investigadora:

5) Título: Insight into the role of copper in the promoted photocatalytic removal of NO using $Zn_{2-x}Cu_xCr\text{-}CO_3$ layered double hydroxide

Autores: Javier Fragoso, María de los Ángeles Oliva, Luis Camacho, Manuel Cruz, Gustavo de Miguel, Francisco Martin, Ivana Pavlovic, Adrián Pastor, Luis Sánchez

Revista: Chemosphere

Código ISSN: 0045-6535

Año: 2021; **volumen:** 275; **número de referencia:** 130030

Editorial: Elsevier

DOI: 10.1016/j.chemosphere.2021.130030

Clic aquí para visitar la versión web del artículo

Base de datos en la que está indexada: Journal Citation Reports

Índice de impacto de la revista (*2020): 7.086

Lugar que ocupa/Nº revistas del área temática (*2020):
Environmental Sciences: 30/274 Q1

---

6) Título: Development of multifunctional coatings for protecting stones and lime mortars of the architectural heritage

Autores: Alessandro Speziale, Jesús Fidel González, Burcu Taşcı, Adrián Pastor, Luis Sánchez, Claudio Fernández, Tamara Oroz, Cristina Salazar, Iñigo Navarro, José María Fernández, José Ignacio Alvarez

Revista: International Journal of Architectural Heritage

Código ISSN: 1558-3066

Año: 2020; **volumen:** 14 (7); **páginas:** 1008-1029.

Editorial: Taylor & Francis

DOI: 10.1080/15583058.2020.1728594

Clic aquí para visitar la versión web del artículo

Base de datos en la que está indexada: Journal Citation Reports

Índice de impacto de la revista: 2.580

Lugar que ocupa/Nº revistas del área temática:

Engineering, Civil: 63/136 Q2

Construction & Building Technology: 35/66 Q3

---

7) Título: Cr^{3+} substituted Zn-Al layered double hydroxides as UV–Vis light photocatalysts for NO gas removal from the urban environment

Autores: Fredy Rodríguez, Adrián Pastor, Gustavo de Miguel, Manuel Cruz, Ivana Pavlovic, Luis Sánchez

Revista: Science of the Total Environment

Código ISSN: 0048-9697

Año: 2020; **volumen:** 706; **número de referencia:** 136009

Editorial: Elsevier

DOI: 10.1016/j.scitotenv.2019.136009

Clic aquí para visitar la versión web del artículo

Base de datos en la que está indexada: Journal Citation Reports

Índice de impacto de la revista: 7.963

Lugar que ocupa/Nº revistas del área temática:

Environmental Sciences: 25/274 Q1

---

8) Título: Hematite porous architectures as enhanced air purification photocatalyst

Autores: José Balbuena, Manuel Cruz, Ana Cuevas, Francisco Martín, Adrián Pastor, Rocío Romero, Luis Sánchez

Revista: Journal of Alloys and Compounds

Código ISSN: 0925-8388

Año: 2019; **volumen:** 797; **páginas:** 166-173

Editorial: Elsevier

DOI: 10.1016/j.jallcom.2019.05.113

Clic aquí para visitar la versión web del artículo

Base de datos en la que está indexada: Journal Citation Reports

Índice de impacto de la revista: 4.650

Lugar que ocupa/Nº revistas del área temática:

Metallurgy & Metallurgical Engineering: 8/79 Q1

Materials Science, Multidisciplinary: 81/314 Q2

Chemistry, Physical: 51/159 Q2

---

9) Título: Zn-Al layered double hydroxides as efficient photocatalysts for NOx abatement

Autores: Fredy Rodríguez, Adrián Pastor, Cristobalina Barriga, Manuel Cruz, Luis Sánchez, Ivana Pavlovic

Revista: Chemical Engineering Journal

Código ISSN: 1385-8947

Año: 2018; **volumen:** 346; **páginas:** 151-158

Editorial: Elsevier

DOI: 10.1016/j.cej.2018.04.022

Clic aquí para visitar la versión web del artículo

Base de datos en la que está indexada: Journal Citation Reports

Índice de impacto de la revista: 8.355

Lugar que ocupa/Nº revistas del área temática:

Engineering, Environmental: 2/52 Q1

Engineering, Chemical: 6/138 Q1

---

10) Título: α-Fe_2O_3/SiO_2 composites for the enhanced photocatalytic NO oxidation

Autores: José Balbuena, Manuel Cruz, Adrián Pastor, Luis Sánchez

Revista: Journal of Alloys and Compounds

Código ISSN: 0925-8388

Año: 2018; **volumen:** 735; **páginas:** 1553-1561

Editorial: Elsevier

DOI: 10.1016/j.jallcom.2017.11.259

Clic aquí para visitar la versión del web artículo

Base de datos en la que está indexada: Journal Citation Reports

Índice de impacto de la revista: 4.175

Lugar que ocupa/Nº revistas del área temática:

Metallurgy & Metallurgical Engineering: 6/76 Q1

Materials Science, Multidisciplinary: 65/293 Q1

Chemistry, Physical: 47/148 Q2

I.II. Comunicaciones en Congresos Científicos

1) Congreso: 2nd International Conference on sustainable, environmental friendly construction materials

Tipo de participación: Comunicación oral, ponente

Título: *Study of inorganic encapsulation systems to prepare biocidal additive for heritage mortars*

Autores: Adrián Pastor, Manuel Cruz, Ivana Pavlovic, Luis Sánchez

Fecha de participación: 01/09/2021

Ámbito: internacional

Entidad organizadora: West Pomeranian University of Technology in Szczecin

Lugar de celebración: Szczecin (Polonia) / online

---

2) Congreso: 2nd International Conference on sustainable, environmental friendly construction materials

Tipo de participación: Comunicación con póster

Título: *Layered Double Hydroxides as photocatalytic additive for De-NO_x building materials*

Autores: Javier Fragoso, Adrián Pastor, Jean-Charles Buffet, Chunping Chen, Manuel Cruz, Dermot O'Hare, Ivana Pavlovic, Luis Sánchez

Fecha de participación: 01/09/2021

Ámbito: internacional

Entidad organizadora: West Pomeranian University of Technology in Szczecin

Lugar de celebración: Szczecin (Polonia) / online

---

3) Congreso: Nanotech France 2021 International Conference and Exhibition

Tipo de participación: Comunicación oral, ponente

Título: *Doped ZnAl-CO_3 layered double hydroxides as $DeNO_x$ photocatalysts with enhanced visible light harvesting*

Autores: Adrián Pastor, Fredy Rodríguez, Gustavo de Miguel, Manuel Cruz, Francisco Martin, Ivana Pavlovic, Luis Sánchez

Fecha de participación: 25/06/2021

Ámbito: internacional

Entidad organizadora: SECTOR Conferences and Exhibitions

Lugar de celebración: París (Francia) / online

---

4) Congreso: IX Congreso científico de investigadores en formación de la Universidad de Córdoba

Tipo de participación: Comunicación oral, ponente

Título: *Profundización en la metodología AMOST aplicada a Hidróxidos Dobles Laminares con propiedades fotocatalíticas*

Autores: Adrián Pastor, Ivana Pavlovic, Luis Sánchez

Fecha de participación: 03/05/2021

Ámbito: nacional

Entidad organizadora: Escuela de Doctorado de la Universidad de Córdoba y Escuela Internacional de Doctorado en Agroalimentación

Lugar de celebración: online

---

5) Congreso: I Congreso Anual de Estudiantes de Doctorado

Tipo de participación: Comunicación oral, ponente

Título: *Influencia del método de preparación de Hidróxidos Dobles Laminares bidimensionales en la actividad fotocatalítica De-NOx*

Autores: Adrián Pastor, Chunping Chen, Manuel Cruz, Jean-Charles Buffet, Dermot O'Hare, Ivana Pavlovic, Luis Sánchez

Fecha de participación: 02/02/2021

Ámbito: nacional

Entidad organizadora: Universidad Miguel Hernández

Lugar de celebración: online

---

6) Congreso: 1st International Electronic Conference on Catalysis Sciences

Tipo de participación: Comunicación con póster

Título: *AMO-NiTi Layered Double Hydroxide Nanosheets for Photocatalytic Removal of NO_x Pollutant*

Autores: Adrián Pastor, Chunping Chen, Manuel Cruz, Jean-Charles Buffet, Dermot O'Hare, Ivana Pavlovic, Luis Sánchez

Fecha de celebración: del 10/11/2020 al 30/11/2020

Ámbito: internacional

Entidad organizadora: Catalysts, MDPI

Lugar de celebración: online

---

7) Congreso: VIII Congreso científico de investigadores en formación de la Universidad de Córdoba

Tipo de participación: Comunicación con póster, ponente

Título: *Estudio de la degradación fotocatalítica de gases NO_x mediante Hidróxidos Dobles Laminares pseudo-2D preparados con el método AMOST*

Autores: Adrián Pastor, Chunping Chen, Jean-Charles Buffet, Dermot O'Hare, Ivana Pavlovic, Luis Sánchez

Fecha de participación: 19/02/2020

Ámbito: nacional

Entidad organizadora: Escuela de Doctorado de la Universidad de Córdoba y Escuela Internacional de Doctorado en Agroalimentación

Lugar de celebración: Córdoba (España)

---

8) Congreso: Reunión Bienal de la Sociedad Española de Catálisis (SECAT'19)

Tipo de participación: Comunicación con póster

Título: *Oxidación fotocatalítica de gases NO_x mediante Hidróxidos Dobles Laminares*

Autores: Javier Fragoso, Adrián Pastor, Fredy Rodríguez, Manuel Cruz, Ivana Pavlovic, Luis Sánchez

Fecha de participación: 26/06/2019

Ámbito: nacional

Entidad organizadora: Sociedad Española de Catálisis

Lugar de celebración: Córdoba (España)

---

9) Congreso: XXXVII Reunión Bienal de la Real Sociedad Española de Química

Tipo de participación: Comunicación oral flash, ponente

Título: *Photocatalytic removal of NO_x gases by Zinc-Aluminum-Iron Layered Double Hydroxides*

Autores: Fredy Rodríguez, Manuel Cruz, Ivana Pavlovic, Luis Sánchez, Adrián Pastor

Fecha de participación: 27/05/2019

Ámbito: nacional

Entidad organizadora: Real Sociedad Española de Química

Lugar de celebración: San Sebastián (España)

---

10) Congreso: International Conference on Green Construction

Tipo de participación: Comunicación oral, ponente

Título: *Improving the biocidal properties of the restoration mortars by carbendazim adsorbed on inorganic substrates*

Autores: Adrián Pastor, Manuel Cruz, Ivana Pavlovic, Luis Sánchez

Fecha de participación: 09/04/2019

Ámbito: internacional

Entidad organizadora: Universidad de Córdoba y VIPSKILLS

Lugar de celebración: Córdoba (España)

---

11) Congreso: Sétima edición del Encuentro sobre Nanociencia y Nanotecnología (NANOUCO VII)

Tipo de participación: Comunicación oral, ponente

Título: *Removal of NOx gases by using photocatalytic Zn-Al layered double hydroxides*

Autores: Adrián Pastor, Fredy Rodríguez, Manuel Cruz, Ivana Pavlovic, Luis Sánchez

Fecha de participación: 22/01/2019

Ámbito: nacional

Entidad organizadora: Instituto Universitario de Nanoquímica de la Universidad de Córdoba (IUNAN)

Lugar de celebración: Córdoba (España)

---

12) Congreso: QIES 2018 (18ª Reunión del Grupo Especializado de Química Inorgánica)

Tipo de participación: Comunicación con póster

Título: *Eliminación de gases NO_x por medio de hidróxidos dobles laminares*

Autores: Adrián Pastor, Fredy Rodríguez, Cristobalina Barriga, Manuel Cruz, Ivana Pavlovic, Luis Sánchez

Fecha de participación: 17/06/2018

Ámbito: nacional

Entidad organizadora: Grupo Especializado de Química Inorgánica y Grupo Especializado de Química de Estado Sólido (Real Sociedad Española de Química)

Lugar de celebración: La Laguna, Tenerife (España)

---

13) Congreso: QIES 2018 (18ª Reunión del Grupo Especializado de Química Inorgánica)

Tipo de participación: Comunicación oral flash, ponente

Título: *Eliminación de gases NO_x por medio de hidróxidos dobles laminares*

Autores: Adrián Pastor, Fredy Rodríguez, Cristobalina Barriga, Manuel Cruz, Ivana Pavlovic, Luis Sánchez

Fecha de participación: 17/06/2018

Ámbito: nacional

Entidad organizadora: Grupo Especializado de Química Inorgánica y Grupo Especializado de Química de Estado Sólido (Real Sociedad Española de Química)

Lugar de celebración: La Laguna, Tenerife (España)

---

14) Congreso: Rehabend 2018

Tipo de participación: Comunicación oral

Título: *Desarrollo de materiales funcionales basados en técnicas de encapsulación para la obtención de productos en base morteros de cal con actividad biocida para la rehabilitación de patrimonio histórico*

Autores: José Manuel Lloris, Mariló Sánchez, Pilar Calero, Adrián Pastor, Manuel Cruz, Ivana Pavlovic, Luis Sánchez, Isabel Mármol; Josefina Pedrajas

Fecha de participación: 15/05/2018

Ámbito: internacional

Entidad organizadora: Grupo de Tecnología de la Edificación de la Universidad de Cantabria

Lugar de celebración: Cáceres (España)

---

15) Congreso: IV Reunión de Jóvenes Investigadores en Coloides e Interfases

Tipo de participación: Comunicación oral, ponente

Título: *Rice husk ash as support of photocatalytic zinc oxide nanoparticles for NO_x gases removal*

Autores: Adrián Pastor, Manuel Cruz, Luis Sánchez

Fecha de participación: 08/02/2018

Ámbito: nacional

Entidad organizadora: Grupo Especializado de Coloides e Interfases de la Real Sociedad Española de Química y Real Sociedad Española de Física

Lugar de celebración: Córdoba (España)

---

16) Congreso: VI Congreso científico de investigadores en formación de la Universidad de Córdoba

Tipo de participación: Comunicación oral, ponente

Título: *Organo-arcillas como soporte de Carbendazima en la preparación de morteros de restauración*

Autores: Adrián Pastor, Manuel Cruz, Ivana Pavlovic, Luis Sánchez

Fecha de participación: 25/01/2018

Ámbito: nacional

Entidad organizadora: Escuela de Doctorado de la Universidad de Córdoba y Escuela Internacional de Doctorado en Agroalimentación

Lugar de celebración: Córdoba (España)

---

17) Congreso: Sexta edición del Encuentro sobre Nanociencia y Nanotecnología (NANOUCO VI)

Tipo de participación: Comunicación con póster

Título: *Preparación de nuevos materiales laminares con propiedades fungicidas*

Autores: Adrián Pastor, Manuel Cruz, Ivana Pavlovic, Luis Sánchez

Fecha de participación: 25/01/2017

Ámbito: nacional

Entidad organizadora: Instituto Universitario de Investigación en Química Fina y Nanoquímica (IUIQFN)

Lugar de celebración: Córdoba (España)

---

18) Congreso: Sexta edición del Encuentro sobre Nanociencia y Nanotecnología (NANOUCO VI)

Tipo de participación: Comunicación oral, ponente

Título: *Utilización de cascarilla de arroz en la preparación de nuevos nanomateriales fotocatalizadores con efecto De-NO_x*

Autores: Adrián Pastor, Manuel Cruz, Luis Sánchez

Fecha de participación: 25/01/2017

Ámbito: nacional

Entidad organizadora: Instituto Universitario de Investigación en Química Fina y Nanoquímica (IUIQFN)

Lugar de celebración: Córdoba (España)

I.III. Contribuciones a capítulos de libros

1) Título del capítulo: *Organo-arcillas como soporte de Carbendazima en la preparación de morteros de restauración*

Autores del capítulo: Adrián Pastor, Manuel Cruz, Ivana Pavlovic, Luis Sánchez

Título del libro: Creando redes doctorales. Vol. VI: "La generación del conocimiento"

Páginas: 321-324

Editorial: UCOPress. Ediciones Universidad de Córdoba. Campus Universitario de Rabanales. Carretera Nacional IV, km. 396. 14071, Córdoba, España

Año de publicación: 2018

ISBN: 978-84-9927-239-9

---

2) Título del capítulo: *Estudio de la degradación fotocatalítica de gases NO_x mediante Hidróxidos Dobles Laminares pseudo-2D preparados con el método AMOST*

Autores del capítulo: Adrián Pastor, Chunping Chen, Jean-Charles Buffet, Dermot O'Hare, Ivana Pavlovic, Luis Sánchez

Título del libro: Creando redes doctorales Vol. VIII. "La investigación del futuro"

Páginas: 415-418

Editorial: UCOPress. Ediciones Universidad de Córdoba. Campus Universitario de Rabanales. Carretera Nacional IV, km. 396. 14071, Córdoba, España

Año de publicación: 2020

ISBN: 978-84-9927-508-6

---

3) Título del capítulo: *Improving the biocidal properties of the restoration mortars by carbendazim adsorbed on inorganic substrates*

Autores del capítulo: Adrián Pastor, Manuel Cruz, Ivana Pavlovic, Luis Sánchez

Título del libro: New trends in Green Construction

Páginas: 147-148

Editorial: UCOPress. Ediciones Universidad de Córdoba. Campus Universitario de Rabanales. Carretera Nacional IV, km. 396. 14071, Córdoba, España

Año de publicación: 2020

ISBN: 978-84-9927-554-3

---

4) Título del capítulo: *Profundización en la metodología AMOST aplicada a Hidróxidos Dobles Laminares con propiedades fotocatalíticas*

Autores del capítulo: Adrián Pastor, Ivana Pavlovic, Luis Sánchez

Título del libro: IX Congreso Científico de Investigadores en Formación de la Universidad de Córdoba: Nuevos desafíos, nuevas oportunidades

Páginas: 213-217

Editorial: UCOPress. Ediciones Universidad de Córdoba. Campus Universitario de Rabanales. Carretera Nacional IV, km. 396. 14071, Córdoba, España

Año de publicación: 2021

ISBN: 978-84-9927-640-3

---

5) Título del capítulo: *Study of inorganic encapsulation systems to prepare biocidal additive for heritage mortars*

Autores del capítulo: Adrián Pastor, Manuel Cruz-Yusta, Ivana Pavlovic, Luis Sánchez

Título del libro: 2nd International Conference on Sustainable, Environmental Friendly Construction Materials (ICSEFCM 2021)

Páginas: 85-90

Editorial: West Pomeranian University of Technology, Szczecin Publishing House al. Piastów 48, 70-311 Szczecin, Polonia

Año de publicación: 2021

ISBN: 978-83-7663-324-4

---

6) Título del capítulo: *Layered Double Hydroxides as photocatalytic additive for De-NO_x building materials*

Autores del capítulo: Javier Fragoso, Adrián Pastor, Jean-Charles Buffet, Chunping Chen, Manuel Cruz-Yusta, Dermot O'Hare, Ivana Pavlovic, Luis Sánchez

Título del libro: 2nd International Conference on Sustainable, Environmental Friendly Construction Materials (ICSEFCM 2021)

Páginas: 129-130

Editorial: West Pomeranian University of Technology, Szczecin Publishing House al. Piastów 48, 70-311 Szczecin, Polonia

Año de publicación: 2021

ISBN: 978-83-7663-324-4

I.IV. Estancias de investigación

1) Institución de destino: Chemistry Research Laboratory, Department of Chemistry, University of Oxford. Oxford, Reino Unido

Fecha: desde 30/06/2021 hasta 30/12/2021

Objetivo de la estancia: Síntesis y caracterización de hidróxidos dobles laminares con actividad fotocatalítica De-NO_x mejorada en el espectro visible.

Supervisor: Prof. Dermot O'Hare

---

2) Institución de destino: Chemistry Research Laboratory, Department of Chemistry, University of Oxford. Oxford, Reino Unido

Fecha: desde 06/06/2019 hasta 06/09/2019

Objetivo de la estancia: Síntesis y caracterización de hidróxidos dobles laminares (AMO/AIM-LDH) para su empleo como fotocatalizadores De-NO_x.

Supervisores: Prof. Dermot O'Hare y Dr. Jean-Charles Buffet

I.IV. Participación en proyectos de investigación

1) Título del proyecto: Nuevos materiales funcionales basados en técnicas de encapsulación para la prevención, conservación y restauración del patrimonio histórico. MATERPAT (RTC-2015-3916-6).

Investigador responsable: Luis Sánchez Granados (Universidad de Córdoba, España)

Entidad financiadora: Ministerio de Economía y Competitividad. Plan Estatal 2013-2016 de Investigación Científica y Técnica y de Innovación.

Contratado a Proyecto: desde 15-01-2016 al 22-10-2017

---

2) Título del proyecto: Sistemas 2D y 3D basados en hidrotalcitas como fotocatalizadores para la eliminación de gases NO_x

Investigador responsable: Luis Sánchez Granados (Universidad de Córdoba, España)

Entidad financiadora: Ministerio de Economía, Industria y Competitividad; Convocatoria 2017.

Duración del proyecto: del 01-01-2018 al 30-09-2021

I.V. Premios

1) Premio de investigación "Jacobo Cárdenas Torres": mejor artículo científico de un investigador menor de 35 años en el área de Ciencias

Título del artículo: *ZnO on rice husk: A sustainable photocatalyst for urban air purification*

DOI: 10.1016/j.cej.2019.03.012

Entidad organizadora: Universidad de Córdoba (España)

Fecha: 19/01/2021

---

2) Premio de investigación nacional: mejor artículo científico publicado por un joven investigador

Título del artículo: *ZnO on rice husk: A sustainable photocatalyst for urban air purification*

DOI: 10.1016/j.cej.2019.03.012

Entidad organizadora: Grupo Especializado de Química del Estado Sólido (Real Sociedad Española de Química)

Fecha: 10/01/2020

---

3) Premio de fotografía científica: obra más votada por el público en el Concurso de Fotografía e Ilustración Científica ConCiencYarte 2020

Título de la obra: *Cocodrilos por el Nilo*

Entidad organizadora: Asociación de Científicos Españoles en Suecia (ACES)

Fecha: 03/12/2020

---

4) Primer premio: certamen de monólogos científicos "Cuéntame tu tesis"

Información del certamen: Certamen incluido en el proyecto FCT-17-11833 V Plan Anual de Divulgación y Cultura Científica y de la Innovación de la Universidad de Córdoba y de la Fundación Española para la Ciencia y la Tecnología

Entidad organizadora: Universidad de Córdoba (España)

Fecha: 28/09/2018

Anexo II.

Difusión científica

II.I. Participación en eventos de difusión científica

1) X Jornadas de Introducción al Laboratorio Experimental de Química.

Lugar de celebración: Universidad de Córdoba, España

Fecha de participación: 31/01/2017

Entidad organizadora: Facultad de Ciencias (Universidad de Córdoba)

Tipo de participación: Preparación y desarrollo experimental de sesiones prácticas de laboratorio para el alumnado de institutos

---

2) Paseo por la Ciencia 2017.

Lugar de celebración: Córdoba, España

Fecha de participación: 22/04/2017

Entidad organizadora: Asociación del Profesorado de Córdoba por la Cultura Científica; Ayuntamiento de Córdoba

Tipo de participación: preparación y exposición de sesiones experimentales de química inorgánica a los viandantes

---

3) XI Jornadas de Introducción al Laboratorio Experimental de Química.

Lugar de celebración: Universidad de Córdoba, España

Fecha de participación: 23/01/2018

Entidad organizadora: Facultad de Ciencias (Universidad de Córdoba)

Tipo de participación: Preparación y desarrollo experimental de sesiones prácticas de laboratorio para el alumnado de institutos

---

4) Paseo por la Ciencia 2018.

Lugar de celebración: Córdoba, España

Fecha de participación: 14/04/2018

Entidad organizadora: Asociación del Profesorado de Córdoba por la Cultura Científica; Ayuntamiento de Córdoba

Tipo de participación: preparación y exposición de sesiones experimentales de química inorgánica a los viandantes

---

5) Certamen "Cuéntame tu tesis"

Lugar de celebración: Córdoba, España

Fecha de participación: 28/09/2018

Información del certamen: Certamen incluido en el proyecto FCT-17-11833 V Plan Anual de Divulgación y Cultura Científica y de la Innovación de la Universidad de Córdoba y de la Fundación Española para la Ciencia y la Tecnología

Tipo de participación: realización y exposición pública de un monólogo humorístico sobre el tema de la presente Tesis Doctoral

---

6) XII Jornadas de Introducción al Laboratorio Experimental de Química.

Lugar de celebración: Universidad de Córdoba, España

Fecha de participación: 01/02/2019

Entidad organizadora: Facultad de Ciencias (Universidad de Córdoba)

Tipo de participación: Preparación y desarrollo experimental de sesiones prácticas de laboratorio para el alumnado de institutos

---

7) Paseo por la Ciencia 2019.

Lugar de celebración: Córdoba, España

Fecha de participación: 06/04/2019

Entidad organizadora: Asociación del Profesorado de Córdoba por la Cultura Científica; Ayuntamiento de Córdoba

Tipo de participación: preparación y exposición de sesiones experimentales de química inorgánica a los viandantes

---

8) XIII Jornadas de Introducción al Laboratorio Experimental de Química.

Lugar de celebración: Universidad de Córdoba, España

Fecha de participación: 20/01/2020

Entidad organizadora: Facultad de Ciencias (Universidad de Córdoba)

Tipo de participación: Preparación y desarrollo experimental de sesiones prácticas de laboratorio para el alumnado de institutos

---

9) Entrevista en televisión local.

Canal de televisión: PTV Córdoba. Córdoba, España

Programa: Córdoba TeVé

Fecha de la entrevista: 12/02/2020

Tipo de participación: Divulgación de la investigación relacionada con el uso de la cáscara de arroz en la descontaminación

Enlace web a la entrevista:

https://www.youtube.com/watch?v=0szkBCIov1s&t=1s

II.II. Referencias de los diferentes actos de difusión realizados en prensa y otros medios de comunicación

1) Referencia: noticia

Titular: *Las claves de la Noche Europea de los Investigadores de Córdoba*


ABCcórdoba CÓRDOBA

Buscar

Sevilla Semana Santa Andalucía Opinión Economía España Internacional Deportes Cultura Gurmé Gente EXCLUSIVO PREMIUM Estilo Más

SEVILLA ANDALUCÍA Almería Cádiz Córdoba Granada Huelva Jaén Málaga Sevilla Oposiciones Compras El Tiempo

CIENCIA

Las claves de la Noche Europea de los Investigadores de Córdoba

● Más de doscientos científicos participan en la sexta edición de la velada divulgativa que se celebra este viernes

Medio de comunicación en donde se ha publicado la noticia: Diario ABC Córdoba

Fecha de publicación: 28/09/2017

Enlace web:

https://sevilla.abc.es/andalucia/cordoba/sevi-claves-noche-europea-investigadores-cordoba-201709272206_noticia.html

2) Referencia: noticia

Titular: *La Noche Europea de los Investigadores registra un éxito total de participantes en 75 actividades repartidas por toda la ciudad*

Medio de comunicación en donde se ha publicado la noticia: Unidad de Cultura Científica y de la Innovación, Universidad de Córdoba

Fecha de publicación: 28/09/2018

Enlace web:

https://www.universidaddecordoba.eu/servicios/comunicacion/actualidad/noticias/item/130494-la-noche-europea-de-los-investigadores-registra-

un-%C3%A9xito-total-de-participantes-en-75-actividades-repartidas-por-toda-la-ciudad

---

3) Referencia: noticia

Titular: *Nuevos materiales permitirán respirar un aire más limpio en la ciudad*

Medio de comunicación en donde se ha publicado la noticia: Unidad de Cultura Científica y de la Innovación, Universidad de Córdoba

Fecha de publicación: 14/12/2018

Enlace web:

https://www.uco.es/servicios/comunicacion/component/k2/item/131994-nuevos-materiales-permitir%C3%A1n-respirar-un-aire-m%C3%A1s-limpio-en-la-ciudad

---

4) Referencia: noticia en radio

Medio de comunicación en donde se ha publicado la noticia: Onda Cero

Programa: Julia en la onda

Fecha de publicación: 20/03/2019

Enlace web (minuto 42:30):

https://dpvclip.antena3.com/mp_audios4//2019/03/29/8CB246BE-B544-4ED3-A519-5B5CE46AA76A/8CB246BE-B544-4ED3-A519-5B5CE46AA76A.mp3

---

5) Referencia: noticia

Titular: *Investigadores de la UCO idean un sistema para descontaminar el aire en grandes ciudades mediante cáscaras de arroz*

Medio de comunicación en donde se ha publicado la noticia: Europa Press

Fecha de publicación: 28/03/2019

Enlace web:

https://www.europapress.es/andalucia/noticia-investigadores-uco-idean-sistema-descontaminar-aire-grandes-ciudades-cascaras-arroz-20190328104713.html

La noticia fue difundida por otros medios de comunicación, entre ellos:

Titular: *Las cáscaras de arroz, una solución para acabar con la contaminación del aire en las grandes ciudades*

Medio de comunicación: 20 minutos

https://www.20minutos.es/noticia/3599698/0/cascaras-arroz-descontaminacion-aire-ciudades/

---

6) Referencia: entrevista en radio al IP, Luis Sánchez Granados

Titular: *Investigadores españoles logran descontaminar el aire de las ciudades*

Medio de comunicación en donde se ha publicado la noticia: Radio Nacional Española

Programa: Marca España

Fecha de publicación: 05/04/2019

Enlace web:

https://www.rtve.es/play/audios/marca-espana/marca-espana-investigadores-espanoles-logran-descontaminar-aire-ciudades-05-04-19/5120987/?media=rne

---

7) Referencia: noticia

Titular: *Cáscara del arroz contra la contaminación*

Medio de comunicación en donde se ha publicado la noticia: National Geographic

Fecha de publicación: 14/02/2020

Enlace web:

https://www.nationalgeographic.com.es/ciencia/cascara-arroz-contra-contaminacion_15189

La noticia fue difundida por otros medios de comunicación, entre ellos:

Titular: *¿Cáscara de arroz para combatir la contaminación?: Sí*

Medio de comunicación: Radio Duna (Santiago, Chile)

https://www.duna.cl/noticias/2020/02/21/uso-de-la-cascara-de-arroz-para-combatir-la-contaminacion/

---

8) Referencia: noticia

Titular: *Crean un material resistente a microorganismos para restaurar el patrimonio*

Medio de comunicación en donde se ha publicado la noticia: Cadena Cope

Fecha de publicación: 03/11/2020

Enlace web:

https://www.cope.es/actualidad/cultura/noticias/crean-material-resistente-microorganismos-para-restaurar-patrimonio-20201103_977919

La noticia fue difundida por otros medios de comunicación, entre ellos:

Titular: *Crean un material más resistente a los microorganismos para restaurar el patrimonio histórico*

Medio de comunicación: Europa Press

https://www.europapress.es/andalucia/noticia-crean-material-mas-resistente-microorganismos-restaurar-patrimonio-historico-20201103101426.html

Titular: *Crean un material más resistente a los microorganismos para restaurar el patrimonio histórico*

Medio de comunicación: Consejo Superior de Investigaciones Científicas (CSIC)

https://pti-pais.csic.es/crean-un-material-mas-resistente-a-los-microorganismos-para-restaurar-el-patrimonio-historico/